Acoustically and Electrokinetically Driven Transport in Microfluidic Devices

A Thesis

Submitted to the Faculty

of

Drexel University

by

Ersin Sayar

in partial fulfillment of the

requirements for the degree

of

Doctor of Philosophy

August 2012

Office of Graduate Studies
Dissertation/Thesis Approval Form

This form is for use by all doctoral and master's students with a dissertation/thesis requirement. Please print clearly as the library will bind a copy of this form with each copy of the dissertation/thesis. All doctoral dissertations must conform to university format requirements, which is the responsibility of the student and supervising professor. Students should obtain a copy of the Thesis Manual located on the library website.

Dissertation/Thesis Title: Acoustically and Electrokinetically Driven Transport in Microfluidic Devices

Author: Ersin Sayar

This dissertation/thesis is hereby accepted and approved.

Signatures:

Examining Committee

Chair — Bakhtier Farouk

Members — E. Coşkun Kumbur; Young I. Cho; M. A. Wheatley; Hongseok Noh

Academic Advisor — Bakhtier Farouk

Department Head

ACKNOWLEDGEMENTS

I express my sincere gratitude to my advisor, Dr. Bakhtier Farouk at Drexel University, for his valuable guidance, support, encouragement and patience during my studies at Drexel University.

I am grateful to Dr. Hongseok Noh, Dr. Nicholas P. Cernansky, Dr. Young I. Cho, Dr. E. Caglan Kumbur, Dr. David L. Miller, Dr. Ryszard M. Lec and Dr. Joe P. Foley of Drexel University for their valuable advice on this thesis as committee members.

I acknowledge the financial support from the Turkish Ministry of National Education that provided me the opportunity to pursue my doctoral study.

I appreciate the help from the fellow laboratory members and peers at Drexel: Dion S. Antao, Nusair M. I. Hasan, Drs. Viralsinh H. Chhasatia and Nasir M. Uddin. I am also grateful to Dr. Abraham Meganathan and Madhaveswer Gentela of ESI US R&D for our collaborative work on extending solid mechanics model to include fully anisotropy.

I would like to thank my relatives Metin Durusoy, Saadet Oksuz and Sadettin Danis for their trust on me by signing the Turkish government's papers providing the financial support. I wish to express my special gratitude and sincerest thank to my parents and my sister for their understanding and encouragement during my stay at Drexel.

TABLE OF CONTENTS

LIST OF TABLES

LIST OF FIGURES

NOMENCLATURE

A_{max}	maximum wave amplitude (m)
c_{ijkl}	elasticity constant (N/m^2),
c_p	phase velocity of FPW, λf (m/s)
c_s	speed of sound (m/s)
d	membrane thickness (m)
D	electric displacement field (C/m^2)
D_i	diffusion coefficient of ions in electrophoresis (m^2/s)
e	electron charge (C)
e_{ijk}	piezoelectric stress constant (C/m^2)
E	electric field intensity (V/m)
f	actuation frequency (Hz)
F	faraday's constant (C/mol)
H	channel height (m)
$\boldsymbol{J}_i$	total flux of the i^{th} species in electrophoresis ($m^{-2}s^{-1}$)
k_b	Boltzmann constant (J/K)
L	channel length (m)
M_ρ	effective mass of the plate (kg/m^2)
n^0	local concentration of the sample plug in electrophoresis (m^{-3})
n^+, n^-	local concentration of positive and negative ions in electroosmosis and electrophoresis (m^{-3})
n_0	bulk concentration of positive and negative ions in electroosmosis and electrophoresis (m^{-3})

N_A	Avogadro number
N_{ions}	total number of species in the system in electrophoresis
p_0	ambient pressure (Pa)
p	pressure (Pa)
Re	Reynolds number, $\rho_f \frac{E_x \varepsilon_r \varepsilon_0 \zeta}{\mu} \frac{H}{\mu}$
S	strain (dimensionless)
t	time (s)
T	absolute temperature (K)
u_i	displacement component in the i^{th} direction (m)
u	displacement vector (m)
u_f	velocity component along x-direction (m/s)
$\overline{u}_{f,in}$	mean velocities at the channel inlet (m/s)
$\overline{u}_{f,out}$	mean velocities at the channel outlet (m/s)
$u_{f,max}$	maximum value of the membrane velocity (m/s)
U_{ref}	reference velocity in electroosmosis, $\frac{E_x \varepsilon_r \varepsilon_0 \zeta}{\mu}$ (m/s)
$\mathbf{v_f}$	velocity vector (m/s)
v_f	velocity component along y-direction (m/s)
$\dot{W}_E$	electrical Joule heating dissipated in the pump (W)
$\dot{W}_P$	pressure work output produced by the pump (W)
$\dot{W}_T$	total power consumed by the pump (W)
$\dot{W}_V$	viscous dissipation work (W)

$\dot{W}_{WAVE,AVG}$	power transmitted along the membrane by the flexural wave (W)
x_j	coordinate, i.e. x_1, x_2 and x_3 represents x, y and z
z_i	valence of ions in electroosmosis and electrophoresis (dimensionless)

Greek Symbols

β^{-1}	thickness of the viscous boundary layer (m)
γ	acoustic evanescent decay distance (m)
ε_0	permittivity of vacuum (C/mV or F/m)
ε_r	dielectric constant, relative permittivity (dimensionless)
ζ	zeta potential (V)
η	thermodynamic efficiency (%)
κ	Debye–Hückel parameter, $(2n_0z^2e^2/\varepsilon\varepsilon_0k_bT)^{1/2}$ (m^{-1})
λ	wave length (m)
Λ_0	molar conductivity (m^2S/mol)
μ	dynamic viscosity of the liquid (Ns/m^2)
$\mu_{ep,i}$	ionic electrophoretic mobility in electrophoresis, ez_iD_i / k_bT (m^2/Vs)
ρ	particle density (kg/m^3)
ρ_e	electric charge density in electroosmosis and electrophoresis (C/m^3)
ρ_f	density of fluid (kg/m^3)
ρ_{FPW}	average density of the composite membrane (kg/m^3)
σ_0	bulk conductivity (S/m)
τ	stress (N/m^2)

ϕ	electric potential (V)
ϕ_{inlet}	applied potential values along the inlet (V)
ϕ_{outlet}	applied potential values along the outlet (V)
ψ	electric double layer streaming potential in electroosmosis and electrophoresis (V)

Subscripts

EOF	electroosmotic flow
f	end of a cycle
FPW	flexural plate wave
i	at the beginning of a cycle
i, j, k, l	Einstein summation convention indices

Superscripts

E	at constant electric field
S	at constant strain
T	transpose

ABSTRACT

Acoustically and Electrokinetically Driven Transport in Microfluidic Devices

Ersin Sayar

Advisor: Dr. Bakhtier Farouk

Electrokinetically driven flows are widely employed as a primary method for liquid pumping in micro-electromechanical systems. Mixing of analytes and reagents is limited in microfluidic devices due to the low Reynolds number of the flows. Acoustic excitations have recently been suggested to promote mixing in the microscale flow systems.

Electrokinetic flows through straight microchannels were investigated using the Poisson-Boltzmann and Nernst-Planck models. The acoustic wave/fluid flow interactions in a microchannel were investigated via the development of two and three-dimensional dynamic predictive models for flows with field couplings of the electrical, mechanical and fluid flow quantities. The effectiveness and applicability of electrokinetic augmentation in flexural plate wave micropumps for enhanced capabilities were explored. The proposed concept can be exploited to integrate micropumps into complex microfluidic chips improving the portability of micro-total-analysis systems along with the capabilities of actively controlling acoustics and electrokinetics for micro-mixer applications.

Acoustically excited flows in microchannels consisting of flexural plate wave devices and thin film resonators were considered. Compressible flow fields were

considered to accommodate the acoustic excitations produced by a vibrating wall. The velocity and pressure profiles for different parameters including frequency, channel height, wave amplitude and length were investigated. Coupled electrokinetics and acoustics cases were investigated while the electric field intensity of the electrokinetic body forces and actuation frequency of acoustic excitations were varied. Multifield analysis of a piezoelectrically actuated valveless micropump was also presented. The effect of voltage and frequency on membrane deflection and flow rate were investigated. Detailed fluid/solid deformation coupled simulations of piezoelectric valveless micropump have been conducted to predict the generated time averaged flow rates. Developed coupled solid and fluid mechanics models can be utilized to integrate flow-through sensors with microfluidic chips.

1. INTRODUCTION

In the introduction chapter, background information on acoustically and electrokinetically driven transport in microfluidic devices, motivation of the present research, research objectives and an outline of the thesis are provided.

1.1 Background

Fundamental concepts on acoustically and electrokinetically driven transport in microfluidic devices are introduced in the following sections. Background information on electrokinetic flows and applications of acoustic wave sensors and actuators are presented. This information will help in introducing the motivations of the conducted research.

1.1.1 Electrokinetically Driven Flows

Electrokinetics or electrokinetically driven flows is the general term describing phenomena that involve the interaction between solid surfaces, ionic solutions and macroscopic electric fields. Two important classes of electrokinetics are electrophoresis and electroosmosis, where the motions of charged solutes (e.g., ions, DNA macromolecules, colloidal particles and solid bodies) and fluids, respectively, occur when an external electric field is applied to the system. All of the phenomena classified under the term electrokinetics are manifestations of the electrostatic component of the Lorentz force (on ions and surface charges) and Newton's second law of motion [1]. Electrokinetic transport exploits a combination of two driving mechanisms – electrophoresis and electroosmosis. Electroosmotic flow (EOF), or electroosmosis is the bulk movement of a solution (often an aqueous solution) past a charged solid surface

when an external electric field is imposed tangentially along the surface [2]. Electrophoresis is the migration of charged solutes (e.g., ions, DNA macromolecules, particles) in electrolytes under an applied electric field due to Coulombic force. Electrophoresis of charged solutes can be described as a simple balance between the electrostatic force and the viscous drag associated with its resulting motion. In an ideal situation, the EOF velocity profile exhibits a plug-like shape, which is desirable for sample solute transport and detection due to little hydrodynamic dispersion of samples. This velocity profile also makes electroosmosis available as a pumping method without involving significant pressure drop. In microfluidic devices, capillary electrophoretic transport is used extensively to control buffer flow and manipulate sample solutes [3]. Examples of capillary electrophoretic transport include particle manipulation, sample injection, separation, mixing, dilution/concentration, and reaction [4].

The schematic of the microchannel for electroosmotic and electrophoresis is shown in Figure 1.1. When a liquid phase containing positive and negative ions contacts a planar, charged surface (ζ, zeta potential), an electric double layer (EDL) field is established [5]. EDL field generates the fluid flow due to electrokinetic forces in electroosmotic flows. Once the electrical potential at the inlet (left boundary in Figure 1.1) is activated, the flow starts to move due to the interactions between the channel walls, buffer electrolyte and the external electric field. Cations (positive charged solutes) on a microchannel wall are pulled toward the anode (negative electrode) due to electrophoresis, generating electrokinetic flow; positively and negatively charged solutes are separated by differences in their electrophoretic mobilities. Depending on the rate of

electroosmotic flow, analytes may be attracted to a microchannel wall through electrostatic attraction.

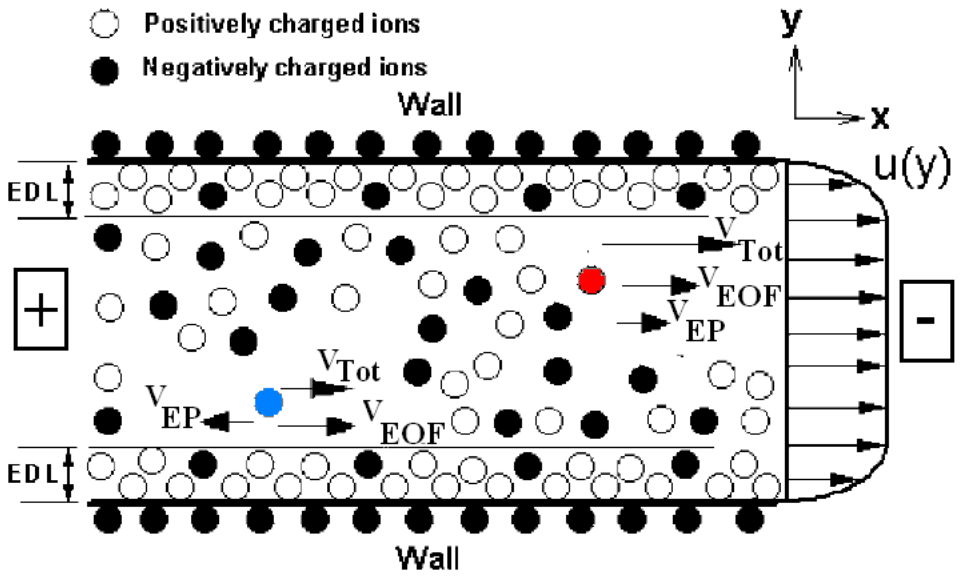

Figure 1.1 Schematic illustration of the electroosmosis-electrophoresis and generated velocity components [6]. Electroosmotic, electrophoretic and total velocity components are shown for a red (positive charged) solute and a blue (negative charged) solute.

Simplified flowfield relations are given below for electrokinetically driven flows in order to quantify each component of the flow (Figure 1.1). Total velocity (v_{Tot}) of each charged solute is the sum of the electrophoretic velocity (v_{EP}) and the velocity imparted by electroosmotic flow (v_{EOF}). Electrophoretic velocity is equal to:

$$v_{EP} = \mu_{ep} E = \frac{e z_i D_i}{k_b T} E \tag{1.1}$$

Electroosmotic flow velocity can be represented as:

$$v_{EOF} = \mu_{EOF} E = \frac{\varepsilon \varepsilon_r \zeta}{\mu} \mathrm{E} \tag{1.2}$$

Total velocity of each charged solute is:

$$v_{Tot} = \frac{ez_i D_i}{k_b T} E + \frac{\varepsilon \varepsilon_r \zeta}{\mu} \mathrm{E} \qquad (1.3)$$

where e is the electron charge, z_i is the valence of charges, D_i is the diffusion coefficient of ions in electrophoresis (m^2/s), k_b is the Boltzmann constant, T is the absolute temperature, E is electric field intensity, ε_0 is the permittivity of vacuum, ε_r dielectric constant, ζ zeta potential and μ dynamic viscosity of the liquid. Cations (positive charged solutes) are pulled toward the anode (negative electrode) yielding to a positive electrophoretic velocity, anions are repelled toward the cathode resulting in a electrophoretic velocity in the negative direction (Figure 1.1). Positively charged solutes have a higher total velocity than negatively charged solutes.

When a liquid phase containing positive and negative ions contacts a planar, negatively charged surface, an electric double layer (EDL) field is established. Therefore, the total potential field in the domain of interest comprises both the applied electric potential and the EDL field. In response to the surface charge generated at a liquid–solid interface, nearby ions of opposite charge in the electrolyte are attracted by the electric field produced by the surface charge, and ions of like charge are repelled in the immobile Stern layer [1]. The spontaneously formed surface charge therefore forms a region near the surface called an electrical double layer (EDL) (composed of Stern , Gouy-Chapman and diffuse layers) that supports a net excess of mobile ions with a polarity opposite to that of the wall. Figure 1.2 shows a schematic of the EDL for a negatively charged wall (e.g., as in the case of a glass surface). The electrostatic potential at the shear plane is called the zeta potential, ζ (Figure 1.2). An electric double layer is normally characterized by it. Shear plane is the boundary of the immobile Stern layer and it is also the boundary

of the fluid flow problem. The zeta potential typically determines flow velocities and flow rates in common thin EDL systems. This quantity can often be interpreted as an empirically measured mobility parameter that determines the local velocity of the flow at the top of the Gouy-Chapman layer.

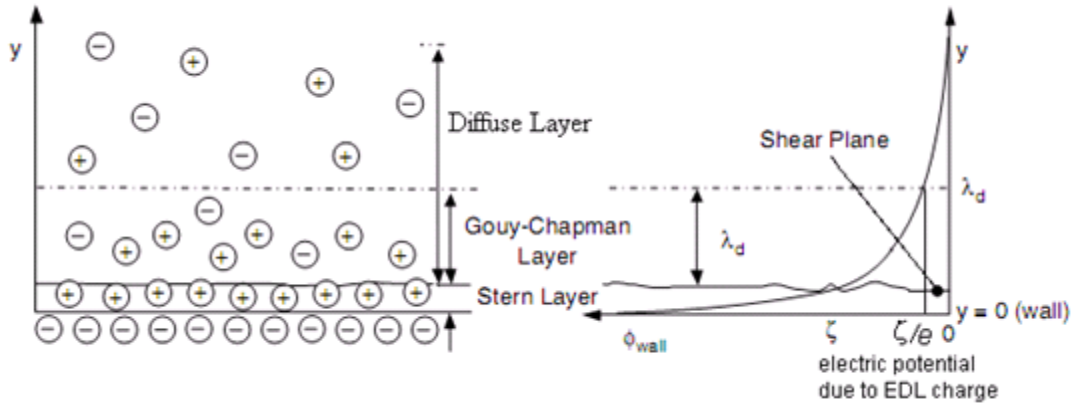

Figure 1.2 Schematic of the electrical double layer [1]. Electrical double layer is an important parameter in electroosmosis and electrophoresis.

Recently there has been a renewed interest in electrokinetic flow in capillaries due to its relevance to many microfluidic systems based on the lab-on-a-chip concept [7]. Microfluidic devices hold great promise for biomedical applications such as DNA sequencing, nucleic acid analysis, enzyme assays, and immunoassays [8, 9].

1.1.2 Acoustic Wave Sensors and Actuators in MEMS Applications

Fundamental concepts on acoustic wave sensors and actuators in microelectromechanical systems applications are introduced in the following sections. Background information on piezoelectricity, waves in piezoelectric elements, acoustic

wave sensors and actuators and acoustically excited flows in microchannels are presented.

1.1.2.1 Piezoelectricity

Acoustic waves are often generated by piezoelectric elements in microelectromechanical systems (MEMs) applications. The conversion of mechanical energy to an electric signal (voltage) and *vice versa* is known as the piezoelectric effect. The materials which exhibit piezoelectric effect normally have no center of symmetry in their structure. A stress applied to such materials will alter the separation between positive and negative charges and leads to net polarization at the surface. An electrical field with voltage potential is created in those materials due to this polarization This property can be used in an actuator, micropump, inkjet printer head, etc. [10]. Acoustic perturbations can be generated by the application of an alternating voltage signal to the transducers patterned on a piezoelectric substrate surface. A piezoelectric material deforms when an external electric field is applied. A sinusoidal voltage signal is applied at the input electrodes, which by the converse piezoelectric effect is converted to mechanical perturbations on the surface. The volume of the piezoelectric material reduces or expands depending on the polarization of the applied electric field.

1.1.2.2 Waves in piezoelectric elements

Acoustic waves in piezoelectric elements can be divided into two groups: bulk acoustic waves (BAWs) and surface acoustic waves (SAWs) [11]. A wave propagating through a piezoelectric substrate is called a bulk wave. A wave propagated on the surface of a piezoelectric substrate is known as a surface generated acoustic wave [12]. Acoustic devices are generally described by way of their wave distribution, either through or on

the surface of the piezoelectric substrate. Unlike BAW, which only interacts with the environment at the opposite surface of the material by traversing through it, SAW travels along or near the surface of the piezoelectric material [13].

Acoustic waves in a substrate differ in velocities, directions and strength of particle displacements within the substrate. Depending on the material (density, elasticity, electric permittivity, piezoelectric coupling coefficient, thermal expansion coefficient and orientation of the material) and boundary conditions (electric field, stress-strain and displacement), there can be different variants of acoustic waves [12]. Particle displacement represents the displacement of representative groups of atoms (similar to the representative volume element in a fluid) with respect to each other. For example, if a solid domain translates in space without any deformation all particle displacements will be zero.

The common types of acoustic waves considered in microfluidic devices, are shown in Figures 1.3a-d. The waves are propagating to the right and the traveling velocities (wave phase velocities) are also given in the figures. A longitudinal wave is a type of compression wave (Figure 1.3a). Compression waves travel with a wave phase velocity proportional to the square root of the ratio of elasticity to density. Therefore, they have the highest wave speed among the ones given in Figures 1.3a-d. Shear waves can be in horizontal or vertical (normal) directions. The schematics in Figures 1.3a-d are two dimensional (planar) representations and a shear horizontal wave is into or out of the plane of deformation (x-y plane). Therefore, only a bulk shear vertical wave is shown in Figure 1.3b. In Figure 1.3c, an idealized case for a surface generated acoustic wave propagating in semi-infinite solid is shown (Rayleigh wave). Wave motion typically

extends to a depth of about one wavelength for surface acoustic waves. If the substrate were plotted for a thicker piezoelectric element, deformation will only be observed within a depth of about one wavelength from the deforming surface (top surface in Figure 1.1c). Wave phase velocities are similar for bulk transverse waves and surface (Rayleigh) waves. In Figure 1.3d, thin solid plate waves are shown. Thin solid plate waves are different from surface acoustic waves because in thin solid plate waves propagating surface waves on to opposite sides (bottom and top surfaces in Figure 1.1d) of the piezoelectric element interact with each other.

Symmetric and anti-symmetric waves can be generated by plate waves. Anti-symmetric plate waves seen in flexural plate wave (FPW) devices are known as 'Lamb waves' [14-19]. Reducing the thickness of the anti-symmetric wave devices enables lowering the wave phase velocities. Lower wave velocity has the following practical significance: The devices with lower wave phase velocities can be operated at a lower actuation frequency compared to counterparts with similar mass sensitivity. Low thickness anti-symmetric wave devices are thus more useful in microfluidics applications than symmetric plate wave devices. Anti-symmetric thin solid plate waves (Lamb waves) in flexural plate wave devices are investigated in detail in the present doctoral dissertation.

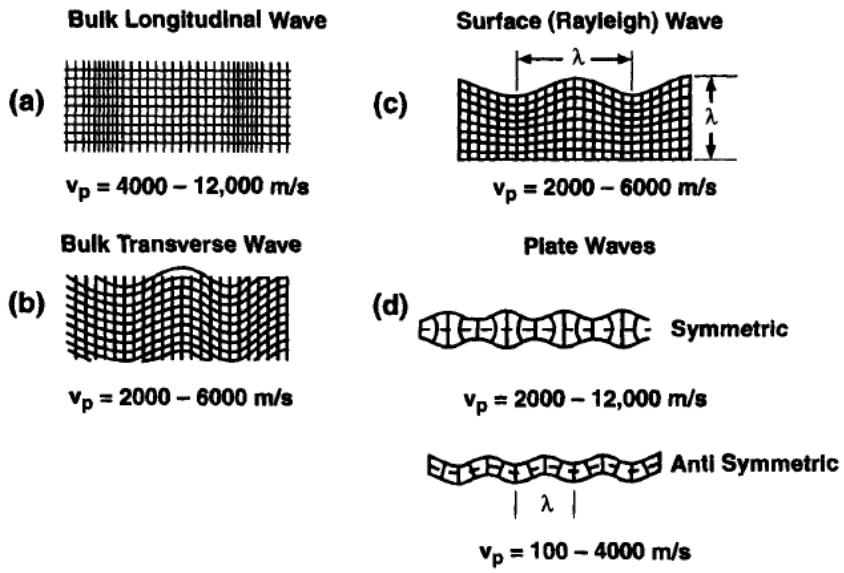

Figure 1.3 Cross-sectional representations of acoustic waves in solids [11]. Typical wave speeds, v_p, are shown below each sketch. a) bulk longitudinal wave. b) bulk transverse wave. c) surface wave. d) plate wave.

While all acoustic wave sensors will function in gases, only a few operate efficiently in liquids. Whether an acoustic wave sensor can operate in liquid is determined by the direction of the particle displacement at the surface of the device. A shear horizontal wave does not radiate appreciable energy into a liquid, allowing functionality without excessive attenuation [12]. Thickness shear mode resonator (TSM), shear horizontal acoustic plate modes (SH-APM), and shear horizontal surface acoustic wave (SH-SAW) are piezoelectric acoustic wave devices. These devices all generate waves that propagate primarily in a shear horizontal motion. Conversely, with few exceptions, SAW devices utilizing Rayleigh waves have a substantial surface-normal displacement that radiates compression waves into the liquid (causing excessive damping) and thus cannot be employed in the liquid phase as a sensor.

First approaches of the SAW sensors used either horizontally polarized surface acoustic waves (SH-SAW) in a delay line configuration on lithium tantalate ($LiTaO_3$) substrates or SAW resonator structures on quartz or $LiTaO_3$ with periodic mass gratings, namely "surface transverse waves" (STW) [20]. STW's have comparatively low attenuation values when operated in liquids. Later Love wave devices were developed, which used a film resonance effect to significantly reduce attenuation [20]. The advantage of higher sensitivity with SAW sensors, coupled with the ability for mass production using planar micro fabrication methods, are key factors responsible for the increasing interest in the SAW class of chemical sensors [11]. Shear horizontal acoustic plate mode (SH-APM) sensors, and flexural plate wave (FPW) sensors can be considered close relatives of SAW devices wherein a different type of wave or mode (plate wave or mode) is employed [15, 16, 19, 21-24].

1.1.2.3 Acoustic wave sensors and actuators

While waves in piezoelectric elements have been introduced in the previous section, common acoustic wave sensors and actuators that utilize the discussed waves are covered in this section.

The acoustic wave devices are in use in electronics for more than 80 years [20]. The use of acoustic wave devices includes timing and frequency control for applications that require extreme precision and stability such as mobile phones, satellite communications, and radio transmitters. Several of the emerging applications for these devices in the medical sciences (biological and chemical sensors) and industrial and commercial applications (vapor, humidity, temperature, and mass sensors) may eventually equal the demand of the telecommunications market [12].

The piezoelectrically actuated fan is a promising application of acoustic wave devices [25, 26]. A piezoelectrically actuated vibrating cantilever induces fluid flow by converting electrical energy to mechanical vibrations, which in turn agitate the surrounding fluid. Such a vibrating cantilever is referred to as a fan, as it provides localized cooling when the flow generated impinges on a heated surface, such as a heat sink mounted on a microelectronic device or a light-emitting diode (LED) package [25]. An electroacoustic technique for the application of electrokinetic measurements is also possible [27]. Ultrasound vibration potential and electrokinetic sonic amplitude can be correlated to the electrophoretic mobility of the sample.

Figure 1.4 below shows the configuration of typical acoustic wave devices. In Figure 1.4 top, bottom and side views of the acoustic sensors are shown. Wave motions are indicated by light arrows showing particle displacement directions and larger bold arrows showing wave propagation direction. The configuration of electrodes, geometry of the devices and deformation (particle displacement) are also sketched in Figure 1.4. Shear (transverse) waves have particle displacements that are normal to the direction of wave propagation. Shear waves can be polarized so that the particle displacements are parallel (also called shear horizontal) to the sensing surface (Figure 1.4, SH-SAW: Shear horizontal surface acoustic wave). Shear waves can be polarized normal to the sensing surface. Normal shear (or shear vertical) waves generated in a thin film resonator (TFR), which is also known as thin film bulk acoustic resonator (FBAR), are shown in Figure 1.4. Shear horizontal wave motion signifies transverse displacements polarized parallel to the sensing surface; shear vertical motion indicates transverse displacements normal to

the planar sensing surface (x-y plane in the present work). Each of these devices, shown schematically in Figure 1.4 uses a unique acoustic mode [11].

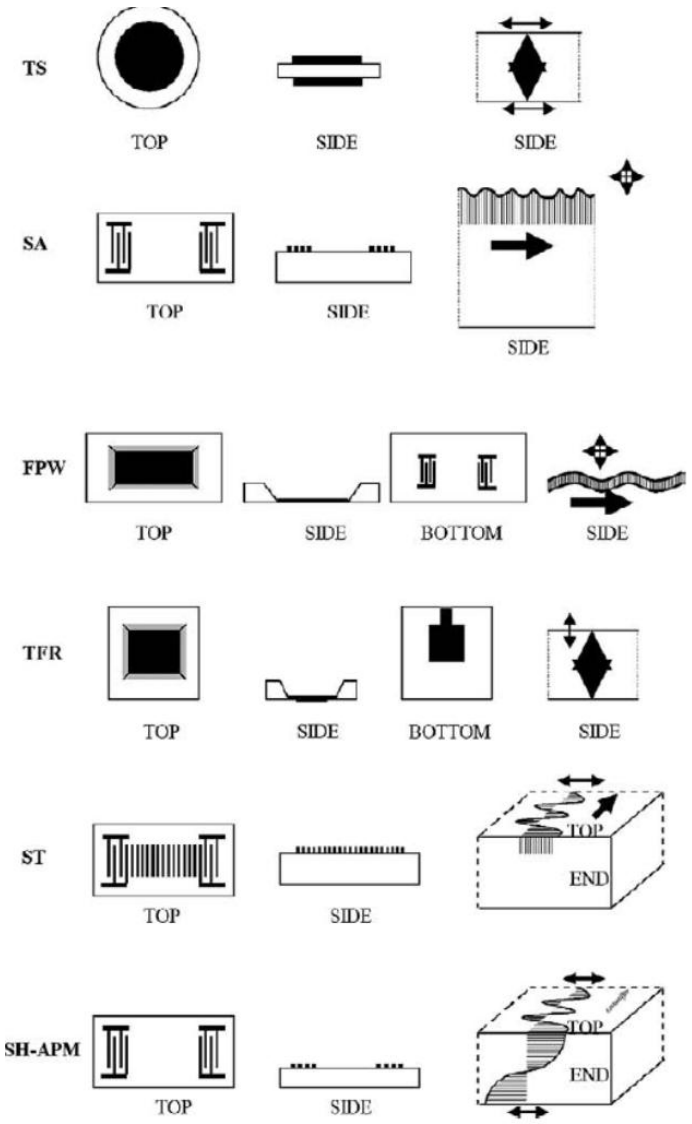

Figure 1.4 Schematic diagram showing various views of two bulk wave devices [12] (TS/TSM and FBAR), two surface wave devices (SA and SH-SAW), and two plate wave devices (FPW and SH-APM).

All acoustic wave devices are sensitive to perturbations of many different physical parameters. The change in the properties of the pathway over which the acoustic wave propagates will result in a change in the output signal. Devices based on piezoelectric elements, which allow transduction between electrical and acoustic energies, have been constructed in a number of configurations for sensor applications and materials characterization. The devices most commonly utilized for sensing applications are the thickness shear mode (TSM) resonator, the surface acoustic wave (SAW) device, the acoustic plate mode (APM) device, and the flexural plate wave (FPW) device [28]. The most broadly used surface wave devices are the SAW and shear-horizontal surface acoustic wave (SH-SAW) sensors, also recognized as the surface transverse (ST) wave sensor [20]. The thin solid plate waves are guided by reflection from multiple surfaces. Typical representatives of plate wave devices are flexural plate wave (FPW) and acoustic plate mode (APM) [12].

Type of the device, wave type generated, parameter determining the resonance frequency, resonance frequency (MHz), thickness *d* of substrate (μm), wavelength of the acoustic wave λ (μm), typical material, and medium of preferential use are given for acoustic wave sensors in Table 1.1 below [12]. Abbreviations used in the table are: TSM, thickness shear mode (i.e., QCM, quartz crystal microbalance); SAW, surface acoustic wave; ST, surface transverse wave; SH-APM, shear horizontal acoustic plate mode; FPW, flexural plate wave; and TRAW, thin rod acoustic wave.

Table 1.1 Comparison of selected acoustic wave sensors [12].

Type	Wave type	Parameter determining the resonance frequency	Res. freq. (MHz)	Thickness d of substrate (μm)	λ (μm) [1]	Material	Medium of preferential use
TSM (QCM)	Bulk, horizontal	Thickness	6	270	540	Quartz	Gas, liquid
SAW	Surface vertical	IDT spacing	158	760	20	Quartz	Gas
SH-SAW	Surface horizontal	IDT spacing	250	200	20	Quartz	Liquid, gas
Love	Surface horizontal	Thickness[2] IDT spacing	110	500	40	Quartz	Liquid, gas
SH-APM	Plate horizontal	Thickness IDT spacing	101	203	50	Quartz	Liquid, gas
FPW	Plate vertical	Thickness IDT spacing	5.5	3.5	100	ZnO	Gas, liquid
TRAW	Bulk longitudinal	Frequency[3]	1.95		50	Au	Liquid, gas

General information about the operational conditions and comparison of acoustic waves for the microfluidic devices can be found in Table 1.1. For the following discussions piezoelectric element is assumed to be quartz otherwise another one is specified. TSM resonator has a resonant frequency of 6.0 MHz and the thickness of the device is half wave length. Wave length is controlled by the interdigitated transducers periodicity and the selection of the wave length depends mostly on actuation frequency and other design parameters of the sensor/actuator device. TSM employs shear horizontal

[1] Wavelength
[2] Thickness d of wave guiding layer
[3] Frequency of coupling piezoelectric transducer

bulk waves. It can be used as a sensor in both gas and liquid mediums. Resonant frequency of surface acoustic wave (SAW) devices is controlled by the periodicity of interdigitated transducers (IDTs, electrode finger pairs). SAW sensors' resonant frequency can go up to 500.0 MHz. Unlike TSM resonators, resonant frequency is independent of the substrate thickness. SAW devices employ shear vertical surface waves. Shear horizontal SAW (SH-SAW) sensor's resonant frequency can also be as high as 500.0 MHz. Resonant frequency of SH-SAW device is controlled by the periodicity of IDTs only (independent of the substrate thickness). A SH-SAW device employs shear horizontal surface waves. It can be used as a sensor in both gas and liquid mediums. Sensors employing Love-mode of acoustic waves have resonant frequencies in the order of 110.0 MHz. The resonant frequency of the device is controlled by the periodicity of IDTs and the thickness of the guiding layer. A Love-mode device employs shear horizontal surface waves. It can be used as a sensor in both gas and liquid mediums. In order to operate properly at high frequencies the IDT spacing should be sufficiently small. IDT periodicity for the SAW, SH-SAW and Love-mode sensors are 20.0 - 40.0 μm. SH-APM device has a resonant frequency of 101.0 MHz and the thickness of the device is four wave lengths. SH-APM employs horizontally polarized plate waves. It can also be used as a sensor in both gas and liquid mediums.

1.1.2.4 Acoustically excited flows in microchannels

Acoustic waves in microfluidics applications are typically generated by applying an alternating voltage signal to transducers patterned on a piezoelectric substrate. The transducer geometry dictates the wavelength of the excited wave. The amplitudes of the acoustic waves depend on the applied voltage input, and are typically in the nanometer

range. Acoustic waves such as Rayleigh waves have a displacement component normal to the surface along the propagation direction. When in contact with a liquid, they tend to couple strongly with the liquid and leak ultrasonic power into the fluid in the form of acoustic waves called leaky acoustic waves. Acoustic waves propagating on the surface of a piezoelectric device can be used to induce acoustic streaming within the fluid [17, 21, 29-38]. Fluid motion induced from high-intensity sound waves is called acoustic streaming [39]. A typical microfluidic chip employs acoustic surface or bulk waves as a pumping mechanism for fluids. Piezoelectric substrate materials in the chip can efficiently convert an electric input signal into a mechanical acoustic wave confined to the surface layer of the substrate, hence the surface acoustic wave. In some devices, electric input signal can be converted into a mechanical acoustic wave influential in the bulk of the piezoelectric element, hence the bulk acoustic wave. The interaction of these waves with an adjoining fluid volume leads to streaming patterns in the fluid or of the motion of the fluid as a whole [32, 40].

1.2 Motivation

The efficient utilization of acoustically excited flows in microfluidic devices requires the understanding of wave propagation and fluid dynamics as well as the interaction of acoustic waves with the fluid in these systems. Most of the analytical techniques require simplification of second order effects such as backscattering, charge distribution, diffraction and mechanical loading [41]. However, these effects become significant for acoustic wave devices operating in the high frequency range. In the previous numerical models, perturbation theory derived parameters were used to predict time-averaged velocities and forces based on the continuum model of Nyborg [35]. These

models ignore the effect of liquid loading. It is hypothesized that a comprehensive understanding of the acoustic wave device-fluid interaction requires the development of fully coupled two or three-dimensional finite element fluid structure interaction models. All the above demonstrate the feasibility of finite element/finite volume models to adequately simulate acoustic wave actuator response under varying conditions.

The mixing of two or more fluids in microfluidic systems is important in biological processes like cell activation, enzyme reactions and protein folding. Mixing of analytes and reagents is difficult due to the low Reynolds number of the flows in electrokinetically driven transport in microscale devices. Various schemes to enhance micro-mixing have been proposed. Mixing in microchannels relies primarily on molecular diffusion or chaotic advection mechanisms. In passive devices, the length of the mixing channel is extended to ensure a well-mixed stream at the outlet. Chang and Yang hypothesized that effective mixing cannot occur in steady two-dimensional flows in microchannels [42].

Acoustic augmentation in low Reynolds number flow regimes can induce a flow transverse to the laminar flow that enhances the mixing of reactants [43-46]. In the present study the main goal is to generate acoustic perturbations to the surrounding fluid for pumping and mixing applications rather than observing the stimuli at an output transducer for sensor applications. Surface normal displacement is useful if one aims to mix confluent fluids or to pump fluids. Acoustic biosensors generally employ bulk acoustic waves (BAW) rather than surface acoustic waves because BAW devices generate waves that mainly propagate in the shear horizontal motion (to minimize the attenuation of the wave in the fluid) [13]. A shear horizontal wave does not radiate

significant energy into liquids, and it minimizes damping in the liquid operation. An exception to the shear horizontal wave requirement occurs for devices using acoustic wave modes that propagate at a velocity lower than that of sound in the liquid. Such modes do not couple with compressive waves in liquid and are thus relatively unattenuated [12]. In the past investigations [17, 21, 22, 47] of acoustically generated flows in microchannels, it was assumed that the acoustic radiation into the fluid would not occur. For the flows with acoustic excitations the energy dissipated by the oscillating wall is not only attenuated by the inertia and viscosity of the fluid, it is also attenuated through the density variations. Based on the above hypothesis, the compressibility of the fluid needs to be considered.

Micropumps are essential components in microelectromechanical systems (MEMS) based biosensors and in drug delivery systems. Transdermal drug delivery is an application where micropumps are often utilized [10, 48-54]. Fluid transport systems such as micrototal analysis systems, point of care testing systems and lab-on-a-chip systems are other applications of micropumps [52, 55]. In chemistry, micropumps are utilized to manufacture very small amounts of chemicals [56].

Piezoelectric elements coupled to thin diaphragms in contact with a fluid chamber are useful to induce fluid motion. Valveless micropumps are similar to diaphragm type positive displacement micropumps but they do not use check valves to direct flow and they can conduct particles without choking. The acoustic method is fast, efficient, and could be operated continuously with a high degree of selectivity and yield and with low power consumption [57]. Piezoelectric actuators have large actuation (displacement) and fast response times. Micropumps based on piezoelectric actuation exhibit high flow rates

and have grown to be the dominant type of micropumps in drug delivery systems and other biomedical applications [52]. Piezoelectrically actuated micropump design and analysis is a complex multidisciplinary problem with coupling in electrical, mechanical and fluid quantities.

Acoustic and electrokinetic effects are hypothesized to be complimentary in the present study. The simultaneous application of the two effects synergistically improve the performance of a microfluid device combining pumping, mixing and sensing functions all in the same device. The effectiveness and applicability of electroosmotic augmentation in flexural plate wave (FPW) micropumps for enhanced capabilities are investigated in the present research. Flow rates generated in FPW micro-scale flow systems are restricted especially when the channel height is greater than the acoustic wave length. The proposed device geometry is hypothesized to be exploited to integrate micropumps into complex microfluidic chips improving the portability of micro-total-analysis systems along with the capabilities of actively controlling acoustics and electrokinetics for micro-mixer applications. A multi-function microfluidic device where acoustic excitations can be used for mixing or sensing and electroosmotic flow generates the required pumping effect in flow-through sensors with microfluidic chips is investigated.

Although a lot of progress has been made in micropump research and performance of micropumps has been continuously increasing, there is still a need to incorporate various categories of micropumps in practical drug delivery and biomedical devices and this will continue to provide a substantial stimulus for micropump research and development in future. Detailed modeling of acoustically and electrokinetically driven transport in microfluidic devices can provide insight into the interplaying

electrical-fluidic and mechanical physical processes and the basic pumping characteristics (velocity, pressure, flow rate, stress, strain, force, voltage and power) that would be difficult to obtain via measurements. This would provide better utilizing of the micropumps and would also provide guidelines for optimizing the micropump design.

1.3 Research Objectives

Microfluidic devices utilizing acoustically and electrokinetically induced flows have been investigated throughout the present research. The overall objective is to develop predictive models for micropumps to be used in microchannels. The models should predict instantaneous velocity, pressure, electrical distributions and stress-strain distributions for electrokinetic flows, acoustically excited flows generated by piezoelectric elements and electrokinetic augmentation in acoustically excited flows in micro-scale systems. The developed models included the modeling of fluidic, structural and electrical fields. In the completed research, compressible form of fluid mass and momentum equations have been used to study propagation of acoustic waves in fluids. Acoustically excited flows driven by a moving wall were investigated and the effect of the amplitude, frequency and the wave length of the wall motion were studied. Poisson-Boltzmann and Nernst-Planck models have been used to study fluid dynamics characteristics of electrokinetic flows. In the Nernst-Planck multi-ion transport models, electrophoretic species transport effects are considered in the convective-diffusive transport equations (for ions and neutral species) with added body source terms. Electrokinetic flow models include mass and momentum conservation equations (with body forces due to electrokinetic effects), electric double layer streaming potential, applied electrostatic field and the distribution of ions, and neutral species (to account for

electrophoretic species transport). The electrokinetic flow models were used to study the effect of intensity of electrokinetic body forces and to study the effect of ionic strength of the electrolyte solution in microfluidic devices. Coupled fluid/solid deformation models have been developed to study flows generated by piezoelectric elements. Solid deformation models are developed for piezoelectric and non-piezoelectric domains including calculations in displacement, electric, stress and strain fields. Solid deformation/materials models have been modified to include full anisotropy. Normal and shear stresses in fluid and solid fields were coupled to simulate interactions of mechanical, electrical and fluid fields. Parametric studies were performed to investigate the effects of actuation potential and frequency, working fluid properties and pump back-pressure. Electrokinetic augmentation in acoustically excited flows is also investigated with coupled electrokinetically-acoustically excited flow models. The strength of the electrokinetic body forces and actuation frequency of the acoustic motion were parametrically varied to optimize resulting velocity fields, flow rates and thermodynamic efficiencies of electroosmotically augmented flows in flexural plate wave acoustic micropumps.

The objectives of the present research are:

- Development of electrokinetic flow models that predict the thermodynamic efficiency and flow rate produced in such systems.
- Development of acoustically excited flow models that consider compressible form of the mass/momentum conservation equations.

- Development of coupled electrokinetically and acoustically excited flexural plate wave micropump model to investigate the thermodynamic efficiencies and the generated flow rates.
- Development of piezoelectric actuators deflection models that consider full anisotropy of material elastic properties and coupling of electrical and mechanical variables in solid domains.
- Development of a coupling algorithm for coupled fluid/solid deformation models to be used for valveless piezoelectric micropumps simulations.

To a significant extent, the objectives were met in the present study. The completed work has resulted in two archived journal papers [23, 58], three conference papers [59-61], two journal papers under review and one additional journal manuscript in preparation.

1.4 Outline of the Thesis

The remaining chapters of the thesis are organized as follows. In Chapter 2, a detailed review of related past works on different important aspects of electrokinetically and acoustically driven transport in microchannels is described. The mathematical model and numerical methods adopted to develop electrokinetically and acoustically driven fluid flow models are described in Chapter 3. Solid deformation models developed for piezoelectric actuators are discussed in chapter 4. Chapter 5 is devoted to electrokinetic flows through microchannels. Electric potentials and velocity of the resultant flow in the electrokinetic flow systems are determined and presented considering body force terms based on Poisson-Boltzmann (equilibrium) model and Nernst-Planck (multi-ion)

transport model formulations. Chapter 6 describes acoustically generated flows in microchannel flexural plate wave sensors. The effect of the compressibility of the working fluids and comparison to computational and experimental results is also given in Chapter 6. Chapter 7 focuses on electroosmotic augmentation in flexural plate wave micropumps. The developed electrokinetic flow (Chapter 5) and acoustically excited flow (Chapter 6) models are also utilized in Chapter 7. In Chapter 8, solid deformation results for material deflection model validation studies are given. Extension of solid deformation model to include full anisotropy in material models is described in detail in Chapter 8. Chapter 9 describes two dimensional multifield analysis of a piezoelectric valveless micropump. Structural and fluid dynamics performance of the piezoelectric valveless micropump is investigated and coupling of solid deformation and fluid mechanics models is described in Chapter 9. In Chapter 10, results predicted with the developed three dimensional structural/fluid dynamic model are discussed and net flow rate predictions of the piezoelectric micropump are compared to the experiments. Finally Chapter 11 summarizes and concludes the research presented in this thesis with a discussion on the future work that might be undertaken.

2. LITERATURE REVIEW

In this chapter, the literature on “acoustically and electrokinetically driven transport in microfluidic devices” is reviewed. The discussions are given for applications involving micropumps (an overview), electrokinetic flows in microchannels, acoustically generated flows in microchannel flexural sensors, piezoelectric valveless micropumps and electrokinetic augmentation in flexural plate wave micropumps.

2.1 Overview of Micropumps

Microelectromechanical systems (MEMS) are a rapidly growing field which enables the manufacture of small devices using microfabrication techniques similar to the ones that are used to create integrated circuits [52]. In the last two decades, MEMS technologies have been applied to the needs of biomedical industry giving rise to a new emerging field called microfluidics.

Microfluidics, a technology of handling tiny volumes of liquids in the range of several nanoliters, has become increasingly important for biomedicine and biochemistry. According to a market report issued by Drug & Market Development, the microfluidic product revenues are forecast to grow by more than 50% per year through 2007 [56]. A report of System Planning Corporation estimated a microfluidics market of 3 to 4.5 billion US$ and an annual growth rate for scales of 25 percent–35 percent [62]. Microfluidics deals with design and development of miniature devices which can sense, pump, mix, monitor and control small volumes of fluids. The development of microfluidic systems has rapidly expanded to a wide variety of fields. The field of microfluidics [62] expanded to the development of numerous micro devices: filters,

mixers, reactors, separators. New effects such as electrokinetic effects, acoustic streaming, magneto-hydrodynamic effect, electrochemical, and more, which previously were neglected in macroscopic applications, now gained their importance in microscale. Principal applications of microfluidic systems are [52, 56] for chemical analysis, biological/medical and chemical sensing, drug delivery/discovery, molecular separation such as DNA-protein analysis, amplification, sequencing or synthesis of nucleic acids and for environmental monitoring. Microfluidic devices may be employed in chemical and microbiological analysis, in order to reduce analysis time and required sample volumes [22]. Microfluidics is also an essential part of precision control systems for automotive, aerospace and machine tool industries.

The use of MEMS for biological purposes (BioMEMS) has attracted the attention of many researchers [52]. There is a growing trend to fabricate micro drug delivery systems. MEMS based microfluidic drug delivery devices in general include microneedles based transdermal devices, osmosis based devices, micropump based devices, microreservoir based devices and biodegradable MEMS devices. Micropumps are essential components in microfluidic drug delivery systems. A micropump consists of the following components: diaphragm membrane, chamber, actuator, microchannels, microvalves, inlet, outlet, *etc* [63]. Micropumps can be categorized into two classes: one type has a moving part and is known as a mechanical micropump; the other has no moving part and is known as a non-mechanical micropump [10, 52, 54, 62]. The piezoelectric, electrostatic, thermopneumatic, electromagnetic, bimetallic, ion conductive polymer films (ICPF), phase change type and shape memory alloy (SMA) are examples of mechanical micropumps. Non-mechanical micropumps can be classified as magneto-

hydrodynamic, electrohydrodynamic, electroosmotic, electrowetting, bubble type, electrochemical and evaporation type .

Excitation voltages and flow rates of mechanical micropumps are shown in Figure 2.1. Excitation voltage is an important parameter of a micropump as it determines the electronics and other components to operate the device [52]. The values of flow rate and voltage are plotted on a logarithmic scale to facilitate comparison. Electrostatic, piezoelectric and thermopneumatic micropumps produce gradually higher flow rates at the expense of high-applied potential values. Micropump with conducting polymer film actuators (such as ICPF) appear to be promising mechanical micropumps which provide adequate flow rates at very low applied voltage. Bimetallic micropumps also require low voltage and provide adequate flow rates. Piezoelectric and electromagnetic mechanical micropumps have been reported extensively for microfluidic systems among the mechanical micropumps [10]. Electrostatic micropumps are easy to fabricate on integrated microfluidic systems but they require high operating voltage. The conducting polymer film actuator has an adequate flow rate at a relatively low operating voltage but with complex geometry. Mechanical micropumps require an external actuator. External actuators include [62] : electromagnetic actuators with solenoid plunger and external magnetic field, disk type or cantilever type piezoelectric actuators, stack type piezoelectric actuators, pneumatic actuators, and shape memory actuators. The most significant drawback of external actuators is their relatively larger dimension, which affects the overall size of the micro-pump. The advantage is the relatively large force and displacement generated by external actuators. Smaller thermo-pneumatic external

actuators can be integrated to reduce the size of the micropumps, but the pumped energy in mechanical pumps also decreases with the miniaturization.

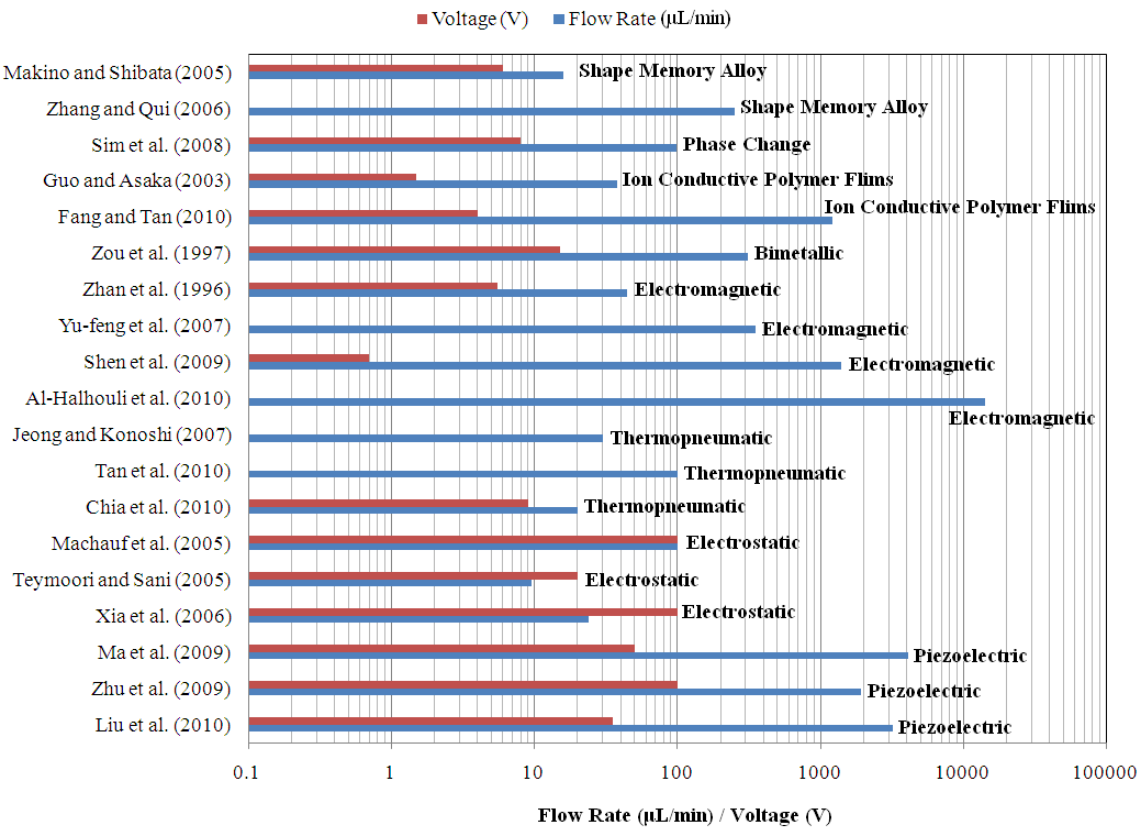

Figure 2.1 Comparison of voltage versus flow rate for mechanical micropumps [10].

Excitation voltages and flow rates of non-mechanical micropumps are shown in Figure 2.2. Electroosmotic micropumps require high operating voltages and produce low flow rates [52]. Electroosmotic micropumps are generally used in microanalysis systems where low flow rates are appropriate. Magnetohydrodynamic (MHD) and electrohydrodynamic (EHD) micropumps produce high flow rates at the expense of high operating voltages. MHD micropump has gained more attention in recent years and has

been presented by many researchers for microfluidic systems [10]. Electrowetting and electrochemical micropumps are promising ones which exhibit high flow rate at low applied voltage [52]. Working fluid properties also influence the flow rates and must be taken into account in choosing non-mechanical micropumps. Electroosmotic and magneto-hydrodynamic micropumps can handle many working fluids which are widely used in chemical and biological analysis. Electrochemical micropumps can also handle a variety of solutions such as insulin and neurotransmitter solution in drug delivery application.

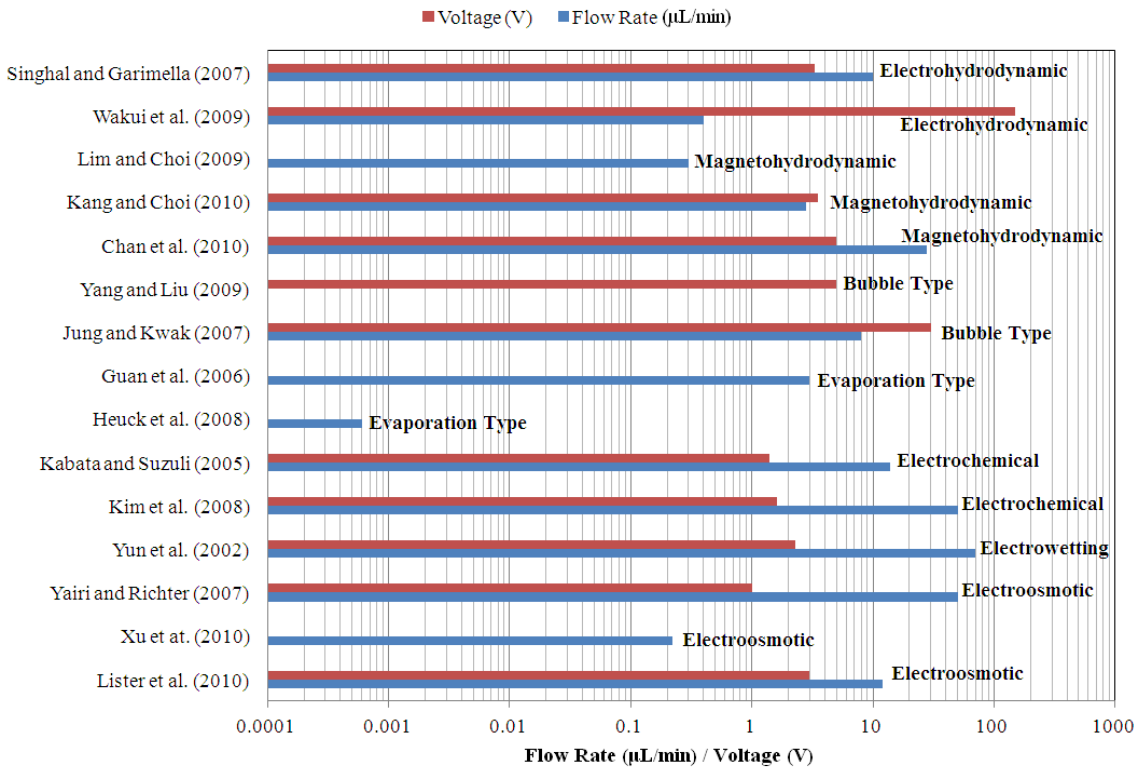

Figure 2.2 Comparison of voltage versus flow rate for non-mechanical micropumps [10]

Micropumps are used to administer small amounts of medication, such as insulin [56]. With MEMS technologies, it is now possible to fabricate small size and high performance devices or systems for processing, delivering, manipulating, analyzing, or constructing biological entities [64]. A number of BioMEMS devices and systems, such as biosensors, immunoisolation devices, drug delivery systems, microneedles and DNA analyzing systems, are already designed and fabricated. The drug delivery system has become a promising but challenging topic in BioMEMS (MEMS for biological applications) due to its commercial and research interests in health care [64]. It is well known that the drug delivery routes affect the therapeutic efficacy. Compared with the conventional drug delivery routes such as oral tablets or injection, the drug delivery system based on MEMS technologies is focused on the safer and more effective use of drugs. The general advantage of the drug delivery system is the possibility of small feature size and mass production at low cost, which is desirable to the commercial application. In order to better administrate the drug release, the controlled drug delivery system incorporating sensing components and micropumps has become more attractive. These systems not only can actively deliver drugs at any time, but also can accurately control the amount of delivered drugs to reduce the side effects of drugs. These advantages make it useful for the chemotherapy for cancer patients, insulin delivery for diabetic patients, chronically ill patients and so on [64]. In a DARPA sponsored collaborative research between M. D. Anderson Cancer Center and Lawrence Livermore National Laboratory [56], micropumps are used to supply one microliter samples of human cells into a microchannel for cell separation, sensing and identification, as a means of cancer treatment. Transdermal drug delivery is an application where

micropumps are often utilized [10, 48-54]. Micropumps are also an essential component in fluid transport systems such as micrototal analysis systems (μTAS), point of care testing (POCT) systems or lab-on-a-chip [52, 55]. Micropumps are used as a part of an integrated lab-on-a-chip consisting of microreservoirs, microchannels, micro filters and detectors for precise movement of chemical and biological fluids on a micro scale. Point of care testing (POCT) system is a μTAS to conduct diagnostic testing on site close to patients to provide better health care and quality of life. In such diagnostic systems, MEMS micropumps are integrated with biosensors on a single chip. In chemistry, micropumps are utilized to manufacture very small amounts of chemicals [56].

2.2 Electrokinetic Micropumps

Electrokinetic micropumps utilizing electroosmosis and electrophoresis through microchannels are generally used in microanalysis systems where low flow rates with a high precision are required [52]. Electrokinetic micropumps can handle many working fluids which are widely used in chemical and biological analysis. Electrokinetic flow plays a very important part in many separation processes, e.g., in the separation of biological particles, including DNA and protein [65]. In these microfluidic systems the target chemical species are delivered by activating electroosmotic flow [7]. Electrokinetic flow describes fluid motion that is induced by an applied electric field, and that is therefore different from the traditional pressure-driven flow [65]. In the traditional pressure-driven flow, when the velocity field is in a steady state, a parabolic shape is assumed for the velocity profile. In an electric-driven flow, an external electric field acts on the net fluid charge of a fluid in the vicinity of the wall and produces a body force that then drives fluid motion. Since the Reynolds number of the fluid motion is low, even the

fluid region that is gradually far away from the wall is prompted into motion due to the effects of viscosity. When the velocity field is in steady state, the shape of the velocity profile in the fully developed region is flat, i.e., it is quite different from the parabolic shape witnessed in traditional pressure driven flow. Since hydration causes the wall of the silica microchannel to be negatively charged at most pH conditions, an accumulation of positive ions (counter-ions) occurs in the aqueous solution adjacent to the wall. This counter-ion rich region is referred to as the electrical double layer (EDL). The potential between the wall and this buffer is known as the zeta potential, ζ . Electroosmotic flow is induced when an electric field is imposed through the electric double layer, where the separation of positive and negative ions occurs because of the zeta potential at the microchannel wall [7]. Electrophoresis is the migration of charged solutes (e.g., ions, DNA macromolecules, particles) in electrolytes under an applied electric field due to Coulombic force. When an electric field is applied tangentially to the EDL, diffuse layer of the EDL is drawn toward the negative electrode resulting in an electroosmotic flow (EOF) in the same direction [65]. The magnitude of the EOF can be approximately expressed as a function of its velocity, i.e., $V_{EOF} = (\varepsilon\zeta /\mu)E$, where ε is the dielectric constant of the fluid, ζ the zeta potential, μ the viscosity, and E the applied electric field intensity. From the expression above, the magnitude of EOF is directly related to the zeta potential, which is a function of the ionic valence, the ionic concentration of the electrolyte solution, and the surface properties of the microchannel wall. The electric force acting on the ions is the driving force of the electroosmotic flow [7]. For a system with a simple electrolyte solution and a homogeneous channel wall, the zeta potential is considered to be uniform [65].

One of the following three models is adopted in the analysis of electrokinetic flows; the Nernst–Planck (NP) model, the Debye–Hückel (DH) model and the Poisson–Boltzmann (PB) model [7]. In the Nernst–Planck model the conservation equations for the cations and anions are solved coupled with the Navier–Stokes equation to find the electric potential in the electric double layer induced by ionic unbalance near the wall [66]. Though the most rigorous model, it is difficult to solve the NP model numerically due to the strong nonlinear couplings between velocity, ion concentrations and the electric potential induced by the ionic unbalance. A commonly accepted approximation to the Nernst– Planck model is the Debye–Hückel model [67]. The DH model can be derived from the NP model when the zeta potential is small. Under many circumstances the ionic distribution in the electric double layer is not disturbed at a fixed zeta potential, and it follows the equilibrium Boltzmann distribution. In these cases the induced electric field is governed by the Poisson–Boltzmann equation and is decoupled from the velocity field, resulting in the Poisson–Boltzmann model which is the most widely employed model in the analysis of electroosmotic flows due to its simplicity [7].

There are attempts to vary wall zeta potential directly by imposing external electric field at the microchannel wall in the literature. When an electric field is applied perpendicular to the channel, a radial electric potential gradient is created across the insulating channel wall that allows the direct control of the zeta potential and the resulting electrokinetic flow. The use of insulating walls (should be ultrathin) allows significantly small voltages to create extraordinary fields required to have effective field-effect flow control. It is also reported [7] that application of a AC voltage across the channel wall generates electroosmotic flows, resulting in pumping or mixing of fluids.

For the analysis of electroosmotic flows generated by the temporally varying zeta potential, as in the above applications, most investigators have adopted the Debye–Hückel model which permits analytic solutions in certain flow configurations. However, the DH model is valid only for small values of zeta potential.

In an ideal case, the electroosmotic flow velocity field exhibits a plug-like shape, which is attractive for sample transport and detection due to little dispersion of samples. In practice, peak dispersion can diminish the performance of a eloctroosmotic flow based detection and separation system. Peak dispersion (also known as band broadening) is the effect of spreading of the chromatographic band while it moves though the microfluidic channel. Peak dispersion occurs due to numerous reasons such as longitudinal diffusion, sample overloading, adsorption of species on capillary walls, adhesion of some particles to the channel wall, pollution caused by the chip-producing process nonuniform zeta potential and electric field, nonuniform geometry, and Joule heating [8, 65].

Micro total analysis systems with electrokinetically driven flows can provide several advantages over bulky instruments. Therefore, electrokinetic flows are widely utilized as a primary method for liquid transport and sample separation in a number of biological and chemical analysis systems. Solving for the electrokinetic velocity field in complex geometries requires a solution of the electric field and charge density in the microchannel, together with a solution to the Navier–Stokes equations [5, 68-73]. Regarding the charge density, both nonlinear and linear forms of EDL field equations with a body force term added to Navier-Stokes equations are widely used in the literature. Another approach is assuming the “Helmholtz–Smoulochowski” slip velocity and not dealing with the EDL field and charge density at all. However, slip velocity approach is

only sufficient for so called linear electroosmosis. The analysis by Zhang et al. [74, 75] shows that the induced pressure distribution is the key to understanding the experimentally observed phenomena of leakage flows. A way of determining the static pressures at the inlet and outlet of microchannels is also proposed by Zhang et al. that takes account of the pressure losses due to flow contraction and expansion. These commonly neglected local pressure losses at the channel entrance and outlet are shown to be important in accurately describing the flow [76].

2.3 Acoustically Excited Flows in Microchannel Flexural Plate Wave Micropumps

Relevant literature review is reported for acoustically generated flows in flexural plate wave micropumps. The present literature review focuses on produced net flow and the effect of compressibility in such systems. Sankaranarayanan et al. [34] presented a computational and experimental study of the acoustic streaming induced by SAWs. A coupled fluid-structure interaction model of a SAW device based on a piezoelectric substrate, YZ-$LiNbO_3$ (Y cut - Z propagating lithium niobate) in contact with a liquid (water) was developed to study the surface acoustic wave interaction with fluid loading. The simulation results [34] predicted strong coupling of surface waves on the substrate with the thin liquid layer causing wave mode conversion from Rayleigh (SAW) waves to leaky SAWs. The coupling led to acoustic streaming. Trends in acoustic-streaming velocity were predicted for varying design parameters such as excitation voltage, device frequency, fluid viscosity and density.

Moroney et al. [17] experimentally observed pumping of water induced by 4.7 MHz flexural plate waves (Lamb) waves traveling in a 4.0 μm-thick composite membrane of silicon nitride and zinc oxide. The observed pumping speed was determined

to be proportional to the square of the wave amplitude. Acoustic streaming induced by ultrasonic flexural vibrations and the associated convection cooling enhancements were investigated by Loh et al. [21]. Analysis based on Nyborg's formulation was performed along with incompressible computational fluid dynamics (CFD) simulations. Acoustic streaming velocities obtained from CFD simulation based on the incompressible flow assumptions exceeded the theoretically estimated velocity by a factor ranging from 10 to 100, depending upon the location along the membrane. Both CFD simulation and analytical studies revealed that the acoustic streaming velocity is proportional to (square of) the vibration amplitude and the wavelength of the vibrating membrane. Acoustic streaming velocity decreased with the excitation frequency. Acoustic streaming pattern, streaming velocity, and associated heat transfer characteristics were experimentally observed. Using acoustic streaming, a temperature drop of 40 °C with vibration amplitude of 25.0 μm at 28.4 kHz was experimentally achieved.

Numerical simulations of a micromachined pump based on acoustic streaming in water has also been reported [22, 47]. Influences of channel height, wave amplitude, and backpressure on the velocity profile and flow rate were investigated assuming incompressible flow. Tsai and Leu [47] numerically investigated micropumping system generated by a traveling wave for a flexural plate wave (FPW) device. The time averaged velocity profiles over one period became a parabolic velocity profile when the channel height was less than l00 μm. When a channel height was greater than 200 μm, the time averaged velocity profiles deviated from the parabolic velocity profile. The pressure wave confinement effect in a microchannel with height less than 100 μm was noticed. The frequency of the FPW pump was found to control the flow rate.

Acoustic streaming patterns are not provided for the entire microchannel in the literature. Aside from that, although the phase velocities of the perturbations are significantly lower than the speed of sound in the fluid, the effect of compressibility should be considered in some sense for the acoustic excitations.

2.4 Electrokinetic Augmentation in Flexural Plate Wave Micropumps

Related past works are reviewed and reported for electrokinetic augmentation in flexural plate wave micropumps. The significance of electrokinetic augmentation and a way to satisfy sufficient flow rates in micromixer applications are discussed in detail. An effective mixing in low Reynolds number flow regimes can be obtained by the chaotic advection mechanism. Acoustic excitations have recently been suggested to promote active mixing in the microscale flow systems [43-46, 77]. Acoustic perturbations in low Reynolds number flow regimes can induce a flow transverse to the laminar flow enhancing the mixing of reactants [43-46] by promoting chaotic advection mechanisms. Enhancement of mixing is especially evident in chemical microsystems in which the chemical reaction is performed on a solid phase and only one reactant is actually diffusing [45].

A numerical model of a micromachined pump based on acoustic streaming in water was presented in the literature [22, 47]. Acoustic perturbations can be produced in materials by piezoelectric transducers. Flexural plate wave (FPW) micropumps featuring Lamb waves (Rayleigh waves guided in layers) have the highest sensitivity to noise ratio [78]. The basic FPW micropump consists of a rectangular flow channel that has a thin membrane on the bottom. The composite membrane is made of low-stress silicon nitride, piezoelectric zinc oxide, and aluminum [22]. The discussion continues with the

previously reported acoustic active micromixers where active mixing comprising ultrasound/piezoelectric membrane action can be achieved by ultrasound using lead–zirconate–titanate (PZT) membranes [44].

Bengtsson and Laurell [45] proposed an acoustic method for inducing rotating vortex flows in microchannels. In their experimental study, an ultrasonic crystal was used to create an acoustic standing wave field in the channel and thus induced a Rayleigh flow transverse to the laminar flow in the channel where a transverse flow enhanced mixing of the reactants. A significant increase of the mixing ratio was detected in a narrow band of frequency for the actuating ultrasound. Hessel et al. [77] reported active mixing principles in microchannels. An ultrasonic micromixer was realized and tested by a dilution experiment, employing the dye uranine [44]. In the absence of ultrasonic mixing, two stable fluid regions with the separated water liquid and the uranine solution were found in the mixing chamber. Upon ultrasonic action, transverse flow occurred, moving material throughout the entire mixing chamber [44]. Initially, a concentration profile with step function at the fluid interface was displayed, while after ultrasonic actuation was executed a uniform concentration on a medium level was obtained throughout the mixing chamber [44]. Yasuda [43] experimentally investigated non-contact handling of micrometer-sized samples in the micro-chamber using acoustic radiation force for mixing the solutions. For mixing, samples such as erythrocytes and fluorescent dye were introduced into the chamber from the inlet which arranged at the side wall of the chamber and laminar flow of the two different kinds of solutions keeping their boundaries was observed. When the 3.5 MHz ultrasound irradiation into the chamber started, the boundaries of the flow of the two samples were broken and the erythrocytes spread and

mixed into all the span of the chamber. The possible damage caused by the 3.5 MHz ultrasound during the mixing process was also measured, and no significant release of the erythrocyte's component was detected. The results suggested the potential use of acoustic radiation force for micro-chamber as a sample preparation process.

Effective mixing can be provided by acoustic excitations in micro-scale systems. However, flow rates generated in such micro-scale flow systems are restricted especially when the channel height is greater than the acoustic wave length. An external syringe pump is often used to generate sufficient flow rates. The study by Tseng et al. [46] considers electrokinetic augmentation to an existing acoustically excited surface acoustic wave (SAW) base flow. Results of [46] present an active method for micro-mixers using surface acoustic waves to rapidly mix co-flowing fluids. Effectiveness and applicability of electrokinetic augmentation in microelectromechanical systems for enhanced pumping and mixing capabilities is also explored in [46]. Tseng et al. report on layouts in which the source of the SAW actuation is placed outside the mixer channels to eliminate any high temperature increase. The experimental results confirm that the proposed electrokinetically augmented SAW micro-mixer provides a high degree of flow control and enhanced mixing performance. The duration of mixing process, the mixing efficiency and the resulted product of the biochemical reaction are improved. Therefore, the developed micro-mixers in [46] can be applied in microfluidic systems for improving mixing efficiency and thus enhancing the reaction.

Acoustic streaming patterns are not provided for the entire microchannel in the literature. The effect of compressibility should be considered in some sense for the acoustic excitations. Regarding the charge density, nonlinear form of EDL field equations

with a body force term added to Navier-Stokes equations should be implemented in the model. The static pressures at the inlet and outlet of microchannels should be refined in order to take account the local pressure losses due to flow contraction and expansion at the channel entrance and outlet.

2.5 Piezoelectric Valveless Micropumps

Literature review is reported below for acoustically generated flows by a thin film bulk acoustic resonator with emphasis to generated net flow, the deformation and electrical field inside piezoelectric elements.

In the review by Nabavi [79] , the recent advances in the numerical and experimental analysis of the steady and pulsating flows through microdiffusers and valveless micropumps were surveyed. The differences between the performance of microdiffusers and micropumps in steady and unsteady flow regimes were described. The use of experimental flow visualization of steady and pulsating flows through microdiffusers and micropumps as a useful tool for better understanding the underlying micro-fluid dynamics was also discussed. Ullmann [80] presented an analysis of the performance of single chamber and double chamber piezoelectric valveless pumps under the different combination modes possible such as a series connection and a parallel connection by a lumped mass model. The pump performance for a parallel and a series connection was analyzed under constant inlet and outlet pressures. It was shown, that a series connection usually is advantageous to a parallel connection even for the purpose of increasing the flow rate (for fixed pressure difference). The model was tested against experimental data and showed good agreement. Olsson et al. [81] presented a lumped-mass model for valveless diffuser pumps. The model was tested for different previously

reported valveless diffuser pumps and shows good agreement with the experimental results. The model predicts the flow–pressure characteristics for different excitation levels. The flows and pressures inside the pump were investigated for 6 different valveless diffuser pump configurations. Morris and Forster [82] showed an exact unsteady solution to the Navier-Stokes equations for the investigation of valveless diffuser pumps. Optimal valve size and best valve shape for maximal valve action over a target Reynolds number range were determined with a low-order linear model. Agreement with experiment using pumps with Tesla-type valves was within 20 percent. Gamboa et al. [83] presented a method for optimizing valve shape using two-dimensional computational fluid dynamics. A Tesla-type valve was optimized using a set of six independent, non-dimensional geometric design variables. The result was a 25% higher ratio of reverse to forward flow resistance averaged over the Reynolds number range $0<Re<2000$ compared to calculated values for an empirically designed, commonly used Tesla-type valve shape. Prototype plastic pumps were fabricated and tested. Steady-flow tests verified the predicted improvement in forward flow resistance. The large performance increase observed demonstrated the importance of valve shape optimization in the overall design process for fixed-valve micropumps. Nisar et al. [52] briefly overviewed MEMS-based micropumps and their applications in drug delivery and other biomedical fields. Actuation methods, working principles, construction, fabrication methods, performance parameters and their medical applications was presented. Various performance parameters such as flow rate, pressure generated and size of the micropump were investigated to optimize an appropriate micropump for a particular application. Generated net flow in micropumps is experimentally investigated and reported in [22, 34,

84]. Experimental studies of hydrodynamics by Jang et al. [84] at the first and at higher resonant modes revealed the expected bulk fluid motion associated with the mode shapes.

Piezoelectric micropumps with flow rectifiers (valveless piezoelectric micropumps) have several advantages:

- Higher pump flow performance than micropumps based on passive check valves [63]
- Low fabrication costs due to the uncomplicated structure,
- A gentle pump principle with no moving mechanical valves, heat and strong electric field involved [62],
- Possibility of pumping any sample (gases, liquids and fluids with solid particles) [64, 85],
- Reduced risk of clogging,
- Compactness,
- Reduced risk of reduction in performance and reliability due to wear and fatigue,
- High frequency response,
- High precision,
- Ease to control [46, 52].
- Low fluid pressure loss along the flow rectifiers comparing to check valves,
- The possibility to have a high excitation frequency,
- Low power consumption [57].

In almost all of piezoelectric actuator applications, bulk piezoelectric substrates are adopted, such as lithium niobate ($LiNbO_3$), quartz, langasite (LGS) and lithium tantalate ($LiTaO_3$). Bulk piezoelectric materials are incompatible with planar integrated circuit technology [52]. Layered piezoelectric acoustic devices are developed to overcome the limitation [86]. Piezoelectric micropumps exhibit small stroke volume at high voltages [10]. The comparatively high actuation voltage and small stroke, i.e. displacement per unit length are regarded as the disadvantages. Piezoelectric actuator shows large deflection and fast response time, but the fabrication of such materials is complicated on a single chip. No mechanical micropump was able to generate a flow rate less than 1µl/min accurately, due to the large viscous forces and their relatively large size [62].

Following design rules are given in [62] to maximize the pump flow with mechanical pumps with check valves or with flow rectifiers:

- Minimize the dead volume by using thinner spacer or wafer,
- Maximize the pump pressure by using actuators with large forces,
- Maximize the stroke volume by using actuators with large stroke or more flexible pump membrane,
- Minimize the critical pressure by using more flexible valve design or valve material with small Young's modulus.

Small dead volumes and large actuation forces in piezoelectric actuators and possibility of thin pump chamber membranes make piezoelectric micropumps attractive

tools in microfluidics. Mechanical micropumps based on piezoelectric actuation have grown to be the dominant type of micropumps [52] in drug delivery systems. Piezoelectric actuation is reasonable based on the performance and size needed for the microfluidics applications [62]. Piezoelectrically actuated valveless micropumps have simple structure and no internal moving valves, there is less risk of clogging the valves when it pumps fluid containing particles [56]. In the present work, optimization of the design of piezoelectric micropump has been done to achieve higher average flow rate with a lower excitation power.

Various factors other than excitation voltages and flow rates relevant to the selection of mechanical micropumps are [10, 46, 52, 62-64, 86]: generated pressure, stroke volume, size (compactness), ease of fabrication- suitability for mass manufacturing, fabrication costs, biocompatibility, pump energy per stroke, high frequency response, high precision and ease to control, robustness, presence of moving parts/heat and strong electric fields, risk of clogging, operation with various types of fluids, and resistance to wear and fatigue. Mechanical micropumps based on piezoelectric actuation have grown to be the dominant type of micropumps [52] in drug delivery systems. Piezoelectric actuation is reasonable based on the performance and size needed for the microfluidics applications [62]. Optimization of the design of piezoelectric micropump has been done to achieve higher strokes at lower voltages in the present work.

A design that uses the shear deformation of a lead zirconate titanate actuator to deflect a diaphragm was proposed by Chen et al. [87]. The theoretical results were compared with the numerical solutions generated by ANSYS and verified by

experiments. The paper by Nguyen and White [22] presents design issues and a numerical model of a flexural plate wave pump . Influences of channel height, wave amplitude, and back pressure on the velocity profile and flow rate are investigated. Thermal transport effects of the acoustic streaming were also discussed in order to integrate a thermal flow sensor into the pump or to apply the pump for cooling purposes. A one-way coupled dynamic model was developed by Cui et al. [64] for the valveless micropump based upon mass conservation. The simulation results showed that the performance of the micropump is related to the stroke volume of the pump diaphragm. The simulations also reveal that there is an optimal thickness of the piezoelectric layer (at 500 V/mm electric field). The effects of the geometrical dimensions on the micropump characteristics and on the micropump efficiency were also analyzed by the same group [88]. The simulation results show that there is an optimal thickness of the piezoelectric layer appropriate for obtaining a large pump flow. Nisar et al. [53] predicted the performance of the micropump considering the diffuser length, diffuser neck width and diffuser angle. They concluded that the excitation voltage is the more dominant factor that affects the flow rate of the micropump as compared with the excitation frequency. However, at extremely high excitation frequencies beyond 8,000 Hz, the flow rate was found to drop as the diaphragm exhibits multiple bending peaks which are not desirable for fluid flow. The numerical study by Fan et al. [56] reported the performance of a piezoelectrically actuated valveless micropump. Simulation of the piezoelectrically actuated valveless micropump indicated that the bi-layer membrane deflection amplitude increases with the increase of the actuating frequency in a low frequency range (< 7500 Hz). However, because of the electro-mechanical–fluid couplings, the membrane deflects

in an undesirable way at high frequencies. The study by Jeong and Kim [89] compared two different numerical models, the fluid structure interactive (FSI) model and the prescribed deformation model, for the evaluation of the performance characteristics of a diffuser-nozzle based piezoelectric micropump. It was found that the behavior of the membrane computed with the FSI model is not in accordance with that computed with the prescribed deformation model, and that the net flow rate in the FSI model is larger than that in the prescribed deformation model.

The efficient utilization of acoustic streaming in acoustic wave devices requires the understanding of wave propagation and fluid dynamics as well as the interaction of acoustic waves with the fluid in these systems. The effects such as backscattering, charge distribution, diffraction and mechanical loading become significant for acoustic wave devices operating in the high frequency range. Previous attempts to address utilization of acoustics in microfluidics devices used simplified analytical models treating the leaky wave as a first-order perturbation on the nonleaky wave associated with surface-wave propagation (or bulk wave propagation). A surface wave such as Rayleigh waves leak some of the energy to the adjoining liquid hence the term “leaky” is used. Previous numerical models used perturbation theory derived parameters to predict streaming velocities and forces based on the continuum model of Nyborg [35]. However, these models ignore the effect of liquid loading and viscous dissipation, owing to simplification of the Navier–Stokes equation. A comprehensive understanding of the acoustic wave device-fluid interaction and the effectiveness of inter-digitated transducer (IDT) configurations in acoustic streaming enhancement require the development of fully coupled two or three-dimensional finite element fluid structure interaction (FSI) models.

All the above demonstrate the feasibility of finite element/finite volume models to adequately model acoustic wave actuator response under varying conditions.

2.6 Applications of Piezoelectric Micropumps

Piezoelectric micropumps have a wide range of practical applications. Micropumps for transdermal insulin delivery, artificial sphincter prosthesis, antithrombogenic micropumps for blood transportation, micropump for injection of glucose for diabetes patients and administration of neurotransmitters to neurons and micropumps for chemical and biological sensing have been reported [52]. Piezoelectric micropumps are also investigated for other drugs for transdermal drug delivery [50-53] applications.

Due to the lack of internal moving valves one can expect advantages of the valveless piezoelectric micropump principle such as simplicity, robustness and high reliability [63]. The valveless piezoelectric pump principle described in the present doctoral thesis has many potential applications. One possibility is as a pump in a local liquid cooling systems of electronics [63]. Micropumps based on piezoelectric actuation exhibit high flow rates and have grown to be the dominant type of micropumps in drug delivery systems and other biomedical applications. Although a lot of progress has been made in micropump research and performance of micropumps has been continuously increasing, there is still a need to incorporate various categories of micropumps in practical drug delivery and biomedical devices and this will continue to provide a substantial stimulus for micropump research and development in future [52].

There is an increasing demand to develop drug delivery devices to meet medical needs. The use of micro electromechanical systems (MEMS) technology can be implemented to resolve the needs. The application of MEMS technology to develop drug delivery devices is advantageous for:

- The medical needs of site specific drug delivery,
- Reduced side effects,
- Increased biocompatibility and
- Increased therapeutic effectiveness [10, 48, 49, 52, 53, 64, 88].

A total drug delivery system consists of a drug reservoir, micropumps, valves, microsensors, microchannels, and necessary circuitry. A typical micropump is a MEMS device, which employs an actuation source to transfer the liquid from the inlet reservoir to the outlet reservoir. Micropumps and microneedles are essential components for such biomedical systems. Micropumps are used for fluid transport and microneedles provide interface between drug reservoir and patient body. Material selection is a critical issue in biomedical devices [10]. Si has been widely used as material for such microfluidic devices, but polymeric materials like PGA, PDMS, PMMA, PLLA, PLA, PC, *etc*. are replacing Si due to biocompatibility, low cost, ease of fabrication and excellent structural properties. Various factors are important during the selection of micropumps for particular biomedicine applications. Operating voltage, pressure and flow rate of micropumps are critical issues to analyze the performance and suitability of micropumps for certain medical applications. Material selection, operating voltage, pressure and flow

rate prediction models are developed for the valveless piezoelectric micropumps in the present study.

2.7 Relevance and Impact of the Present Research

Modeling of acoustically and electrokinetically driven transport in microfluidic devices poses significant challenges. While the solid deformation models are developed in a Lagrangian framework fluid models are in a Eulerian framework. Coupling these two models is complex. When the domain of the flow deforms, conservation of mass in such systems becomes harder to control numerically especially for the liquids which are practically incompressible. For flows with deforming boundaries, iteratively solved wall motions (solved with the solid deformation models) pose additional complexity when compared to flows with specified wall motions. With the solid/fluid mechanics coupled models, the deformation of the solids and the pressure-velocity fields in the fluids are both unknown. All these field equations must be solved simultaneously while considering coupling energy and force interactions among these fields.

Yeo and Friend [90] experimentally demonstrate that acoustic waves offer a powerful mechanism for driving a host of fast microfluidic actuation and micro/bioparticle manipulation schemes. Applications of acoustic excitations are not limited by the chemical and electrical composition of the solution or the charge distribution of the affected particles unlike electrokinetic mixing methods. A complex network of microchannels or a long mixing channel is not required in acoustic mixers (providing easy to fabricate and compact devices). By changing the power applied to the acoustic transducer the fluid on the top of it vibrates, translates, forms a long slender jet,

and, eventually atomizes, so the same device can be used for several applications [90, 91].

Acoustically excited flows in microchannels find applications in various processes ranging from:

- Microfluidic pumping,
- Micro particle positioning (concentration, separation or mixing),
- Transporting fluid droplets across a surface,
- Chaotic convection of droplets,
- Micromixing,
- Surface reactions,
- Sonic cleaning,
- Biological detection [90, 92].

Micro-scale acoustic wave devices are utilized as sensors, actuators and combined sensor/actuator devices. Piezoelectric elements coupled to thin diaphragms in contact with a fluid chamber are useful to induce fluid motion. Piezoelectrically actuated valveless micropumps have a wide range of practical applications:

- Micropumps for transdermal insulin delivery,
- Artificial sphincter prosthesis,
- Antithrombogenic micropumps for blood transportation,
- Micropump for injection of glucose for diabetes patients ,
- Administration of neurotransmitters to neurons,

- Micropumps for chemical and biological sensing,
- Micropumps for transdermal drug delivery [50-53] for drugs (other than insulin).

In the past investigations [17, 21, 22, 47] of acoustically generated flows in microchannels, it was assumed that the acoustic radiation into the fluid would not occur. However, Weinberg et al. [24] noted that fluid effects on damping and effective mass are neglected by the assumptions in [17, 21, 22, 47]. For the flows with acoustic excitations the energy dissipated by the oscillating wall is not only attenuated by the inertia and viscosity of the fluid, it is also attenuated through the density variations. Therefore, the compressibility of the fluid needs to be considered in some sense [23]. Tseng et al. [46] proposes inclusion of electrokinetic base flow to an existing acoustically generated flow (via surface acoustic waves). The proposed device geometry can be exploited to integrate micropumps into complex microfluidic chips improving the portability of micro-total-analysis systems along with the capabilities of actively controlling acoustics and electrokinetics. These applications are motivation for investigating electroosmotically augmented flows in flexural plate wave (FPW) micropumps in the present study.

The present study also addresses the development of a comprehensive numerical model for the coupled multifield (structural and fluid flow) analysis of piezoelectric valveless-micropump MEMS devices for liquid transport applications. Numerical investigations of the piezoelectric micropumps have been reported [48, 49, 52, 53, 56, 64, 88]. To analyze the flow in valveless micropumps, Ullmann [80] and Olsson et al. [81] used lumped-system methods. These approaches ignored spatial variation and focused mainly on the temporal variation. Most of the previous studies (such as Pan et al. [93])

have been conducted to identify the deflection of the piezoelectric valveless micropump rather than the prediction of generated flow rates. Some of these studies did not couple the piezoelectric actuation to the pressure and shear forces generated by the fluid (one-way coupling only) [64, 88, 94, 95]. The previous numerical investigations of the micropumps where two way fluid solid coupling was considered did not report the cycle averaged mass flow rates and time-averaged velocity patterns [48, 49, 52, 53, 56]. Some of the previous numerical investigations concentrated on the generated instantaneous flow rates [48, 49, 52, 53, 56, 64, 88]. However, the net cycle-averaged flows generated by such devices need to be evaluated by averaging the velocity field over a sufficient number of perturbation cycles. The prediction of cycle-averaged flows generated by valveless piezoelectric micropumps is addressed in the present study. The effect of actuation electrical voltage and frequency on pump structural layer deflection and flow rate through the inlet/outlet of a piezoelectric valveless micropump are investigated. Time-averaged velocity fields are computed. The effects of actuation voltage-frequency ,pump back-pressure and working fluid properties on the flow rates are predicted - including the effects due to compressibility. The previous studies [53, 56, 64] explained the dependence of net flow rates to actuation frequency using the instantaneous deflection shapes of the bi-layer membrane without calculating time-averaged velocity. Flow rates are calculated in the present study by integrating time-averaged velocity fields. The mathematical model and simulations can play a major role in understanding the different interplaying fields in acoustically and electrokinetically driven transport. The size and the operation frequency of the investigated flows add constraints to conduct successful experimental measurements of the investigated microfluidic devices. The developed

model would be able to predict all structural and fluid flow related phenomena on a temporal basis for the given design and operating conditions. The developed model can be used as a process tool to complement experimental measurements and aid the microfluidic device design optimization process.

3. FLUID FLOW MODELS

3.1 Introduction

A computational study of acoustically and electrokinetically driven transport in microfluidic devices is carried out. Electroosmosis; the bulk movement of a solution past a charged solid surface, and electrophoresis; the migration of charged solutes, under an applied electric field are investigated. Poisson-Boltzmann and Nernst-Planck models of the electrokinetic flows are studied where Laplace equations are used to model applied electrostatic field. Acoustically generated flow fields are considered where a model based on compressible flow is developed with a vibrating wall. The velocity and pressure profiles for different parameters including actuation frequency, channel height, wave amplitude and wave length are investigated. Electrokinetically augmented acoustically excited flows were studied as well, where a vibrating wall produced acoustic perturbations in electrokinetic flows through microchannels. A structural/fluid dynamic predictive model is developed for piezoelectric valveless micropumps. Two-way coupling of forces between solid and liquid domains is considered in the systems where actuator deflection causes fluid flow and vice-versa. Governing equations are solved for electrical, mechanical and fluidic fields. Finite element methods are considered to predict actuator deflection and finite volume methods are employed to model fluid flow at different operational parameters. The effect of actuation voltage and frequency, pump back-pressure and working fluid properties (density, viscosity and the speed of sound in the working fluid) on membrane deflection and flow rate are investigated. The model predictions in the above cases are compared with the available data in the literature for electrokinetically induced flows, and for the flows generated in channels by acoustic

excitations. The proposed devices can enable active control of acoustics and electrokinetics for pumping liquids in microchannels. Models are employed for micropumps utilizing electrokinetic flows and piezoelectric element actuated acoustic waves. Instantaneous velocity, pressure, electrical distributions and stress-strain distributions are predicted for electrokinetic flows, electrokinetically augmented acoustically excited flows and acoustically excited flows generated by piezoelectric elements.

Electrokinetic flows are the method of choice for pumping applications in microchannels. To have better mixing in such flows inclusion of acoustic perturbations are promising. Electroosmosis; the bulk movement of a solution past a charged solid surface, and electrophoresis; the migration of charged solutes, under an applied electric field are investigated. Electrokinetic flows and inclusion acoustic disturbances in these flows are investigated. In the Nernst-Planck formulation of electrokinetic flows, electrophoretic effects are also considered in the formulations. The investigation of acoustically and electrokinetically driven transport in microfluidic devices is performed in three steps: i) simulation of flow fields due to electrokinetic and acoustic effects including only liquid regions of microchannels, ii) investigation of electrokinetic augmented acoustically excited flows in microchannels to predict instantaneous and time averaged pressure and velocity fields generated by acoustic-electrokinetic effects and iii) development of structural/fluid dynamic predictive model for piezoelectric micropump with field couplings in electrical, mechanical and fluid quantities. Models are developed for electrokinetic flows, acoustically excited flows and electrokinetically augmented acoustically excited flows where the study of flow fields due to electrokinetic and

acoustic effects including only liquid regions of microchannels is considered. Then, fluid-structure interactive model for piezoelectric micropump is created with field couplings in electrical, mechanical and fluid quantities.

3.2 Electrokinetic Flows

This section is devoted to the investigated mathematical models of the electrokinetic transport in microfluidic devices. Numerical simulations are developed for equilibrium Poisson-Boltzmann and multi-ion transport Nernst-Planck models of electrokinetic flows.

Poisson-Boltzmann model considers the charge density to conform with the Boltzmann equilibrium distribution [96]. This assumption is valid once zeta potential has small values or the ionic strengths of the solutions employed are relatively low (corresponds to a thick electrical double layer). The thickness of the electrical double layer is inversely proportional to the ionic strength of the solutions used. For solutions with relatively low ionic strengths and for thick (above 10.0 nm) electrical double layer (EDL) the Boltzmann equilibrium distribution condition is satisfied [5, 71]. Other assumptions are that the microfluidic system is isothermal, and the flow has a small Peclet number or is in a fully developed hydrodynamic state [97]. The Boltzmann distribution is applicable when the system is in the thermodynamic equilibrium state.

The ionic concentration distribution may be distorted from the equilibrium by the presence of the flow if the flow in the microfluidic system has a high Peclet number [97]. For this given reason Nernst-Planck model of electrokinetic flows is also investigated. Numerical simulation of the electrokinetic flows requires the simultaneous solution of the electric double layer streaming potential, ionic - sample concentration distributions,

velocity components, and applied electrostatic field throughout the domain of interest [5, 68-73]. Mathematical formulation and numerical methods employed in implementing these models are discussed below.

3.2.1 Equilibrium Model: Poisson-Boltzmann

Numerical models are developed for equilibrium Poisson-Boltzmann model of electroosmotic flows. Governing equations for mass-momentum conservation, EDL streaming potential and applied electrical electrostatic field are given below. With equilibrium model, electroosmotic flows are investigated.

3.2.1.1 The modified Navier–Stokes equations including electrokinetic effects

The present model is based on the compressible form of the Navier–Stokes equations, including a term for electrokinetic migration that is coupled to the Gouy–Chapman model [1] of the interfacial electric double layer. Fluid properties of dilute potassium chloride-water electrolytes are used while treating the liquid as compressible and Newtonian. Compressibility of the working fluid is introduced here because electroosmotic flows are perturbed with acoustic excitations to consider electrokinetically augmented flows in flexural plate wave acoustic micropumps. The fundamental equations used to describe the generation and propagation of acoustic waves in aqueous solution are the compressible form of the two-dimensional continuity and the momentum equations [23]. A thermodynamic relation is used to close the set of equations for a fluid medium:

$$\rho - \rho_0 = \frac{p - p_0}{c_s^2} \tag{3.1}$$

where ρ_0 is nominal fluid density (a constant), p_0 is nominal pressure (atmospheric) and c_s is the speed of sound (1480 m/s) in the working fluid (water). The equation of state of water was also used by other investigators [19, 98] for analyzing acoustically driven water flows in microchannels.

The Navier–Stokes equations have to be modified for the case of microchannel flow to include the electrical forces generated due to electroosmosis by the interaction between EDL field and the electrostatic potential field. The equations of motion are given by

$$\frac{\partial \rho}{\partial t} + \nabla \cdot (\rho \boldsymbol{v}_f) = 0 \tag{3.2}$$

$$\frac{\partial (\rho \boldsymbol{v}_f)}{\partial t} + \nabla \cdot (\rho \boldsymbol{v}_f \boldsymbol{v}_f) = -\nabla p + \nabla \cdot \tau_{ij} + \rho_e \boldsymbol{E} \tag{3.3}$$

$$\boldsymbol{E} = -\nabla(\phi + \psi) \tag{3.4}$$

Equation (3.3) can be re-written as

$$\frac{\partial (\rho \boldsymbol{v}_f)}{\partial t} + \nabla \cdot (\rho \boldsymbol{v}_f \boldsymbol{v}_f) = -\nabla p + \nabla \cdot \tau_{ij} + 2 n_0 z e \sinh\left(\frac{ze\psi}{k_b T}\right)\{\nabla(\phi + \psi)\} \tag{3.5}$$

In equation (3.5), $\mathbf{v_f}$ is the velocity vector containing u_f and v_f components along the *x* and *y* directions, ρ is the density, p is the pressure, E is the electric field intensity, ϕ is the applied electrostatic potential and ψ is the EDL streaming potential, and ρ_e is the net charge density. The components of the viscous stress τ are related to velocity gradients to produce the shear stress terms in terms of the shear viscosity and the second coefficient of viscosity. The body source term in equation (3.5) introduces electroosmotic body forces to the momentum equations.

3.2.1.2 EDL streaming potential equation ψ

An EDL field (see equation (3.5) above) will be established due to the electrolyte - wall material interaction. Electrical potential induced by the electric double layer can be described as EDL streaming potential, ψ. Consider a liquid phase containing positive and negative ions in contact with a planar charged surface, the relationship between the electrical potential ψ and the net charge density per unit volume ρ_e at any point in the solution is described by the two-dimensional Poisson equation

$$\frac{\partial^2 \psi}{\partial x^2} + \frac{\partial^2 \psi}{\partial y^2} = -\frac{\rho_e}{\varepsilon_r \varepsilon_0} \tag{3.6}$$

where ε_r is the dielectric constant (which is assumed to be a constant for water, 80.0) of the medium, and ε_0 is permittivity of vacuum. For any fluid consisting of two kinds of ions (n) of equal ionic strengths and opposite charge, the equilibrium distribution of ions of each type is given by the Boltzmann distribution

$$n^{\mp} = n_0 e^{\pm \frac{ze\psi}{k_b T}} \tag{3.7}$$

where $e^{\pm \frac{ze\psi}{k_b T}}$ is the Boltzmann factor. Under thermodynamic equilibrium, the local net charge density in a unit volume of the fluid is given by

$$\rho_e = (n^+ - n^-)ze = -2n_0 ze \sinh \frac{ze\psi}{k_b T} \tag{3.8}$$

where n^+ and n^- are the concentrations of the positive and negative ions (m^{-3}), n_0 is the bulk concentration of ions (m^{-3}), k_b is the Boltzmann constant, z is the ionic valence, e is the charge of an electron and T is the absolute temperature. Substituting equation (3.8) into equation (3.6), we obtain the nonlinear two dimensional Poisson–Boltzmann equation:

$$\frac{\partial^2 \psi}{\partial x^2} + \frac{\partial^2 \psi}{\partial y^2} = \frac{2 n_0 z e}{\varepsilon_r \varepsilon_0} \sinh \frac{z e \psi}{k_b T} \tag{3.9}$$

Using equation (3.9), one can obtain the distribution of the EDL potential in the microchannel. To consider electrokinetic effects on fluid flow through a microchannel, the distribution of electrical potential and net charge density must be evaluated. The solution of the above equation is utilized to predict electroosmotic body forces in momentum equations.

3.2.1.3 Laplace equation for the applied electrostatic field ϕ

For the current study of electroosmotic flows, it is assumed that the applied electrostatic potential ϕ (see equation (3.5) above) is much larger than the streaming potential ψ induced by the current due to transport of charges by the liquid flow. Electrical conductivity of the buffer is assumed as constant. In that situation, applied electrical potential and EDL streaming potential are uncoupled. We can obtain the distribution of the electrostatic field by solving the Laplace equation

$$\frac{\partial^2 \phi}{\partial x^2} + \frac{\partial^2 \phi}{\partial y^2} = 0 \tag{3.10}$$

3.2.1.4 Numerical method considered for Poisson-Boltzmann model

Discretization of convection terms are 2nd order accurate upwind scheme for velocity, 2nd order accurate central difference scheme for density. A symmetric grid (100 x 200) with a power law coefficient of 1.065 is considered, which corresponds to a ratio of 5.0 between the coarsest to the finest grid size. Finite volume method is followed. The governing equations are solved using the SIMPLEc algorithm [99]. The resultant system of equations is solved by CFD-ACE+ 2010 solver. Algebraic multigrid linear equations solver [100] was employed for velocity, pressure correction and electric double layer

(EDL) streaming potential (ψ). Simulations were performed via steady-state time marching method.

3.2.2 Multi-ion Transport Model: Nernst-Planck

A mathematical model is developed for electroosmosis and electrophoresis. Numerical simulation of the present microfluidic flows and manipulations requires the solution of the EDL streaming potential, ionic - sample concentration distributions, velocity components, and applied electrostatic field throughout the computational domain [5, 68-73]. Regarding the numerical simulation of electrokinetic flows, most previous studies assumed the velocity profile to be fully developed in the microchannels and considered the charge density to conform to the Boltzmann equilibrium distribution. These assumptions are not strictly valid when i) electrokinetic flow simulation investigates an entrance region, ii) the ionic strengths of the solutions are relatively high and iii) the electrical double layer (EDL) is thin (below 10.0 nm) [5, 71]. The Boltzmann distribution is applicable only when the system is in the thermodynamic equilibrium state. This study develops a Nernst–Planck mathematical model of the electrokinetic transport in a microchannel similar to [101].

Once an electrical field is applied to a microchannel, the transient process of establishing electrokinetic flow has duration of no more than a few hundred microseconds and is dependent on the microchannel dimensions and on the ionic concentrations of the buffer. This duration is typically much shorter than the related characteristic times for injecting, separating, or mixing, etc. Thermal effects can also be neglected since the dissipation capability of a microfluidic chip is sufficiently high that no joule heating effect is observed for electrical fields of up to 800 V/cm. To further

simplify the governing equations, the following assumptions have been made: (i) no chemical reactions, (ii) the aqueous electrolyte solution is Newtonian, (iii) the gravitational effect is negligible, (iv) the diffusion coefficient is constant, and (v) the joule heating effect is negligible [69].

A physical model has been developed based on: (i) the full Navier-Stokes equations modified to include the effects of the body forces due to the electrostatics and net charge density, ρ_e, (ii) the Poisson's equation for the EDL streaming potential, ψ, (iii) equations for the positive - negative ionic concentration distributions and for the neutral sample plug distribution, and (iv) the Laplace equation for the applied electrostatic field ϕ.

3.2.2.1 The modified Navier–Stokes equations including electrokinetic (electroosmotic and electrophoretic) effects

The Navier-Stokes equations mathematically represent the fluid flow in general cases. However, in the case of microchannel flows, these equations must be modified to take account of the electrical force generated by the interaction between the net charge density and the electric potential field. The equations of motion for a compressible Newtonian liquid, equation (3.5), can be expressed in the following form:

$$\frac{\partial(\rho \boldsymbol{v}_f)}{\partial t} + \nabla \cdot (\rho \boldsymbol{v}_f \boldsymbol{v}_f) = -\nabla p + \nabla \cdot \tau_{ij} - \frac{F}{N_A} \sum_{i=1}^{N_{ions}} z_i n_i \nabla(\phi + \psi) \qquad (3.11)$$

In this equation, $\boldsymbol{v_f}$ is the velocity vector containing u_f and v_f components along the x and y directions, ρ the density of the liquid, p is the pressure, ψ is the EDL streaming potential, N_{ions} is the total number of species involved in the system, F is the Faraday's constant, z_i is the valence, n_i is the concentration of the i^{th} species, N_A is the Avogadro number and ϕ is the applied electrostatic field. The components of the viscous

stress τ are related to velocity gradients to produce the shear stress terms in terms of the shear viscosity and the second coefficient of viscosity. $-\frac{F}{N_A}\sum_{i=1}^{N_{ions}} z_i n_i \nabla(\phi+\psi)$ term represents the electroosmotic body force due the electrical force generated by the interaction between the net charge density and the electric potential field. Electrophoretic transport (ion convection and electro-migration) interacts with the momentum equations through the concentration (n_i) and EDL streaming potential (ψ) terms.

3.2.2.2 Poisson's Equation for the EDL streaming potential ψ

When a liquid phase containing positive and negative ions contacts a planar, negatively charged surface, an EDL field is established. The total electrostatic potential field in the domain of interest comprises both the applied electrical field and the EDL streaming potential. According to electrostatics theory, the relationship between the electric potential, ψ, and the net charge density per unit volume, ρ_e, is described at any point in the solution by the Poisson's equation. In multi-ion transport situation Boltzmann distribution, equation (3.7), fails to represent the distribution of charges. The net charge density of ions ρ_e is required to be estimated based on the ions, and neutral species distribution. Net charge density of ions, ρ_e can be expressed in the following form:

$$\rho_e = \frac{F}{N_A}\sum_{i=1}^{N_{ions}} z_i n_i \tag{3.12}$$

where N_{ions} is the total number of species involved in the system, F is the Faraday's constant, z_i is the valence, N_A is the Avogadro number, n_i is the concentration of the i^{th} species [73]. The driving force of the electrokinetic flow is given by the final terms of the u- and v-momentum equations, equation (3.11). It is noted that the driving force is not

uniform across the channel height since the net charge density distribution is non-uniform across the microchannel cross section Here n_i is a local value, F is a universal constant, z_i is a constant which only depends on the chemistry of the corresponding species. Further details regarding the governing equations can be found in [5, 72, 73, 97];

Plugging equation (3.12) into equation (3.6) governing equation for net charge density of ions ρ_e is obtained as:

$$\nabla.\nabla\psi = -\frac{F\sum_{i=1}^{N_{ions}} z_i n_i}{N_A \varepsilon_r \varepsilon_0} \tag{3.13}$$

where, ε_r is the dielectric constant (relative permittivity) of the medium, and ε_0 is permittivity of vacuum. Electrophoretic species transport is considered via the concentration (n_i) in the right hand of equation (3.13).

3.2.2.3 Governing equations for ions, and for neutral species distribution

To facilitate a comprehensive understanding of the sample flow distribution in a microchannel, it is necessary to solve the sample diffusion equation through a process of numerical simulation. Under the previously given assumptions, the conservation equation for given analyte n_i is expressed as:

$$\frac{\partial n_i}{\partial t} = -\nabla.\boldsymbol{J}_i \tag{3.14}$$

where $\boldsymbol{J}_i$ is the total flux of the i^{th} species. The total flux vector $\boldsymbol{J}_i$ of the i^{th} species is given by the expression

$$\boldsymbol{J}_i = \boldsymbol{v}_f n_i - \frac{\mu_{ep,i} n_i}{N_A}\nabla(\phi+\psi) - D_i \nabla n_i \tag{3.15}$$

In the above equation D_i is the diffusion coefficient (m^2/s), z_i is the valence and $\mu_{ep,i}$ is the ionic/electrophoretic mobility (m^2/Vs), n_i is the concentration (m^{-3}) of i^{th} species, $\boldsymbol{v_f}$ is the velocity vector (m/s), ϕ is the applied electrostatic field (Volt), N_A is the Avogadro number, and ψ is the EDL streaming potential (Volt). Governing equations for ions, and for neutral species distribution are solved for negative, positive charged and neutral species at each iteration. Combining equations (3.14) and (3.15) governing equations for ions, and for neutral species distribution are obtained:

$$\frac{\partial n_i}{\partial t} = -\nabla.(\boldsymbol{v_f} n_i - \frac{\mu_{ep,i} n_i}{N_A}\nabla(\phi+\psi) - D_i \nabla n_i) \tag{3.16}$$

In equations (3.15) and (3.16) ionic/electrophoretic mobility (m^2/Vs), $\mu_{ep,i}$ is used, where $\mu_{ep,i}$ and D_i are other constants which only depend on the corresponding species.

$$\mu_{ep,i} = ez_i D_i / k_b T \tag{3.17}$$

Electrophoretic species transport is considered via $\frac{\mu_{ep,i} n_i}{N_A}\nabla(\phi+\psi)$ term in the right hand of equation (3.16). This term is an electromigration term due to the Coulombic interactions of charged solutes with the external field and EDL streaming potential.

3.2.2.4 Numerical method considered for Nernst-Planck model

Discretization of convection terms are 2^{nd} order accurate upwind scheme for velocity, 2^{nd} order accurate central difference scheme for density. A symmetric grid (100 x 200) with a power law coefficient of 1.065 is considered, which corresponds to a ratio of 5.0 between the coarsest to the finest grid size. Finite volume method is followed. The governing equations are solved using the SIMPLEc algorithm [99]. The resultant system

of equations is solved by CFD-ACE+ 2010 solver. Algebraic multigrid linear equations solver [100] was employed for velocity, pressure correction, electric double layer (EDL) streaming potential (ψ) and ions - neutral species distribution. Time dependent simulations were performed via implicit Crank-Nicholson scheme with a blending factor of 0.6. The problem is simulated using a time step of 1.0-10.0 μs. The time required to reach steady state was about 1000 time steps.

3.3 Acoustically Excited Flows in Microchannels

Mathematical models used to simulate acoustically excited flows in microchannels are introduced below. Acoustically excited flows in the present study are simulated via a moving wall problem for flexural plate wave micropumps and via a coupled fluidic/structural model for piezoelectric valveless micropumps.

3.3.1 Acoustically Excited Flows: The Moving Wall Model

Mass and momentum conservation equations are solved to investigate the dynamics of the fluid flow. The fluid dynamics models considered are similar for acoustically excited flows driven by a moving wall and by a piezoelectric element. For the acoustically excited flows in microchannels, continuity and momentum equations are solved for a moving wall problem and for a coupled fluid/solid deformation problem without the electrokinetic forces. The governing conservation equations for acoustically excited flows in microfluidic devices are discussed below.

The compressibility of the water needs to be considered in some sense for the flows generated by acoustic excitations. In the present model fluid properties of water is used while treating the liquid as compressible and Newtonian. The predicted time-

averaged water velocities computed with a compressible flow model agreed significantly better with the experimental data than the predictions obtained with an incompressible flow model [23]. The effect of compressibility should be considered in modeling acoustically driven flows in pumps. Compressible form of the equation of state of water was also used by other investigators [19, 98] for analyzing acoustically driven water flows in microchannels. Typically the fluid flow Mach numbers are small, and also the variations of the density of the fluid are below 1.0 % in the present study. The Mach number criterion is used for gas flows in pressure driven flows to determine if a compressible flow model should be used. However, for liquids the criterion is not strictly applicable [19, 23, 98].

The fundamental equations used to describe the generation and propagation of acoustic waves in water is the compressible form of the two or three-dimensional continuity and momentum equations. Conservation of mass is defined in equation (3.2). The momentum equations, equation (3.3), simplifies to the following equation for acoustically excited flows due to a zero electrokinetic body force contribution in such flows

$$\frac{\partial(\rho \boldsymbol{v}_f)}{\partial t} + \nabla \cdot (\rho \boldsymbol{v}_f \boldsymbol{v}_f) = -\nabla p + \nabla \cdot \tau_{ij} \tag{3.18}$$

where $\mathbf{v_f}$ is the velocity vector containing u_f and v_f components along the x and y directions, t is time, ρ is density and p is the pressure. The components of the viscous stress τ can be related to velocity gradients to produce the shear stress terms in terms of the shear viscosity and the second coefficient of viscosity.

A thermodynamic relation is required to close the set of equations for the fluid medium. A thermodynamic relation $p = p(\rho, s)$ is used to close the set of equations for a fluid medium [102]:

$$p - p_0 = A\left(\frac{\rho - \rho_0}{\rho_0}\right) + B\left(\frac{\rho - \rho_0}{\rho_0}\right)^2 + ... \tag{3.19}$$

The subscript '0' denotes the fluid properties at equilibrium, and ρ is the fluid density. The coefficients A and B represent the adiabatic bulk modulus of elasticity and the so-called nonlinear modulus, respectively [103];

$$A \equiv \rho_0 \left(\frac{\partial c^2}{\partial \rho}\right)\Big|_{s,\rho=\rho_0} \tag{3.20}$$

$$B \equiv \rho_0^2 \left(\frac{\partial c^2}{\partial \rho}\right)^2 \Big|_{s,\rho=\rho_0} \tag{3.21}$$

where c is the acoustic wave speed and the s subscript indicates the process occurs with constant entropy. For isentropic waves, the pressure is linearly related to the density through the speed of sound in the fluid. The isentropic assumption is often used for acoustic problems. The equation of state is represented as [19]:

$$\rho - \rho_0 = \frac{p - p_0}{c_s^2} \tag{3.22}$$

where ρ_o is nominal fluid density (a constant), p_0 is nominal pressure (atmospheric) and c_s is the speed of sound in working fluid. Isentropic assumption is not valid for all frequencies such as very low frequencies when the energy does not radiate. However, for the cases investigated (0.2 - 8.0 kHz) the first order approximation to equation (3.19) can be applied.

In order to consider the flexural plate wave device pumping capability, the dependence of velocity profile on channel height, wave amplitude, wave length and actuation frequency are investigated. The vibrating wall boundary conditions are discussed in the results sections of this thesis.

3.3.1.1 Numerical Method: Acoustically Excited Flows Driven by a Moving Wall

Discretization of convection terms are 2^{nd} order accurate upwind scheme for velocity, 2^{nd} order accurate central difference scheme for density. For the flows with moving and deforming boundaries, grid generation is considered at every timestep. Re-meshing is introduced by using the transfinite interpolation (TFI) scheme [104]. The TFI scheme determines the interior node distribution based on the motion of the boundary nodes. A symmetric grid (100 x 200) with a power law coefficient of 1.065 is considered, which corresponds to a ratio of 5.0 between the coarsest to the finest grid size. Finite volume method is followed. The governing equations are solved using the SIMPLEc algorithm [99]. The resultant system of equations is solved by CFD-ACE+ 2010 solver. Conjugate gradient squared linear equations solver was employed with an implemented "incomplete Cholesky factorization" as a pre-conditioner [100]. Time dependent simulations were performed via implicit Crank-Nicholson scheme with a blending factor of 0.6. The problem is simulated using 100 time steps per cycle (f ranging between 1.0 to 3.0 MHz). The time required to reach pseudo-periodic state was 60-120 flexural cycles.

3.3.2 Acoustically Excited Flows Driven by a Piezoelectric Element

A structural/fluid dynamic predictive model was developed for piezoelectric valveless micropumps. Effects of actuation frequency, electrical potential, working fluid

and pump back-pressure are investigated in such systems. Piezoelectric micropump design and analysis is a complex multidisciplinary problem with field couplings in electrical, mechanical and fluid quantities. The governing equations for the piezoelectric solid and the fluid domains are summarized in this section. The model for piezoelectric actuators/non-piezoelectric materials and the coupling relations of the mechanical, electrical and fluid fields are covered in more detail in the following chapters. Problem geometries considered and the boundary and initial conditions are discussed in the results sections of this thesis.

3.3.2.1 Solid (piezoelectric) domain:

Propagation of acoustic waves in piezoelectric element is governed by the mechanical equation of motion and the electromagnetic field equations. The conservation relations for mechanical energy and electromagnetic field yield two second order coupled wave equations. First wave equation represents the conservation of mechanical energy:

$$-\rho \frac{\partial^2 u_i}{\partial t^2} + c_{ijkl}^E \frac{\partial^2 u_k}{\partial x_j \partial x_l} + e_{ijk}^T \frac{\partial^2 \phi}{\partial x_k \partial x_j} = 0 \tag{3.23}$$

where ρ is the particle density, x_j is the coordinate, u_i is the displacement component in the i^{th} direction, c_{ijkl} is the elasticity constant and has units (N/m^2), the constant e_{ijk} is the piezoelectric stress constant and have units (C/m^2) and φ is the electric potential.

The second coupled wave equation is for the conservation of electrical energy and it is expressed as:

$$e_{ikl} \frac{\partial^2 u_k}{\partial x_i \partial x_l} - \varepsilon_{ik}^S \frac{\partial^2 \phi}{\partial x_i \partial x_k} = 0 \tag{3.24}$$

where ε_{ij} is the dielectric permittivity constant and have units (F/m) and the constant e_{ikl} is the piezoelectric stress constant and have units (C/m^2). The piezoelectric stress

matrices in both equations, (3.23) and (3.24), are transposes of each other, hence the superscript (T). The superscripts on the elastic stiffness constants and the dielectric permittivity constants imply that these are the properties at constant electric field and strain, respectively.

3.3.2.2 Fluid domains:

Mathematical models are developed for acoustically excited flows generated by piezoelectric valveless micropumps. Fluid dynamics model considered are similar for acoustically excited flows driven by flexural plate wave and by a piezoelectric element. The difference is for flexural plate wave devices the solid deformation model is not considered and the perturbations generated by the deforming solids are approximated by introducing moving wall functions along the deflecting surfaces. Both structural and flow field analysis of the microfluidic device are considered for acoustically excited flows driven by a piezoelectric element in valveless piezoelectric micropumps. Two-way coupling of forces between solid and liquid domains in the systems where actuator deflection causes fluid flow and vice-versa is considered. The governing equations for the flow fields and structural layer motions are solved numerically. For the acoustically excited flows in microchannels, continuity and momentum equations are solved for a coupled fluid/solid deformation problem without the electrokinetic forces. The fundamental equations used to describe the generation and propagation of acoustic waves in water is the compressible form of the two/three dimensional continuity and momentum equations. The compressibility of the water is considered for the flows generated by acoustic excitations. Mass and momentum equations for fluid dynamics model are described in section 3.3.1 above.

3.4 Electroosmotic Augmentation in Flexural Plate Wave Micropumps

The present model for electroosmotic augmentation in FPW micropumps is based on the implementation of TFI scheme for re-meshing to accommodate the vibrating wall, and the solution of the modified Navier–Stokes equations including electrokinetic body force effects. EDL streaming potential, ψ is solved using the governing equations which are listed in 'electrokinetic flow model' section using the estimated grid locations (due to the flexural deflections of FPW actuator) at each time step. For the propagation of acoustics waves in the fluid, a compressible form of the Navier-Stokes equations is considered (see section 3.3.1 above). The moving wall is characterized by the boundary conditions. The effects due to the coupling of electrokinetic flow to acoustically excited flows and moving wall boundary conditions are discussed in the results sections of this thesis. Numerical methodology followed for the analysis of electroosmotic augmentation in flexural plate wave micropumps is discussed next.

Discretization of convection terms are 2^{nd} order accurate upwind scheme for velocity, 2^{nd} order accurate central difference scheme for density. For the flows with moving and deforming boundaries, grid generation is considered at every timestep. Re-meshing is introduced by using the transfinite interpolation (TFI) scheme [104]. The TFI scheme determines the interior node distribution based on the motion of the boundary nodes. A symmetric grid (100 x 200) with a power law coefficient of 1.065 is considered, which corresponds to a ratio of 5.0 between the coarsest to the finest grid size. Finite volume method is followed. The governing equations are solved using the SIMPLEc algorithm [99]. The resultant system of equations is solved by CFD-ACE+ 2010 solver. Algebraic multigrid linear equations solver [100] was employed for velocity, pressure

correction and electric double layer (EDL) streaming potential (ψ). Time dependent simulations were performed via implicit Crank-Nicholson scheme with a blending factor of 0.6. The problem is simulated using 100 time steps per cycle (frequency f ranging between 1.0 to 10.0 MHz) for acoustically driven flows or electroosmotically augmented flows in FPW micropumps. The time required to reach pseudo-periodic state was 20-30 flexural cycles.

3.5 Summary

Fluid flow models are developed for electrokinetic flows with Poisson-Boltzmann and Nernst-Planck models. Poisson-Boltzmann model assumes the distribution of ions is in accordance to the Boltzmann equilibrium distribution. Nernst-Planck multi-ion transport model solves for the distribution of ions, and neutral species. Species distribution equations are convective-diffusive transport equations with added body source terms to account for electrophoretic species transport.

The developed flow models for acoustically excited flow in microfluidic devices include two/three-dimensional compressible forms of the mass and momentum conservation equations. Acoustically excited flows are excited with specified wall motions in the moving wall models. Acoustically excited flows driven by piezoelectric elements are investigated by coupled solid/fluid mechanics models. Solid deformation models developed for such flow geometries are discussed in the following chapter.

Electroosmotic augmentation in flexural plate wave micropumps is investigated with a commercial software, albeit with significant modifications and augmentations to the standard version. The compressibility of the liquid and interactions of electrokinetic and surface driven flows (not readily found in the standard version of the software) are

investigated. A compressible model (for liquids) is developed by developing user-developed Fortran routines [100]. Electrokinetic body force terms (to the governing equations of fluid flow) and two additional differential equations (to simulate the electric double layer streaming potential and applied electrostatic field) are also included with the user-developed routines.

4. SOLID DEFORMATION MODEL FOR PIEZOELECTRIC ACTUATORS

The governing equations for the solid (non-piezoelectric and piezoelectric) domains and the model development procedure for the full anisotropic model are discussed below. The numerical scheme considered is discussed afterwards. The boundary and initial conditions are discussed in the results sections of this thesis.

4.1 Development of Full Anisotropic Model

To develop a generic model for acoustically excited flows, the solid deformation model needed to be expanded from orthotropic materials to fully anisotropic materials. Initially the users of the commercial code CFD-ACE+ could only enter solid material elasticity data through engineering quantities (Young's Modulus, Shear Modulus and Poisson's ratio). This limits the solid deformation model to orthotropic materials because of the only 12 possible elements (9 of them are independent) of the elasticity matrix.

In collaboration with CFD-ACE+, the required mathematical model was expanded from index notations in the literature to fully expanded form of governing equations for solid domains. All necessary solver manipulations were programmed to include full anisotropy. With the recently implemented updates to the model, CFD-ACE+ users can directly enter 6 x 6 elasticity data or invoke a user defined property routine (user defined property routine was also developed by the present study). By using user defined elasticity specification, temperature /chemical composition etc. dependent property data was enabled to the users. Another improvement implemented to model during the project was each of the computational cells within a medium can have different material orientation. This will enable us to model a circular piezoelectric

element in polar coordinates in the future. Full anisotropy model was benchmarked to software (Abaqus) for an axially loaded anisotropic cube (material: trigonal 3m symmetry class, $LiNbO_3$ [105]). The results were within 2% range.

Strain, *S* is the dimensionless ratio of the length of the stressed material to its unstressed length:

$$S_{ij} = \frac{1}{2}\left(u_{i,j} + u_{j,i}\right) \tag{4.1}$$

where u_i is the displacement component in the i^{th} direction. For indices i, and j, the index values are 1, 2 or 3 (representing the two/three dimensions of physical Euclidean space). Sample expansions in 11, 12, 21 planes are given as:

$$S_{11} = \frac{1}{2}\left(u_{1,1} + u_{1,1}\right) = u_{1,1} = \frac{\partial u_1}{\partial x_1}$$
$$S_{21} = \frac{1}{2}\left(u_{2,1} + u_{1,2}\right) = \frac{1}{2}\left(\frac{\partial u_2}{\partial x_1} + \frac{\partial u_1}{\partial x_2}\right) = S_{12} \tag{4.2}$$

Using the Newton's 2^{nd} law of motion acceleration of a mass can be related to the net force on the body. The equation of motion for a vibrating particle in the absence of body forces is:

$$\sum_{j=1}^{3} \frac{\partial \tau_{ij}}{\partial x_j} = \rho \frac{\partial^2 u_i}{\partial t^2} \tag{4.3}$$

where ρ is the particle density, x_j is the coordinate and u_i is the displacement component in the i^{th} direction. Completion of the characterization of a solid requires postulation of a relationship between stress and strain which is the constitutive relation for non-piezoelectric solids:

$$\tau_{ij} = c_{ijkl} S_{kl} \tag{4.4}$$

where τ is the stress and c_{ijkl} is the elasticity constant both have units (N/m^2). c_{ijkl} is a rank 4 tensor and in three-dimensional space, it can contain $3^4 = 81$ different constants. From energy and symmetry considerations, these 81 possible independent terms can be reduced to a maximum of 21, which are 6 diagonal terms and 15 off-diagonal terms of the 6x6 symmetric elasticity constant tensor (c_{ijkl}) [105]. Abbreviated notations are followed below based on IEEE Standard on Piezoelectricity, ANSI/IEEE Std 176-1987 [106]. Relation between full and abbreviated notations can be given as 11:1, 22:2, 33:3, 23:4, 13:5, and 12:6. The form of the stiffness matrix for elastic materials simplifies to the following form for a three-dimensional case:

$$c = \begin{bmatrix} c_{11} & c_{12} & c_{13} & c_{14} & c_{15} & c_{16} \\ c_{12} & c_{22} & c_{23} & c_{24} & c_{25} & c_{26} \\ c_{13} & c_{23} & c_{33} & c_{34} & c_{35} & c_{36} \\ c_{14} & c_{24} & c_{34} & c_{44} & c_{45} & c_{46} \\ c_{15} & c_{25} & c_{35} & c_{45} & c_{55} & c_{56} \\ c_{16} & c_{26} & c_{36} & c_{46} & c_{56} & c_{66} \end{bmatrix} \rightarrow \begin{bmatrix} c_{11} & c_{12} & c_{13} & c_{14} & c_{15} & c_{16} \\ & c_{22} & c_{23} & c_{24} & c_{25} & c_{26} \\ & & c_{33} & c_{34} & c_{35} & c_{36} \\ & & & c_{44} & c_{45} & c_{46} \\ & \text{sym} & & & c_{55} & c_{56} \\ & & & & & c_{66} \end{bmatrix} \quad (4.5)$$

Stress on a plane can be related to the particle displacement using the divergence operator using the following formula.

$$\vec{F} = m\vec{a} \Rightarrow \tau_{ij,j} = \rho \ddot{u}_i \quad (4.6)$$

Expansions in x, y and z directions yield the following formula:

$$\frac{\partial \tau_{11}}{\partial x_1} + \frac{\partial \tau_{21}}{\partial x_2} + \frac{\partial \tau_{31}}{\partial x_3} = \rho \frac{\partial^2 u_1}{\partial t^2} \quad (4.7a)$$

$$\frac{\partial \tau_{21}}{\partial x_1} + \frac{\partial \tau_{22}}{\partial x_2} + \frac{\partial \tau_{32}}{\partial x_3} = \rho \frac{\partial^2 u_2}{\partial t^2} \quad (4.7b)$$

$$\frac{\partial \tau_{31}}{\partial x_1} + \frac{\partial \tau_{32}}{\partial x_2} + \frac{\partial \tau_{33}}{\partial x_3} = \rho \frac{\partial^2 u_3}{\partial t^2} \quad (4.7c)$$

These set of equations motion can be implemented in general by two possible ways. In the first approach particle displacements and stresses are needed to be calculated sequentially and stored in memory according to the following relations:

$$\begin{aligned}
\tau_1 &= c_{11}S_1 + c_{21}S_2 + c_{31}S_3 + c_{41}S_4 + c_{51}S_5 + c_{61}S_6 \\
\tau_2 &= c_{21}S_1 + c_{22}S_2 + c_{32}S_3 + c_{42}S_4 + c_{52}S_5 + c_{62}S_6 \\
\tau_3 &= c_{31}S_1 + c_{32}S_2 + c_{33}S_3 + c_{43}S_4 + c_{53}S_5 + c_{63}S_6 \\
\tau_4 &= c_{41}S_1 + c_{42}S_2 + c_{43}S_3 + c_{44}S_4 + c_{54}S_5 + c_{64}S_6 \\
\tau_5 &= c_{51}S_1 + c_{52}S_2 + c_{53}S_3 + c_{54}S_4 + c_{55}S_5 + c_{65}S_6 \\
\tau_6 &= c_{61}S_1 + c_{62}S_2 + c_{63}S_3 + c_{64}S_4 + c_{65}S_5 + c_{66}S_6
\end{aligned} \tag{4.8}$$

In the second approach stress terms comprising displacements are directly plugged into the equation of motion i.e. equations (4.1) and (4.4) are plugged into equation (4.6). From equations (4.3) and (4.4), the mechanical equation of motion simplifies to:

$$-\rho \frac{\partial^2 u_i}{\partial t^2} + c_{ijkl}^{E} \frac{\partial^2 u_k}{\partial x_j \partial x_l} = 0 \tag{4.9}$$

There is no need to store stresses in the memory with this method. The equation of motion governing the relation of inertia and elasticity is fully expanded in all three directions prior to the implementation and it is given below in x direction:

$$\rho\frac{\partial^2 u_1}{\partial t^2} = c_{11}\frac{\partial^2 u_1}{\partial x_1 \partial x_1} + c_{61}\frac{\partial^2 u_1}{\partial x_1 \partial x_2} + c_{51}\frac{\partial^2 u_1}{\partial x_1 \partial x_3} + c_{61}\frac{\partial^2 u_2}{\partial x_1 \partial x_1}$$
$$+c_{66}\frac{\partial^2 u_2}{\partial x_1 \partial x_2} + c_{65}\frac{\partial^2 u_2}{\partial x_1 \partial x_3} + c_{51}\frac{\partial^2 u_3}{\partial x_1 \partial x_1} + c_{65}\frac{\partial^2 u_3}{\partial x_1 \partial x_2}$$
$$+c_{55}\frac{\partial^2 u_3}{\partial x_1 \partial x_3} + c_{61}\frac{\partial^2 u_1}{\partial x_2 \partial x_1} + c_{66}\frac{\partial^2 u_1}{\partial x_2 \partial x_2} + c_{65}\frac{\partial^2 u_1}{\partial x_2 \partial x_3}$$
$$+c_{21}\frac{\partial^2 u_2}{\partial x_2 \partial x_1} + c_{62}\frac{\partial^2 u_2}{\partial x_2 \partial x_2} + c_{52}\frac{\partial^2 u_2}{\partial x_2 \partial x_3} \qquad (4.10)$$
$$+c_{51}\frac{\partial^2 u_3}{\partial x_2 \partial x_1} + c_{64}\frac{\partial^2 u_3}{\partial x_2 \partial x_2} + c_{54}\frac{\partial^2 u_3}{\partial x_2 \partial x_3}$$
$$+c_{51}\frac{\partial^2 u_1}{\partial x_3 \partial x_1} + c_{65}\frac{\partial^2 u_1}{\partial x_3 \partial x_2} + c_{55}\frac{\partial^2 u_1}{\partial x_3 \partial x_3}$$
$$+c_{41}\frac{\partial^2 u_2}{\partial x_3 \partial x_1} + c_{64}\frac{\partial^2 u_2}{\partial x_3 \partial x_2} + c_{54}\frac{\partial^2 u_2}{\partial x_3 \partial x_3} +$$
$$+c_{31}\frac{\partial^2 u_3}{\partial x_3 \partial x_1} + c_{63}\frac{\partial^2 u_3}{\partial x_3 \partial x_2} + c_{53}\frac{\partial^2 u_3}{\partial x_3 \partial x_3}$$

Equation (4.10) is the fully expanded form of equation (4.9) in x direction. The governing equation (4.9) is expanded in all x, y and z directions and missing terms are added to the CFD-ACE+ code.

When solving for acoustic waves the magnetic field is assumed to be static and hence the electric field is assumed to be the gradient of the scalar potential:

$$E_i = -\nabla\varphi \qquad (4.11)$$

where φ is the electric potential. This is often called the quasi static approximation and has negligible effect on the solution [41]. Structural materials used in the fabrication of micropumps are insulators; therefore the absence of electric charge within the material can be expressed by:

$$\frac{\partial D_i}{\partial x_i} = 0 \qquad (4.12)$$

The governing equation for electrical quantities, equation (4.12), simplifies to the Laplace's equation

$$\frac{\partial^2 \phi}{\partial x_i \partial x_k} = 0 \tag{4.13}$$

Propagation of acoustic waves in non-piezoelectric domains is governed by the equations (4.9) and (4.13). The governing equations (4.9) and (4.13) for non-piezoelectric solids, are uncoupled and simplified.

4.2 Piezoelectric Solids

The propagation of acoustic waves in piezoelectric materials is governed by mechanical equations of motion and Maxwell's equation for the electrical field (electromagnetic field equations). The equations are coupled by the piezoelectric constitutive equations given by:

$$\tau_{ij} = c^E_{ijkl} S_{kl} - e^T_{ijk} E_k \tag{4.14}$$

$$D_i = e_{ikl} S_{kl} + \varepsilon^S_{ij} E_j \tag{4.15}$$

where D is the electric displacement field and has units (C/m^2), S is the strain (unitless), τ is the stress (N/m^2), c_{ijkl} is the elasticity constant and has units (N/m^2), ε_{ij} is the dielectric permittivity constant and have units (F/m); E_j is the electric field component and has units (V/m) and the constants e_{ijk} and e_{ikl} are the piezoelectric stress constants and have units (C/m^2). The piezoelectric stress matrices in both equations are transposes of each other, hence the superscript (T). The piezoelectric matrix couples the electric and mechanical fields. The superscripts on the elastic stiffness constants and the dielectric permittivity constants imply that these are the properties at constant electric field and

strain, respectively. The piezoelectric stress constants (e_{ijk} and e_{ikl}) are zero in non-piezoelectric materials.

Substituting equation (4.3) and equation (4.11) in the first piezoelectric constitutive equation (4.14) yields the first wave equation:

$$-\rho \frac{\partial^2 u_i}{\partial t^2} + c_{ijkl}^E \frac{\partial^2 u_k}{\partial x_j \partial x_l} + e_{ijk}^T \frac{\partial^2 \phi}{\partial x_k \partial x_j} = 0 \tag{4.16}$$

Piezoelectric materials are insulators; therefore the absence of electric charge within the material can be expressed by the second coupled wave equation as:

$$e_{ikl} \frac{\partial^2 u_k}{\partial x_i \partial x_l} - \varepsilon_{ik}^S \frac{\partial^2 \phi}{\partial x_i \partial x_k} = 0 \tag{4.17}$$

Equations (4.16) and (4.17) are two second order coupled wave equations. In equations (4.14) – (4.17), Einstein summation convention is used. For indices i, j, k, and l the index values are 1, 2 or 3 (representing the two/three directions of physical Euclidean space). The governing equations (4.16) and (4.17) are wave equations. Equation (4.16) yields two/three displacement equations with polarizations in two/three spatial directions when expanded in full form. Equation (4.17) yields voltage equation. The piezoelectric stress constants (e_{ijk} and e_{ikl}) couple the two/three displacement equations and voltage equation in equations (4.16) and (4.17). The piezoelectric micropump is modeled using a 2D or 3D model. The solutions of the displacement and voltage depend on the x, y and z directions.

The solid deformation/material models are improved for the development of full anisotropic model. Modifications done on the models are discussed above. The terms due to the direct and converse piezoelectric effects (last term in equation 4.16 and first term in equation 4.17) were established well in previous versions of the model; therefore in the listed governing equations in the previous section these terms are omitted.

4.3 Numerical Scheme Considered for Piezoelectric Actuators

For the solid domains 2nd order strain analysis is invoked with a consistent mass matrix type. The resultant system of linear equations for the piezoelectric domains is not positive definite and symmetric. Accordingly, a direct linear equations solver PCGLSS 5.0 [100] is used for the solution of dynamic structural model. It limits the allowable number of grid points for solid domains. Time dependent simulations were performed via implicit Euler scheme. The time step was chosen such that the cyclic variation of the piezoelectric actuator is well-resolved.

The problem is simulated using 100 time steps per cycle. For example for frequency of 1.0 kHz, time step is 10^{-5} s. Decreasing the time step by another 50% did not have any appreciable effect on the results. The time required to reach pseudo-periodic state is 10.0 perturbation cycles. Rectangular structured brick elements are used for the solid domains.

4.4 Summary

To develop a generic model for acoustically excited, the solid deformation model is needed to be expanded from orthotropic materials to fully anisotropic materials.

The following enhancements to the CFD-ACE code (in collaboration with ESI-CFD) have been made to the solid deformation models:

- Users can now choose between isotropic, orthotropic and anisotropic material properties.
- For orthotropic materials, users can now enter the elastic stiffness matrix directly or enter available engineering data such as Young’s Modulus, Shear Modulus and Poisson's Ratio.

- Anisotropic materials can be specified using all 21 independent elements of the elastic stiffness matrix.
- User subroutine capability has been made available to all inputs through the user developed property routines. This includes the engineering data components in each direction and the stiffness matrix itself.
- User subroutine capability has also been made available for specifying material axes through the user developed property routines. This allows users to fully control the material axes direction on a cell-by-cell basis.

5. ELECTROKINETIC FLOWS THROUGH MICROCHANNELS

In this chapter detailed analysis of the elecrokinetic flows are studied for the models developed and provided in section 3.2. Problem geometry, volume and boundary conditions, validation of the model and results-discussion are given below for Poisson-Boltzmann models (section 3.2.1) and Nernst-Planck models (section 3.2.2). Conclusions obtained from the investigations are discussed thereafter.

5.1 Introduction

The effectiveness and applicability of utilizing electrokinetic flows through microchannels for enhanced pumping capabilities is investigated. The investigated concept is exploited to integrate electrokinetic flow based micropumps into complex microfluidic chips improving the portability of micro-total-analysis systems and promoting pumping capacity of acoustic micro-mixers for mixing applications. A computational study of electrokinetic flows in microchannels is presented where body forces are added to the momentum equations for analyzing the dynamics of the flow. A transient analysis of the flow of dilute potassium chloride-water electrolytes is performed for microchannels. The nonlinear electric double layer streaming potential and the applied electrostatic field are solved numerically. For non-equilibrium model distribution of ions and charged species are also solved simultaneously using convective-diffusive transport equations to account for electrophoretic species transport (with added body source terms). Electrokinetic flow cases are investigated for varying strength of electrolyte solutions and applied electric field strengths. Inclusion of electrokinetic effects is an efficient approach whenever high flow rates are required in microfluidics

applications. The model predictions are compared with the theoretical and experimental results available in the literature for electrokinetic flows.

Solving for the electrokinetic velocity field in complex geometries requires a solution of the electric field and charge density in the microchannel, together with a solution to the Navier–Stokes equations [5, 68-73]. Regarding the charge density, either linear or nonlinear forms of EDL field equations with a body force term added to Navier-Stokes equations are widely used in the literature. Fluid flow in a manifold of intersecting channels can be directed in the desired direction by the appropriate application of potentials to various channels within the manifold. This valveless control of fluid flow is subject to leakage between the channels at their intersection region [107]. The analysis by Zhang et al. [74, 75] shows that the induced pressure distribution is the key to understand experimentally observed phenomena of leakage flows in electrokinetic flows. In the present investigation, the induced electric double layer potential and velocity fields obtained from the Nernst–Planck model, and the Poisson–Boltzmann model are compared systematically. The present study requires the simultaneous numerical solution of the governing equations of mass/momentum conservation, electrical field and ionic charge distribution.

5.2 Geometry and Volume Conditions

5.2.1 Schematic of the Problem Geometry

The schematic of the microchannel for electrokinetic flows is shown in Figure 5.1. Hydration causes the wall of the microchannel to be negatively charged at most pH conditions, an accumulation of positive ions (counter-ions) occurs in the aqueous solution adjacent to the wall. This counter-ion rich region is referred to as the electrical double

layer (EDL) [17]. The potential between the wall and the solution is known as the zeta potential, ζ .Top and bottom surfaces are charged with zeta potential (ζ). Due to the difficulties in predicting properties of Stern layer it is a common approach to use the zeta potential while describing the electrical double layer [1].When a liquid phase containing positive and negative ions contacts a planar, charged surface (ζ, zeta potential), an EDL field is established [5]. Zeta potential induces an EDL field to drive fluid with electrokinetic body forces in electrokinetic flows through microchannels. Once the DC electrical potential at the inlet (left boundary in Figure 5.1) is activated, the flow starts to move due to the interactions between the channel walls, buffer electrolyte and the external electric field. The electrokinetic flow geometry can be defined by the height of the channel *H* and length of the microchannel *L* respectively.

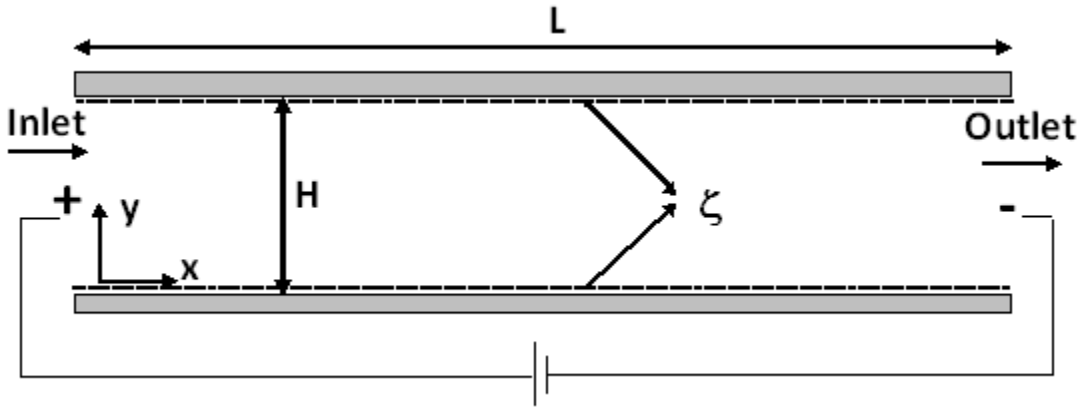

Figure 5.1 Schematic of the microchannel for electrokinetic flows.

5.2.2 Properties of the Buffer Electrolyte and Initial Conditions

In most electrophoresis and electroosmosis experiments, the microchannel is filled with an aqueous electrolyte solution. The sample is then injected into the channel

and an electric potential activated to carry out sample separation [108]. Consequently, the initial conditions are assumed as follows: the fluid is initially stationary throughout the microchannels and the zeta potential of the walls is given by ζ, and the ionic concentration and EDL potential (ψ) are both assumed to conform to the Boltzmann equilibrium distribution initially. Symmetric buffer electrolyte, potassium chloride (KCl) is considered as the working fluid. Electrophoretic mobilities of potassium and chloride ions are $\mu_{ep,K^+} = 7.7\ 10^{-8} m^2/Vs$ and $\mu_{ep,Cl^-} = 7.7\ 10^{-8} m^2/Vs$ respectively. Ion diffusion coefficients (D_{K^+} and D_{Cl^-}) for both potassium and chloride are 2.0 10^{-9} m^2/s. The following physical constants are also used in calculations: e= 1.6021 x 10^{-19} C , ε_0 =8.854 x 10^{-12} C/ (m·V), k_b = 1.3805 x 10^{-23} J/(moI·K) and F=96485.3 C/mol. Initially, pressure is atmospheric and all other dependent variables are zero. A body force generates a liquid flow (Figure 5.1) and space dependent displacements drive the adjoining fluid as described in section 3.2: 'electrokinetic flows' model.

5.3 Boundary Conditions

For electrokinetic flows, zero gradient boundary conditions are specified for velocity and EDL streaming potential ψ along the inlet and outlet boundaries (left and right boundaries in Figure 5.1, respectively). For the EDL streaming potential equation, the wall value is given by the zeta potential ζ. ϕ_{inlet} and ϕ_{outlet} (applied potential values along the inlet and outlet, respectively) are specified for the electrostatic field equation (ϕ). Walls are assumed to be insulated against applied electrical potential. Boundary conditions of pressure are predicted following Zhang et al. [74, 75]. Details of the modeled boundary conditions (Figure 5.1) are:

Inlet

$$\frac{\partial u}{\partial x} = 0 \; ; \; \frac{\partial v}{\partial x} = 0 \; ; \; p = p_0 - \frac{16}{\pi}\frac{\mu}{H}\bar{u}_{f,in} \tag{5.1}$$

Outlet

$$\frac{\partial u}{\partial x} = 0 \; ; \; \frac{\partial v}{\partial x} = 0 \; ; \; p = p_0 + \frac{16}{\pi}\frac{\mu}{H}\bar{u}_{f,out} \tag{5.2}$$

where p is the pressure, p_0 is the ambient pressure, H is the height of the channel, μ is the dynamic viscosity of the buffer solution, $\bar{u}_{f,in}$ and $\bar{u}_{f,out}$ are the mean velocities at the channel inlet and outlet, respectively. The specification of the pressure boundary condition (equations 5.1 and 5.2) is applicable for situations where the flow starts and terminates at large reservoirs (as in the present case). The inlet and outlet both terminate at large reservoirs for the problems considered (not specifically shown in Figure 5.1). The use of 'zero gradient' boundary condition for velocity in our case is a 'numerical' rather than a 'physical' boundary condition. If pressure value (Dirichlet type boundary condition) is specified at both inlet and outlet, specifying velocities (Dirichlet) is numerically inadmissible [109]. The pressure boundary conditions include the effects of sudden contraction and sudden expansion at the inlet and outlet.

5.3.1 Poisson Boltzmann Model

The boundary conditions employed for the Poisson-Boltzmann model (discussed in section 3.2.1) are listed below.

Initially, the fluid is stationary throughout the microchannels and the zeta potential of the walls is given by ζ, and the ionic concentration n_i is assumed to conform to the Boltzmann equilibrium distribution as given below:

$$u_f = 0 \; ; \; v_f = 0 \; ; \; p = 0 \; ; \;\; \psi = \zeta \; ; \; \phi = 0 \tag{5.3}$$

Inlet

At the flow inlet, the zero velocity gradient is assumed because the mass flow rate is determined by the activated electrical potential in electrokinetic flows. Boundary conditions along the inlet can be given as:

along $x = 0$

$$\frac{\partial u_f}{\partial x} = 0 \; ; \; \frac{\partial v_f}{\partial x} = 0 \; ; \; p = p_0 - \frac{16}{\pi}\frac{\mu}{H}\bar{u}_{in} \; ; \quad \frac{\partial \psi}{\partial x} = 0 \; ; \quad \phi = \phi_{inlet} \tag{5.4}$$

Outlet

The channel length is assumed to be long enough that the flow is fully developed at the outflow boundary according to the given relations:

along $x = L$

$$\frac{\partial u_f}{\partial x} = 0 \; ; \; \frac{\partial v_f}{\partial x} = 0 \; ; \; p = p_0 + \frac{16}{\pi}\frac{\mu}{H}\bar{u}_{out} \; ; \quad \frac{\partial \psi}{\partial x} = 0 \; ; \; \phi_{outlet} = 0 \tag{5.5}$$

Bottom and Top Boundaries

Zero slip boundary conditions are used along the walls for velocity for all cases considered. The boundary conditions for n_i^+ and n_i^- at the wall surfaces are assumed to be the corresponding values of the Boltzmann distributions. Boundary conditions are:

along $y = 0$ and $y = H$

$$u_f = 0 \; ; \; v_f = 0 \; ; \; p = 0 \; ; \quad \psi = \zeta \; ; \; \partial\phi / \partial y = 0 \tag{5.6}$$

5.3.2 Nernst-Planck Model

For the Nernst-Planck model (discussed in section 3.2.2) investigations boundary conditions given in equations (5.3) - (5.6) are employed and additional boundary conditions specified are listed below.

Initial

Initially, the ionic concentration n_i is assumed to conform to the Boltzmann equilibrium distribution as given below:

$$n_i^{\pm} = n_{i,0}^{\pm} e^{\frac{\mp z_i e \zeta}{k_b T}} \; ; \; n_i^0 = n_{i,0}^0 \tag{5.7}$$

Inlet

Boundary conditions along the inlet can be given as:

along $x = 0$

$$n_i^{\pm} = n_{i,0}^{\pm} \; ; \; n_i^0 = n_{i,0}^0 \tag{5.8}$$

Outlet

The channel length is assumed to be long enough that the flow is fully developed at the outflow boundary according to the given relations:

along $x = L$

$$\frac{\partial n_i^{\pm}}{\partial x} = 0 \; ; \; \frac{\partial n_i^0}{\partial x} = 0 \tag{5.9}$$

Bottom and Top Boundaries

The boundary conditions for n_i^+ and n_i^- at the wall surfaces are assumed to be the corresponding values of the Boltzmann distributions. Boundary conditions are:

along $y = 0$ and $y = H$

$$n_i^{\pm} = n_{i,0}^{\pm} e^{\frac{\mp z_i e \zeta}{k_b T}} \;\; ; \;\; \frac{\partial n_i^0}{\partial y} = 0 \qquad (5.10)$$

5.4 Validation of the Model

Table 5.1 lists the cases considered in the present study. Electrokinetic flow is first modeled in a microchannel (Figure 5.1) using the Poisson-Boltzmann equation set (cases 1 - 3). In case 1 the parameters of electrokinetics model are chosen from the values used in [110], H= 0.9 μm, L/H = 4.5, bulk concentration of ions, n_0 = 0.0075 N_A m^{-3} (N_A is the Avogadro number), zeta potential $\zeta = -0.05V$ and E_x = 210.0 (kV m^{-1}). The values in [97], H= 2.0 μm, L/H = 3.0, bulk concentration of ions, n_0 = 0.01 N_A m^{-3}, zeta potential $\zeta = -0.0675V$ and E_x = 1254.0 (kV m^{-1}) are the chosen parameters in case 2. In case 3, a microchannel (L = 100.0 μm) is considered in order to investigate local pressure loss/gain due to flow contraction and expansion where n_0 = 0.93 N_A m^{-3} (ion concentration) and zeta potential $\zeta = -0.1V$.

Table 5.1 List of the cases considered in electrokinetic flows

Case	**H (μm)**	**E_x (kV/m)**	**n_0 (N_A m^{-3})**
1	0.9	210.0	0.0075
2	2.0	1254.0	0.01
3	5.0	25.0	0.93

Using the Nernst-Planck multi-ion transport equations, electrokinetic flow is simulated in case 2 and EDL streaming potential values and pressure fields predicted by the Nernst-Planck model are compared to the Poisson-Boltzmann model predictions. Ionic valence is

z =1.0 for the symmetric buffer electrolyte considered (potassium chloride KCl). ε_r, the dielectric constant is assumed to be 80.0 for KCl electrolyte.

Validation of the present numerical model is performed by comparison of both EDL streaming potential ψ and axial velocity results with the published results for the problem geometry defined in Figure 5.1. The numerical results are validated with the experimental results reported by Chen and Santiago [110] and with the analytical results presented in Patankar and Hu [111]. The present steady state axial velocity results (Figure 5.2) in the fully developed region of the microchannel are compared with the experimental results and analytical solution. The area under the curve in Figure 5.2 represents the volumetric flow rate per unit width and it is calculated as 6.34 10^{-9} m^2/s. Flow rate is calculated as 14.46 µl/min. Chen and Santiago [110] reports the flow rate as 15.0 µl/min experimentally and 14.0 µl/min with one-dimensional analytical model of Patankar and Hu [111]. Considered width of the electrokinetic pump is 0.038 m similar to [110]. Numerical solutions are also compared with results presented in Zhang et al. [74, 75] to confirm the induced pressure predictions. The channel width does not have any influences on the flow profile. The depth of the micropump is considerably shallow comparing to the width of the micropump. The variations in the width direction can be ignored. Two dimensional models can adequately simulate flows in straight planar micropumps [111].

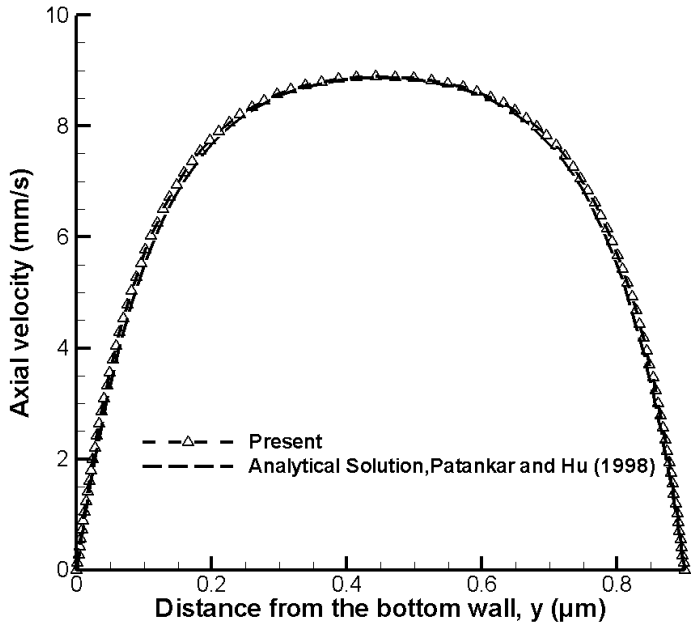

Figure 5.2 Comparison of predicted axial velocity [111]. L/H=4.5, x = 2.0 μm, κ = 8.2, E_x =210.0 (kV m^{-1}) and *Re* = 0.011 (case 1).

To ensure the numerical accuracy of the predicted velocity field and zeta potential distribution, first the analytical results presented in Patankar and Hu [111] are used. They showed that the analytical solution for the velocity as

$$u_f(y) = (1 - \frac{\cosh(\kappa(\frac{y}{H} - 0.5))}{\cosh(0.5\kappa)})U_{ref} \qquad (5.7)$$

where $U_{ref} = \frac{E_x \varepsilon_r \varepsilon_0 \zeta}{\mu}$ (m/s) and Debye–Hückel parameter $\kappa = (\frac{2n_0 z^2 e^2}{\varepsilon_r \varepsilon_0 k_b T})^{1/2} H$. Reynolds number for electrokinetic flows is defined as $\mathrm{Re} = \frac{\rho U_{ref} H}{\mu} = \frac{\rho E_x \varepsilon_r \varepsilon_0 \zeta H}{\mu}$. Characteristic thickness of the electric double layer (EDL) is the Debye length (λ_D) [1]. Debye length is inversely proportional to the concentration (n_0) of the electrolyte as $\lambda_D = (\frac{\varepsilon_r \varepsilon_0 k_b T}{2n_0 z^2 e^2})^{1/2}$. In the present study, n_0 has the following values for the cases considered: 0.0075 N_A m^{-3},

0.01 N_A m^{-3} and 0.93 N_A m^{-3}. The corresponding EDL thicknesses are 109.8 nm, 96.7 nm and 10.0 nm, respectively. Also κ represents the ratio of the channel depth to the Debye length (λ_D) and it quantifies the significance of the EDL field to the flow i.e. a small value of κ (8.2) yields a parabolic velocity profile and greater value (κ = 500, 1036 and 2590) yields a plug-like velocity profile. The numerical results match well with both analytical approach by Patankar and Hu and experimental approach by Chen and Santiago.

For small zeta potential, equation (3.9) can be approximated by the first terms in a Taylor series. For the microchannel (Figure 5.1) between two parallel flat plates variations in the axial direction are insignificant. Equation (3.9) can be reduced to

$$\frac{\partial^2 \psi}{\partial y^2} = \frac{2n_0 z^2 e^2}{\varepsilon_r \varepsilon_0 k_b T} \psi \tag{5.8}$$

Characteristic thickness of the electric double layer (EDL) is the Debye length given as $\lambda_D = (\frac{\varepsilon_r \varepsilon_0 k_b T}{2n_0 z^2 e^2})^{1/2}$ [1]. Debye length (λ_D) determines the effect of net charge density (ρ_e) on the EDL streaming potential, ψ as shown in the below equation:

$$\frac{\partial^2 \psi}{\partial y^2} = \frac{1}{\lambda_D^2} \psi \tag{5.9}$$

The boundary conditions are $\psi = \zeta = -0.675\ V$ at the channel walls (y = 0 and y = H = 2.0 μm). The analytical solution for EDL streaming potential is given by

$$\psi(y) = \frac{\cosh(\kappa(\frac{y}{H} - 0.5))}{\cosh(0.5\kappa)} \zeta \tag{5.10}$$

In Figure 5.3, the EDL potential (ψ) distributions are plotted for the numerical results and the analytical solution when $\kappa = 20.0$. The present solutions agree well with other published data. The Nernst-Planck multi-ion transport model predicts the distribution of ions using the equation (3.16) whereas Poisson-Boltzmann model (at x = 0.01 μm and 3.0 μm in Figure 5.3) assumes equilibrium distribution of ions (equation 3.7). According to Poisson-Boltzmann model charge neutrality is assumed to be satisfied in the bulk of the electrolyte.

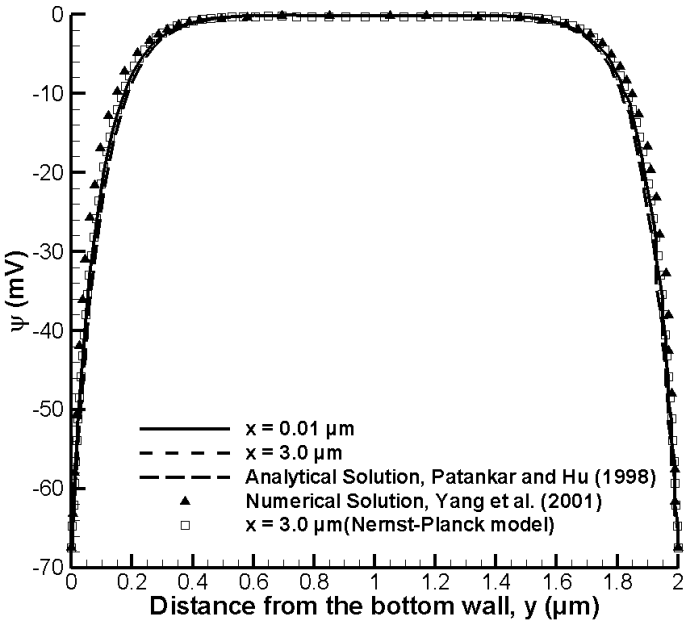

Figure 5.3 Comparison of EDL potential profile on x=constant planes [97, 111]. L/H = 3.0, κ = 20.0, E_x = 1254.0 (kV m^{-1}) and *Re* = 0.12 (case 2).

The present numerical predictions of the Nernst-Planck model slightly vary from the Poisson-Boltzmann model predictions due to the non-neutral charge distribution in the bulk of the electrolyte. For a fixed zeta potential $(\zeta = -0.675\ V)$, the fluid velocity

predictions of the Poisson-Boltzmann model agree with those of the Nernst-Planck model at a relatively large value of the Debye length ($\lambda_D = 96.7$ nm), which occur at low ionic concentration (n_0 = 0.01 N_A m^{-3}). The maximum value of axial velocity is found to be 60.0 mm/s with both models.

5.5 Results and Discussion

Figure 5.4 shows distribution of gauge pressure versus the distance from the bottom wall (y coordinate) at various axial positions. In an electrokinetic flow, an applied electric field acts on the net charge near the wall to produce a body force, which drives the fluid (Figure 5.4). The zeta potential of the channel wall influences the distribution of ions in the EDL. The interaction between the fluid charge near the wall and electric field is the main factor driving the fluid motion. The electrokinetic force is dominant close to the wall region due to the contribution from the term $2n_0 ze \sinh(\frac{ze\psi}{k_b T})\{\nabla(\phi+\psi)\}$ in equation (3.5). This force is approximately zero in the bulk region of the channel. The electrokinetic flow is the fluid motion driven by an applied electric field, differs from the classical pressure-driven flow. In the pressure-driven flow, when the velocity field is in a steady state, the driving force $\partial p / \partial x$ is constant for a flow with constant cross section in the fully developed region. Pressure boundary conditions (equations 5.1 and 5.2) are used following Zhang et al. [74], such that the local pressure loss and gain are recovered satisfying the momentum equations (3.5). The present pressure field predictions of the Nernst-Planck model slightly vary from the Poisson-Boltzmann model due to the non-neutral charge distribution in the bulk of the electrolyte. The Nernst-Planck multi-ion transport model predicts the distribution of ions using the equation (3.16) whereas

Poisson-Boltzmann model (at x = 0.01 μm, 3.0μm and 6.0 μm in Figure 5.4) considers the charge density to conform the Boltzmann equilibrium distribution. Charge neutrality is assumed to be satisfied in Poisson-Boltzmann equilibrium models. The convective effects of ion transport due to electrophoretic transport (ion convection and electro-migration) yield to slight deviations from the equilibrium as shown in Figure 5.4.

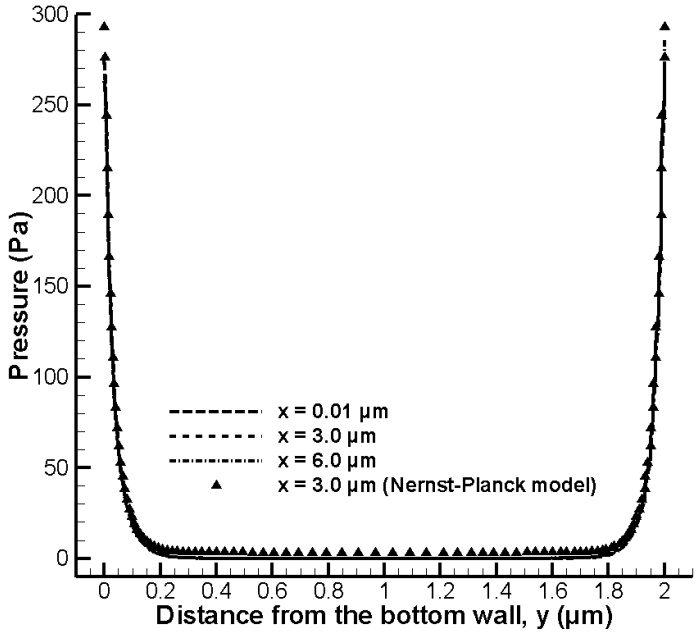

Figure 5.4 Pressure profile on x = constant planes. L/H = 3.0, κ = 20.0, E_x = 1254.0 (kV m^{-1}) and *Re* = 0.12 (case 2)

Example of the results using the present pressure boundary conditions (equations 5.1 and 5.2) is shown in Figure 5.5. In Figure 5.5, velocity vectors are shown for the entire microchannel (Figure 5.1). For the channel considered L/H is 20.0 (case 3). The inlet and outlet boundary conditions of pressure are updated including the effects due to the momentum of the flow. The velocity profile becomes slightly concave due to the

induced pressure gradient (see Figure 5.5). Viscous dissipation of the fluid causes an irreversible pressure loss at the channel inlet and outlet where flow contraction and expansion occur, which leads to a pressure difference at the channel inlet and outlet despite, there being no applied pressure in the reservoirs (side reservoirs are not shown in problem geometries). Not only the velocity distribution is affected but also the flow rate is reduced due to the increased dispersion as a consequence to the generated pressure field. If microchannels are connected crossing one another, the induced pressure distributions cause undesirable leakage to the side channels. It is currently believed to be the reason for the experimentally observed leakage phenomena through microchannels in the literature [74]. Maximum value of the axial fluid velocity is found to be 8.8 mm/s, 60.0 mm/s and 1.74 mm/s for electric field strengths of 210.0 kV/m, 1254.0 kV/m and 25.0 kV/m. Electrokinetic flow velocities increases with the strength of the electric fields.

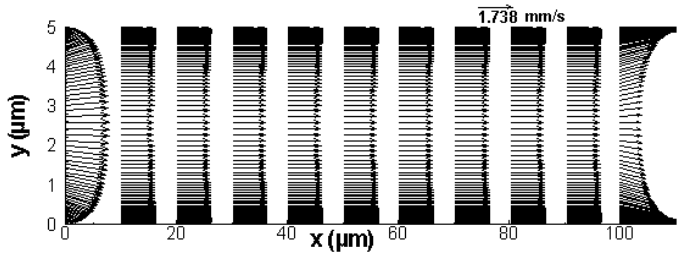

Figure 5.5 Vectors of velocity representing the effect of induced pressure on the axial velocity profile. κ = 500.0, E_x = 25.0 (kV m^{-1}) *Re* = 0.008, and L/H = 20.0. (case 3)

Happel and Brenner [112] showed, the pressure loss is no longer linearly proportional to mean velocity once the Reynolds number is greater than 1.6. On account of the linearity assumption is invoked, the deviation of the predicted velocity increases by

increasing Reynolds number. Predicted velocity profiles meet the stated Reynolds number limitation in the current study.

A dilute electrolyte solution with a small value of Debye–Hückel parameter (κ) yields a parabolic velocity as shown in Figure 5.2 whereas a higher concentration electrolyte with a higher κ yields a plug-like velocity profile as in Figure 5.5. Helmholtz–Smoulochowski" slip velocity approach fails to represent the induced parabolic velocity in electrokinetic flows. Hence, the present electrokinetic flow models are superior to the models treating electroosmotic flow as a wall slip boundary condition.

5.6 Conclusions

A computational study of electrokinetic flows in microchannels is presented where body forces are added to the momentum equations for analyzing the dynamics of the flow. A transient analysis for the flow of dilute potassium chloride-water electrolytes is performed in microchannels. Poisson-Boltzmann model (for electroosmotic flows) and Nernst-Planck (NP) transport models (for both electroosmotic-electrophoretic flows) are compared. The nonlinear electric double layer streaming potential and the applied electrostatic field are solved numerically. For non-equilibrium NP model distribution of ions and charged species are also solved simultaneously using convective-diffusive transport equations to account for electrophoretic species transport. The governing equations of mass/momentum conservation, electrical field and ionic charge distribution are solved simultaneously.

The convective effects of ion transport due to electrophoretic transport in NP model yield to slight deviations in electric double layer streaming potential field and pressure field from the equilibrium in PB model. For a fixed zeta potential, the fluid

velocity predictions with the Poisson-Boltzmann model agree with the predictions with the Nernst-Planck model at a relatively large value of the Debye length. Electrokinetic flow velocities are found to increase with the intensity of the electric fields. A dilute electrolyte solution yields a parabolic velocity whereas a higher concentration electrolyte yields a plug-like velocity profile. Helmholtz–Smoulochowski slip velocity approach fails to represent the induced parabolic velocity in electrokinetic flows. Hence, the present electrokinetic flow models are found to better represent electrokinetics than the models treating electroosmotic flow component of electrokinetics as a wall slip boundary condition. The model predictions compares well with experimental and theoretical results available in the literature for the electrokinetic flows.

A way of determining the static pressures at the inlet and outlet of microchannels is also presented that takes account of the pressure losses due to flow contraction and expansion. Local pressure loss at the channel inlet and outlet (where flow contraction and expansion occur) lead to a pressure difference at the channel inlet and outlet despite, there being no applied pressure in the side reservoirs. Not only the velocity distribution is affected but also the flow rate is reduced due to the increased dispersion as a consequence to the generated pressure field.

6. ACOUSTICALLY GENERATED FLOWS IN MICROCHANNEL FLEXURAL PLATE WAVE SENSORS[4]

Acoustically generated flowfields in flexural plate wave sensors filled with a Newtonian liquid (water) are considered. A computational model based on compressible flow is developed for the sensor with a moving wall for pumping and mixing applications in microchannels. For the compressible flow formulation, an isothermal equation of state for water is employed. The velocity and pressure profiles for different parameters including flexural wall frequency, channel height, amplitude of the wave and wave length are investigated for four microchannel height/length geometries. It is found that the flowfield becomes pseudo-steady after sufficient number of flexural cycles. Both instantaneous and time averaged results show that an evanescent wave is generated in the microchannel. The predicted flows generated by the FPWs are compared with results available in the literature.

6.1 Introduction

There is an increasing demand for small, reliable, disposable, and inexpensive sensors in industrial, medical, and a variety of other science and engineering fields [13]. Acoustic wave biosensors have been suggested as detection devices where the sensor utilizes acoustic waves as a detection mechanism to obtain medical information about the analyte of interest.

[4] Results presented in this chapter appeared in "Acoustically Generated Flows in Microchannel Flexural Plate Wave Sensors: Effects of Compressibility," by E. Sayar and B. Farouk *Sensors and Actuators A-Physical*, vol. 171, pp. 317-323, 2011.

In the present work, acoustically generated flowfields in microchannels as found in flexural plate wave (FPW) sensors (including the effects due to compressibility) are modeled. FPWs are generated by the application of an alternating voltage signal to interdigitated transducers (IDTs) patterned on a piezoelectric substrate. In FPW sensors, the oscillating membrane is assumed thin compared to the wavelength of the vibrating mode so that the top and the bottom surfaces are strongly coupled and a single wave propagates along the membrane [24, 33]. The present study focuses primarily on steady streaming results induced by the flexural plate waves (FPW). The present work builds on and clarifies the results in [17, 21, 22, 47] pertaining to progressive FPW operation in a compressible viscous liquid. In order to consider the FPW pumping capability, the dependence of velocity profile on the channel height, wave amplitude, wave length, and actuation frequency are investigated.

6.2 Problem Description and Geometry

An FPW device with an oscillating wall is shown in Figure 6.1. For a flexural plate wave sensor, (bottom surface in Figure 6.1) induced perturbation propagates across the piezoelectric material thickness and the nature of the induced wave does not change along the thickness. Wave motion can be described by sinusoidal functions. The geometrical parameters of the FPW micropump are chosen from the values used in [22]. The membrane (comprising of the piezoelectric material) has typical width of 3.0 mm and a length of 8.0 mm. The dimensions of FPW micropumps are often in the same range as mentioned in [22]. A representative length ($L = 3\lambda$) is considered for the simulation domain where λ is the flexural wavelength. Since the nature of the device is periodic, the simulated length of the channel, L, can represent the device (using periodicity at both

ends). The glass slide closing the flow domain is considered as rigid (top wall in Figure 6.1). The bottom geometry can be defined by $A_0\ (t)$, the amplitude of the wave, height H, thickness of the membrane d, and length of the microchannel L respectively.

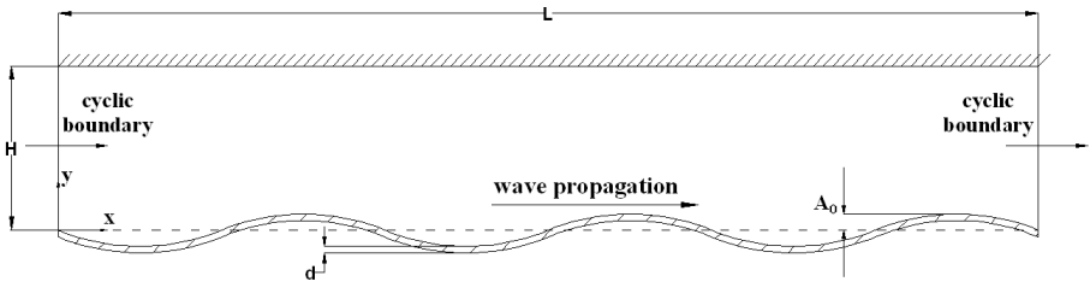

Figure 6.1 Schematic of the FPW acoustic device considered.

Table 6.1 lists the cases considered in the present study. In case 1 the parameters are chosen from the values used in [22], H = 50.0 μm, L = 300.0 μm, f = 3.0 MHz. In case 2 a shallow microchannel (H = 5.0 μm) is considered. In cases 3 and 4, the amplitude of the perturbations A_{max} is varied while keeping other parameters same as in Case 1. In case 5 a shallow microchannel (H = 25.0 μm) is considered. In cases 6 and 7 the effect of actuation frequency f is investigated.

Table 6.1 List of the cases considered for the FPW sensor

Case	H (μm)	L/H	Max. Amplitude (nm)	Wall Frequency (MHz)	Wave Length (μm)
1	50.0	6.0	6	3	100
2	5.0	60.0	10	3	100
3	50.0	6.0	10	3	100
4	50.0	6.0	4	3	100
5	25.0	12.0	10	3	100
6	100.0	4.5	10	1	150
7	100.0	4.5	10	3	150

6.3 Boundary Conditions

The boundary conditions for the dependent variables need to be specified for the problem geometry (Figure 6.1) considered. A moving wall is considered for the bottom flexural surface, and a rigid wall for the upper surface. Along the walls zero slip boundary conditions (relative to the stationary or moving wall) are used for the velocity components.

For acoustically driven flows, the FPWs are generated by the application of an alternating voltage signal to the IDTs patterned on a piezoelectric substrate (bottom wall in Figure 6.1). A vibrating membrane (bottom) perturbs a compressible fluid (Figure 6.1). The vertical displacement Δy of the membrane is given by:

$$\Delta y = -A_o(t)\sin(\omega t - kx) \tag{6.1}$$

where A_0 (t) is the wave amplitude, $\omega = 2\pi f$ is the angular frequency of the wave, and f is the cyclic frequency (Hz), $k = 2\pi/\lambda$ is the wave number, $c_p = \lambda f$ is the phase velocity [113] and λ is the wavelength. With a membrane thickness d, the horizontal wall displacement is

$$\Delta x = \left(A_o(t)\pi d / \lambda \right) \cos(\omega t - kx) \qquad (6.2)$$

For the cases considered (Table 6.1), the FPW has a frequency of 1.0 -3.0 MHz, and wave amplitude of 4.0 -10.0 nm, a membrane thickness (d) of 3.0 μm and a wavelength λ of 100.0 -150 .0 μm. The channel considered is three wave-lengths long (3λ = 300.0 – 450.0 μm) for the cases investigated. Width of the channel is also varied between 5.0 – 100.0 μm. In order to consider a realistic initial condition and to eliminate immediate water hammer effects, the wave amplitude is described as a function of time: $A_0(t) = A_{\max}(1 - \exp(-tf))$ i.e., the perturbation increases gradually from zero. Periodic boundary conditions are used at the inlet and outlet for all cases following Nguyen and White [22]. The fluid is initially quiescent and the pressure is atmospheric.

6.4 Validation of the Model

Verification of the present numerical model is performed by comparison of the time averaged axial velocity results with the published results [22, 33] for the problem geometry given in Figure 6.1. Numerical solutions are also compared with experimental measurements by Moroney [114]. For the geometry defined in Figure 6.1 (flexural plate wave) time dependent and averaged velocity profiles are calculated.

Figure 6.2 shows the comparison of the present model predictions (Case 1) of time-averaged axial velocity profile along the width of the microchannel at x = 150 μm with the results of Nguyen and White. The results were obtained with (a) an incompressible flow model, (b) with a compressible flow model. The incompressible flow model results agree well with the results of Nguyen and White [22] but differs from the measurements by Moroney [114]. The time averaged maximum axial velocity is 174 μm/s for the present compressible flow model prediction while the value for the

incompressible flow model is about 900 μm/s. The measured time averaged maximum axial velocity is reported by Moroney [114] to be 85 μm/s. The incompressible flow numerical result [17, 22] of 900 μm/s is more than 10 times the measured value.

The experimental results in reference [114] were produced using micro PIV techniques. For the micro PIV technique, polystyrene spherical tracer beads with 2.3 μm were used. For the FPW, the frequency is about 3.0 MHz [114]. The acoustic radiation force acting on large particles is a gradient force, while the acoustic streaming force acting on small particles is due to viscous drag from the vortex motion in the carrier bulk liquid is a rotation force. For the small particle limit (for microbead diameter < 2.6 μm) the acoustic radiation force is negligible and the particle flows with the streaming velocity of the flow, independent of the particle radius [29]. For very small particles (<< 2.6 μm) particle diffusion is no longer negligible. The tracer particles (2.3 μm) used by Moroney [114] are close to the small particle limit and hence direct acoustic force plays a negligible role. The microbeads used in [114] follow the bulk flow and hence can measure the correct streaming velocity of the flow. Hence our predicted results (using the compressible flow model) are close to the experimental results [114]. However, due to the high velocity gradient near the surface and the complicated interaction between flowing fluid and tracer solid particles, the experimentally measured velocity of the particles [114] is expected to be somewhat smaller than the actual fluid velocity, as predicted in our simulations.

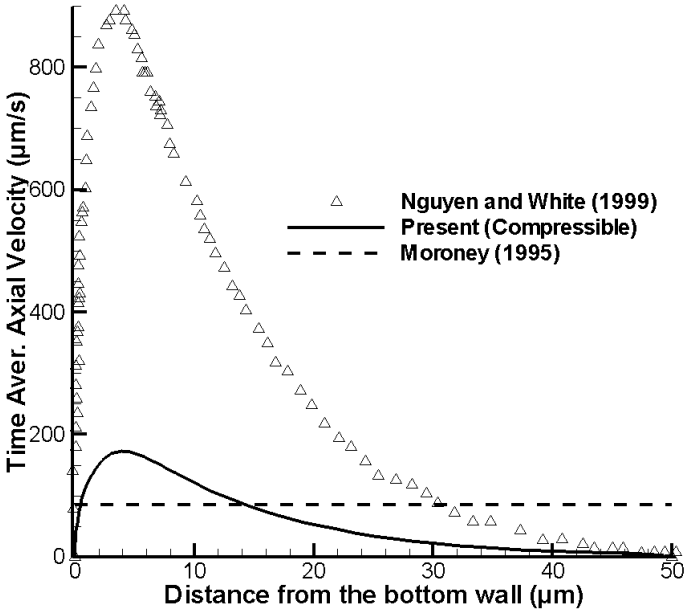

Figure 6.2 Velocity profile in a 50μm channel [22, 38].Amax = 6 nm, f = 3 MHz, λ = 100 μm, H = 50 μm, L/H = 6.0, x = 150.0 μm and d = 3 μm (Case 1).

6.5 Results and Discussion

6.5.1 Acoustically Driven Flows in Microchannel: Quasi-Periodic State

In Figure 6.3 vectors of velocity are plotted at an instant of time ($t = 2\ 10^{-5}$ sec) for the entire microchannel (Table 6.1: Case 1). The y-axis is magnified by a factor of two for better representation. Bulk acoustic wave (BAW) propagates along the membrane and excites longitudinal and shear waves into the fluid [115]. The motion of the membrane results in the observed fluid recirculation patterns. Points on the device surface move elliptically in a clockwise direction as the flexural wave travels from left to right. Membrane drifts the bulk of the fluid from left to right. The longitudinal sound waves generated in the fluid medium are attenuated by the viscous fluid during their transmission through the medium. The extent of the decay is dictated by the magnitude of the imposed wave amplitude (practically controlled by the applied input voltage) as well

as the viscous dissipation and the compression encountered by the longitudinal wave in the fluid medium. The shear waves damp out proportional to the shear viscosity and the frequency. The BAW does not decay along the direction of propagation as shown by the velocity vectors in Figure 6.3 (along the bottom wall) due to the strongly coupled- single wave nature of the FPW. It can be concluded from Figure 6.3 that the vertical velocity component provides an enhancement of the mixing process, which is almost zero for low Reynolds number electroosmotic flows.

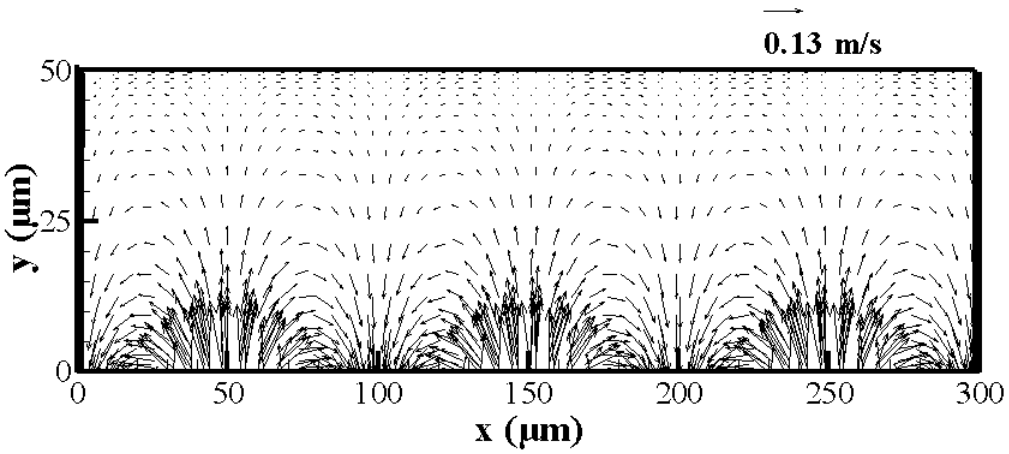

Figure 6.3 Velocity vector plot at a given time instant (t = 6000th time step). A_{max} = 6 nm, f = 3 MHz, λ = 100 μm, H = 50 μm, L/H = 6.0 and d = 3 μm (Case 1).

Figure 6.4 describes the contours of the pressure field at a fixed phase in the microchannel when t= 20.0 μs (Case 1). FPW wave propagation generates vortex structures near the wall. In the FPW device, for a time averaged flow rate of 1.5 10^{-7} m^3/s an equivalent pressure gradient of 100.0 kPa/m is calculated using the Poiseulle flow

model. – hence the device can be useful for micropumping purposes. The instantaneous pressure field changes with time within a flexural cycle.

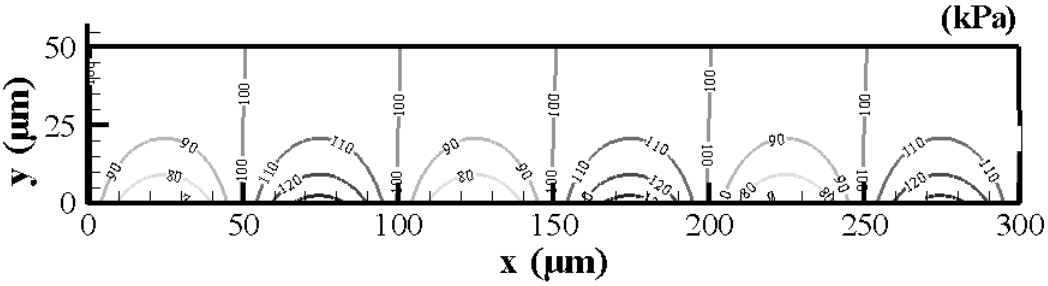

Figure 6.4 Contours of the pressure generated as a result of the recirculation at the surface of the FPW device at the beginning of 60th cycle. A_{max}= 6 nm, f = 3 MHz, λ = 100 μm, H = 50 μm, L/H = 6.0, and d = 3 μm (Case 1).

In Figure 6.5 variation of instantaneous pressure along the direction (x) is plotted at selected constant y lines (Case 1). Our simulation results indicate that the extent of recirculation decreases with increasing distance from perturbing surface. It can therefore be seen from Figure 6.5 that the generated pressure at the device surface also decays rapidly with distance from the membrane. The optimization of design parameters such as applied wave amplitude, transducer periodicity and frequency could help generate sufficient pressure field along the entire width. It can facilitate mixture of species that are otherwise molecular diffusion limited.

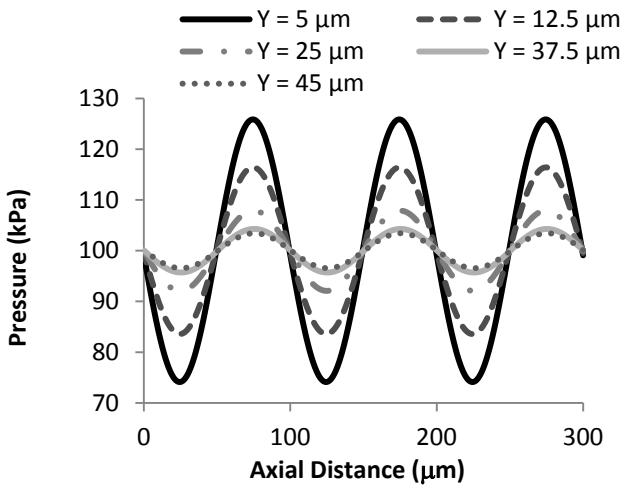

Figure 6.5 Instantaneous pressure versus propagation direction (x) along selected y=constant lines. At the beginning of 60th cycle, A_{max}= 6 nm, f = 3 MHz, λ = 100 µm, H = 50 µm, L/H = 6.0, and d = 3 µm (Case 1).

In Figure 6.6 axial velocity is plotted along the y-axis at t = 2.0 10^{-5} sec for selected constant x lines (Case 1). Total internal reflection occurs when acoustic radiation strikes a medium boundary at an angle larger than a particular critical angle of incidence. The critical angle can be calculated by the wave phase velocity on the membrane (300 - 450 m/s) and wave velocities in the liquid (1480 m/s). The calculated critical angle is 11.7° - 17.7°. The total internal reflection occurs since the reflection angle is greater than the critical angle of incidence in the present study. Therefore, an evanescent wave is generated. The magnitude of the first order particle velocity (instantaneous velocity), u_f , exponentially decays for the evanescent disturbance in the fluid adjacent to the membrane as [17] :

$$u_f = u_{f,\max}\exp(-y/\gamma) \tag{6.3}$$

$$\gamma = \frac{\lambda}{2\pi\sqrt{1-(c_p/c_s)^2}} \tag{6.4}$$

where $u_{f,max}$ is the maximum value of the membrane velocity (0.113 m/s), y is the vertical distance from the membrane, γ is the acoustic evanescent decay distance, λ is the wave length of FPW (100 μm), c_p is the phase velocity of FPW (300 m/s) and c_s is the speed of sound in water (1480m/s). Evanescent decay distance is calculated as 16.25 μm from equation (6.4) following Moroney et al. [17]. Based on the present instantaneous axial velocity as in Figure 6.6, evanescent decay distance is calculated as 16 μm. In Figure 6.6, slightly lower velocities are observed within the viscous boundary layer (0.3 μm) due to the shear. The medium outside the boundary layer vibrates irrotationally in accordance with the sound field. It can be seen that the mode conversion from bulk acoustic wave to a combination of shear and longitudinal waves leads to an exponential decay in the fluid away from the actuator surface (y = 0).

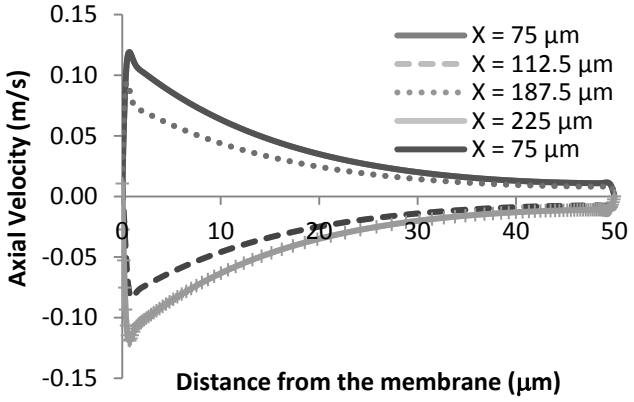

Figure 6.6 Axial velocity along the width of the microchannel at t = 2.0 10^{-5} sec. A_{max}= 6 nm, f = 3 MHz, λ = 100 μm, H = 100 μm, d = 3 μm and L/H = 6 (Case 1).

Figure 6.7 depicts the comparison of *u*-distribution versus the wall distance at different time levels (4 consecutive phases within a cycle) for the FPW problem for Case

1. The nature of the flow in an FPW sensor possesses similarity to the classical Stokes' second problem. In FPW, the flow is generated on a wavy surface (sinusoidal) and the domain is bounded by the upper rigid boundary (y = H). The flow is generated by the elliptical motion of the boundary in FPW devices. Stokes' second problem refers to a case for the semi-infinite domain in the fluid-mechanics benchmark problems [116]. The flow above an infinitely long flat plate is at rest initially and suddenly the plate is forced to an oscillatory motion with a specific frequency. The oscillatory nature of the flow generates damped harmonic waves in the velocity field.

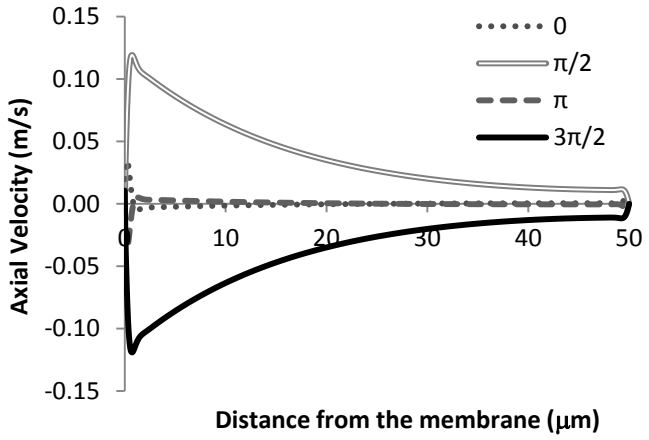

Figure 6.7 Instantaneous axial velocity profiles of 50 μm channel. Each line represents a distinct phase in the 60th cycle. A_{max} = 6 nm, f = 3 MHz, λ = 100 μm, H = 50 μm, d = 3 μm, L/H = 6 and x = 75.0 μm (Case 1).

In an FPW device, the boundary is oscillating with time, it is expected that the fluid will also oscillate in the y direction in time with a specific frequency. In the first half of the cycle (0 - π in Figure 6.7) the first order particle velocity is along the positive x direction in the bulk of the fluid. Similarly, in the second half of the cycle (π - 2π in Figure 6.7) the

first order particle velocity is along the negative x direction in the bulk of the fluid. Therefore, at 0 and π, flow reversal is observed at regions close to the FPW membrane.

In Figure 6.8 variation of instantaneous pressure along the width of the channel (y) is plotted (Case 1). When a boundary condition defining FPW is applied, the pressure changes with time. The generated pressure at the device surface decays rapidly with distance from the membrane. Figure 6.8 depicts the comparison of pressure distribution along the wall distance at different time levels (4 consecutive phases within a cycle). The bottom boundary in Figure 6.1 is oscillating elliptically with time resulting in reversals in the direction of the flow. Accordingly, at phase angles of 0 and π sharp pressure gradients are observed within the viscous boundary close to the bottom wall (Figure 6.8).

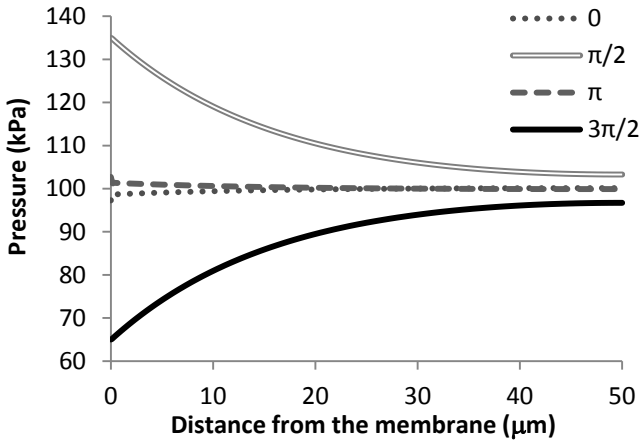

Figure 6.8 Instantaneous pressure profiles along the width of the channel. Each line represents a distinct phase in the 60th cycle. A_{max} = 6 nm, f = 3 MHz, λ = 100 μm, H = 50 μm, L/H = 6.0, d = 3 μm and x = 75.0 μm (Case 1).

6.5.2 Time Averaged Velocity Field: Streaming Velocity

Figure 6.9 shows model predictions of time-averaged velocity profile (case 1). Grid density is finer adjacent to the both the rigid and the oscillating boundaries

(symmetric grid). In Figure 6.9, different from the previous work by Nguyen and White [22] no flow reversals are observed close to the top boundary in the present predictions. However Nguyen and White [22] reports flow reversals – this may be the due to incompressible flow formulations. Incompressible flow formulation can result in excessively high velocities as shown earlier in Figure 6.2. Another important observation is that a FPW micropump can produce about 0.1 MPa/m of pressure – hence the micropump can be useful for micropumping purposes.

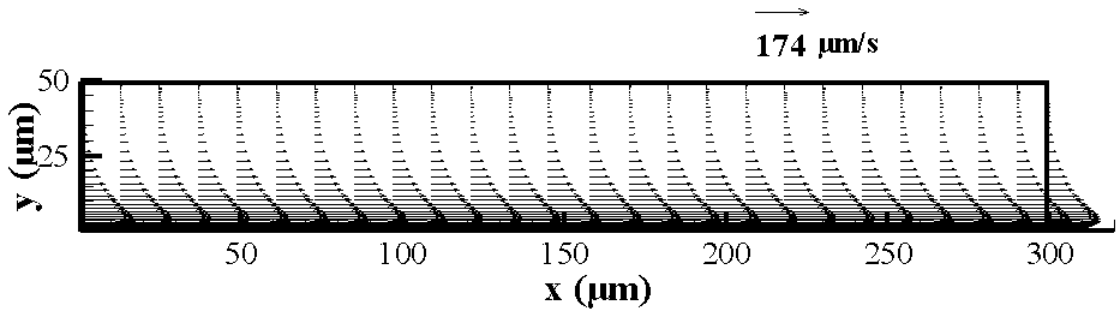

Figure 6.9 Vectors of time averaged velocity. f = 3 MHz, λ = 100 μm, d = 3 μm., A_{max} = 6 nm, H = 50 μm and L/H = 6 (Case 1).

A series of simulations are performed to observe the effect of changing channel height, amplitude of the acoustic perturbation (driving voltage), excitation frequency, and transducer periodicity on the streaming velocity and its patterns. Wave amplitude is varied in between 4 nm to 10 nm while varying channel heights between 5 μm - 100 μm are considered. Frequency (1 to 3 MHz) and transducer periodicity (100 - 150 μm) are also varied (Table 6.1).

Figure 6.10 shows time-averaged velocity profile (Case 2) for a shallower microchannel (H = 5 μm). The time averaged velocity profile over one period become parabolic for a shallower channel whereas the velocity profile is asymmetric for a deeper microchannel (Case 1, Figure 6.9). Nguyen and White [22] found out that the thickness of the evanescent decay length determines the transition from a parabolic profile to an asymmetric velocity profile. When the channel height (such as 25 μm, 50 μm or 100 μm) is greater than 16 μm [17] (evanescent decay distance) the time averaged velocity profiles deviate from parabolic velocity profile to an asymmetric wall-jet driven velocity profile. The velocities in the channel beyond the evanescent decay distance are small (See Figure 6.9).The thickness of the viscous boundary layer is also found to be 0.3 μm.

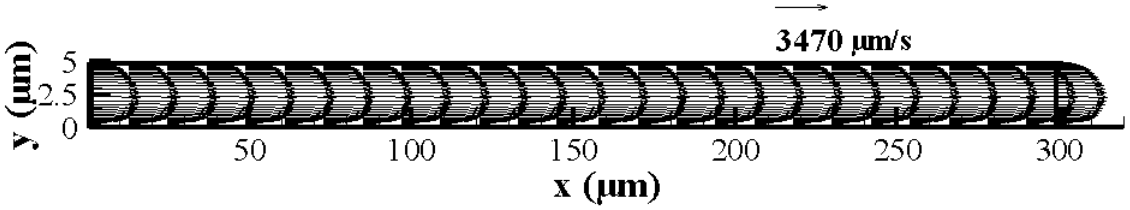

Figure 6.10 Vectors of time averaged velocity. f = 3 MHz, λ = 100 μm, d = 3 μm, A_{max}= 10 nm, H = 5 μm and L/H = 60 (Case 2).

Figure 6.11 depicts the velocity profile as function of distance from the membrane and wave amplitude in a microchannel with constant height along the vertical midplane (Cases 1, 3 and 4). The time averaged velocity profiles are shown at the 63rdcycle. Channel height is kept constant at 50 μm while varying wave amplitudes between 4.0 nm - 10.0 nm are considered. Maximum values of the generated time averaged axial

velocities were found to be quadratically scaling ($\bar{u}_f \propto A_{max}^2$) with the acoustic wave amplitudes for a microchannel (H = 50.0 μm). The pseudo-periodic state solutions are confirmed by the negligible standard deviation between velocity profiles for the same phases during several consecutive cycles. As seen in Figure 6.11, most of the fluid motion is confined to within the first 20 μm. At distances 20 μm from the substrate surface, the wave motion is significantly dampened. This behavior is observed across the entire applied amplitude range 4 nm –10 nm simulated in this study. The streaming patterns near the device membrane are directly influenced by the motion of the moving boundary.

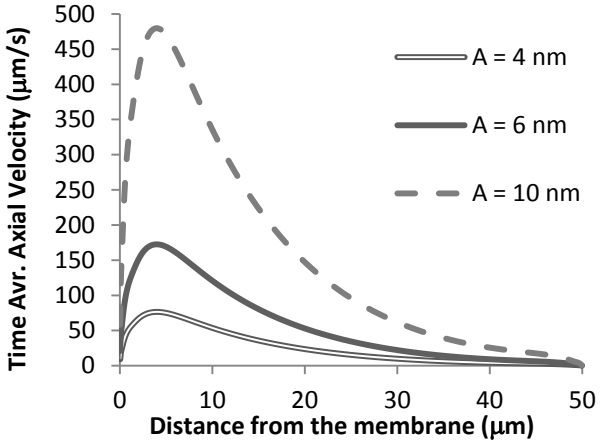

Figure 6.11 Velocity profile over the channel with height of 50 μm driven by different wave amplitudes. A_{max} = 4-10 nm, f = 3 MHz, λ = 100 μm, H = 50 μm, d = 3 μm, L/H = 6, x = 75.0 μm. (Cases 1, 3-4)

Figure 6.12 depicts time-averaged velocity profiles over one cycle for different microchannel heights when the frequency f = 3 MHz is applied (Cases 2, 3 and 5)**.** The wave amplitude is kept constant as 10 nm for the cases 2, 3 and 5. When channel height

is greater than 16 μm, the evanescent decay distance, (as in H = 25.0 μm and H = 50.0 μm) the velocity profiles start to deviate from parabolic velocity profile. This curve shows similarity to the Nyborg's streaming theory that the maximum velocity does not depend on channel height with a channel height that is greater than the evanescent decay distance of the acoustic wave in the fluid. The attenuation of the wave away from the actuator surface results in a decrease of the magnitude of time averaged velocity for deeper microchannels (H = 25.0 μm and H = 50.0 μm). For shallow channel (H = 5.0 μm), FPW couples well with the flow generating higher velocities.

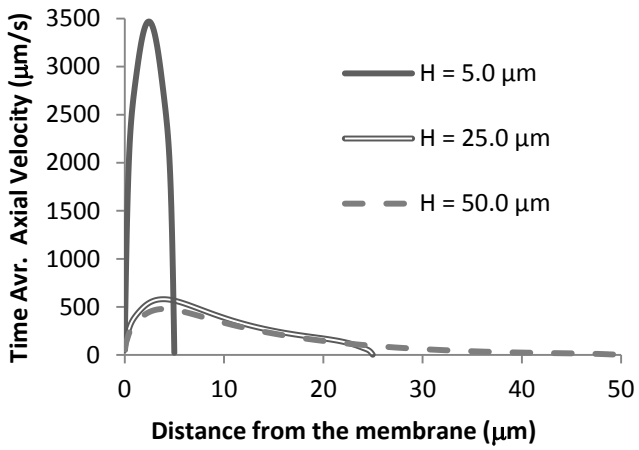

Figure 6.12 Velocity profile with different channel heights driven by a wave whose amplitude is 10 nm. A_{max} = 10 nm, f = 3 MHz, λ = 100 μm, H = 5, 25 and 50 μm, d = 3 μm, L/H = 60, 12 and 6, x = 75.0 μm. (Cases 2-3, 5)

Time averaged tangential velocity profile over the channel height of 100 μm driven by two different wave frequencies is shown in Figure 6.13 (Cases 6, 7). The profiles are plotted along the width of the microchannel. As the frequency of the flexural wave device increases, time dependent velocity also increases. This results in an increase

in the acoustic streaming velocity which is proportional to the square of the irrotational instantaneous velocity [34]. The streaming velocity depends on the excitation frequency as well as the energy dissipation into the fluid, which itself is linearly dependent to the FPW frequency. Figure 6.13 shows results similar to those shown in Figure 6.12 for a varying actuation frequencies (1 MHz to 3 MHZ), a longer wavelength (150 μm instead of 100 μm), and a deeper microchannel (100 μm). For the actuation frequency of 3 MHz, the maximum value of the time-averaged velocity is decreased by a factor of about 0.7 in Figure 6.13 (H = 100 μm) compared to that shown in Figure 6.12 (based on H = 50 μm). Decrease in actuation frequency by a factor of 3, yields a drop in time averaged velocity by a factor of 0.29. Figures 6.9 - 6.13 show that the streaming velocity increases from zero and reaches a peak value after decreasing again. The normal component of the time averaged velocity is significantly lower than the tangential component for the range of conditions simulated in this work.

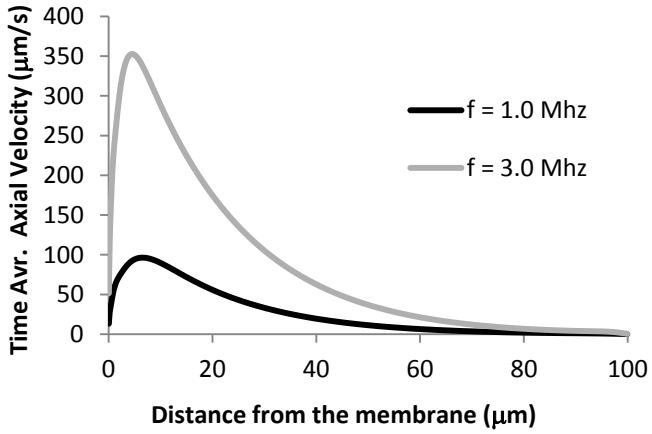

Figure 6.13 Velocity profile over the channel with height of 100 μm driven by different wave frequencies. A_{max} = 10 nm, f = 1 MHz and 3 MHz, λ = 150 μm, H = 100 μm, d = 3 μm, L/H = 4.5, x = 75.0 μm. (Cases 6, 7)

6.6 Conclusions

The flowfields generated in a microchannel due to ultrasonic flexural waves are presented. The compressibility of the liquid is considered with an isothermal equation of state. The pumping performance is investigated with different variable parameters: wave amplitude, channel height, wave length and actuation frequency. For a shallow microchannel (H = 5.0 μm), FPW couples well with the flow generating higher velocities. The attenuation of the wave away from the actuator surface results in a decrease of the magnitude of time averaged velocity for deeper microchannels (H = 25.0 - 50.0 μm) The model predictions were compared with results [22, 114] available in the literature. White and his coworkers conducted numerical simulations [17, 22, 33] for similar problems, albeit considering incompressible flow formulation. Their simulation results had to be corrected by a factor of 10 in order to fit the measurement data by Moroney [114]. The predicted results in the present study compare more favorably with the measurement data. The predicted velocity field proved the existence of induced vertical velocity component which can enhance mixing process significantly. Fluid loading on an oscillating FPW device is modeled capturing attenuation of perturbation due to the inertia and viscosity of the fluid as well as through the density variations. The device geometry considered can be exploited to integrate micropumps into microfluidic chips. Source of discrepancy between the present study and the experimental work is perhaps due to deviation of the membrane motion from the specified sinusoidal forms, the limitations of the equation of state, and the complicated interaction between fluid and tracer particles during the experiments by Moroney [114]. In our future studies, the equation of state will be improved including the effects of temperature.

7. ELECTROOSMOTIC AUGMENTATION IN FLEXURAL PLATE WAVE MICROPUMPS

7.1 Introduction

The effectiveness and applicability of electroosmotic augmentation in flexural plate wave (FPW) micropumps for enhanced capabilities are investigated. Flow rates generated in FPW micro-scale flow systems are restricted especially when the channel height is greater than the acoustic wave length. The proposed concept can be exploited to integrate micropumps into complex microfluidic chips improving the portability of micro-total-analysis systems along with the capabilities of actively controlling acoustics and electrokinetics for micro-mixer applications. A computational study of electroosmotic augmentation in FPW micropumps is presented where FPWs are considered by a moving wall model. A transient analysis of compressible flows of water is performed for microchannels. An isothermal equation of state for water is employed. The nonlinear Poisson-Boltzmann and Laplace equations are used to model the induced electric double layer (EDL) potential and the applied electric potential. Coupled electrokinetics and acoustics cases are investigated for two channel heights while the electric field intensity of the electrokinetic body forces and actuation frequency of acoustic excitations are varied. Volumetric flow rates and thermodynamic efficiencies of the considered micropumps are investigated establishing guidelines to better understand the flow rate in current practical mixer applications. For deeper microchannels increasing the actuation frequency of the wall motion does not improve the generated flow rate significantly. Inclusion of electroosmotic effects is more efficient than increasing the

intensity of acoustic perturbations whenever high flow rates are required in micromixer applications.

The mixing of two or more fluids in microfluidic systems is important in biological processes like cell activation, enzyme reactions and protein folding. Mixing of analytes and reagents is difficult due to the low Reynolds number of the flows in microscale devices. Various schemes to enhance micro-mixing have been proposed in the past years. The review by Chang and Yang [42] reports recent developments in the electrokinetic micro-mixing schemes based on DC and AC electrokinetics, including electrowetting-on-dielectric (EWOD), dielectrophoresis (DEP) [117], and electroosmosis (EO). Mixing in microchannels relies primarily on molecular diffusion or chaotic advection mechanisms. In passive devices, only molecular diffusion limited mixing mechanism is effective. The length of mixing channel is extended to ensure a well-mixed stream at the outlet.

The present study investigates electroosmotically augmented flows in flexural plate wave (FPW) micropumps. A multi-function microfluidic device where acoustic excitations can be used for mixing or sensing and electroosmotic flow generates the required pumping effect in flow-through sensors with microfluidic chips is investigated. A computational study of electroosmotic augmentation in FPW micropumps is presented by the developed moving wall model. The model predictions are compared with results available in the literature for electroosmotic flows, and for the flows generated by acoustic waves. Coupled electrokinetics and acoustics cases are investigated while the electric field intensity of the electrokinetic body forces and actuation frequency of acoustic perturbations are varied. Volumetric flow rates and thermodynamic efficiencies

of the considered micropumps are investigated establishing guidelines to better understand the flow rate in current practical mixer applications.

Solving for the electroosmotic velocity field in complex geometries requires a solution of the electric field and charge density in the microchannel, together with a solution to the Navier–Stokes equations [5, 68-73]. Details regarding the developed electro-osmotic flow models (for purely electrokinetically driven flows) can be found in section (3.2) and the results on this model are given in chapter (5). For the flows with acoustic excitations, the compressibility of water needs to be considered in some sense [23]. Flexural plate wave micropumps model is discussed in section (3.3.1). Results of the purely acoustically generated flows model for flexural plate wave sensors can be found in chapter (6).The present work is the first study to investigate the net flow in a deep FPW device. Previous works [17, 19, 22, 118] are for acoustic streaming in shallow FPW cavities for chemical vapor or liquid viscosity sensing applications. This study is also the first work that predicts the thermodynamics efficiencies of FPW micropumps. The present study requires the simultaneous numerical solution of the governing equations of mass/momentum conservation, electrical field and ionic charge distribution.

7.2 Problem Description and Geometry

The problem geometry for a coupled electrokinetics-acoustics case is shown in Figure 7.1. The flow starts to move due to electrokinetic and acoustic effects, once the DC electrical potential at the inlet (left boundary in Figure 7.1) and AC electrical potential on the piezoelectric elements are activated. A moving wall is considered for the bottom flexural surface, and a rigid wall for the upper surface. Top and the bottom surfaces are charged with zeta potential (ζ). Zeta potential induces an EDL field to drive

fluid with electrokinetic body forces in addition to the acoustic excitations in electroosmotically augmented flows through FPW micropumps.

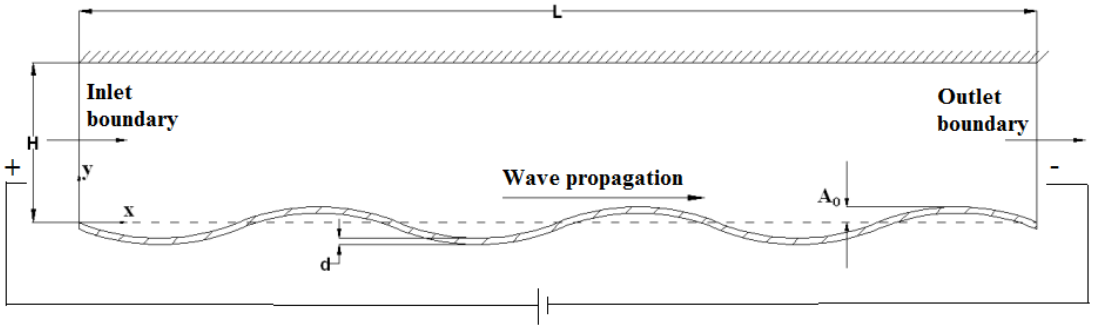

Figure 7.1 Schematic of the electroosmotically augmented FPW micropump.

A FPW micropump with an oscillating wall (bottom surface) is shown in Figure 6.1. Wave motion can be described by sinusoidal functions. The FPW acoustic device geometry (Figure 6.1) can be defined by $A_0\ (t)$, the amplitude of the wave, height H, thickness of the membrane d, and length of the microchannel L respectively. Further details of the problem description and geometry of the flexural plate wave acoustic device are given in section (6.3).

The problem geometry shown in Figure 5.1 is for the cases where only electroosmosis is investigated. When a liquid phase containing positive and negative ions contacts a planar, charged surface (ζ, zeta potential), an EDL field is established [5]. Once the DC electrical potential at the inlet (left boundary in Figure 5.1) is activated, the flow starts to move due to the interactions between the channel walls, buffer electrolyte

and the external electric field. Details of the problem description can be found in section (5.2).

7.3 Boundary Conditions

For purely electroosmotic flows, zero gradient boundary conditions are specified for velocity and EDL streaming potential ψ along the inlet and outlet boundaries (left and right boundaries in Figure 5.1, respectively). For the streaming potential equation, the wall value is given by the zeta potential ζ , ϕ_{inlet} and ϕ_{outlet} (applied potential values along the inlet and outlet, respectively) are specified for the electrostatic field equation (ϕ). Walls are assumed to be insulated against applied electrical potential. The specification of the pressure boundary conditions (equations (5.1) and (5.2) is applicable for situations where the flow starts and terminates at large reservoirs as in the present case. These boundary conditions are discussed in detail in section (5.3).

For acoustically driven flows (for the problem geometry see Figure 6.1), a vibrating (bottom) membrane perturbs a compressible flow and the time and space dependent displacements drive the adjoining fluid as described in section (6.3). Periodic boundary conditions are used at the inlet and outlet for acoustically excited flows.

For electroosmotically augmented flows in FPW micropumps (for the problem geometry see Figure 7.1), streaming potential value on the walls is given by the zeta potential ζ . ϕ_{inlet} and ϕ_{outlet} are applied potential values along the inlet and outlet. Along the inlet / outlet pressure is specified according to the equations (5.1) and (5.2). Zero slip boundary conditions are used along the walls for velocity for all cases considered. Initially, pressure is atmospheric and all other dependent variables are zero. A vibrating

(bottom) membrane perturbs a compressible flow (Figure 7.1). and the time and space dependent displacements drive the adjoining fluid as described in section (6.2).

7.4 Results and Discussion

Table 7.1 below lists the cases considered in the present study. Electroosmotic flow is first modeled in a microchannel (Figure 5.1) using the Poisson-Boltzmann equation set (case 1). In case 1 the parameters of electroosmotic flow model are chosen from the values used in [110], H= 0.9 μm, L/H = 4.5, bulk concentration of ions, n_0 = 0.0075 N_A m^{-3} (N_A is the Avogadro number), zeta potential $\zeta = -0.05V$ and E_x = 210.0 (kV m^{-1}). A FPW micropump is modeled by a moving oscillating wall as shown in Figure 6.1 (cases 3 - 7). In case 2, H = 100.0 μm, λ = 150.0 μm, f = 1.0 MHz and A_{max} = 10.0 nm and effect of acoustic excitation is investigated for comparison with electroosmotic augmentation in FPW micropumps predictions. In cases 2 -5, channel height is varied (H = 5.0 μm, 25.0 μm, 50.0 μm and 100.0 μm).

Electroosmotic flow is considered in a H= 100.0 μm deep channel in case 6. In cases 7 - 11, electroosmotic augmentation in a shallow (H= 100.0 μm) FPW micropump (Figure 7.1) with varying electric field intensities (E_x = 3.0 -100.0 kV/m) is studied. The results (for cases 7 – 11) are compared with predictions obtained in case 4 (pure electroosmotic flow). Electroosmotic augmentation in a deeper (H= 250.0 μm) FPW micropump (Figure 7.1) with varying electric field intensities (E_x = 0.0 -100.0 kV/m) is considered in cases 12 - 17. Electroosmotic augmentation in a shallow FPW micropump (in cases 11, 18 - 21) with varying actuation frequencies (f = 1.0 -10.0 MHz) is investigated. Electroosmotic augmentation in a deep FPW micropump (in cases 17, 22 - 25) with varying actuation frequencies (f = 1.0 -10.0 MHz) is also studied.

In cases 6 -25 bulk concentration of ions is 0.01 N_A m^{-3} and zeta potential $\zeta = -0.04V$. The FPW has wave amplitude of 10.0 nm, membrane thickness (d) of 3.0 μm and a wavelength λ of 150.0 μm for the cases 2 - 25.

Table 7.1 List of the cases considered on electroosmotic augmented FPW micropumps

Case	**H (μm)**	**E_x (kV/m)**	**Wall Freq. f (MHz)**
1	0.9	210.0	-
2	100.0	-	1.0
3	5.0	-	1.0
4	25.0	-	1.0
5	50.0	-	1.0
6	100.0	3.0	-
7	100.0	3.0	1.0
8	100.0	5.0	1.0
9	100.0	10.0	1.0
10	100.0	50.0	1.0
11	100.0	100.0	1.0
12	250.0	-	1.0
13	250.0	3.0	1.0
14	250.0	5.0	1.0
15	250.0	10.0	1.0
16	250.0	50.0	1.0
17	250.0	100.0	1.0
18	100.0	100.0	2.0
19	100.0	100.0	3.0
20	100.0	100.0	5.0
21	100.0	100.0	10.0
22	250.0	100.0	2.0
23	250.0	100.0	3.0
24	250.0	100.0	5.0
25	250.0	100.0	10.0

7.4.1 Validation of the Electroosmotic Flows Model

Validation of the present numerical model is performed by comparison of both EDL streaming potential ψ and axial velocity results with the published results for the problem geometry defined in Figure 5.1. The model validation of electroosmotic flows given in section (5.4) is summarized here. The numerical results are validated with the experimental results reported by Chen and Santiago [110] and with the analytical results presented in Patankar and Hu [111]. The present steady state axial velocity results (Figure 5.2) in the fully developed region of the microchannel are compared with the experimental results and analytical solution. The area under the curve in Figure 5.2 represents the volumetric flow rate per unit width and it is calculated as 6.34 10^{-9} m^2/s. Flow rate is calculated as 14.46 µl/min. Chen and Santiago [110] reports the flow rate as 15.0 µl/min experimentally and 14.0 µl/min with one-dimensional analytical model of Patankar and Hu [111]. Considered width of the electroosmotic pump is 0.038 m similar to [110]. The numerical results match well with both analytical approach by Patankar and Hu and experimental approach by Chen and Santiago.

In Figure 7.2, the EDL potential distributions are plotted for the numerical results and the analytical solution when $\kappa = 8.2$. The present solutions agree well with other published data.

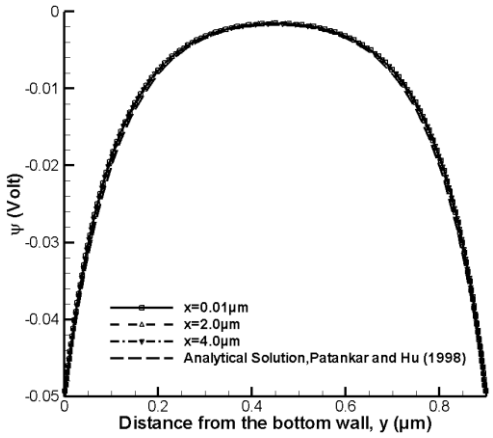

Figure 7.2 Comparison of EDL potential profile on x=constant planes [97, 111]. L/H = 4.5, κ = 8.2, E_x = 210.0 (kV m^{-1}) and *Re* = 0.*011* (case 1)

7.4.2 Validation of the Model for Flows in Flexural Plate Wave Micropumps

Validation of the present numerical model for acoustically driven flows is performed by comparison of the time averaged axial velocity results with the results [22] for the problem geometry given in Figure 6.1 (FPW micropump). Numerical solutions are also compared with experimental measurements by Moroney [114]. The model validation of flexural plate wave micropumps given in section (6.4) is summarized here.

Figure 6.2 shows the comparison of the present model predictions of time-averaged axial velocity profile along the depth of the microchannel at x = 150 μm with the numerical results of Nguyen and White [22]. Nguyen and White [22] used *incompressible* flow formulation which differs from the measurements by Moroney [114]. The measured time averaged maximum axial velocity is reported by Moroney [114] to be 85 μm/s. The incompressible flow numerical result [17, 22] of 900 μm/s is more than 10 times the measured value. The time averaged maximum axial velocity is 174 μm/s for the present *compressible* flow model. Our predicted results (using the compressible flow model) are close to the experimental results in [114].

7.4.3 Acoustically Driven Flows in Flexural Plate Wave Micropumps: Quasi-periodic State

In Figures 7.3a-c time dependent velocity vectors are shown for the entire microchannel at the 30th cycle with half cycle time spacing (case 2). In Figure 7.3a vectors of velocity are provided for the microchannel at the beginning of the 30th cycle. Figure 7.3b shows the vectors half a cycle later and Figure 7.3c is for the end of the 30th cycle. Comparing the velocity fields in Figure 7.3a and Figure 7.3c, quasi-periodic behavior of the flow field is observed. When estimated velocity differences between subsequent cycles for all the grid points are observed to be less than the convergence criteria ($\chi = \frac{\bar{u}_{f,j+1} - \bar{u}_{f,j}}{\bar{u}_{f,j}} \leq 0.01$), the flow field is assumed to be quasi-steady.

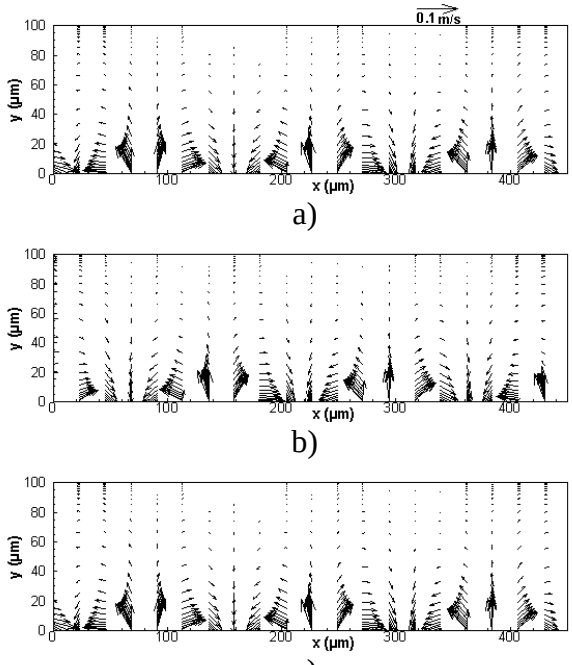

Figure 7.3 Vectors of velocity at the 30th cycle (acoustics only). a) at the beginning of 30th period. b) half a cycle later. c) at the end of 30th period. A_{max} = 10 nm, f = 1 MHz, λ = 150 μm, H = 100 μm, L/H = 4.5, and d = 3 μm. (case 2)

7.4.4 Net Flows in Microchannel Flexural Plate Wave Micropumps

A series of simulations are performed to observe the effect of changing channel height (Figure 6.1). Wave amplitude is kept constant at 10 nm while varying channel heights between 5 μm - 100 μm are considered. Frequency (1 MHz) and transducer periodicity (150 μm) are kept constant (cases 2 – 5, Table 7.1).

Figure 7.4 shows time-averaged velocity field (case 3) for a shallower microchannel (H = 5 μm). The time averaged velocity profile over one period becomes parabolic for a shallower channel whereas the velocity profile is asymmetric for a deeper microchannel. Model predictions of time-averaged velocity field for a deeper microchannel are shown earlier in Figure 6.9. Nguyen and White [22] found out that the thickness of the evanescent decay length determines the transition from a parabolic profile to an asymmetric velocity profile. The magnitude of the first order particle velocity (instantaneous velocity), u_f , exponentially decays for the evanescent disturbance in the fluid adjacent to the membrane as [17] :

$$u_f = u_{f,\max}\exp(-y/\gamma) \tag{7.1}$$

where $u_{f,max}$ is the maximum value of the membrane velocity, y is the vertical distance from the membrane and γ is the acoustic evanescent decay distance. It is defined as

$$\gamma = \frac{\lambda}{2\pi\sqrt{1-(c_p/c_s)^2}} \tag{7.2}$$

where λ is the wave length of FPW (150 μm), c_p is the phase velocity of FPW ($c_p = \lambda f$ = 150 m/s) and c_s is the speed of sound in water (1480 m/s). Evanescent decay distance (γ) is calculated as 24.0 μm.

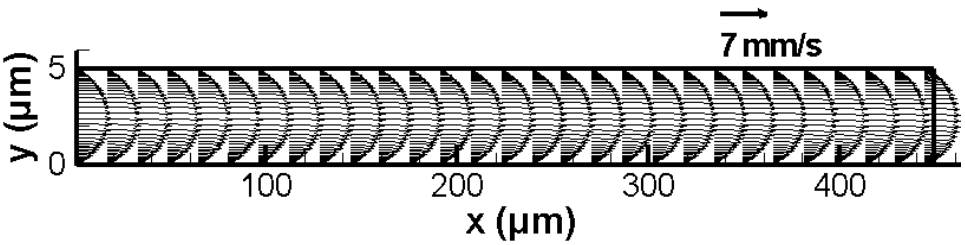

Figure 7.4 Vectors of time averaged velocity. f = 1.0 MHz, λ = 150.0 μm, d = 3.0 μm, A_{max}= 10.0 nm, H = 5.0 μm and L/H = 90.0. (case 3).

Figure 7.5 depicts time-averaged velocity profiles over one cycle for different microchannel heights when the frequency f = 3 MHz is applied (cases 2 -5)**.** The wave amplitude is kept constant as 10 nm for the cases 2 - 5. When channel height is larger than 24.0 μm (the evanescent decay distance, γ) as in H = 25.0 μm, H = 50.0 μm and H = 100.0 μm the velocity profiles start to deviate from parabolic velocity profile. This curve shows similarity to the Nyborg's streaming theory [17] that the maximum velocity does not depend on channel height with a channel height that is greater than the evanescent decay distance of the acoustic wave in the fluid. The attenuation of the wave away from the actuator surface results in a decrease of the magnitude of time averaged velocity for deeper microchannels (H = 25.0 μm - H = 50.0 μm). For shallow channel (H = 5.0 μm), FPW couples well with the flow generating higher velocities. When the channel height is greater than γ (such as 25 μm, 50 μm or 100 μm), the velocities in the channel beyond the evanescent decay distance are predicted to be small. The thickness of the viscous boundary layer [17], β^{-1} is found to be 0.56 μm where $\beta^{-1} = \sqrt{\frac{2\mu}{\rho\omega}}$. ω is the angular frequency of the wave, μ is the dynamic viscosity and ρ is the density of the fluid.

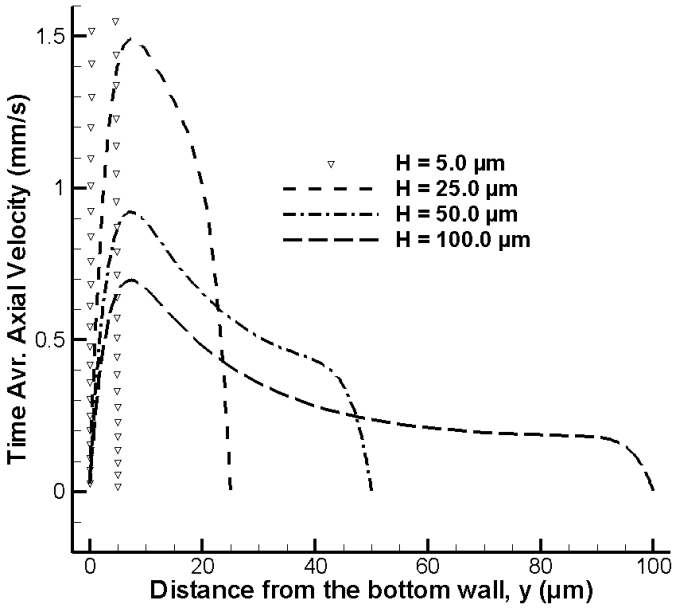

Figure 7.5 Velocity profiles with different channel heights, A_{max} = 10 nm, f = 1 MHz, λ = 150 μm, d = 3 μm, H = 5 - 100 μm, x = 75.0 μm (cases 2-5).

7.4.5 Electroosmotically Augmented Flows in Flexural Plate Wave Micropumps

Inclusion of electroosmotic effects on flexural plate waves (FPW) are investigated next by a coupled electroosmosis-acoustics problem for the given problem geometry in Figure 7.1. Coupling of electroosmotic flows and acoustically excited flows is discussed first and parametrical studies in electroosmotically augmented flows in flexural plate wave micropumps are discussed thereafter.

Coupling of electroosmotic flows to acoustically excited flows in FPW micropumps

Coupling of electroosmotic flow to acoustic flow has two major influences on each other, viz. i) the electrokinetic terms in momentum equations affect the acoustic waves in an electroosmosis-coupled FPW micropump. ii) the physical location of the

electric double layer changes in coupled electrokinetic-acoustic cases. To investigate the interactions, a coupled “moving grid”-“body force driven flow” compressible flow model (using user-developed Fortran routines in commercial CFD-ACE+ multiphysics package [100]) is developed. Electrokinetic flow is only useful for mass flow here and did not contribute significantly to the mixing or any other physical effects in acoustic devices [46]. Under many circumstances the ionic distribution in the electric double layer is not disturbed at a fixed zeta potential, and it follows the equilibrium Boltzmann distribution. In the equilibrium case the induced electric field is governed by the Poisson–Boltzmann equation and is decoupled from the velocity field. The considered Poisson–Boltzmann model is the most widely employed model in the analysis of electroosmotic flows [7].

In Figure 7.6, time averaged axial component of velocity is plotted along the depth of the microchannel varying simulation conditions: pure acoustically excited flow (FPW only, case 2), pure electroosmotic flow (EOF only, case 6), linear combination (add together) of FPW only and EOF only simulation results and present coupled model for electroosmotic augmented flows in flexural plate wave devices (case 7). Coupled electroosmotic-FPW micropump induces a much stronger flow field as shown in Figure 7.6 (A_{max} = 10 nm, f = 0 and 1 MHz, λ = 150 μm, H = 100 μm, d = 3 μm, L/H = 4.5, x = 225.0 μm, κ = 1036 and E_x = 0 and 3 kV m^{-1}). Without the electroosmotic flow, local velocity near the perturbing wall (Figure 6.1, bottom wall) has a larger magnitude in the negative direction (reducing the net flow rate when averaged over time). With the coupling of the EOF, the magnitude of the negative component of the axial velocity decreases due to the induced unidirectional flows in EOFs. The magnitude of the present coupled EOF-FPW micropump model predictions of the time-averaged axial velocity are

greater than the results of a simple linearly combined of FPW and EOF flows as shown in Figure 7.6.

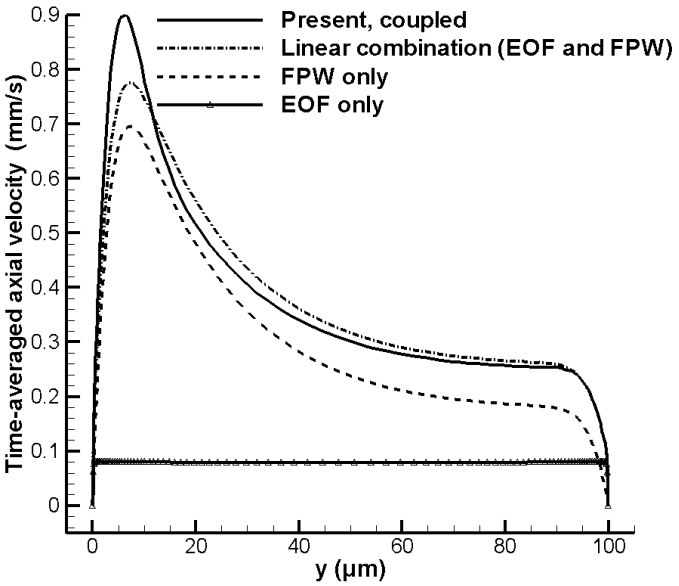

Figure 7.6 Time averaged axial velocity profiles of 100 μm channel for electroosmotically augmented flows in FPW micropumps (cases 2, 6 and 7).

Parametric studies

A series of simulations are performed to observe the effect of changing channel height, intensity of electrokinetic body forces and frequency of acoustic excitations (Figure 7.1). In cases 7 - 11 (Table 7.1), electroosmotically augmented flows in a shallow (H= 100.0 μm) FPW micropump under varying electric field intensity (E_x = 3.0 - 100.0 kV/m) conditions are investigated. The results are compared with predictions obtained in case 2 (pure acoustically excited flow). In cases 12 - 17 (Table 7.1), electroosmotic augmentation in a deeper (H= 250.0 μm) FPW micropump under varying electric field intensity is investigated. Electroosmotic augmentation in a shallow FPW micropump (in

cases 11, 18 - 21) by varying the actuation frequencies of acoustic excitations (f = 1.0 - 10.0 MHz) is investigated. Electroosmotic augmentation in a deep FPW micropump (in cases 17, 22 - 25) is also investigated by varying the actuation frequencies of acoustic excitations.

In Figure 7.7, time averaged axial component of velocity is plotted along the depth of the microchannel varying the electric field intensity. Intensity of acoustic perturbations is kept constant (A_{max} = 10 nm, f = 1 MHz, λ = 150 μm) while the electric field intensity of the electrokinetic body forces is varied (Table 7.1: cases 7 - 11). Results from case 2 are also shown in Figure 7.7. The time averaged axial velocity shows the evanescent wave pattern (an attenuating wave away from the actuator surface) closer to the perturbing wall and a typical EOF flat velocity profile adjacent to the top rigid wall (Figure 7.1). The amplitude of time averaged velocity increases with increasing electrokinetic body force in electroosmotic augmented flows in FPW micropumps. According to the Nyborg's incompressible streaming theory [17] the location of the maximum velocity does not depend on the body forces that are evenly distributed on the fluid. The compressible model for fluid dynamics model is considered and the location of the maximum velocity increases (from y = 4.63 μm to 6.43 μm) with increasing electrokinetic forces.

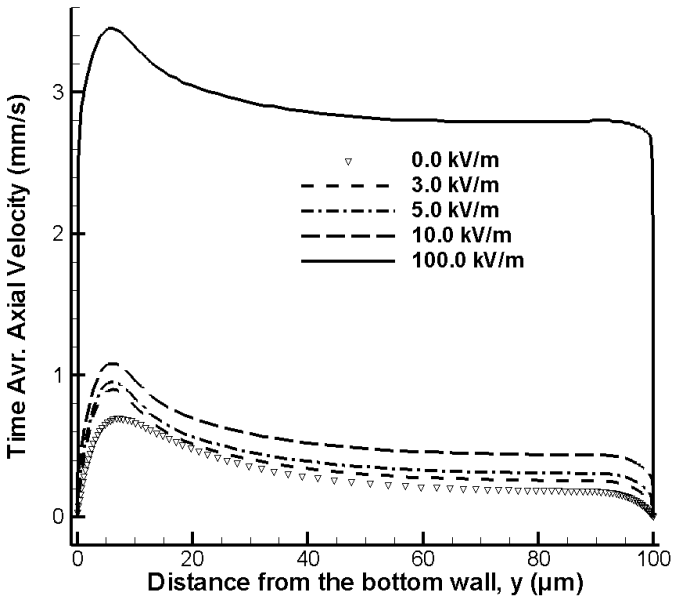

Figure 7.7 Time averaged axial velocity profiles of 100 μm channel for electroosmotically augmented flows in FPW micropumps. A_{max} = 10 nm, f = 1 MHz, λ = 150 μm, H = 100 μm, d = 3 μm, L/H = 4.5, x = 225.0 μm, κ = 1036 and E_x = 0 - 100 kV m−1. (cases 2, 7-11)

A deeper micropump is considered next. In Figure 7.8, time averaged axial component of velocity is plotted along the depth of the microchannel varying the electric field intensity for a deeper micropump where channel height is increased from 100.0 μm (cases 2, 7 – 11) to 250 μm. Intensity of acoustic perturbations is kept constant (A_{max} = 10 nm, f = 1 MHz, λ = 150 μm) while the electric field intensity of the electrokinetic body forces is varied (Table 7.1: cases 12 - 17). The time averaged velocity profile over one period is asymmetric wall-jet driven velocity profile superimposed on the plug like velocity profile of EOFs (Figure 7.1). The amplitude of time averaged velocity increases with increasing electrokinetic body force according to the momentum equation (equation (3.5)) resulting in higher flow rates for deeper microchannels.

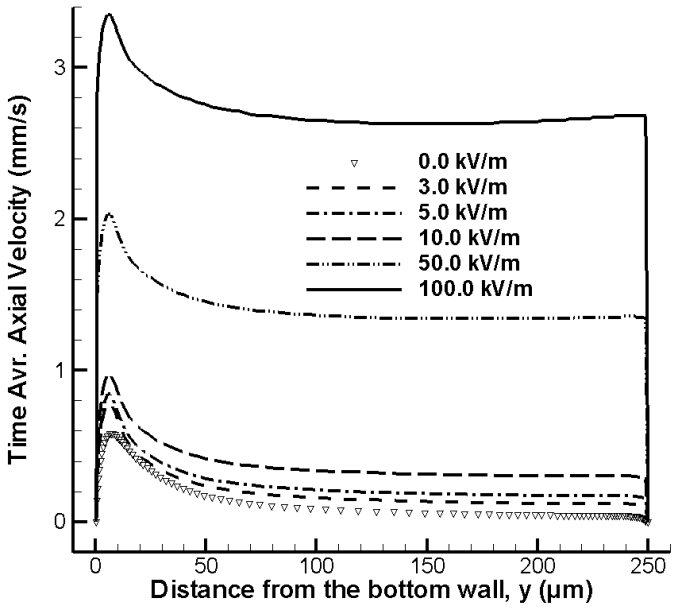

Figure 7.8 Time averaged axial velocity profiles of 250 μm channel for electroosmotically augmented flows in FPW micropumps. A_{max} = 10 nm, f = 1 MHz, λ = 150 μm, H = 250 μm, d = 3 μm, L/H = 1.8, x = 225.0 μm, κ = 2590 and E_x = 0 - 100 kV m−1. (cases 12 - 17)

Figure 7.9 shows the temporal and spatial variation of the instantaneous vertical velocity (v_f) along the depth of the microchannel for case 9 over one cycle (30^{th} cycle). The horizontal axis is given in terms of non-dimensional time $(t-t_i)f$, where f is the cyclic frequency, t is the time and t_i is the time at the beginning of a flexural cycle (t_i = 30.0 μs). For electroosmotically augmented flows in FPW micropumps, the v_f component of velocity over one period is found to be asymmetric due to fact that a moving wall is considered along the bottom boundary whereas a rigid boundary is considered along the top boundary (Figure 7.1). The predicted velocity field shows the existence of induced vertical velocity component, which is almost zero for low Reynolds number electroosmotic flows. The induced vertical velocity can enhance mixing processes significantly.

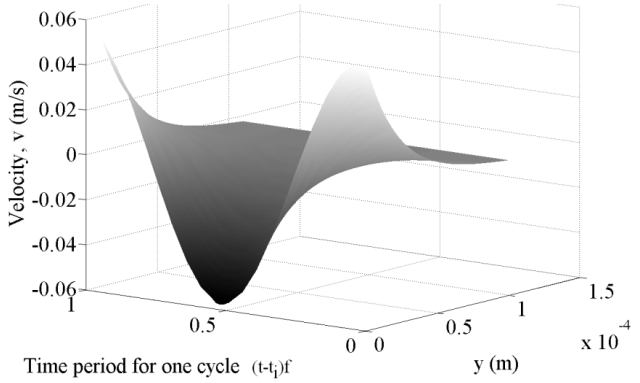

Figure 7.9 Temporal and spatial variation of vertical velocity along the depth of the microchannel at x = 225.0 μm for one cycle. t_i = 30.0 μs, A_{max} = 10 nm, f = 1 MHz, λ = 150 μm, H = 100 μm, d = 3 μm, L/H = 4.5, and E_x = 10 (kV m−1) (case 9).

In Figure 7.10, time averaged axial component of velocity is plotted along the depth of the microchannel for varying actuation frequency of the wall (Table 7.1: cases 11, 18 - 21). As the frequency of the flexural wave micropump increases, the velocity also increases. The location of the maximum velocity (from the vibrating wall) is found to be invariant with increasing frequency. The thickness of the viscous boundary layer (β^{-1}) also varies between 0.13 and 0.42 μm in cases 11, 18 - 21.

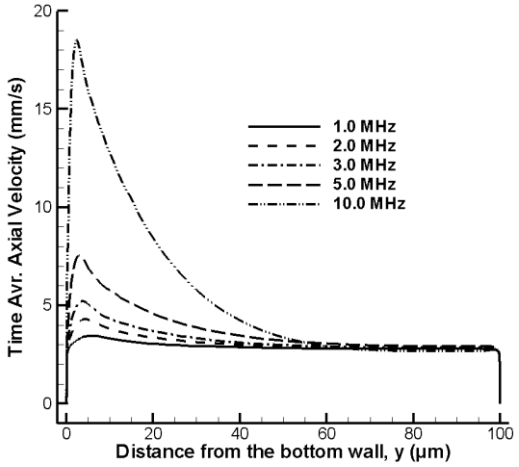

Figure 7.10 Time averaged axial velocity profiles of 100 μm channel for electroosmotically augmented flows in FPW micropumps, A_{max} = 10 nm, f = 1 – 10 MHz, λ = 150 μm, H = 100 μm, d = 3 μm, L/H = 4.5, x = 225.0, κ = 1036 μm and E_x = 100 kV m−1. (cases 11, 18 - 21)

A deeper microchannel is considered next. In Figure 7.11, time averaged axial component of velocity is plotted along the depth of the microchannel (at x = 225.0 μm) for varying actuation frequency of the wall (Table 7.1: cases 17, 22 - 25). As the frequency of the flexural wave micropump increases, the velocity also increases (Figure 7.11). The time averaged axial velocity shows an attenuating wave away from the actuator surface and a typical EOF flat velocity profile adjacent to the top rigid wall (Figure 7.1). Instantaneous velocity generated by the actuator surface exponentially decays in the fluid adjacent to the surface (equation (7.1)).

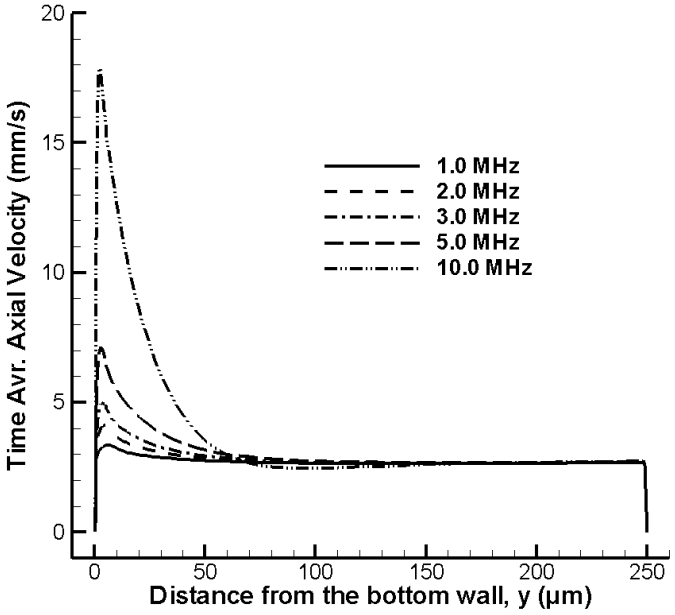

Figure 7.11 Time averaged axial velocity profiles of 250 μm channel for electroosmotically augmented flows in FPW micropumps, A_{max} = 10 nm, f = 1 – 10 MHz, λ = 150 μm, H = 250 μm, d = 3 μm, L/H = 1.8, x = 225.0 μm, κ = 2590 and E_x = 100 kV m−1. (cases 17, 22 - 25)

Time-averaged volumetric flow rates generated by the electroosmotic augmented FPW micropumps are shown in Figures 7.12a and 7.12b where A_{max} = 10 nm, λ = 150 μm, H = 100, 250 μm, d = 3 μm, L/H = 4.5, and x = 225.0 μm. Figure 7.12a shows flow rate for varying frequency of acoustic excitations and Figure 7.12b shows the same for varying intensity of electrokinetic forces. When the actuation frequency is doubled (5.0 to 10.0 MHz) the flow rate increases 47.2% and 23.3% for shallow and deep micropumps, respectively. For deeper microchannels, increasing the actuation frequency of the wall motion does not improve the generated flow rate significantly (Figure 7.12a, H = 250.0μm) as opposed to the apparent flow rate enhancement in shallow microchannels (Figure 7.12a, H = 100.0μm). The flow rate increases 82.1% and 91.7% when the electrokinetic forces are doubled (50.0 to 100.0 kV/m) for shallow and deep micropumps, respectively. Inclusion of electrokinetic effects is more efficient than increasing the intensity of acoustic perturbations whenever high flow rates are required in micromixer applications (Figure 7.12b). Further increasing the frequency of acoustic perturbations requires shorter interdigitated transducers periodicity and more sophisticated electronics equipment which are disadvantages on the manufacturing costs and compactness of a lab-on-a-chip system. Effective mixing is not possible with pure EOF. Combining EOF with FPW can provide both effects of pumping and mixing in a high performance micro-mixer.

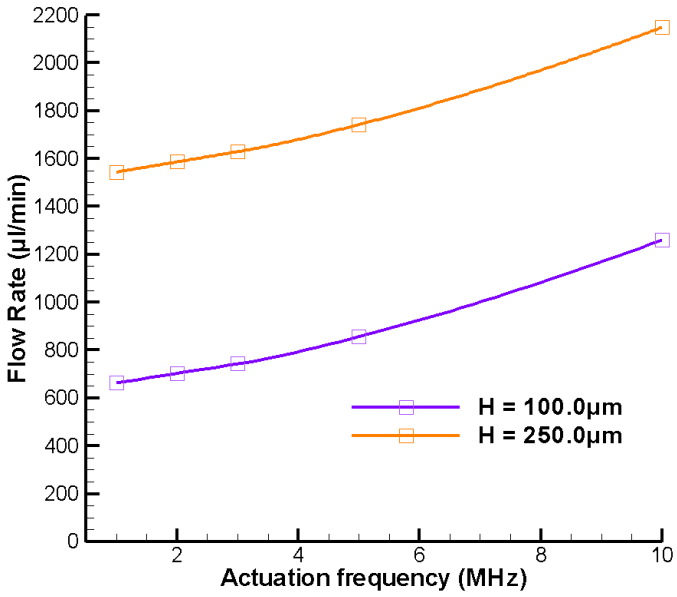

a)

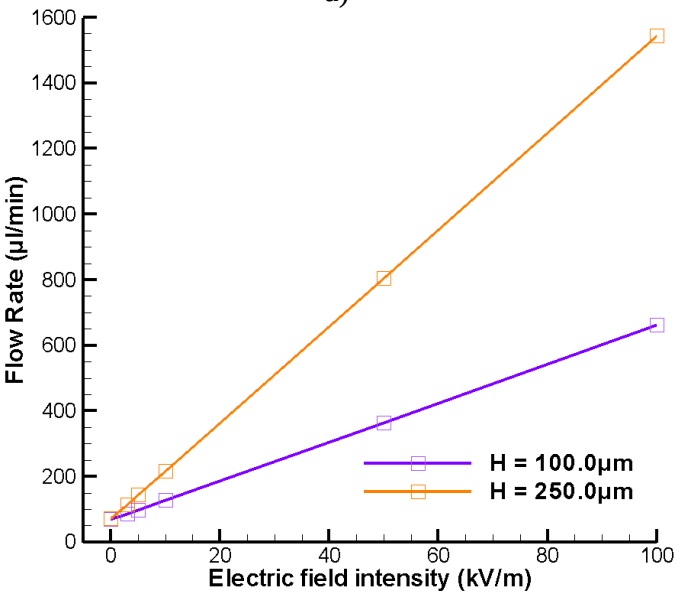

b)

Figure 7.12 Time-averaged flow rate for electroosmotically augmented flows in FPW micropumps. a) effect of actuation frequency. f = 1 – 10 MHz and E_x = 100 kV m^{-1} (cases 11, 17 - 25). b) effect of electric field intensity. E_x = 0 - 100 kV m^{-1} and f = 1 MHz (cases 2, 7 - 17).

The thermodynamic efficiency of a planar EOF pump by evaluating the power dissipation in the flow similar to [110] is analyzed. The First Law thermodynamic

efficiency is defined as useful pressure work over total power consumption. The total power consumed by the EOF pump, $\dot{W}_{T,EOF}$ can be divided into three parts as follows:

$$\dot{W}_{T,EOF} = \dot{W}_P + \dot{W}_V + \dot{W}_E \tag{7.3}$$

where $\dot{W}_P$ is the pressure work output produced by the pump and $\dot{W}_V$ and $\dot{W}_E$ are, respectively, viscous dissipation and electrical Joule heating dissipated in the pump.

Pressure work output of the pump is defined as [110]:

$$\dot{W}_P = W\int_0^L dx\int_0^H u\frac{dP}{dx}dy \tag{7.4}$$

The viscous dissipation for the pumping liquid is [110]

$$\dot{W}_V = W\int_0^L dx\int_0^H \mu(\frac{du}{dy})^2 dy \tag{7.5}$$

Joule heating due to electroosmotic flow can be found using the following formula [110]:

$$\dot{W}_E = WLH\sigma_0 E_x^2\left\{1+\frac{1}{2}(\frac{ze\zeta}{k_bT})^2 r(\kappa/2)\right\} \tag{7.6}$$

where, $r(\kappa/2) = \frac{1}{2\cosh^2(\kappa/2)}\left(\frac{1}{\kappa}\sinh(\kappa)+1\right)$, Λ_0 is the molar conductivity (2.0 x 10^{-2} m^2S/mol [110]) and bulk conductivity $\sigma_0 = 2n_0\Lambda_0 / N_A$.

The total power consumed by the FPW-EOF pump, $\dot{W}_{T,FPW}$ can be divided into two parts as follows:

$$\dot{W}_{T,FPW} = \dot{W}_E + \dot{W}_{WAVE,AVG} \tag{7.7}$$

where $\dot{W}_E$ is the electrical Joule heating dissipated in the pump and $\dot{W}_{WAVE,AVG}$ is the power transmitted along the membrane by the flexural wave [119].

Time averaged acoustic power flowing in the flexural wave, $\dot{W}_{WAVE,AVG}$, is equal to the kinetic energy per unit length in the membrane multiplied by the velocity of the wave [119]. $\dot{W}_{WAVE,AVG}$ can be found as [114]

$$\dot{W}_{WAVE,AVG} = \frac{1}{2} A_0^2 \omega^2 M_\rho W c_p \tag{7.8}$$

In equation (7.8), effective mass of the plate, M_ρ, is $M_\rho = \gamma\rho + \rho_{FPW}\mathrm{d}$. γ is the acoustic evanescent decay distance and c_p is the phase velocity of FPW (both defined in equation (7.2)), ρ_{FPW} is the average density of the aluminum oxide- silicon nitride composite membrane (4500.0 kg/m^3) and d is the membrane thickness. Pressure work output produced by FPW-EOF pump, $\dot{W}_{P,FPW}$, is given as:

$$\dot{W}_{P,FPW} = \frac{\int_{t_i}^{t_f} \left(W \int_0^L dx \int_0^H u \frac{dP}{dx} dy \right) dt}{t_f - t_i} \tag{7.9}$$

t_i and t_f are the times at the beginning and end of a flexural cycle, respectively. Thermodynamic efficiency of the device, η is calculated as

$$\eta_{EOF} = \dot{W}_P / \dot{W}_{T,EOF}$$
$$\eta_{FPW} = \dot{W}_{P,FPW} / \dot{W}_{T,FPW} \tag{7.10}$$

The power consumption (equations 7.3 - 7.6 and 7.10) for case 1 is predicted as 0.56mW and thermodynamic efficiency of 0.69%. Analytical results in [110] shows 0.58mW power consumption and 0.81% theoretical efficiency. In [110] 0.42 mW power consumption and 0.49% efficiency are also reported experimentally. Power consumption for the FPW wave generator is measured as about 2 mW at 25.0 nm wave amplitude and 3.39 MHz frequency in (Moroney, 1995, pp. 1 and 142) [114]. $\dot{W}_{WAVE,AVG}$ is calculated as

2.31 mW. Our thermodynamic efficiency and power consumption calculations are in good agreement with [110] and [114] for electroosmotic flows and acoustically induced flows, respectively.

Thermodynamic efficiencies for electroosmotically augmented flows in FPW micropumps are calculated using the equations (7.3) - (7.10). Figure 7.13a shows the thermodynamic efficiency (%) of the system under varying frequency of acoustic excitations. Figure 7.13b shows the thermodynamic efficiency (%) of the system under varying intensity of electrokinetic forces where A_{max} = 10 nm, λ = 150 μm, H = 100, 250 μm, d = 3 μm, L/H = 4.5 and x = 225.0 μm. With increasing intensity of electrokinetic forces the pressure work output produced by the pump $\dot{W}_P$ (varies between 1.5 10^{-6} mW to 5.4 10^{-6} mW) and electrical Joule heating $\dot{W}_E$ (0.0 - 38.0 mW) increases significantly.

With increasing frequency the pressure work output produced by the pump $\dot{W}_P$ (varies between 1.0 10^{-5} mW to 6.4 10^{-3} mW) and power transmitted along the membrane by the flexural wave $\dot{W}_{WAVE,AVG}$ (0.42 mW to 152.0 mW) increases significantly. Electrical Joule heating $\dot{W}_E$ is 15.2 mW and 38.0 mW for H= 100 and 250 μm, respectively. Viscous dissipation $\dot{W}_V$ varies between 2.1 10^{-8} mW to 8.8 10^{-6} mW. Using equation (7.10) and above power values, thermodynamic efficiency is shown to increase with increasing actuation frequency.

Power transmitted along the membrane by the flexural wave $\dot{W}_{WAVE,AVG}$ is 0.42 mW in cases 4, 9 - 19. Viscous dissipation $\dot{W}_V$ varies between 2.0 10^{-8} mW to 3.8 10^{-8} mW. Using equation (7.10) and above power values, thermodynamic efficiency is found to decrease with increased electric field intensity due to the increased Joule heating

losses. Based on the thermodynamic efficiency, increasing the actuation frequency of the flexural wave is more efficient than increasing the intensity of electric field (Figures 7.13a-b). Inclusion of electroosmotic effects is more effective than increasing the intensity of acoustic perturbations whenever high flow rates are required in micromixer applications. (Figures 7.12a-b).

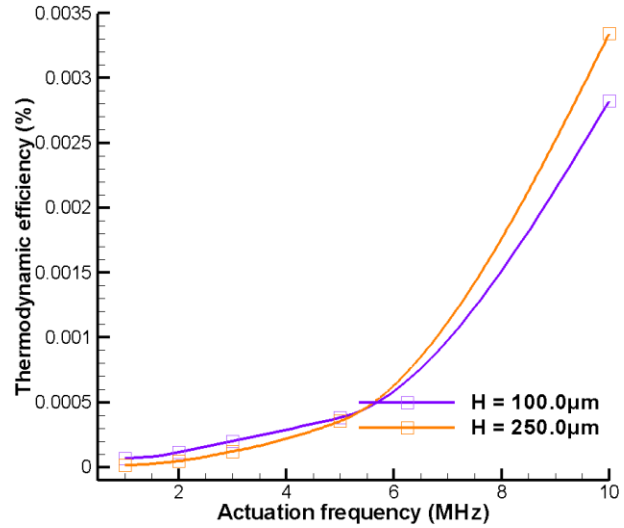

a)

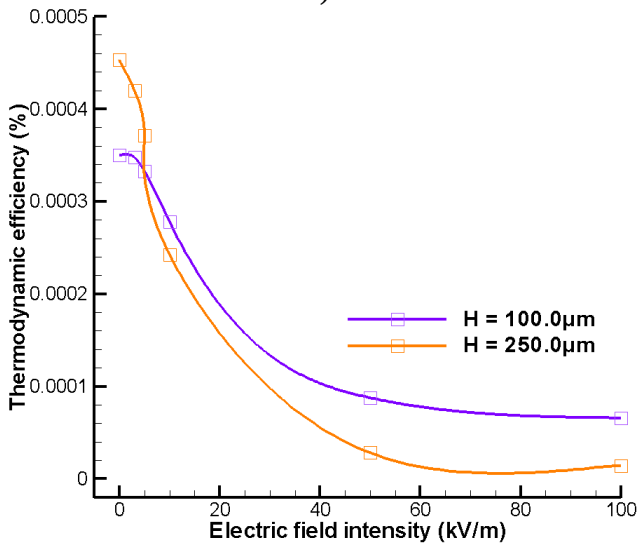

b)

Figure 7.13 Predicted thermodynamic efficiencies for electroosmotically augmented flows in FPW micropumps. a) effect of actuation frequency. f = 1 – 10 MHz and E_x = 100 kV m^{-1} (cases 11, 17 - 25). b) effect of electric field intensity. E_x = 0 - 100 kV m^{-1} and f = 1 MHz (cases 2, 7 - 17).

7.5 Conclusions

Inclusion of electroosmotic flows in acoustically generated flows in flexural plate wave (FPW) micropumps is investigated for enhancing pumping performance. Acoustic excitations have recently been suggested to promote active mixing in the microscale flow systems [43-46, 77]. Mixing of analytes and reagents is a critical step in realizing lab-on-a-chip systems.

Acoustic perturbations in microchannels are modeled by a moving wall problem for the FPW micropump. The compressible flows in FPW micropump is modeled by the Navier-Stokes equations along with an isothermal equation of state. The time averaged velocity fields are investigated by varying the channel height, wave amplitude, wave length and actuation frequency. The model predictions were compared with the theoretical and experimental results available in the literature [22, 114] for acoustically excited flows. Poisson-Boltzmann equations of electroosmosis were modeled. Results are compared with theoretical results of [111] and with experimental measurements reported in [110]. Coupled electrokinetic and acoustic cases are investigated by varying the frequency of acoustic excitations and the electric field intensity of the electrokinetic body forces. For the coupled problem, the time averaged axial velocity shows the evanescent wave pattern (an attenuating wave) away from the actuator surface. A typical electroosmotic flow flat velocity profile is predicted adjacent to the top rigid wall. The amplitude of time averaged velocity increases with increasing electrokinetic body force and increasing actuation frequency of acoustic perturbations. Based on the thermodynamic efficiency, increasing the actuation frequency of the flexural wave is more efficient than increasing the intensity of electric field. Inclusion of electroosmotic

effects is more effective than increasing the intensity of acoustic perturbations whenever high flow rates are required in micromixer applications. For electroosmotically augmented micropumps, the predicted velocity field showed the existence of induced vertical velocity component which can enhance mixing process significantly. The proposed device geometry can be exploited to integrate micropumps into complex microfluidic chips improving the portability of micro-total-analysis systems along with the capabilities of actively controlling acoustics and electrokinetics. This study provides a background for the comparison of efficiency between acoustics based active mixing methods and DC-AC electrokinetics mixing methods.

8. STRESS, STRAIN AND DISPLACEMENT FIELDS IN AN ANISOTROPIC SOLID

8.1 Introduction

Stress, strain and displacement fields and reaction forces in an anisotropic solid are investigated with the developed solid deformation models. Deformation of an anisotropic cube-shaped lithium niobate ($LiNbO_3$) specimen is studied with a three-dimensional test problem. The goal of the results discussed in this chapter is to present model validation for the developed full anisotropic materials/solid deformation models discussed in section 4.1. To develop a generic model for acoustically excited flows, the solid deformation model is needed to be expanded from orthotropic materials to fully anisotropic materials. This task was completed in collaboration with ESI-CFD. Stress, strain and displacement fields and reaction forces prediction models developed in the present study are used to investigate the design of MEMS based piezoelectric valveless micropumps in the following chapters. The governing equations for the solid (piezoelectric and non-piezoelectric) domains are discussed in chapter 4.

The enhancements to the models are studied with benchmark tests for validation. Base-line tests are also investigated for the consistency of the developed models with the previous version of the commercial model. Deformation of an anisotropic cube-shaped lithium niobate ($LiNbO_3$) specimen is studied with a three-dimensional test problem. The specimen is uniformly compressed along its X material principal axis (see ref. [105] for material principal axis). The displacement, stress, strain fields and reaction forces are calculated with the developed models. The predicted results are compared to another commercial code (Abaqus [120]). 18 elements (12 of them are independent) of the elastic

stiffness matrix for anisotropic lithium niobate crystal are entered directly. The elements of the stiffness matrix are also indirectly input through the user developed property routines for comparisons. Material axes directions are diverted from the usual (0, 0, 0) Euler direction [105] using the graphical user interface of the model and also through user developed subroutines in order to test the cell-by-cell basis material axes specifying capabilities.

The following enhancements have been made to the solid deformation models: anisotropic materials can be specified using all 21 independent elements of the elastic stiffness matrix. The engineering data components in each direction and the stiffness matrix itself can be input through the user developed property routines. User subroutine capability has also been made available for specifying material axes in order to fully control the material axes direction on a cell-by-cell basis.

8.2 Geometry and Volume Conditions

8.2.1 Schematic of the Problem Geometry

Deformation of an anisotropic cube-shaped lithium niobate ($LiNbO_3$) specimen is studied with a three-dimensional structural mechanics models (Figure 8.1). The specimen under a static deformation is considered in the present case. The displacement, stress, strain fields and reaction forces are calculated with the developed models. The sample consists of a cube with 3.0 mm side length.

Uniform deformations are generated when an isotropic material is compressed along its axial direction (x-axis). The problem geometry and material properties are chosen to highlight the resultant non-uniform deformations even under an axial uniform load for anisotropic materials. The purpose of the investigation is to prove the accuracy

of the developed full anisotropic materials models. The three-dimensional (x-y-z) geometry used in the present study is shown in Figure 8.1.

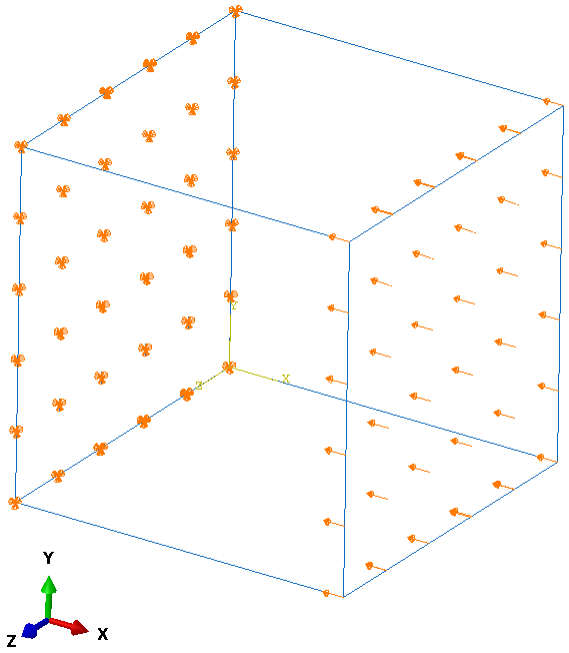

Figure 8.1 Problem geometry considered for stress, strain and displacement field simulations.

The lithium niobate is compressed uniformly along the x direction (right square face in Figure 8.1), and it expands in y and z directions. The deformations in y and z directions are not similar due to the anisotropy in material elastic properties. The left face is rigid. Other faces of the cube (top, bottom, front and back) are free to move.

8.2.2 Material Properties

Material properties considered are listed in this section. Property data is given below for the lithium niobate ($LiNbO_3$) material. The material data is provided following

the conventional IEEE standards on piezoelectricity [106]. The density ρ, and the elasticity matrix c of lithium niobate are [121]:

Density $\rho = 4630 kg/m^3$

Elasticity matrix $$c = \begin{bmatrix} 20.3 & 5.3 & 7.5 & 0.9 & 0 & 0 \\ 5.3 & 20.3 & 7.5 & -0.9 & 0 & 0 \\ 7.5 & 7.5 & 24.5 & 0 & 0 & 0 \\ 0.9 & -0.9 & 0 & 6.0 & 0 & 0 \\ 0 & 0 & 0 & 0 & 6.0 & 0.9 \\ 0 & 0 & 0 & 0 & 0.9 & 7.5 \end{bmatrix} x10^{10}\, N/m^2$$

8.3 Boundary Conditions

The boundary conditions for the dependent variables need to be specified for the problem geometry (Figure 8.1) considered. Left side of the structural layer is considered to be clamped and the displacements are zero. Along the right boundary, x component of displacement is -0.3 mm i.e. that 10.0% strain is specified on the right Four sides of the specimen are free. All dependent variables are initially zero.

8.4 Validation Studies and Discussion

Verification of the present numerical model is performed by comparison of the stress, strain, displacement and reaction force field predictions with the Abaqus commercial code [120] for the problem geometry given in Figure 8.1. Figure 8.2 shows the present calculations of displacement magnitude fields, $|u|$, on the front, right and top boundaries of the computational domain at the steady state. The same fields are obtained also with the Abaqus software and the results are shown in Figure 8.2b. The magnitude of displacement $|u|$ is defined as:

$$|u| = \sqrt{u_x^2 + u_y^2 + u_z^2} \tag{8.1}$$

where u_x, u_y and u_z are the displacement components in x, y and z directions, respectively. Both model predictions in Figures 8.2a-b shows the maximum value of displacement magnitudes as 0.3072 mm. The present full anisotropic solid deformation model results agree well with the results of the predictions with the Abaqus software where the difference is negligible. The results of the developed solid deformation model (Figure 8.2a) matches very well with the other data (Figure 8.2b).

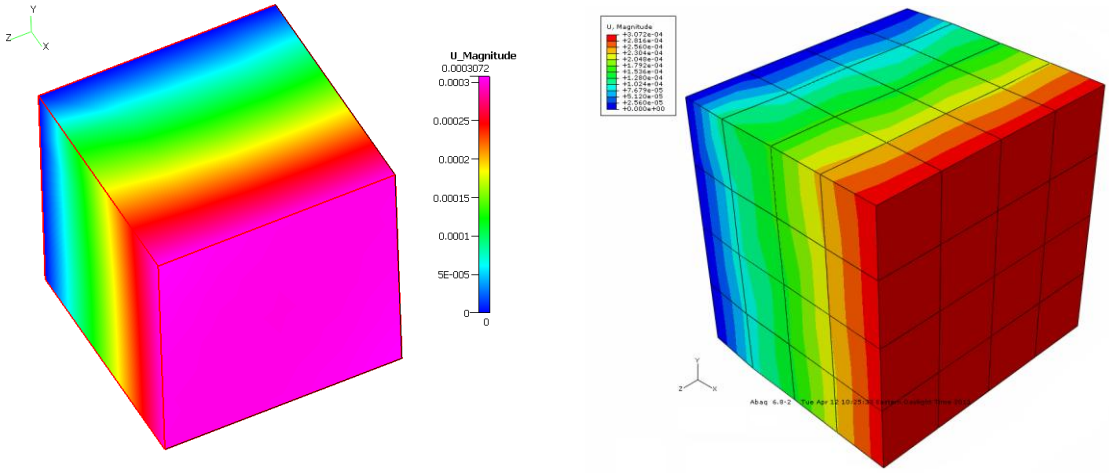

a) b)

Figure 8.2 Comparison of the displacement magnitude fields. a) present model b) another commercial solver.

Figure 8.3 shows the present calculations of contours of steady state strain in x direction (S_{xx}), on the front, right and top boundaries of the computational domain at the steady state. The same fields are obtained also with the Abaqus software and the results are shown in Figure 8.3b. The present solid model shows anisotropic deformations showing the x-component of maximum strain around the coordinate (0.0015, 0.003,

0.003)m. Under the present axial uniform load, this proves the sufficient treatment of anisotropy because the results would have shown a linearly decreasing pattern for S_{xx} (similar to the pattern given Figure 8.2a) if the material were isotropic. The maximum values of normal strain are -0.09261 and 0.08707 respectively in Figures 8.3a-b. The results of the developed solid deformation model (Figure 8.3a) match well with the other data (Figure 8.3b) where the difference is about 5%. The difference is due to the stress and strain fields generated via Abaqus software are at Gaussian integration points whereas the results obtained with the present models are available at cell centers. The discussed differences in plotting the figures yield the minor differences in the patterns. In other words, results are not available at the same physical coordinates with the two considered models.

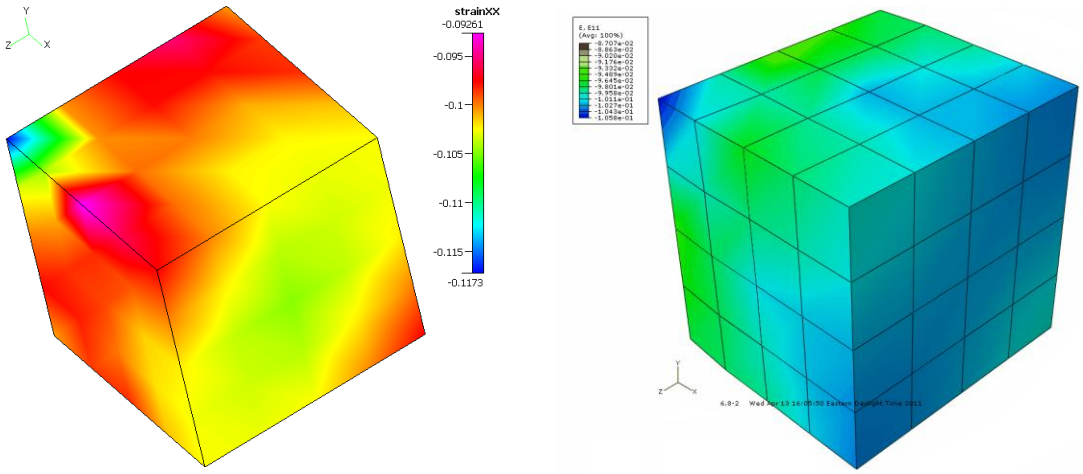

a) b)

Figure 8.3 Contours of steady state strain in x direction (S_{xx}). a) present model b) commercial solver Abaqus.

Figure 8.4 shows the present predictions of reaction force fields in x direction, on the front, right and top boundaries of the computational domain at the steady state. The reaction forces provide the resulting x, y, and z directed forces at all fixed boundaries (units Newton). The same fields are obtained also with the Abaqus software and the results are shown in Figure 8.4b. The maximum values of reaction forces at each fixed node of the structural model are 9312.0 N and 9060.0 N respectively in Figures 8.4a, b. The results of the developed solid deformation model (Figure 8.4a) matches well with the other data (Figure 8.4b) where the difference is about 2.5%.

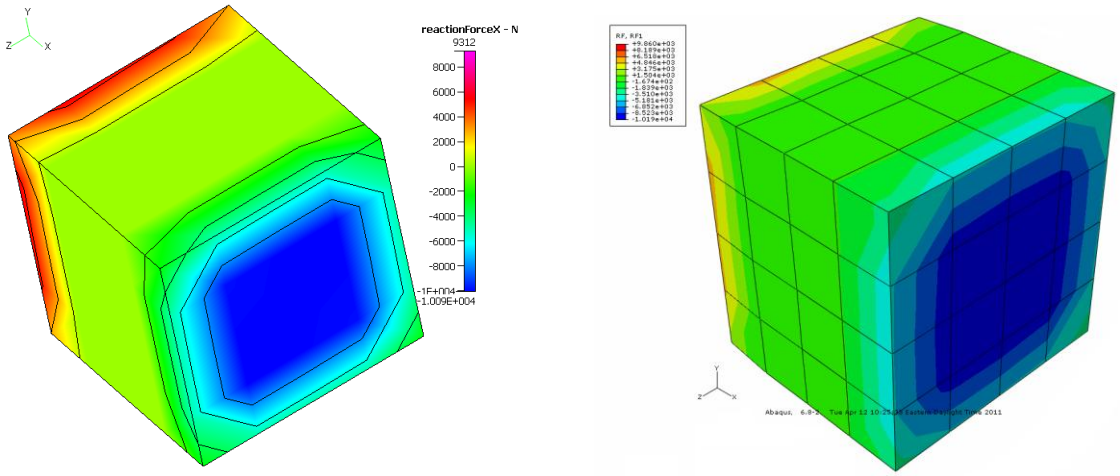

a) b)

Figure 8.4 Reaction force fields in x direction, on the front, right and top boundaries. a) present model b) another commercial solver.

Figure 8.5 shows the present calculations of contours of steady state normal stress in x direction (τ_{xx}), on the front, right and top boundaries of the computational domain at the steady state. The same fields are obtained also with the Abaqus software and the results are shown in Figure 8.5b. The present solid model shows anisotropic deformations

under an axial uniform load due to the effect of anisotropy in material elastic properties. The present solid model shows anisotropic deformations showing the x-component of maximum stress around the coordinate (0.0015, 0.003, 0.003)m. Under the present axial uniform load, this proves the sufficient treatment of anisotropy because the results would have shown a linearly decreasing pattern for τ_{xx} (similar to the pattern given Figure 8.2a) if the material were isotropic. The maximum values of normal stress are -16.05 GPa and -16.65 GPa respectively in Figures 8.5a and 8.5b. The results of the developed solid deformation model (Figure 8.5a) match well with the other data (Figure 8.5b) where the difference is about 3.5%. The results are not available at the same physical coordinates with the two considered models which yield the minor differences in the patterns and magnitudes of the predicted stresses.

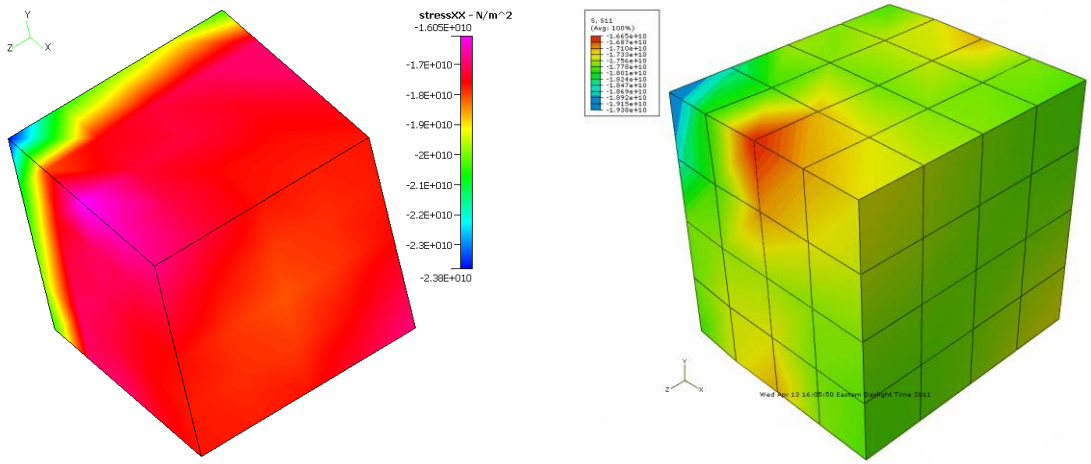

a) b)

Figure 8.5 Contours of steady state normal stress in x direction (τ_{xx}). a) present model b) commercial solver Abaqus.

8.5 Summary

The effect of specified static deformation on the structural material stress, strain, displacement fields and reaction forces are investigated for an anisotropic cube-shaped lithium niobate specimen. Three-dimensional governing equations for the structural deformations are considered. The specified static deformation generated strain, stress, displacement and reaction forces for the considered anisotropic material. The present solid model shows anisotropic deformations showing the x-component of maximum strain (S_{xx}) and stress (τ_{xx}) around the coordinate (0.0015, 0.003, 0.003)m for the cube with 3.0 mm side length. Under the present axial uniform load, this proves the sufficient treatment of anisotropy because the results would have shown a linearly decreasing pattern for S_{xx} and τ_{xx} if the material were truly isotropic. Stress, strain and displacement fields and reaction forces prediction models developed in the present study are used to investigate the design of MEMS based piezoelectric valveless micropumps in the following chapters.

9. TWO DIMENSIONAL MULTIFIELD ANALYSIS OF A PIEZOELECTRIC VALVELESS MICROPUMP[5]

Coupled multifield analysis of a piezoelectrically actuated valveless micropump device is carried out for liquid (water) transport applications. The valveless micropump consists of two diffuser/nozzle elements; the pump chamber, a thin structural layer (silicon) and a piezoelectric layer, PZT-5A as the actuator. Two-way coupling of forces between solid and liquid domains is considered in the systems where actuator deflection causes fluid flow and vice-versa. Flow contraction and expansion (through the nozzle and the diffuser respectively) generates net fluid flow. Both structural and flow field analysis of the microfluidic device are considered. The effect of the excitation voltage and actuation frequency on silicon-PZT-5A bi-layer membrane deflection and flow rate is investigated. For the compressible flow formulation, an isothermal equation of state for the working fluid is employed. The governing equations for the flow fields and the silicon-PZT-5A bi-layer membrane motions are solved numerically. At frequencies below 5000 Hz, the predicted flow rate increases with actuation frequency. The fluid-solid system shows a resonance at 5000 Hz due to the combined effect of mechanical and fluidic capacitances, inductances, and damping. Time-averaged flow rate starts to drop with increase of actuation frequency above (5000 Hz). The velocity profile in the pump chamber becomes relatively flat or plug-like, if the frequency of pulsations is sufficiently large (high Womersley number). The pressure, velocity and flow rate prediction models

[5] Results presented in this chapter appeared in "Multifield analysis of a piezoelectric valveless micropump: effects of actuation frequency and electric potential, " by E. Sayar and B. Farouk *Smart Materials and Structures*, vol. 21, p. 075002, 2012.

developed in the present study can be utilized to optimize the design of MEMS based micropumps.

9.1 Introduction

Numerical investigations of the piezoelectric micropumps have been reported [48, 49, 52, 53, 56, 64, 88]. Most of the previous studies have been conducted to identify the deflection of the piezoelectrically actuated valveless micropump rather than the prediction of generated flow rates. Some of these studies did not couple the piezoelectric actuation to the pressure and shear forces generated by the fluid (one-way coupling only) [64, 88]. The previous investigations of the micropumps where two way fluid solid coupling was considered did not report the cycle averaged mass flow rates and time-averaged velocity patterns [48, 49, 52, 53, 56]. Some previous investigations concentrate on the generated instantaneous flow rates [48, 49, 52, 53, 56, 64, 88]. However, the net flow generated by the device should be evaluated by averaging velocity field over sufficient number of perturbation cycles.

The present study addresses the development of a comprehensive numerical model for the coupled multifield analysis of piezoelectrically actuated valveless-micropump MEMS devices for liquid transport applications. The effect of actuation voltage and frequency on pump diaphragm deflection and flow rate through the inlet/outlet of a piezoelectrically actuated valveless micropump are investigated. Time-averaged velocity fields are computed and the effects of actuation frequency and applied voltage on the flow rates are predicted - including the effects due to compressibility. The previous works [53, 56, 64] explained the dependence of net flow rates to actuation frequency using the instantaneous deflection shapes of the bi-layer membrane without

calculating time-averaged velocity. Flow rates are calculated in the present study by integrating time-averaged velocity fields for the entire micropump. The dependence of net flow rates to actuation frequency is also provided.

9.2 Coupling of the Mechanical, Electrical and Fluid Fields

Once the piezoelectric element is electrified, the applied electrical energy transforms to mechanical and electrical energy according to the equation of motion (4.3) and piezoelectric constitutive equations (4.14) and (4.15). Mechanical and electrical energy propagate through the bulk of the piezoelectric element (PZT-5A) creating deformations on structural (silicon) layer .The mechanical waves in silicon also interact with the surrounding liquid from its bottom surface creating displacements in normal and tangential directions. Along the fluid-solid interface, the displacements generated by the silicon/PZT-5A bi-layer generate flow in the fluid according to:

$$\boldsymbol{v}_f = \boldsymbol{v}_s = \frac{\partial \boldsymbol{u}}{\partial t} \tag{9.1}$$

where **u** is the displacement vector in silicon, $\mathbf{v_s}$ is the velocity vector in silicon and $\mathbf{v_f}$ is the velocity vector in fluid. The fluid flow generated by the displacements in silicon affects the mechanical waves in solid layers. Therefore, the force interactions between solid and fluid layers should be in dual ways. The mechanical deformations should affect the fluid flow and the fluid flow should affect the driving mechanical deformations in solid layers. Numerically this method is invoked by specifying implicit pressure and implicit shear stress across the bottom of the bi-layer membrane. Mathematical representation of the implicit pressure and implicit shear stress are as follows:

$$\tau_{22}^{s} n_2^{s} + \tau_{22}^{f} n_2^{f} = 0 \tag{9.2}$$

$$\tau_{21}^{s} n_1^{s} + \tau_{21}^{f} n_1^{f} = 0 \qquad (9.3)$$

where s represents solid, f fluid, τ_{22} normal component of stress (y direction), τ_{21} shear component of stress (x-y plane), n_1 outward normal in x direction and n_2 outward normal in y direction. Positive pressure in liquid generates negative normal stress in solid ($\tau_{22}^{f} = -p$). In the present work, the flow is generated primarily by the vertically deforming surface and the domain is bounded by the bottom rigid boundary (y = 0 μm). The flow is generated by the up and down motion of the interface boundary. In the valveless micropump, as the boundary oscillates with time, it is expected that the fluid will also oscillate in the y direction over time with a specific frequency.

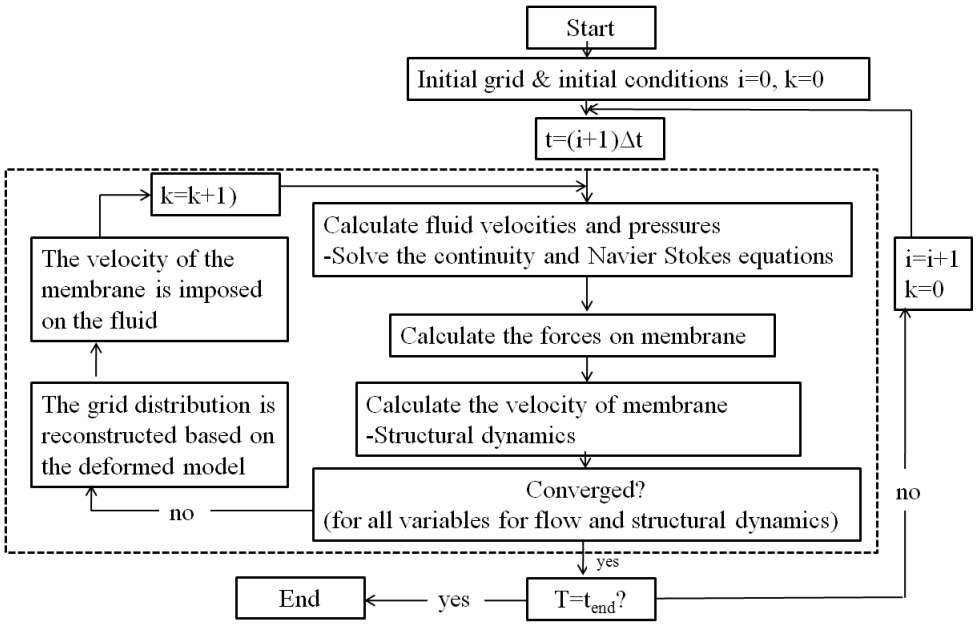

Figure 9.1 Flow chart of the fluid structure interactive (FSI) algorithm

Flow chart of the fluid structure interactive (FSI) algorithm is shown in Figure 9.1. The model first calculates the shear and normal forces (by the solution of pressure and velocities for the fluid) that are to be imposed on the solid domains. Using these forces governing equations for the solid domains are solved. If the convergence for all variables for flow and structure dynamics is achieved, the calculations proceed to the next time step. Otherwise, computational grid is reconstructed based on the deformation of the solid model. Pressure and velocities for the fluid are solved again and so on.

9.3 Advantages and Significance of Fluid-solid Coupling

An analytic solution can only be obtained for very simplified cases for the investigations of piezoelectric micropumps. In most cases numerical solution is necessary due to the nonlinearities of the problem [22]. The most accurate is probably to use the concept of continuum theory which couples the relevant mechanical, electrodynamic and thermal field quantities in terms of a system of partial differential equations [81]. This approach can be implemented using finite element programs. Finite element (FE) models developed so far have been mostly limited to solving for the fluid domain where the solid motion is superimposed as a boundary condition for the investigations of piezoelectric micropumps. Simulation results of Fan et al. [56] show that the pumping efficiency depends not only on the actuating frequencies and maximum magnitude of the membrane deflection, but also on the complicated membrane deflection shape. Membrane shape is not known without the solution of the dynamic model. To capture the dynamics of fluid-solid interaction, the equations of motion for the fluid elements must be solved in conjunction with the acoustoelectric equations for the motion of the solid [18, 34, 35, 37, 64, 122]. This numerical technique provides a greater flexibility in modeling

piezoelectric micropumps because it can handle the wave equations in two and three dimensions. This allows capturing the full device response and enhances the ability to model complex geometries and test different designs for optimum performance [86]. Acoustic energy transfers from the piezoelectric substrate to a solid/liquid boundary, where the Rayleigh wave then becomes leaky. This excites longitudinal waves into the liquid at an angle following the refraction law. The absorption of the acoustic energy from the piezoelectric actuator devices to the fluids is very efficient due to coupling of longitudinal pressure waves into the fluids. Since the speed of sound depends on the density of the transmission medium, phase matching conditions require radiation of the acoustic wave into the fluid at an angle given by the refraction law. Without a fluid-solid coupled model this interaction cannot be properly represented [28, 46, 90]. The nonlinear motions shown by the micropump require the development of coupled models [123]. Resonance frequency of the solid membrane and the fluid-solid system are significantly different. This issue also requires the use of fluid-solid interactive dynamic models [56, 63, 81].

Finite element (FE) models involving coupling of fluid and solid domains have been constructed using acoustic elements for modeling the fluid region. However, these models solve only the simplified Navier-Stokes equation for the pressure field in the fluid and ignore viscous effects. Uniform mean density and mean pressures are assumed by this models. The application of these models is limited to the study of wave damping [34]. There are two main couplings in the micropump design: the electro-mechanical coupling of piezoelectric actuator and the fluid–solid coupling between the working fluid and the pump membrane [64]. A coupled-field analysis is required to analyze the

interactions between the solid motion and the induced fluid flow. To the best of our knowledge, no FE model involving coupled-field analysis of fluid–piezoelectric-solid devices has been presented in the literature so far, for valveless piezoelectric micropumps. Previous models [18, 34, 35, 37, 122] involving fluid-piezoelectric interaction were developed to study flow profiles in the interface region of a surface acoustic wave biosensor device. In the present work, coupled multifield (structural and fluid flow) analysis of a piezoelectric valveless micropump is carried out for liquid transport applications. Parameters studied in this model include the effect of the excitation voltage and actuation frequency, pump back-pressure and working fluid properties (fluid density, speed of sound in the working fluid and viscosity). Comparisons of model predicted average flow rates with experimental data on piezoelectric micropump performance are also presented.

This analysis used the two-way coupling option. The solver iterates between each physics field piezoelectric and fluid until loads transferred across the interfaces converge. A converged steady-state flow field was obtained, and then the pressure loading from that flow field was applied to the stress module to calculate the resulting stresses. Next, the geometry deformations from the structural analysis were fed back to the flow modules. The Navier–Stokes equations contain a nonlinear term, and the nonlinear fluid motion is coupled back into the kinematic equation for the structure model [123]. Consequently, the micropump membrane also shows nonlinear motions. A purely Eulerian frame for the fluid domain introduces complexity in fluid-solid coupling. For the flows with moving and deforming boundaries, grid generation is considered at every time-step. Re-meshing

is introduced by using the transfinite interpolation (TFI) scheme [104]. The TFI scheme determines the interior node distribution based on the motion of the boundary nodes.

9.4 Problem Description and Geometry

9.4.1 Schematic of the Problem Geometry

Flow generated by piezoelectric valveless micropump is modeled in a microchannel (Figures 9.2a-c) using mechanical equations of motion for the solids, the electromagnetic field equations for the actuator and mass/momentum conservation equations for the fluid. The valveless micropump consists of two diffuser/nozzle (outlet/inlet) elements; the pump chamber, a thin structural layer (silicon) and a piezoelectric layer, PZT-5A as the actuator. The selected problem geometry is similar to the one reported by Cui et al. [88]. The two-dimensional (x-y) geometry used in the present study considers a 90° rotated diffuser geometry compared to the pumping chamber and the membrane displacement direction as shown in the experimental three-dimensional schematic (in Figure 1 of Cui et al [88]).

A piezoelectric material deforms when an external electric field is applied. A sinusoidal voltage signal is applied at the input electrodes, which by the converse piezoelectric effect is converted to mechanical perturbations on the surface. The volume of the element reduces or expands depending on the polarization of the applied electric field. When the piezoelectric element (PZT-5A, particulate (lead) zirconate titanate) located in between two electrodes is electrified the bi-layer membrane moves up or down for the piezoelectric micropump. The bi-layer membrane consists of silicon pump diaphragm and PZT-5A piezoelectric layer. The piezoelectric valveless micropump

device configuration adopted in this study has a thin film bulk acoustic resonator (FBAR) structure, where two electrodes are patterned on the top and the bottom surfaces of the piezoelectric substrate in which the electrodes fully cover the surfaces. The mechanical wave propagates across the piezoelectric element generating a bulk wave. Figure 9.2a shows that the valveless micropump consists of two diffuser/nozzle elements and the pump chamber (bottom layer); one thin pump diaphragm (middle layer) and one piezoelectric layer, PZT-5A (top layer) as the actuator. Two dimensional structural schematic of the micropump is shown in Figures 9.2b and 9.2c. The micropump is made from silicon and glass. As these two kinds of materials have good chemical stability, the proposed micropump is biocompatible.

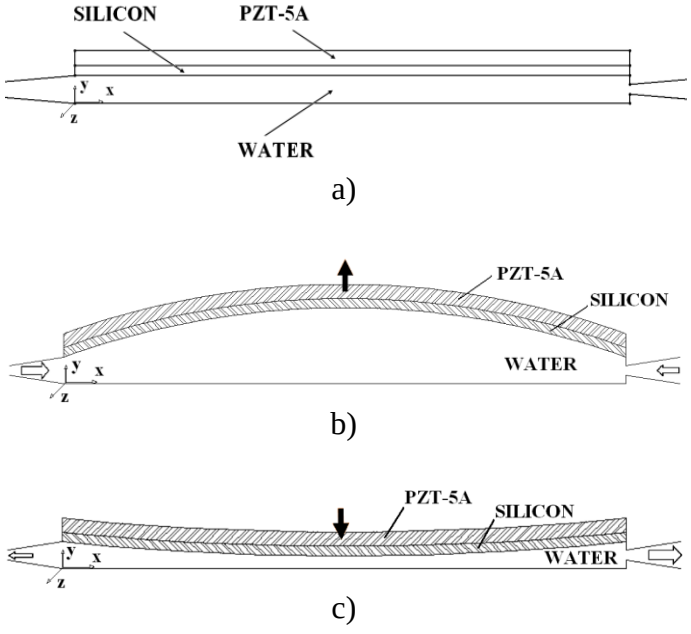

Figure 9.2 Piezoelectric valveless micropump a) problem geometry considered b) schematic of the supply phase (*not to scale*) c) schematic of the pump phase (*not to scale*).

The length of the pump chamber is 6.0 mm, the height of the (undeformed) pump chamber (H) is 280.0 μm, the diffuser and nozzle lengths are each 1.1 mm, the height of the narrowest part is 100 μm for both the diffuser and the nozzle, the divergence and convergence angles are both 9.4º, the thickness of the silicon layer is 100 μm and the thickness of the PZT-5A layer is 150 μm. When the pump diaphragm moves to increase the volume of the pump chamber, the fluid is pushed into the pump across the inlet and the outlet. The pump is in the supply phase (Figure 9.2b). If the flow resistance in the nozzle direction is higher than that in the diffuser direction, more fluid flows into the pump chamber through the inlet. On the other hand, when the pump diaphragm moves to decrease the volume of the pump chamber, the pump is in the pumping phase (Figure 9.2c). More fluid goes out of the pump through the outlet; hence, the net fluid transport from the inlet to the outlet is achieved.

9.4.2 Material and Working Fluid Properties

Material properties and the working fluid properties considered are listed in this section. Property data is given below for the piezoelectric material (PZT-5A), pump diaphragm (silicon) and working fluid. The material data is provided following the conventional IEEE standards on piezoelectricity [106].

Piezoelectric material PZT-5A [64]

The density ρ, piezoelectricity (e), permittivity ε and the elasticity matrix c of PZT-5A are given below:

Density $\rho = 7700 kg/m^3$

Piezoelectricity $$e = \begin{bmatrix} 0 & 0 & -5.4 \\ 0 & 0 & -5.4 \\ 0 & 0 & 15.8 \\ 0 & 12.3 & 0 \\ 12.3 & 0 & 0 \\ 0 & 0 & 0 \end{bmatrix} C/m^2$$

Permittivity $$\varepsilon = \begin{bmatrix} 8.107 & 0 & 0 \\ 0 & 8.107 & 0 \\ 0 & 0 & 7.346 \end{bmatrix} x10^{-9} F/m$$

Elasticity matrix $$c = \begin{bmatrix} 12.1 & 7.54 & 7.52 & 0 & 0 & 0 \\ 7.54 & 12.1 & 7.52 & 0 & 0 & 0 \\ 7.52 & 7.52 & 11.1 & 0 & 0 & 0 \\ 0 & 0 & 0 & 2.11 & 0 & 0 \\ 0 & 0 & 0 & 0 & 2.11 & 0 \\ 0 & 0 & 0 & 0 & 0 & 2.26 \end{bmatrix} x10^{10} N/m^2$$

Silicon [64]

The density, Young's modulus and Poisson's ratio of silicon are:

Density $\rho = 2330\ kg/m^3$, Young's modulus $E = 162 \times 10^9\ Pa$ and Poisson's ratio $\upsilon = 0.22$

Working fluid (water) [64]:

Properties of the working fluid are given below:

Density $\rho = 997 kg/m^3$, dynamic viscosity $\mu = 0.0014 kg/m.s$ and speed of sound in working fluid $c_s = 1480 m/s$.

9.5 Boundary Conditions

The boundary conditions for the dependent variables need to be specified for the problem geometry (Figure 9.2a) considered. Along the inlet and outlet boundaries (left and right boundaries in Figure 9.2a, respectively) zero gradient boundary conditions are specified for velocity. Along the walls zero slip boundary conditions are used for velocity. Rather than using zero pressure at inlet and outlet, in the present work the pressure boundary conditions introduced by Zhang et al. [74, 75] are employed. Details of the modeled boundary conditions (Figure 9.2a) are:

Inlet

$$\frac{\partial u_f}{\partial x} = 0 \; ; \; \frac{\partial v_f}{\partial x} = 0 \; ; \; p = p_0 - \frac{16}{\pi}\frac{\mu}{H}\bar{u}_{f,in} \tag{9.4}$$

Outlet

$$\frac{\partial u_f}{\partial x} = 0 \; ; \; \frac{\partial v_f}{\partial x} = 0 \; ; \; p = p_0 + \frac{16}{\pi}\frac{\mu}{H}\bar{u}_{f,out} \tag{9.5}$$

where p is the pressure, p_0 is the ambient pressure, H is the height of the channel, μ is the dynamic viscosity of the working fluid, $\bar{u}_{f,in}$ and $\bar{u}_{f,out}$ are iteratively calculated area averaged instantaneous velocities along the channel inlet and outlet, respectively. The flow starts (inlet) and terminates (outlet) at large reservoirs. Density along the inlet and outlet boundaries is specified using the equation of state (3.22) and the pressure boundary conditions predicted by the equations (9.4) and (9.5). The above pressure boundary conditions include the effects of sudden contraction and sudden expansion at the inlet and outlet. Happel and Brenner [112] showed, the local pressure loss/gain is linearly

proportional to mean velocity if the Reynolds number ($\frac{\overline{\overline{\rho u_f}} H}{\mu}$) is less than 1.6 where $\overline{\overline{u_f}}$ is the time and space-averaged axial velocity of fluid at the mid-section of the pump chamber (x = 3.0 mm). This condition is mostly satisfied by the present predictions. Happel and Brenner [112] did not consider the specific case of oscillatory flow through fluidic "diodes". The pressure losses due to flow contraction and expansion through a infinitely thin slit is covered in [112].

Two sides and the top surface of the PZT-5A crystal are traction (stress) free. Bottom of the crystal is coupled to the silicon layer by implicit pressure and implicit shear stresses. 'Implicit pressure' and 'implicit shear stress' terms are used to represent unknown quantities that are calculated in an iterative manner. Two sides of the silicon layer are considered to be clamped. Bottom of the silicon layer is the fluid structure interface. It is also coupled to liquid layer by implicit pressure and implicit shear stresses. Bottom surface of the micropump is glass. Glass is considered as perfectly rigid. Boundary conditions of electrical variables are as follows: the sides of all three layers have zero gradient and the piezoelectric element is grounded at its top surface and sinusoidal voltage is applied at the bottom. The fluid is initially quiescent and the pressure is atmospheric and all dependent variables are zero.

9.6 Numerical Scheme Considered

For the solid domains 2nd order strain analysis is invoked with a consistent mass matrix type. The resultant system of linear equations for the piezoelectric domains is not positive definite and symmetric. Accordingly, a direct linear equations solver PCGLSS 5.0 [100] is used for the solution of dynamic structural model. It limits the allowable

number of grid points for solid domains. Time dependent simulations were performed via implicit Euler scheme. The time step was chosen such that the cyclic variation of the piezoelectric actuator is well-resolved.

For the liquid domain, finite volume method is used to discretize the governing equations. The governing equations for the liquid domain are solved using the SIMPLEc algorithm [99]. The resultant system of equations is solved by CFD-ACE+ 2010 solver. Conjugate gradient squared linear equations solver was employed with an implemented "incomplete Cholesky factorization" as a pre-conditioner [100]. Terms for the discretization of convection terms are formulated according to the 2^{nd} order accurate upwind scheme for velocity, and 2^{nd} order accurate central difference scheme for density. For the flows with moving and deforming boundaries, grid generation is considered at every time-step. Re-meshing is introduced by using the transfinite interpolation (TFI) scheme [104]. The TFI scheme determines the interior node distribution based on the motion of the boundary nodes.

The problem is simulated using 100 time steps per cycle. The same time step is used for the solid and liquid zones. For example for frequency of 1.0 kHz, time step is 10^{-5} s. Decreasing the time step by another 50% did not have any appreciable effect on the results. The time required to reach pseudo-periodic state is 10.0 perturbation cycles. The velocity and the computational grid cell center coordinates are stored for one cycle (100 time steps). The stored velocity and coordinates are averaged to get time averaged velocity vectors. Rectangular structured brick elements are used both for the solid and the liquid domains. Total computation time (per case) is varied 7 hours (two-dimensional

cases) to 1 week (three-dimensional) on a Dell Optiplex 360 computer equipped with Intel Core 2 Duo processor and 3.0 GB of memory.

9.7 Results and Discussion

Table 9.1 lists the cases considered in the present study. In cases 1-a thru 1-e, grid dependency study is considered varying the number of computational cells while f = 400.0 Hz and V_{p-p} = 80.0 V. In cases 1-a, 2 and 3 the parameters are chosen from the values used in [88], f = 400.0 Hz and actuation voltages are V_{p-p} = 80.0, 100.0 V and 140.0 V respectively. First three cases are chosen to investigate how the predictions by the present work and [88] differ with the change of applied electric potential. In cases 4 to 11, the frequency of the perturbations is varied (f between 0.2 - 8.0 kHz) at an actuation voltage of V_{p-p} = 80.0 V, while keeping other parameters same as in case 1-a. By varying only frequency of the perturbations effect of actuation frequency on generated flow is investigated. The previous works [53, 56, 64] explained the dependence of net flow rates to actuation frequency using the instantaneous deflection shapes of the bi-layer membrane without calculating time-averaged velocity. Flow rates are calculated by integrating time-averaged velocity for the entire micropump in the present study. The goal of the cases 4 to 11 is to optimize actuation frequency while trying to maximize the pump flow rate. Three simulations are performed to observe the effect of driving voltage on the time-averaged velocity (cases 1-a, 2 and 3). Nine simulations are performed to observe the effect of actuation frequency on the time-averaged velocity (cases 1-a, 4-11). Material properties and micropump geometry are kept constant for all calculations.

Table 9.1 List of the cases considered for piezoelectric valveless micropumps (two-dimensional model)

Case	Voltage (V)	Freq. (Hz)
1a-1e	80	400
2	100	400
3	140	400
4	80	200
5	80	1000
6	80	2000
7	80	4000
8	80	5000
9	80	6000
10	80	7000
11	80	8000

A grid density of 216 x 48 is considered for fluid domains in cases 1a, and cases 2 -11. For solid domains, a grid density of 144 x 50 is considered.

9.7.1 Validation of the Model

In Figure 9.3, the predicted flow rate is plotted versus varying number of solid grids (cases 1a thru 1e) with grid sizes of 144 x 50, 158 x 50, 173 x 50, 116 x 50 and 130 x 50 respectively. It is found that predicted flow rate converges if the number of solid elements is above 6864 (cases 1a thru 1c). All the flow rate predictions, except cases 1d and 1e (the number solid elements is not sufficient for these cases), are within ±1.0%. A grid density of 144 x 50 is considered for solid domains (it corresponds to 6864 solid elements) in the present work (cases 1a, and cases 2 -11). For fluid domain, a grid density of 216 x 48 is considered. A similar analysis was done to determine the grid size for the fluid domain.

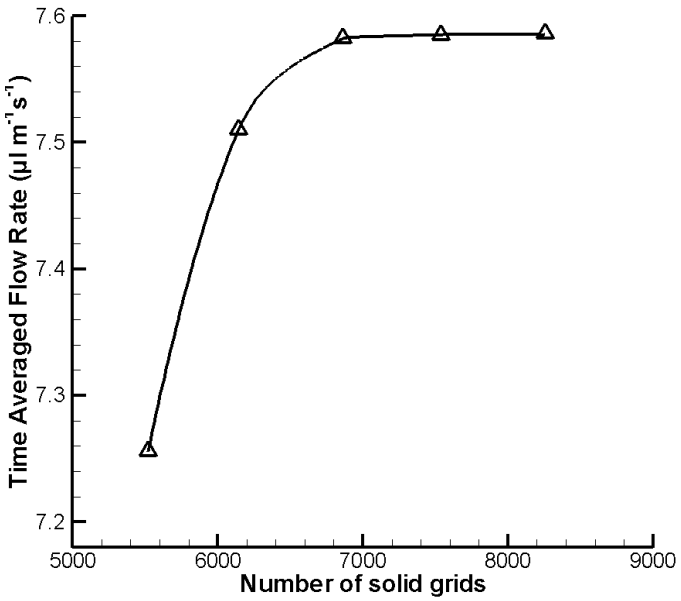

Figure 9.3 Comparison of time-averaged volumetric flow rates (at the location x = 3.0 mm, at the 10^{th} cycle) for varying number of solid grids where f = 400.0 Hz, and V_{p-p} = 80.0 V. (cases 1a thru 1e)

Verification of the present numerical model is also performed by comparison of the instantaneous displacement of the interface in between solid and fluid layers with the published results [64, 88] for the problem geometry given in Figure 9.2a. Figure 9.4 shows the comparison of the present model predictions (cases 1-a, 2 and 3) of the vertical instantaneous displacement (y component) along the interface between solid and fluid layers (x coordinate) of the microchannel at y = 280.0 μm. The present coupled multifield model results agree well with the results of Cui et al. [88] where the difference is below 2% at t = 25 msec.

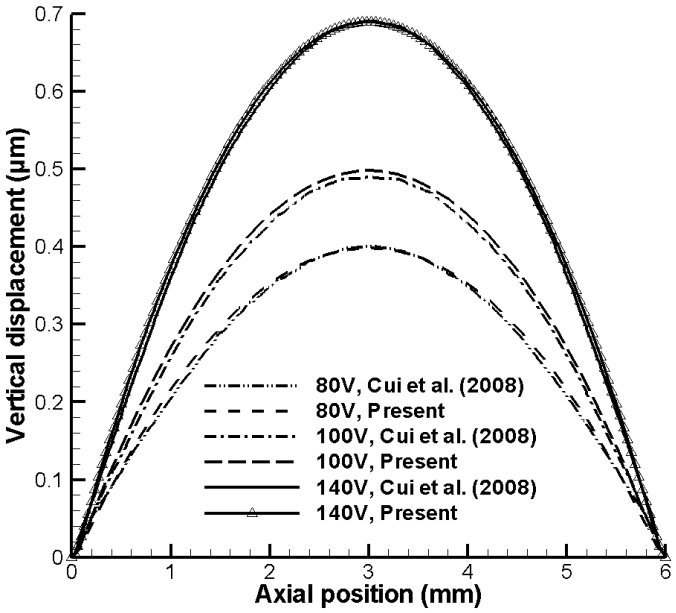

Figure 9.4 Comparison of the instantaneous displacement along the interface between solid and fluid layers to the work by Cui et al. [88] (along the bottom of the silicon layer). t = 25 msec, y= 280.0 μm, f = 400.0 Hz and V_{p-p} = 80.0, 100.0 or 140.0 V (cases 1-a, 2 and 3).

Predicted flow rates at a higher actuation frequency (3.5 kHz) are compared with the results given in Olsson et al. [81, 124]. Olsson et al. [124] experimentally measured the average flow rate of a 6.0 mm diameter flat-walled double chamber silicon pump as 1946.0 μl/min at 3350.0 Hz. Olsson et al. [81] calculated flow rate of the single chamber pump as 973.0 μl/min using the experimental results in [124]. Time averaged flow rate at 4000.0 Hz is predicted as 313.7 μl/min for a single chamber pump. In the present study, maximum vertical displacement is predicted as 0.48 μm (at 80. 0 V excitation voltage) whereas Olsson et al. reports the same as 0.64 μm (at 200. 0 V). The membrane material, thickness and diffuser geometry in [81] are similar in the present study and [124]. Net flow increases quadratically with excitation voltage. Therefore, the present flow rate predictions are within a reasonable range with Olsson et al. [81, 124]. The pump chamber

is circular (6.0 mm diameter (D)) in the x-z plane and has a height of 0.280 mm in y direction in Olsson et al. Present calculations are in the x-y plane, hence 4.7 mm is the average width of the circular fluid domain ($\pi D^2/4/D = \pi D/4$) is considered for flow rate validation.

9.7.2 Parametric Studies

Reynolds (Re), Strouhal (St) and Womersley (α) numbers represent the relative importance of inertia over viscous forces; oscillating flow mechanisms over inertia and oscillating flow frequency in relation to viscous effects, respectively. The definition of Re, St and α dimensionless numbers can be given as follows:

$$\mathrm{Re} = \frac{\overline{\overline{\rho u_f}} H}{\mu} \tag{9.6}$$

$$St = \frac{fH}{\overline{\overline{u_f}}} \tag{9.7}$$

$$\alpha = (2\pi \,\mathrm{Re}\, St)^{1/2} = (2\pi f \frac{\rho H^2}{\mu}) \tag{9.8}$$

In equations (9.6) and (9.7), $\overline{\overline{u_f}}$ is the time and space-averaged axial velocity of fluid at the mid-section of the pump chamber (x = 3.0 mm). The calculated values of Re, St and α dimensionless numbers for all cases studied are listed in Table 9.2. Flows with lower St number show stronger inertia effects comparing to the high St number flows.

Table 9.2 List of predicted nondimensional parameters

Case	Velocity (μm/s)	Re	St	α
1	27	0.0054	4136	11.8
2	42	0.0084	2650	11.8
3	83	0.0165	1355	11.8
4	7	0.0014	8260	8.4
5	161	0.0321	1738	18.7
6	598	0.1193	936	26.5
7	3963	0.7902	283	37.5
8	10376	2.0689	135	41.9
9	9259	1.8462	181	45.9
10	3749	0.7476	523	49.6
11	1757	0.3503	1275	53.0

Figure 9.5a shows the time-averaged axial velocity profile as a function of distance from the bottom of the fluid domain (y-coordinate) and applied voltage in a microchannel along the vertical midplane (cases 1a, 2 and 3). The time-averaged velocity profiles are shown at the 10^{th} cycle. Actuation frequency is kept constant at 400.0 Hz while varying peak to peak actuation voltages between 80.0 V – 140.0 V are considered. The pseudo-periodic state solutions are confirmed by the negligible standard deviation between velocity profiles for the same phases during several consecutive cycles. At 400.0 Hz, the frequency of pulsations is sufficiently low that a parabolic velocity profile has time to develop during each cycle, as seen in Figure 9.5a. Amplitude of the oscillations generated by the membrane increases with the increase of the driving electrical potential. As the amplitude of the membrane deflection increases, the generated flow also increases. It is also found that time-averaged vectors of velocity patterns do not change significantly with increasing driving voltage (not shown here). At a low actuation frequency (400 Hz), the excitation voltage is a dominant factor on the flow rate of the micropump.

In Figure 9.5b, the variations of the x component of the normalized time-averaged fluid velocity along the y coordinate are shown for various values of the Womersley (α) number (actuation frequency) for cases 1-a, 4 – 11 at x = 3.0 mm. The time averaged velocity is normalized by the maximum space and time averaged velocity for the case considered. The actuation frequency (f) is varied between 0.2 kHz and 8.0 kHz which corresponds to α = 8.4 – 53.0. The time averaged velocity (listed in Table 9.2) increases with the increase of actuation frequency (below 5.0 kHz) then it drops significantly with frequency (Table 9.2). With the increase of actuation frequency, the velocity profile becomes relatively flatter. The variation of normalized velocity appears to be continuous and gradual with the increases of α.

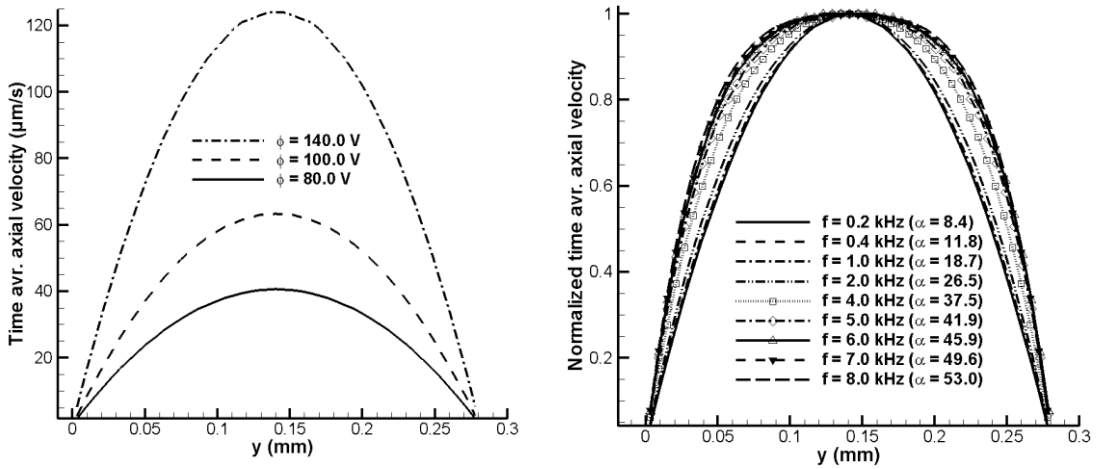

a) b)

Figure 9.5 Time-averaged axial velocity along the y-axis. x = 3.0 mm, 10th cycle. `**a)** effect of applied voltage. f = 400.0 Hz and V_{p-p} = 80.0 V, 100.0 V and 140.0 V (cases 1-a, 2 and 3) **b)** effect of actuation frequency on normalized time-averaged axial velocity along the y-axis. V_{p-p} = 80.0 V and α= 8.4 -53.0 (f = 200.0 Hz – 8000.0 Hz, cases 1-a, 4 - 11).

9.7.3 Acoustically Driven Flows in Micropump: Quasi-periodic State

In Figures 9.6a - d velocity vectors are plotted at the beginning of 10th cycle, one-third cycle later, two-third cycle later and at the beginning of the 11th cycle (case 1-a) respectively. Comparing the velocity fields in Figures 9.6a and 9.6d, quasi-steady behavior of the flow field is observed. When estimated velocity differences between subsequent cycles for all the calculated points are observed to be less than the specified convergence criteria ($\eta = \frac{\overline{u}_{f,j+1} - \overline{u}_{f,j}}{\overline{u}_{f,j}} \leq 0.01$), the flow-field is assumed to be quasi-steady.

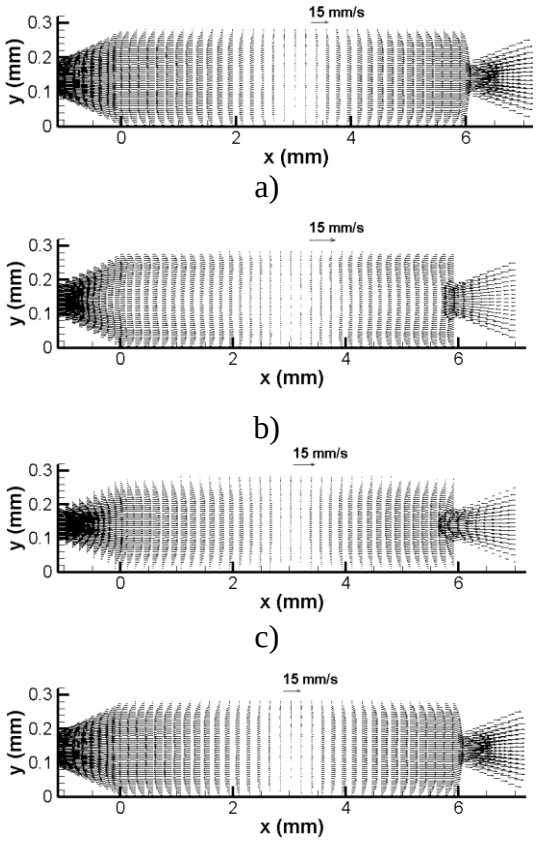

Figure 9.6 Vectors of velocity at the 10th cycle, case 1-a a) at the beginning of 10th cycle b) one third of a cycle later c) two thirds of a cycle later d) at the beginning of 11th cycle; f = 400.0 Hz and V_{p-p} = 80.0 V (only flow domains are shown).

Figure 9.7 shows the contours of the pressure field for case 1-a at the end of the 10^{th} cycle in the micropump, t = 25 msec. The deflection of the PZT-5A and silicon bi-layer membrane generates suction or discharge within the fluid. The resistance to flow is different at the nozzle from that at the diffuser. The pressure is asymmetric with respect to the vertical mid-plane of the device. This asymmetry is the driving force that leads to a net flow in the investigated micropump. Our simulation results indicate that the extent of suction or discharge pressures increases or decreases with increasing distance from the center of the device depending on the phase that the system goes through in an actuation cycle (the membrane displacement is maximum or minimum at the center for the device at the low frequency range of the present work). The generated pressure at the device surface also grows or decays with distance from the center of the membrane.

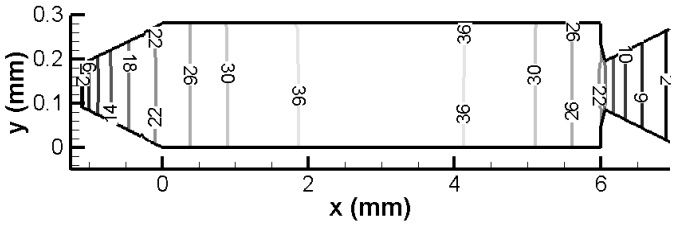

Figure 9.7 Instantaneous gauge pressure (Pa) generated by the oscillating membrane as a result of the asymmetry in the flow domain at the end of 10^{th} cycle. t = 25 msec, f = 400.0 Hz and V_{p-p} = 80.0 V (case 1-a) (only flow domains are shown).

The variation of design parameters such as applied electric potential, actuation frequency and geometric variables (such as the thickness of the silicon and piezoelectric layers, diffuser length and divergence angles) could help generate sufficient pressure field along the entire length of the pump. It may also facilitate mixing of species that are

otherwise molecular diffusion limited. The instantaneous pressure field changes with time within a cycle. For the flows with acoustic excitations the energy dissipated by the oscillating wall is not only attenuated by the inertia and viscosity of the fluid, it is also attenuated through the density variations (density variations cause variations in pressure). Hence the compressibility of water is considered in the present work.

In Figure 9.8 time-dependent mass flow rates through the outlet of the micropump are shown during the 10^{th} cycle. During the supply mode the instantaneous flow rate is positive (flow is into the pump chamber) and during the pump mode it is negative (flow is out of the pump chamber). The mass flow rate is provided per unit depth of the device. While the previous studies [48, 49, 52, 53, 56, 64, 88] report on the maximum value of instantaneous flow rates, instantaneous velocities are integrated along the outlet at each time step during one perturbation cycle. The instantaneous flow rates can be adjusted by varying parameters such as applied electric potential, actuation frequency and geometric variables.

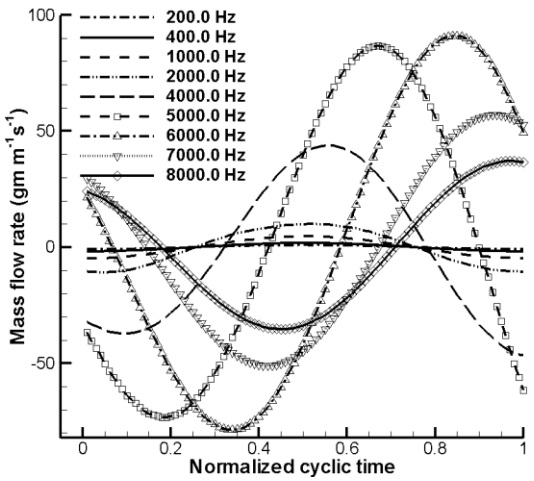

Figure 9.8 Time-dependent mass flow rates during the 10^{th} cycle. f = 200.0 Hz – 8000.0 Hz and V_{p-p} = 80.0 V (cases 1-a, 4-11).

In Figure 9.9 pressure (for liquid domain) and y component of normal stress (with a negative sign) are plotted along the y-axis at t = 25 msec for selected constant x lines (case 1-a). At y = 280.0 μm, we have the fluid-structure interface. The match of pressure and normal stress guarantees that the two way coupling is performed satisfactorily (see section 9.2). The small kinks at y = 280.0 μm are due to the viscous boundary layer in fluid. The flow reversal is primarily caused by an adverse pressure gradient imposed on the boundary layer by the bulk flow. At these axial locations (x), the instantaneous local flow changes its direction (similar to the Stokes' second problem) and spikes become stronger in the fluid. The thickness of the viscous boundary layer is 28.8 μm (f = 400.0 Hz). The magnitude of stress decays away from the liquid solid interface since the top boundary of the device is free to deflect.

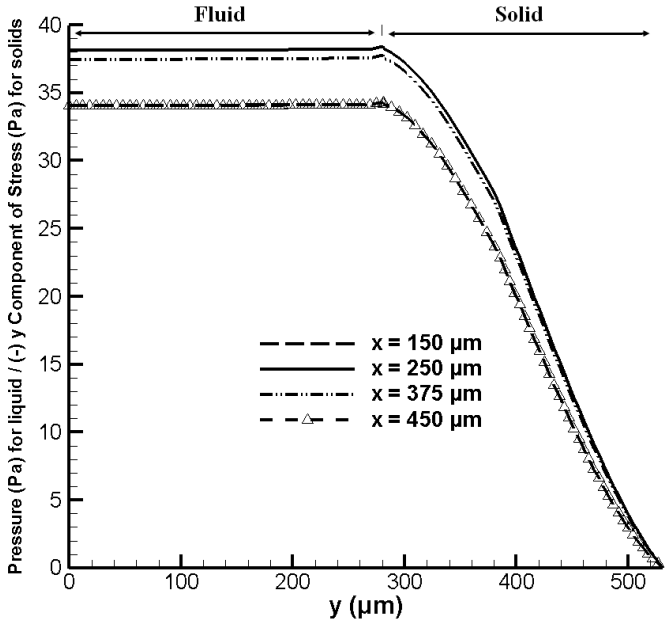

Figure 9.9 Pressure variations for solid and liquid domains along the y-axis at t = 25 msec for selected constant x lines t = 25 msec, f=400.0 Hz and $V_{p\text{-}p}$ = 80.0 V (case 1-a).

Figure 9.10a shows the y-variation of u_f at x = 3.0 mm at different time levels (4 consecutive phases within a cycle) for case 1-a. The flow is generated by the up and down motion of the interface boundary. In the valveless micropump, as the boundary is oscillating with time, it is expected that the fluid will also oscillate in the y direction in time with a specific frequency. Between phase angles 0 to π acceleration of the fluid is in positive x direction and similarly between phase angles π to 2π it is in the negative x direction. Bulk of the fluid responds to accelerations faster than the boundary layers due to the increased viscous friction in boundary layers. Same effect can also be seen in Figures 9.6a-d. Hence the velocity profile is wavy at phase angles 0 and 2π. At phase angles of 2π/3 and 4π/3 the flow in the shear layers and the bulk of the flow follows each other generating plug like and parabolic velocity profiles. The total area under the individual curves also confirms net flow in positive x direction.

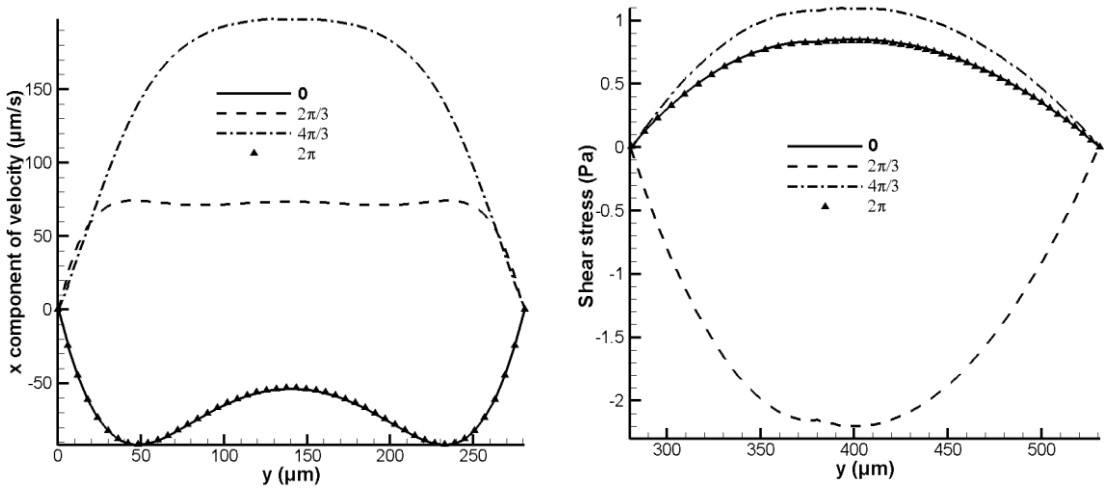

Figure 9.10 a) instantaneous axial velocity profiles along the y-axis. b) shear stress in x-y plane along the y-axis. Each line corresponds to a different time in the 10th cycle in both figures. Plots are along the height of the channel. x = 3.0 mm, f = 400.0 Hz and V_{p-p} = 80.0 V (case 1-a).

In Figure 9.10b variation of instantaneous shear stress (τ_{xy}) along the width of the channel (y) is plotted (case 1-a). Instantaneous shear stress changes with time, when a sinusoidal electrical signal is applied on electrodes. Figure 9.10b shows shear stress in x-y plane along the vertical distance (y) at different time levels (4 consecutive phases within a cycle).

In Figures 9.11a-c, contours of instantaneous strain in y direction (S_{yy}) for the entire solid domains (top two layers in Figure 9.2a) are shown at the beginning of 10^{th} cycle, one-third cycle later and two-third cycle later. Only solid domains are shown in Figures 9.11a-c for case 1-a at the 10^{th} cycle, f = 400.0 Hz and V_{p-p} = 80.0 V. The y axis is magnified 6 times for clarity. The top layer, PZT-5A, is free to deflect along its sides and top face. The bottom layer, silicon, is clamped rigidly from its sides. In Figure 9.11a, the structure is in 0 phase angle and the strain is uniform everywhere where as in Figure 9.11b, the structure is bended downward (negative y direction). The maximum strain is observed towards the edges of the PZT-5A layer where it is free to deflect along its two sides and its top boundary. Note that in Figure 9.11c, the structure is bended upward. Accordingly, the maximum strain is observed towards the edges of the silicon layer where it is clamped to the structure.

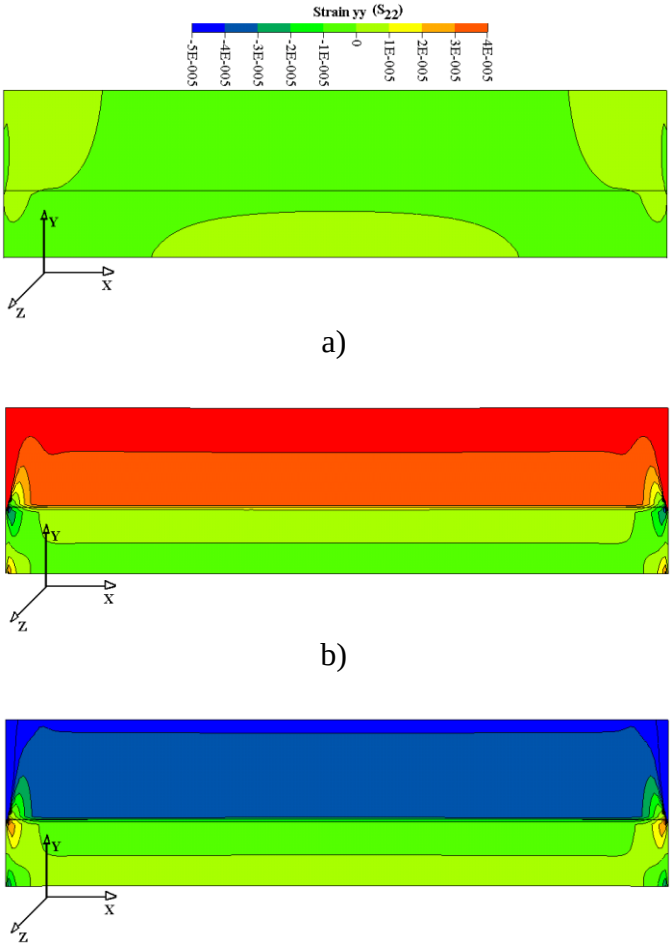

Figure 9.11 Contours of instantaneous normal strain in y direction for solid domains at the 10^{th} cycle a) at the beginning of 10^{th} cycle b) one third of a cycle later c) two thirds of a cycle later. f = 400.0 Hz and V_{p-p} = 80.0 V (case 1a).

9.7.4 Time-averaged Velocity Field in Micropump: Net Flow

Figure 9.12a shows time-averaged velocity profile (case 4) for a lower actuation frequency where as Figure 9.12b (case 4) shows it for a higher actuation frequency. The velocity profiles are parabolic in Figure 9.12a, where as in Figure 9.12b they become relatively flat. The net flow is shown from nozzle to diffuser of the micropump via averaging velocities over time. The time-averaged velocity profile over one period become parabolic (or relatively flat) for all cases being investigated. Nguyen and White

[22] found out that the thickness of the evanescent decay length determines the transition from a parabolic profile to an asymmetric velocity profile. By comparing Figures 9.12a and 9.12b it is seen that the time-averaged velocity increases approximately by 3 orders of magnitude when the actuation frequency increases from 200.0 Hz to 8000.0 Hz. At a low value of actuation voltage (below 140 V), the excitation frequency is the dominant factor on the time-averaged velocity of the micropump.

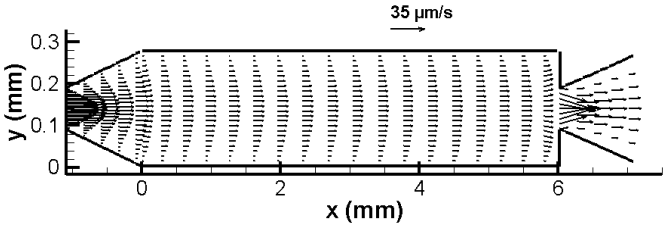

a)

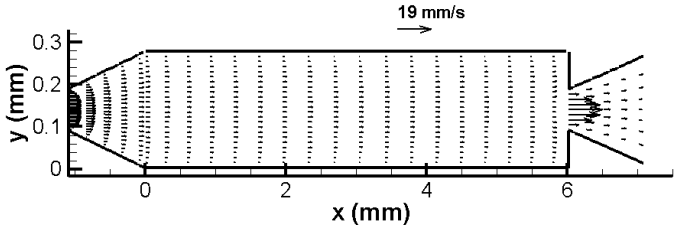

b)

Figure 9.12 Vectors of time-averaged velocity. Vp-p = 80.0 V, 10th cycle. a) f = 200.0 Hz (case 4). b) f = 8000.0 Hz. (case 11) (only flow domains are shown, magnified 6 times in y direction).

In Figure 9.13 effect of actuation frequency on time-averaged volumetric flow rates is shown. The results are through the 10^{th} cycle for the actuation frequency range of 200.0 Hz to 8000.0 Hz, (x = 3.0 mm and V_{p-p} = 80.0 V (cases 1-a, 4-11). The volumetric

flow rate is provided per unit depth of the device (since a two dimensional model is considered). The unit of it is µl (micro liters) per meter second.). In Figure 9.13, the fluid-solid system shows a resonance at 5.0 kHz due to the combined effect of mechanical and fluidic capacitances, inductances, and damping. At actuation frequencies below 2000.0 Hz elasticity of the piezoelectric element and structural materials is dominant. Mechanical system response is more dominant than the fluidic response at frequencies below 5000.0 Hz; with increasing actuation frequency the predicted flow rate increases due to the increasing membrane velocity per unit applied potential [82]. At higher frequencies, the Womersley number (α) is also higher. At higher α, the effect of the high frequency perturbations on the water is weakened due to the reduced cyclic times. This results in a change in the velocity profile whereby, if the Womersley number is sufficiently large, the velocity profile becomes relatively flat or plug-like (Figure 9.5b). As shown in Figure 9.13 below 5000 Hz, the time averaged flow rate increases with increasing frequency. At high frequency, the working fluid (water) ceases to follow the perturbations due to its inertia and viscosity. At higher frequencies although the value of instantaneous velocity is higher than in lower frequencies (Figure 9.5b), the steady component of velocity is lower at higher frequencies. Time-averaged flow rate starts to drop with increase of actuation frequency above (5000 Hz). The actuation frequencies reported in Figure 9.13 are significantly lower than the first natural frequency (67007 Hz) of the mechanical system (solids only). The first natural frequency of the piezoelectric actuator (silicon and PZT-5A) is estimated following reference [64]. The first natural frequency refers only to that of a second order mechanical system response. It does not

reflect the combined resonance due to mechanical and fluidic capacitances, inductances, and damping.

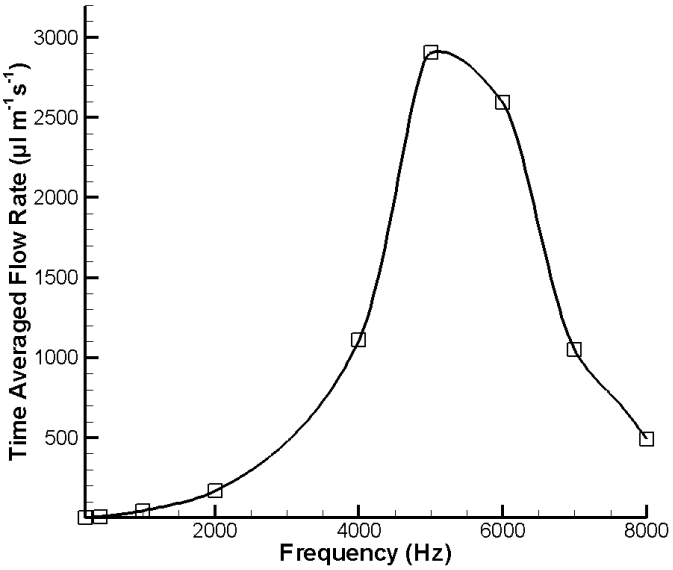

Figure 9.13 Time-averaged volumetric flow rates through the 10th cycle. f = 200.0 Hz – 8000.0 Hz, x = 3.0 mm and V_{p-p} = 80.0 V (cases 1-a, 4-11).

9.8 Conclusions

The flow fields generated in a microchannel (micropump) due to a thin film bulk acoustic resonator are presented considering electrical, mechanical and fluidic fields. The compressibility of the liquid is considered with an isothermal equation of state in the present work. The model predictions are compared with results available in the literature [88]. Although, some previous investigations [48, 49, 52, 53, 56, 64, 88] considered instantaneous flow rates albeit considering incompressible flow formulation, the net flow generated by the device can be better evaluated by averaging velocity field over sufficient number of perturbation cycles. Instantaneous velocities are predicted at each time step

and the results are time-averaged to get the mass flow rates. It is shown that the difference in flow resistance due to flow contraction and expansion (through a nozzle and a diffuser respectively) generates net fluid flow as the bi-layer structural-piezoelectric membrane deflects up and down continuously.

The present model predictions of the vertical displacement along the interface between solid and fluid layers are compared to the work by Cui et al. [88]. The solid bi-layer deflection results agree well with their results, where difference is below 2%. To our knowledge, time-averaged velocity fields are shown for the entire piezoelectric valveless micropump for the first time in the present work. With increasing actuation frequency the predicted flow rate increases up to 5000.0 Hz. Then it drops significantly with increasing frequency.

The time-averaged velocity increases approximately by 3 orders of magnitude when the actuation frequency increases from 200.0 Hz to 5000.0 Hz,. At a low actuation voltage (80 V), the excitation frequency determines the time-averaged velocity of the micropump. A way of determining the static pressures at the inlet and outlet of microchannels is also presented that takes account of the pressure losses due to flow contraction and expansion. The pressure, velocity and flow rate prediction models developed in the present study can be utilized to optimize the design of MEMS based micropumps. Flow rates are calculated by integrating time-averaged velocity for the entire micropump in the present study. Different from previous studies the present work quantitatively provides the dependence of net flow rates to the actuation frequency.

10. PIEZOELECTRIC VALVELESS MICROPUMP: DEVELOPMENT OF A THREE DIMENSIONAL STRUCTURAL/FLUID DYNAMIC MODEL

Coupled multifield (structural and fluid flow) analysis of a piezoelectric valveless micropump is carried out for liquid transport applications. The valveless micropumps consist of trapezoidal prism inlet/outlet elements; the pump chamber, a thin structural layer (Pyrex glass) and a piezoelectric element (PZT-5A), as the actuator. Two-way coupling of forces and displacements between the solid and the liquid domains in the systems are considered where actuator deflection and motion causes fluid flow and vice-versa. Flow contraction and expansion (through the trapezoidal prism inlet and outlet respectively) generates net fluid flow. The effect of the driving voltage and actuation frequency on the structural-piezoelectric bi-layer membrane deflection and the flow rate are investigated. The effects of the working fluid properties (density, viscosity and speed of sound in the fluid) on the micropump performance are investigated for six different working fluids (acetone, methanol, ethanol, water, and two hypothetical fluids). For the compressible flow formulation, an isothermal equation of state for the working fluid is employed. Three-dimensional governing equations for the flow fields and the structural-piezoelectric bi-layer membrane motions are considered. The predicted flow rate increases with actuation frequency up to a critical value. The present fluid-solid system shows optimum performance at this critical actuation frequency due to the combined effect of mechanical and fluidic capacitances, inductances, and damping. Time-averaged flow rate starts to drop with increase of actuation frequency above the critical value. The pressure, velocity and flow rate prediction models developed in the present study can be utilized to optimize the design of MEMS based micropumps. Comparison of the pumping

characteristics of the micropumps operating with different working fluids can be utilized to optimize the design of MEMS based micropumps in drug delivery and biomedical applications.

10.1 Introduction

The present study addresses the development of a comprehensive numerical model for the coupled multifield (structural and fluid flow) analysis of piezoelectrically actuated valveless-micropump MEMS devices for liquid transport applications. The effect of actuation electrical voltage - frequency and working fluid on pump structural layer deflection and flow rate through the inlet/outlet of a piezoelectric valveless micropump are investigated - including the effects due to compressibility of the fluid. The previous works [53, 56, 64] explained the dependence of net flow rates to actuation frequency using the instantaneous deflection shapes of the bi-layer membrane without calculating the liquid velocity field. Flow rates are calculated in the present study by integrating time-averaged velocity fields. Comparison of the pumping characteristics of the micropumps operating with different working fluids has not been investigated extensively by the previous works. Flow rates, pressure fields and pump membrane deflections of a piezoelectric micropump are investigated for pumping mediums consisting of acetone, methanol, ethanol, water, and two hypothetical fluids.

Valveless piezoelectric micropumps can pump any sample in biology and biochemistry fields [85]. The generated flow rate and backpressure characteristics of micropumps depend on the properties of working fluid. Previous works on piezoelectric micropumps considered water [48, 53, 64, 80, 82, 83, 88, 95, 125-129], air [125, 129], ethanol [53, 130, 131], insulin [50] , methanol [127], glucose solutions [51] and blood

[132] as working fluids. Comparison of the pumping characteristics of the micropumps operating with different working fluids has not been investigated extensively by the previous works. Flow rates, pressure fields and pump membrane deflections of a piezoelectric micropump are investigated for six different working fluids. The pumping medium consists of acetone, methanol, ethanol, water, and two hypothetical fluids in the present study.

10.2 Geometry and Volume Conditions

10.2.1 Schematic of the Problem Geometry

Flows generated by piezoelectric valveless micropump is modeled in a microchannel (Figures 10.1a-c) using mechanical equations of motion for the solids, the electromagnetic field equations for the actuator and mass/momentum conservation equations for the fluid. Valveless micropump consists of trapezoidal prism (outlet/inlet) elements; pump chamber, a thin structural layer and a piezoelectric element as the actuator (Figure 10.1a). 'diffuser/nozzle' term was not used to define the outlet/inlet geometries because of alternating (subsonic) flow directions over one cycle. The selected problem geometry is similar to the one reported in the experimental study [124]. The three-dimensional (x-y-z) geometry used in the present study considers a single pump with rectangular prism shaped Pyrex 7740 Borosilicate glass (structural layer) – PZT-5A (piezoelectric element) bi-layer membrane and pump chamber whereas the experimental geometry in [124] is cylindrical and comprises of two parallel pumps. Front, top and side views of pump are given in Figures 10.1a, b and c, respectively.

Pumps considered in the present work are made of Pyrex 7740 borosilicate glass structural layer and PZT-5A piezoelectric element. The length (L) and the width of the pump chamber is 6000.0 µm. Length and the width of the piezoelectric element is 3800.0 µm. The depths (D_f) of the (undeformed) pump chamber and the trapezoidal prism inlet/outlet are 80.0 µm. Depth of the structural layer (D_{str}), Pyrex 7740 borosilicate glass is 500.0 µm and the depth of the piezoelectric element (D_{piezo}), PZT-5A is 200.0 µm. The inlet/outlet lengths are each 1.1 mm. The width of the narrowest part is 80.0 µm for both the trapezoidal prism inlet and outlet, and the divergence and convergence angles are both 9.8º. Divergence and convergence angles are determined using [124].

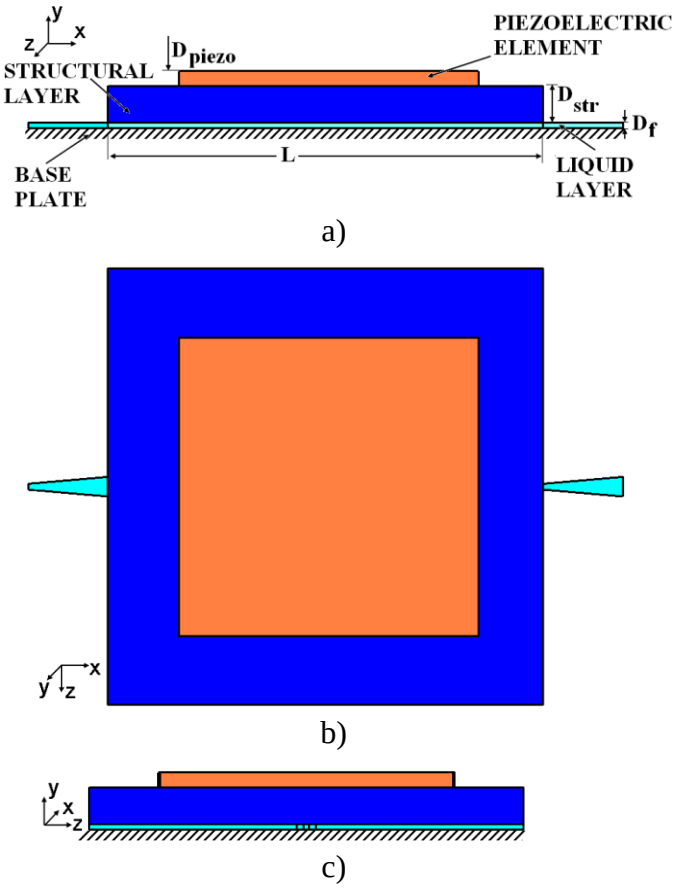

Figure 10.1 Piezoelectric valveless micropump geometry considered. a) front view b) top view c) side view.

When the piezoelectric element PZT-5A *(PZT: particulate (lead) zirconate titanate)* located in between two electrodes is electrified the bi-layer membrane moves up or down for the piezoelectric micropump. A sinusoidal voltage signal is applied at the input electrodes, which by the converse piezoelectric effect is converted to mechanical perturbations on the surface. When the pump structural layer moves to increase the volume of the pump chamber, the fluid is pushed into the pump across the inlet and the outlet. The pump is in the supply phase. If the flow resistance in the inlet direction is higher than that in the outlet direction, more fluid flows into the pump chamber through the inlet. When the pump structural layer moves to decrease the volume of the pump chamber, the pump is in the pumping phase. More fluid goes out of the pump through the outlet; hence, the net fluid transport from the inlet to the outlet is achieved. The piezoelectric valveless micropump device configuration adopted in this study has a thin film bulk acoustic resonator (FBAR) structure. Figures 10.1a-c shows that the valveless micropump consists of trapezoidal prism inlet/outlet elements and the pump chamber (bottom layer); one thin structural layer (middle layer) and one piezoelectric element (top layer) as the actuator.

10.2.2 Material and Working Fluid Properties

Material properties and the working fluid properties considered are listed in this section. Piezoelectric element is PZT-5A and pump structural layer comprises of Pyrex 7740 Borosilicate glass. The material data is provided following the conventional IEEE standards on piezoelectricity [106]. Material properties are kept constant for all calculations. The density ρ, piezoelectric stress constant (e), permittivity ε and the elasticity matrix c of PZT-5A are given in section 9.4.2.

Glass [133]:

Material properties of Pyrex 7740 borosilicate glass are density $\rho = 2230.0\ kg/m^3$, Young's modulus $E = 62.75 \times 10^9\ Pa$ and Poisson's ratio $\upsilon = 0.2$.

Working fluid [64, 134]:

The pumping medium consists of acetone, methanol, ethanol, water, and two hypothetical fluids in the present study. The hypothetical fluids have the same density and speed of sound as ethanol but different kinematic viscosities. Density, speed of sound in working fluid and kinematic viscosity of the working fluids are listed in Table 10.1.

Table 10.1 List of the fluid properties

Fluid	**Density, ρ (kg/m^3)**	**Kinematic Viscosity, υ (m^2/s) x10^{-6}**	**Speed of sound, c_s (m/s)**
Hypothetical fluid 1	790.0	0.20	1207.0
Acetone [134]	790.0	0.41	1174.0
Methanol [134]	791.8	0.75	1130.0
Ethanol [134]	790.0	1.52	1207.0
Water [64]	997.0	1.04	1480.0
Hypothetical fluid 2	790.0	15.2	1207.0

10.3 Boundary and Initial Conditions

The boundary conditions for the dependent variables need to be specified for the problem geometry (Figures 10.1a-c) considered. A symmetric model along the z = 0.0 μm plane is considered. All boundary conditions specified on the z = 0.0 μm plane are

hence of symmetric kind. Along the walls of the fluid model, zero slip boundary conditions are used for velocity. In the present work, the pressure boundary conditions similar to [53, 64, 80, 88] are employed. Zero pressure is specified along the inlet (left boundary in Figure 10.1b) and a back-pressure (P_b) is specified along the outlet (right boundary in Figure 10.1b). Density along the inlet and outlet boundaries is specified using the equation of state (equation 3.22) and the specified pressure boundary conditions. The pressure boundary conditions include the effect of pumping resistance seen by the pump.

Three sides and the top surface of the piezoelectric element are traction (stress) free. Bottom of the element is coupled to the structural layer by transferring loads between structural layer and piezoelectric materials. Back side of the structural layer is considered to be clamped. Two sides (left and right boundaries in Figure 10.1b) and the top surface (the exposed regions, shown in blue in Figure 10.1b) of the structural layer are traction (stress) free. Bottom of the structural layer is the fluid structure interface. Structural layer is coupled to liquid layer by the principle of continuity of stresses along the interface between the fluid and solid region. Loads are calculated iteratively and transferred in between fluid and solid domains until the equilibrium condition of stresses is satisfied. Side and bottom surfaces of the micropump (volume occupied by the working fluid) are silicon. Silicon is considered as perfectly rigid. Boundary conditions of electrical variables are as follows: the sides of all three layers are insulated and the piezoelectric element is grounded at its top surface. Two electrodes are patterned on the top and the bottom surfaces of the piezoelectric substrate and electrodes fully cover the

surfaces. Sinusoidal voltage is applied along the bottom of the piezoelectric element according to:

$$\phi = 0.5V_{p-p}\sin(2\pi ft+\theta) \qquad (10.1)$$

where φ is the electric potential (V), V_{p-p} is the magnitude of electric potential (peak to peak), f is the cyclic frequency (Hz) and θ is the phase angle of the input signal. The fluid is initially quiescent and the pressure is atmospheric and all dependent variables are zero for the pump operation under zero back-pressure. In order to consider a realistic initial condition and to eliminate immediate water hammer effects the back-pressure is gradually applied on the micropump. Under non-zero back-pressure (P_b = 4.45 kPa, 8.9 kPa and 17.8 kPa) operation, the simulations are performed with all dependent variables initially zero (P_b = 0.0 kPa case). 10.0 perturbation cycles later backpressure is increased to P_b = 4.45 kPa, instantaneous velocity is stored for another 10.0 successive cycles. At the 20^{th} perturbation cycle back-pressure is set to 8.9 kPa and velocity data is stored for another 10 cycles and for P_b = 17.8 kPa the same procedure is repeated.

10.4 Results and Discussion

A mechanical micropump is considered including fluidic diodes (inlet/outlet elements) to direct the fluid flow (Figures 10.1a-c). Fluidic diodes have different flow resistances when the direction of the flow through the device is reversed. For a reciprocating flow through inlet/outlet elements and pump chamber, the micropump performs the function of generating net flow in the positive direction. Reciprocating flow is generated by the cyclic deformations of a piezoelectric element in the present study.

Force and displacement fields are coupled in two ways between the fluid and the structure (glass and piezoelectric element).

Table 10.2 lists the cases considered in the present study. In cases 1 thru 4, the parameters are chosen from the experimental conditions used in [124].

Table 10.2 List of the cases considered with a three-dimensional model of piezoelectric micropumps

Case	**Freq. (Hz)**	**Voltage (V)**	**Back-pressure, P_b (kPa)**	**Working Fluid**
1	2000.0	200.0	0.0	Water
2	2000.0	200.0	4.45	Water
3	2000.0	200.0	8.9	Water
4	2000.0	200.0	17.8	Water
5	1500.0	200.0	0.0	Water
6	3350.0	200.0	0.0	Water
7	4300.0	200.0	0.0	Water
8	3350.0	150.0	0.0	Water
9	3350.0	175.0	0.0	Water
10	2000.0	200.0	0.0	Hyp. fluid 1
11	2000.0	200.0	0.0	Acetone
12	2000.0	200.0	0.0	Methanol
13	2000.0	200.0	0.0	Ethanol
14	2000.0	200.0	0.0	Hyp. fluid 2

Single chamber micropump (Figures 10.1a-c) operated under back-pressures (P_b) of 0.0 kPa, 4.45 kPa, 8.9 kPa and 17.8 kPa are investigated in cases 1-4 (V_{p-p} = 200.0 V and f = 2000.0 Hz, see equation (10.1) for the definition of V_{p-p}). First four cases are chosen to investigate how the predictions by the present work and [124] differ. In case 5 (Table 10.2), the frequency of the perturbations is decreased slightly (f = 1500.0 Hz) at

the same excitation voltage (V_{p-p} = 200.0 V). The frequency of the perturbations is f = 3350.0 Hz and 4300.0 Hz in cases 6 - 7, respectively. The goal of cases 1, 5 - 7 are to investigate dependence of flow rate to the actuation frequency. In cases 6, 8 and 9 (Table 10.2), the excitation voltage is varied (V_{p-p} = 150.0 V - 200.0 V) at the same actuation frequency (f = 3350.0 V). By varying only excitation voltage, dependence of the flow rate to the electric potential is isolated in cases 6, 8 and 9. In cases 5 thru 9, flow rate is at its maximum (P_b = 0.0 kPa) under the given conditions. Seven simulations are performed to observe the effect of actuation frequency and back-pressure on the time-averaged velocity (cases 1 - 7). Three simulations are investigated to observe the effect of excitation voltage (cases 6, 8 and 9). In cases 1 - 9, working fluid is water. Working fluids of acetone, methanol, ethanol, and two hypothetical fluids are considered in cases 10 thru 14. The goal of cases 1, 10 - 14 are to investigate dependence of flow rate to the working fluid. For cases 1, 10 - 14 actuation frequency f of 2000.0 Hz and excitation voltage V_{p-p} of 200.0 V are considered.

10.4.1 Acoustically Driven Flows in Micropump: Quasi-periodic State

Instantaneous flowfields are shown in Figures 10.2a - d (case 1) at the beginning of 10^{th} cycle, one-third cycle later, two-third cycle later and at the beginning of the 11^{th} cycle (case 2) respectively. Velocity vectors of water are plotted over the z = 0 mm plane. Comparing the velocity fields in Figures 10.2a and 10.2d, quasi-steady behavior of the flow field is observed. When estimated velocity differences between subsequent cycles for all the calculated points are observed to be less than the specified convergence criteria ($\eta = \frac{\bar{u}_{f,j+1} - \bar{u}_{f,j}}{\bar{u}_{f,j}} \leq 0.01$), the flow-field is assumed to be quasi-steady.

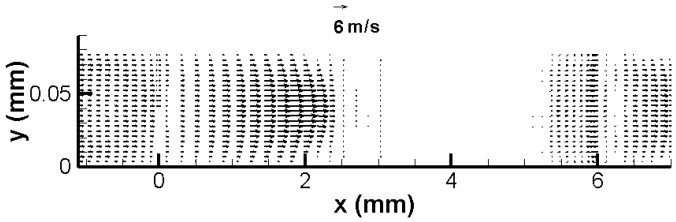

a)

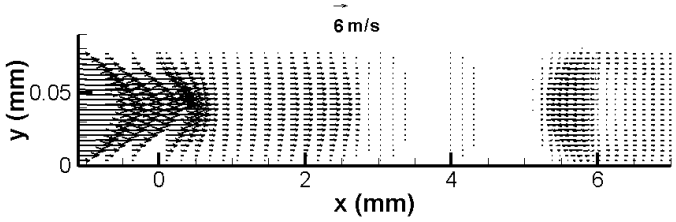

b)

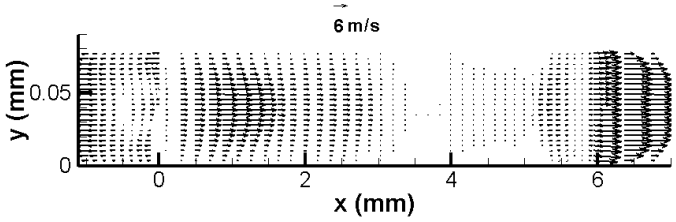

c)

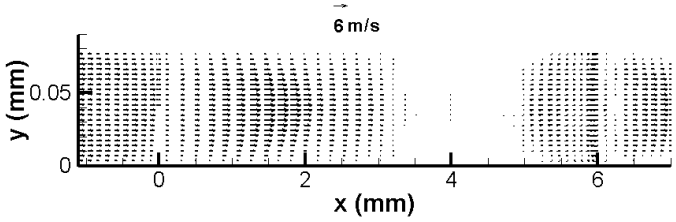

d)

Figure 10.2 Vectors of fluid velocity in water at the 10^{th} cycle, case 1, z = 0.0 mm a) at the beginning of 10^{th} cycle b) one third of a cycle later c) two thirds of a cycle later d) at the beginning of 11^{th} cycle; f = 2000.0 Hz, V_{p-p} = 200.0 V and P_b = 0.0 kPa.

In Figures 10.3a-c time-dependent volumetric water flow rates through the outlet of the micropump are shown during the 10^{th} cycle. During the supply mode the

instantaneous flow rate is positive (flow is into the pump chamber) and during the pump mode it is negative (flow is out of the pump chamber). Instantaneous velocities are integrated over the outlet area at each time step during one perturbation cycle in the present study.

In Figure 10.3a, the temporal variations of flow rates through the outlet of the micropump are shown during the 10^{th} cycle for various values of the pumping backpressure for cases 1 – 4 (Table 10.2). Backpressure (P_b) is varied (0.0 kPa - 17.8 kPa) while f = 2000.0 Hz and V_{p-p} = 200.0 V are kept constant for the flow of water. The deflection of the pump membrane attenuates yielding to reduced flow rates produced by the micropump at higher values of the backpressure. In Figure 10.3b, time-dependent volumetric water flow rates are shown for various values of the actuation frequency (Table 10.2:cases 1, 5 – 7) along the outlet. In cases 1, 5-7 back-pressure seen by the pump (P_b = 0.0kPa) and excitation voltage (V_{p-p} = 200.0 V) are kept constant. The present fluid-solid system (Figures 10.1a-c) shows optimum performance (highest flow rate) at the actuation frequency of 2000.0 Hz. The flow rate increases with the increase of actuation frequency (below 2000.0 Hz) then it drops with frequency (Figure 10.3b). Figure 10.3c shows temporal variation of water flow rates for various excitation voltages in the micropump over the outlet for cases 6, 8 and 9 (Table 10.2). Actuation frequency is kept constant at 3350.0 Hz and P_b at 0.0 kPa while varying peak to peak excitation voltages between 150.0 V – 200.0 V are considered. The generated flow increases by the increase of the driving electrical potential. At excitation voltage above 200.0 V (for an excitation frequency of 3350.0 Hz) the pressure in the pump attained values less than the vapor pressure at the given temperature (leading to cavitation).

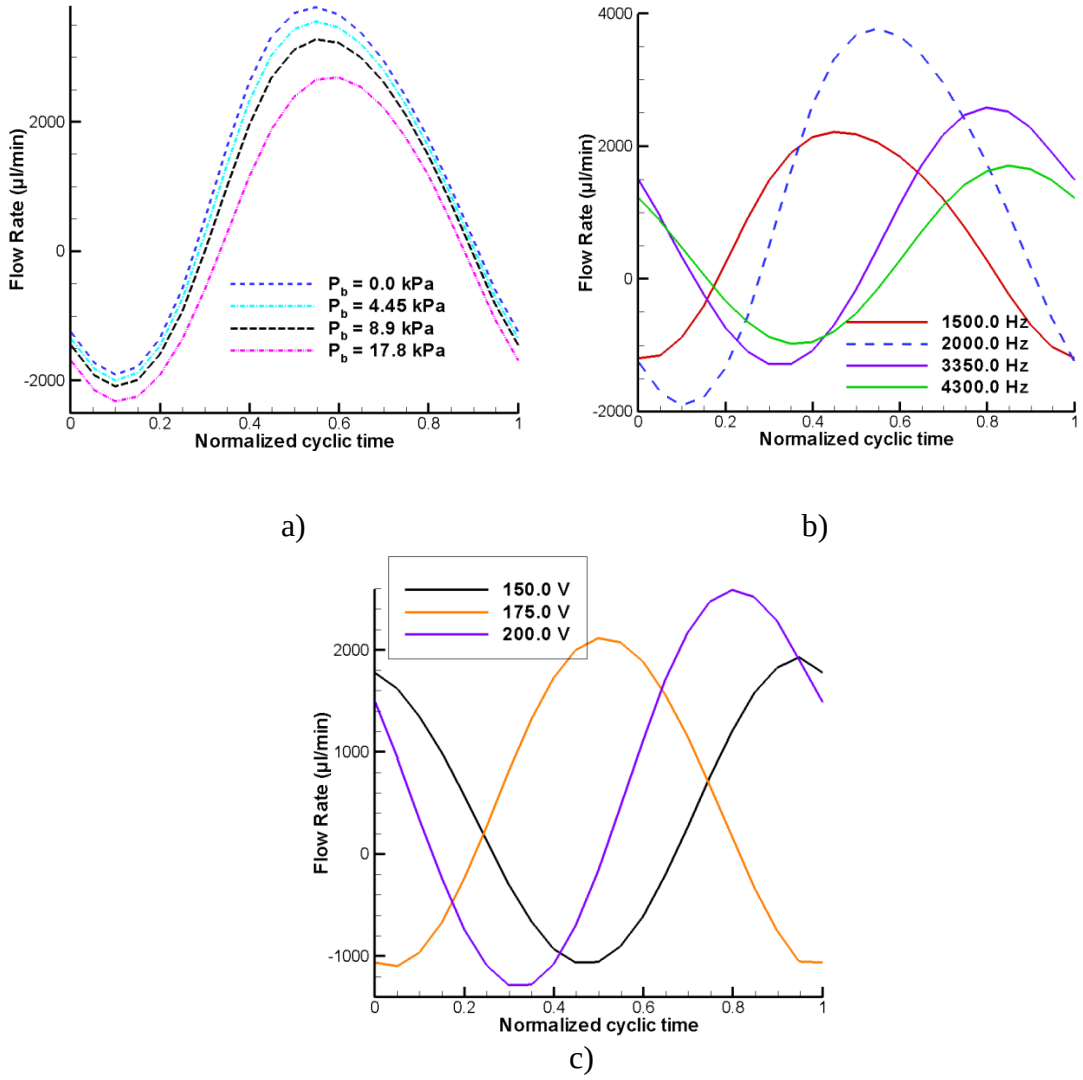

Figure 10.3 Time-dependent flow rates of water during the 10th cycle and x= 7.1mm (over the outlet). a) effect of backpressure P_b = 0.0 kPa - 17.8 kPa. f = 2000.0 Hz and V_{p-p} = 200.0 V. (cases 1 - 4). b) effect of actuation frequency f = 1500.0 Hz - 4300.0 Hz. V_{p-p} = 200.0 V and P_b = 0.0 kPa (cases 1, 5-7). c) effect of excitation voltage V_{p-p} = 150.0 V - 200.0 V. f = 3350.0 Hz, and P_b = 0.0 kPa. (cases 6, 8 and 9).

In Figure 10.4, time-dependent volumetric flow rates are shown for various working fluids (Table 10.2:cases 1, 10 – 14) along the outlet. In cases 1, 10-14 frequency (f = 2000.0 Hz), pump back-pressure (P_b = 0.0kPa) and excitation voltage (V_{p-p} = 200.0 V) are kept constant while acetone, methanol, ethanol, water, and two hypothetical fluids are considered as working fluids. For the fluids with lower kinematic viscosity (relatively

lower dynamic viscosity over density ratio) the inertial forces become stronger comparing to viscous forces. In lower kinematic viscosity fluids (hypothetical fluid 1, acetone and methanol for example), wall perturbation attenuates weakly in the bulk of the flow yielding to stronger flow rate fluctuations as shown Figure 10.4. Forward and backward flows have similar time-dependent flow rates within a perturbation cycle in low viscosity fluids and highly viscous fluids. In low viscosity fluids and highly viscous fluids, similar forward and backward flow rates diminish the pumping performance of the piezoelectric micropump yielding to a low net flow rate.

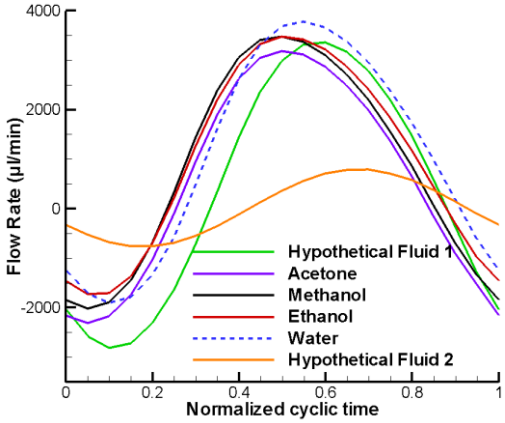

Figure 10.4 Effect of working fluid on the time-dependent flow rates during the 10th cycle and x= 7.1mm (over the outlet). f = 2000.0 Hz, V_{p-p} = 200.0 V and P_b = 0.0 kPa (cases 1, 10-14).

The instantaneous pressure field (case 1) along the horizontal mid plane of the water layers (y = 40.0 µm plane) at the end of the 10th cycle in the micropump, t = 5.0 msec is shown in Figure 10.5. The deflection of the PZT-5A and glass bi-layer membrane generates suction or discharge within the fluid. The resistance to flow is different at the

inlet from that at the outlet. The pressure is asymmetric with respect to the vertical mid-plane of the device. This asymmetry is the driving force that leads to a net flow in the investigated micropump. Our simulation results indicate that the extent of suction or discharge pressures increases or decreases with increasing distance from the center of the device depending on the phase that the system goes through in an actuation cycle. The generated pressure at the device surface also grows or decays (depending on the phase of the cycle) with distance from the center of the membrane.

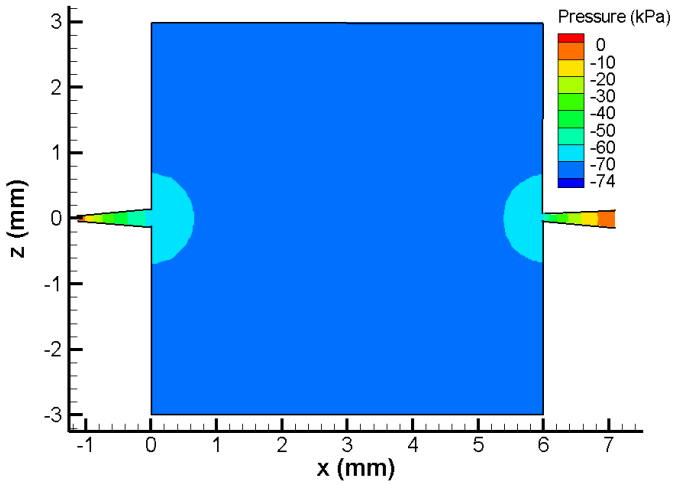

Figure 10.5 Instantaneous gauge pressure (Pa) generated in water by the oscillating membrane as a result of the asymmetry in the flow domain at the end of 10^{th} cycle. y = 40.0 µm, t = 5.0 msec, f = 2000.0 Hz, V_{p-p} = 200.0 V and P_b = 0.0 kPa (case 1).

The variation of design parameters such as applied electric potential, actuation frequency and geometric variables (the thickness of the glass layer and piezoelectric elements, inlet/outlet lengths and divergence angles) could help generate sufficient pressure field along the entire length of the pump. It may also facilitate mixing of species

that are otherwise molecular diffusion limited. Varying phase angle of the input electrical signal (θ) and operating more than one micropump in series or parallel are other methods to optimize fluctuations in flow rates and pressure [63]. The instantaneous pressure field changes with time within a perturbation cycle. For the flows with acoustic excitations the energy dissipated by the oscillating wall is not only attenuated by the inertia and viscosity of the fluid, it is also attenuated through the density variations (density variations cause variations in pressure). Hence the compressibility of the working fluid is considered in the present work.

Figure 10.6 shows the x-variation of liquid (water) velocity along the intersection of y = 40.0 μm and z = 1000.0 μm planes at different time levels (4 consecutive phases within a cycle) for case 1.

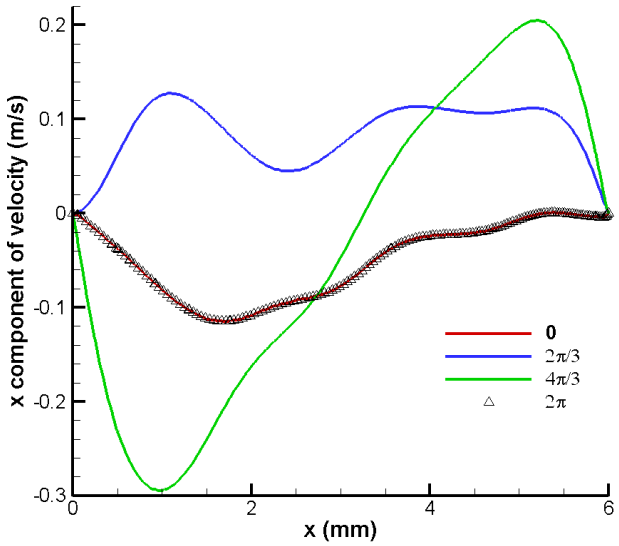

Figure 10.6 Instantaneous axial velocity profiles of water along the x-axis. Plot is along the axial direction of the channel. y= 40.0 μm, z = 1000.0 μm, f = 2000.0 Hz, V_{p-p} = 200.0 V and P_b = 0.0 kPa (case 1). Each line corresponds to a different time in the 10^{th} cycle.

The flow is generated by the up and down motion (y direction) of the interface boundary. In the valveless micropump, as the boundary is oscillating with time, it is expected that the fluid will also oscillate in the y direction in time with a specific frequency. Individual curves in Figure 10.6 can be explained with a comparison to the well-established driven cavity problem. The flow resistances in inlet and outlet elements are not the same in the present work. If the difference in flow resistances in outlet and inlet were not present (as it can be observed in driven cavity problem), curves at phase angles of $2\pi/3$ and $4\pi/3$ would have been identical (with a change of sign). The area under individual curves are not the same (Figure 10.6) in the present valveless piezoelectric micropump. Hence, the device results in net flow. Same effect can also be seen in Figures 10.2a-d. Comparing the velocity fields in Figure 10.6 at phase angles 0 and 2π, quasi-steady behavior of the flow field is observed.

10.4.2 Displacement and Stress Field Predictions of the Structural Model

The instantaneous solid domain y-component normal stress and liquid (water) domain pressure variations are plotted in Figure 10.7 along the y-axis over the z = 25.0 μm plane at t = 5.0 msec for selected constant x lines (case 1). At y = 80.0 μm, we have the fluid-structure interface. The match of pressure and normal stress at y = 80.0 μm and y =580.0 μm (Pyrex glass, PZT-5A interface) guarantees that the two way coupling is performed satisfactorily (see section 9.2). The thickness of the viscous boundary layer [17], β^{-1} is found to be 12.88 μm where $\beta^{-1} = \sqrt{\frac{2\mu}{\rho\omega}}$. ω is the angular frequency, μ is the dynamic viscosity and ρ is the density of the fluid. Dynamic viscosity is defined as $\mu = \upsilon\rho$ where υ is the kinematic viscosity. The magnitude of stress decays away from

the liquid solid interface since the top boundary of the device (top of the PZT-5A) is free to deflect.

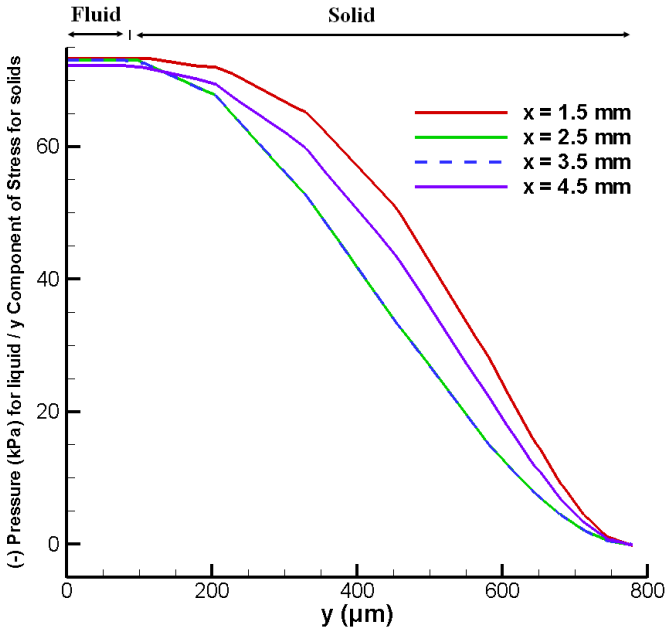

Figure 10.7 Pressure variations for solid and liquid (water) domains along the y-axis at t = 5.0 msec for selected constant x lines. z = 25.0 µm, f=2000.0 Hz, V_{p-p} = 200.0 V and P_b = 0.0 kPa (case 1).

In Figures 10.8a-c, contours of instantaneous displacement in y direction (u_y) along the interface between solid and water layers (over y = 80.0 µm plane) are shown at the beginning of 10^{th} cycle, one-third cycle later and two-thirds cycle later (case 1, f = 2000.0 Hz and V_{p-p} = 200.0 V).

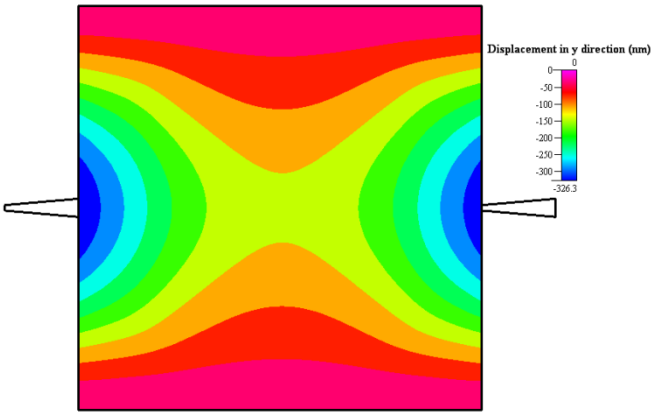

a)

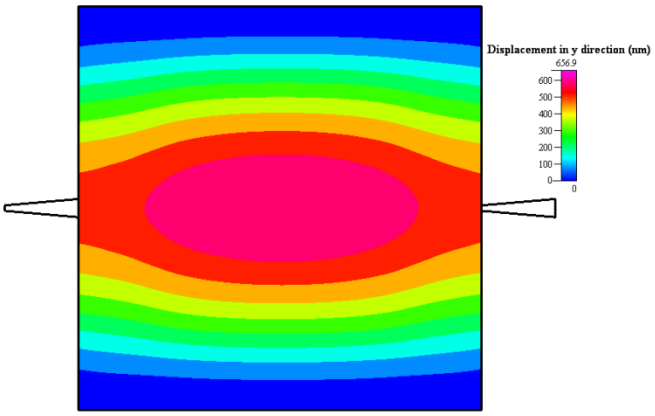

b)

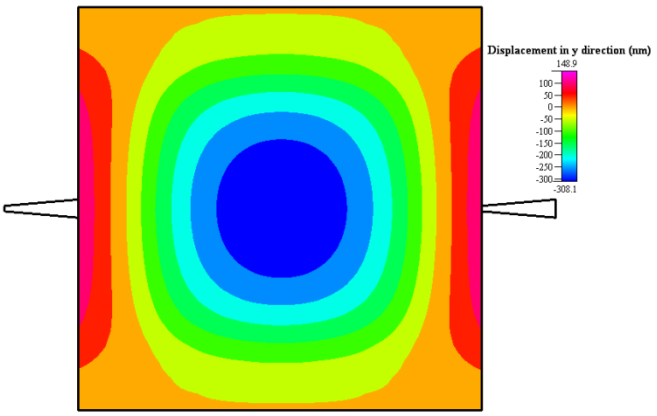

c)

Figure 10.8 Contours of displacement in y direction along the interface between solid and fluid (water) layers a) at the beginning of 10^{th} cycle b) at one third of a cycle later c) at two thirds of a cycle later. y = 80.0 μm, f = 2000.0 Hz, V_{p-p} = 200.0 V and P_b = 0.0 kPa (case 1).

The bi-layer membrane deflects in a complicated shape (solid domains are wavy in Figure 10.8a) and two peaks appear at f = 2000.0 Hz at the beginning of 10^{th} cycle. Different actuating frequencies induce different deflection shapes; hence it affects the pumping rate. When the actuating frequency is low, the membrane bends in one direction and it has only one peak. Contours of displacement in y direction are shown one third of a cycle later in Figure 10.8b. In Figure 10.8b solid domains bend upward (positive y) sucking fluid from the inlet and outlet. The maximum displacement in y direction is 656.9 nm at the given instant of time. Two thirds of a cycle later (Figure 10.8c) fluid-solid interface is wavy. Interface is bended upward towards the left-right sides and bended downward in the center. The maximum amplitude of displacement is observed in the center of the interface in Figure 10.8c (308.1 nm). The interface shown in Figures 10.8a – c is clamped rigidly from its front and back sides. Displacement in y direction is zero along the rigid sides of the interface plane. Along the left and right sides of the interface plane, solid layer (Pyrex glass) is free to deflect. There is water layer under the solid and fluid interface (y < 80.0 μm). Pyrex glass occupies the domain above the interface (80.0 μm <y < 580.0 μm). PZT-5A element occupies the domain 580.0 μm <y < 780.0 μm. The top of the micropump (y = 780.0 μm) is free to deflect.

10.4.3 Time-averaged Velocity Field in Micropump: Net Flow

In Figure 10.9a, the variations of the time-averaged axial component of water velocity (z-averaged) along the y coordinate are shown for various backpressure values for cases 1 – 4 at the 10^{th} cycle along the outlet (x = 7.1 mm). Backpressure (P_b) is varied (0.0 kPa - 17.8 kPa) while f = 2000.0 Hz and V_{p-p} = 200.0 V are kept constant. At high backpressures shear and normal forces imposed on the solid membranes increases. The

deflection of the pump membrane attenuates yielding to reduced flow rates produced by the micropump at higher values of the backpressure. The velocity profile over the outlet of the pump is parabolic. The velocity profiles slightly deviates from the parabolic, if the back-pressure seen by the pump is sufficiently large (Figure 10.9a, P_b = 17.8 kPa).

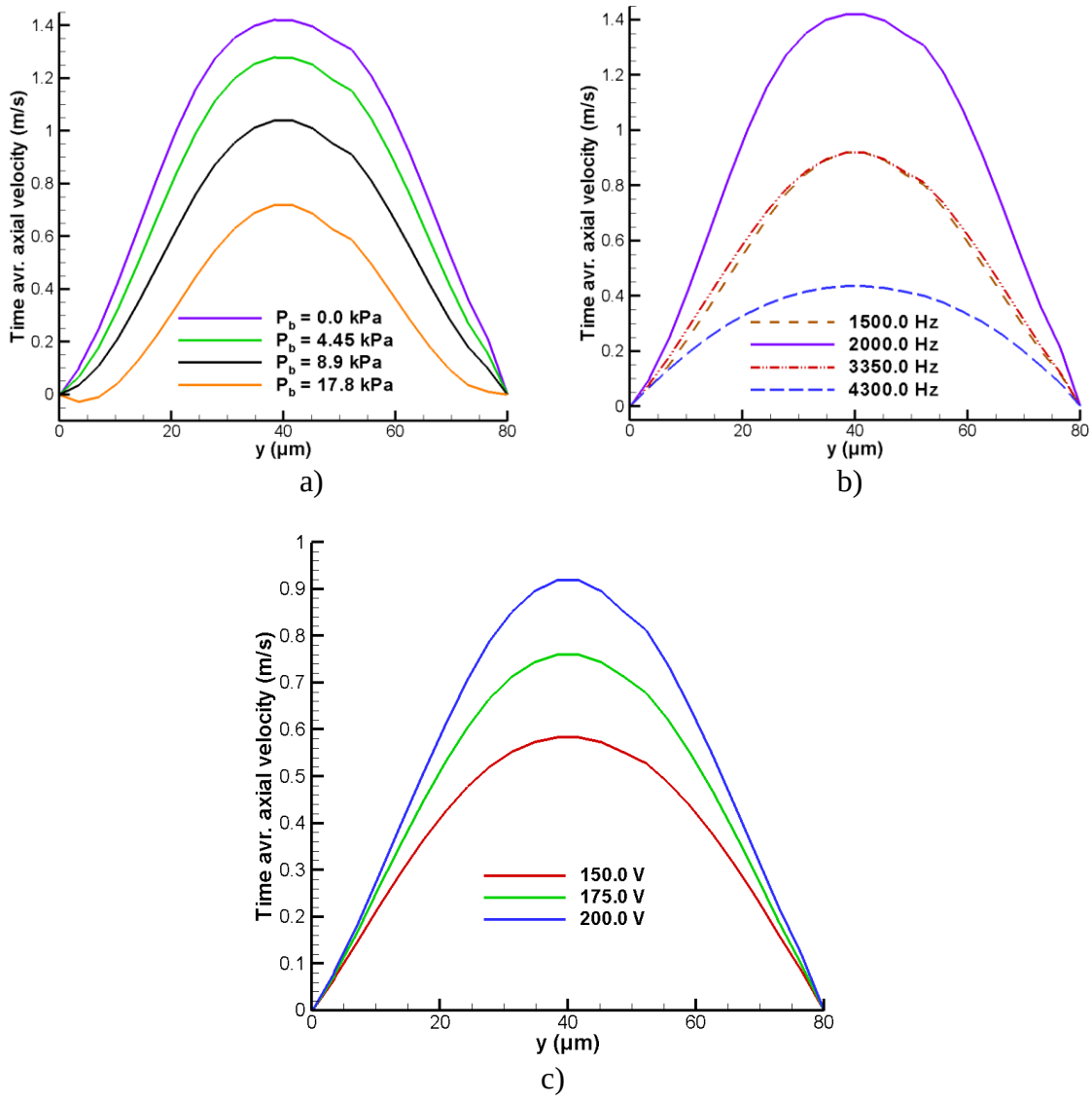

Figure 10.9 Time-averaged axial velocity of water along the y-axis. a) effect of backpressure P_b = 0.0 kPa - 17.8 kPa. f = 2000.0 Hz and V_{p-p} = 200.0 V. (cases 1 - 4). b) effect of actuation frequency f = 1500.0 Hz - 4300.0 Hz. V_{p-p} = 200.0 V and P_b = 0.0 kPa (cases 1, 5-7). c) effect of excitation voltage V_{p-p} = 150.0 V - 200.0 V. f = 3350.0 Hz, and P_b = 0.0 kPa. (cases 6, 8 and 9).

Figure 10.9b shows similar variations in water as a function of actuation frequency (cases 1, 5 – 7) and Figure 10.9c shows the variations as a function of the actuation voltage parameters (cases 6, 8 and 9). In Figure 10.9b, the variations of the x component of the time-averaged water velocity along the y coordinate are shown for various values of the actuation frequency for cases 1, 5 – 7 (Table 10.2) along the outlet. The actuation frequency (f) is varied between 1500.0 Hz and 4300.0 Hz while amplitude of excitation voltage is kept constant at 200.0 V and P_b = 0.0 kPa. The time averaged velocity increases with the increase of actuation frequency (below 2000.0 Hz) then it drops with frequency (Figure 10.9b). If the time averaged velocity is normalized by the maximum space and time averaged velocity for the case considered, the velocity profile becomes relatively flatter with the increase of actuation frequency.

Figure 10.9c shows the time-averaged axial water velocity profile as a function of the y-coordinate for various applied voltages (cases 6, 8 and 9). Actuation frequency is kept constant at 3350.0 Hz and P_b at 0.0 kPa. Amplitude of the oscillations generated by the membrane increases by the increase of the driving electrical potential. As the amplitude of the membrane deflection increases, the generated flow also increases.

Figure 10.10 shows the variations of the time-averaged axial component of fluid velocity (z-averaged) along the y coordinate similarly for various working fluids (cases 1, 10 – 14). Pumping of acetone, methanol, ethanol, water, and two hypothetical fluids are considered. The significance of oscillating flow mechanisms over viscous flow mechanisms changes with working fluid (Table 10.1). For the fluids with lower kinematic viscosity, the oscillatory forces applied on the fluid elements become stronger comparing to viscous forces causing deviation from the typical parabolic velocity profile to a flat-

like velocity profile. Net pump flow is proportional to the time-averaged velocity fields. In low viscosity fluids and highly viscous fluids amplitude of the time-averaged velocity decreases. Therefore, pump operates optimal with moderate viscosity fluids.

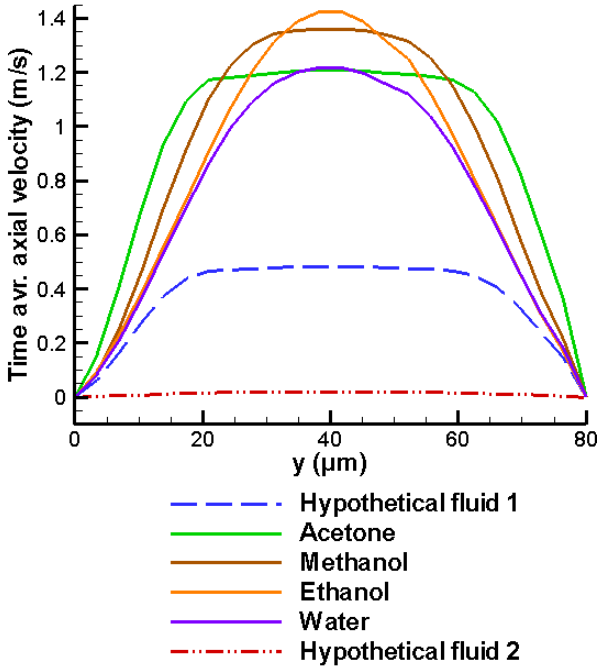

Figure 10.10 Effect of working fluid on the time-averaged axial velocity along the y-axis. x = 7.1 mm, 10^{th} cycle. The time-averaged fluid velocity is also averaged over the width (z coordinate). f = 2000.0 Hz, V_{p-p} = 200.0 V and P_b = 0.0 kPa (cases 1, 10-14).

The flow-fields developed at the inlet and outlet elements are shown in Figures 10.11a and b. The time-averaged velocity field of the inlet at a high actuation frequency (f = 4300.0 Hz) is shown in Figure 10.11a whereas Figure 10.11b shows it for the outlet for water (both for case 6). The velocity profile in the inlet (Figure 10.11a) is similar to a jet flow in a diverging passage (the cross section of the flow is diverging from the inlet through the pump chamber) where the velocity is zero along the enclosing walls.

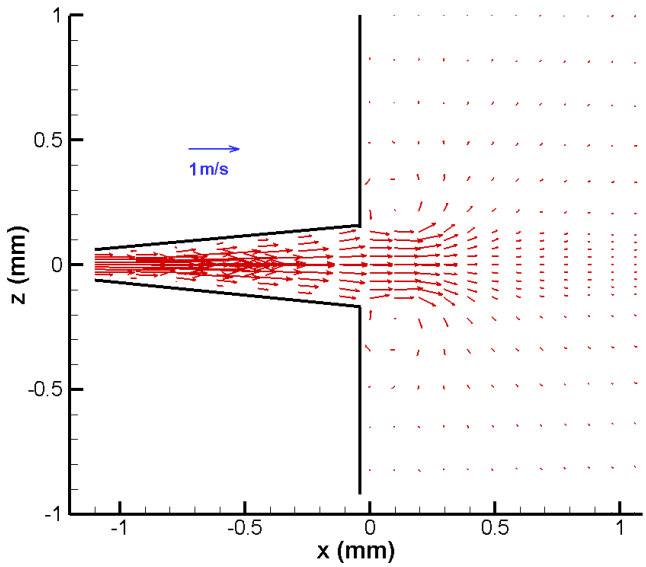

a)

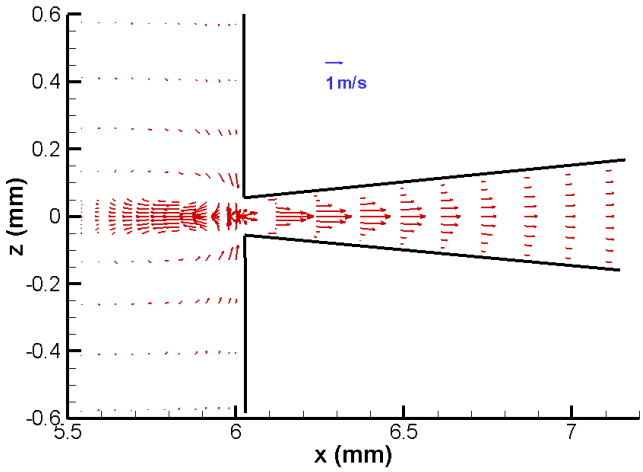

b)

Figure 10.11 Vectors of time-averaged velocity field in water along the 10th cycle. $V_{p\text{-}p}$ = 200 V, f = 4300 Hz, y = 40 µm and P_b = 0.0 kPa (case 6). a) velocity in inlet. b) velocity in outlet.

At x = 0.0 mm the cross section of the flow area changes from 0.0215 mm^2 (0.268 mm by 0.080 mm) to 0.48 mm^2 (6.0 mm by 0.080 mm). The velocity profile in the outlet (Figure 10.11b) is similar to a jet flow in a converging passage (the cross section is converging from the outlet through the pump chamber) where the velocity is zero along

the enclosing walls. At x = 6.0 mm the cross section of the flow area changes from 0.48 mm^2 (6.0 mm by 0.080 mm) to 0.0064 mm^2 (0.080 mm by 0.080 mm). Hence, the local pressure drop is drastic about x = 6.0 mm generating flow reversal. The design of the outlet can be improved to overcome this loss. The net flow is shown from inlet to outlet of the micropump via averaging velocities over time in Figures 10.11a-b.

The net flow rate developed by the pump varies with the excitation voltage and the actuation frequency. In Figure 10.12a time averaged flow rates through the outlet of the micropump are shown during the 10^{th} cycle under various actuation frequencies (f = 1500.0 Hz - 4300.0 Hz). In cases 1 and 5-7 back-pressure for the pump (P_b = 0.0kPa) and excitation voltage (V_{p-p} = 200.0 V) are kept constant. The present fluid-solid system (the geometry shown in Figures 10.1a-c) shows optimum performance (highest pumping rate) at the actuation frequency of 2000.0 Hz due to the combined effect of mechanical and fluidic capacitances, inductances, and damping. At f = 1500.0 Hz, 3350.0 Hz and 4300.0 Hz (cases 5-7), the flow rate is reduced by 31.8%, 26.5% and 59.5% comparing to the net flow of 941.0 µl/min at f = 2000.0 Hz (case 1). At frequencies below 2000 Hz, the predicted flow rate increases with actuation frequency. Time-averaged flow rate starts to drop with increase of actuation frequency above (2000.0 Hz).

In Figure 10.12b time averaged net flow rates through the outlet of the micropump are shown during the 10^{th} cycle under various excitation voltages (V_{p-p} = 150.0 V - 200.0 V). Effect of excitation voltage on flow rate is investigated while f = 3350.0 Hz and P_b = 0.0 kPa are considered in cases 6, 8 and 9. At V_{p-p} = 150.0 V and 175.0 V (cases 7-8), the flow rate is reduced by 48.3%, and 36.3% comparing to the net flow at V_{p-p} = 200.0 V. Net flow generated by the micropump increases with increasing

excitation voltage. At excitation voltage above 200.0 V (for an excitation frequency of 2000.0 Hz) the instantaneous pressure in the pump attained values less than the vapor pressure at the given temperature (leading to cavitation). Actuation frequency and excitation voltage of the micropump are limited by the presence of the cavitations in the fluid systems and structural integrity of the solid materials used for fabrication (such as fracture and aging).

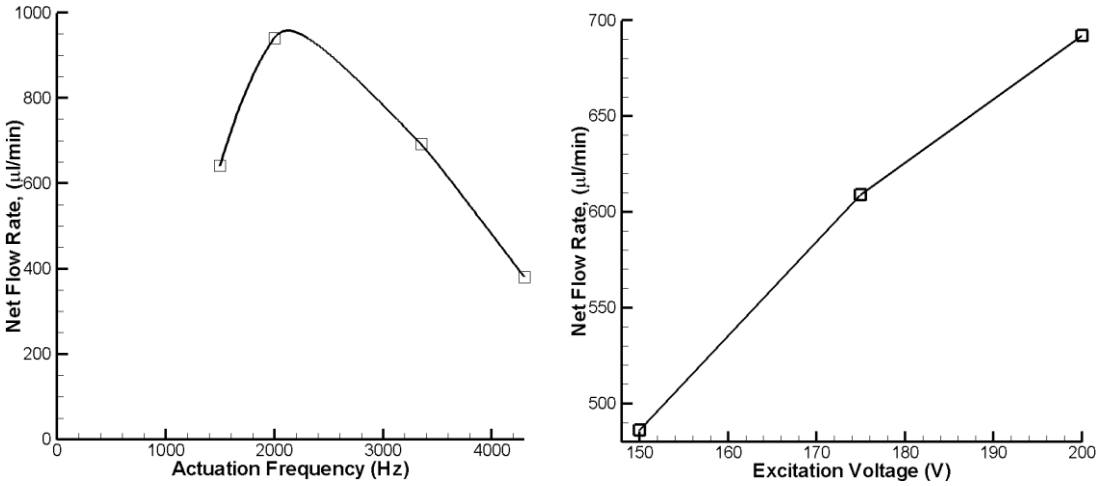

a) b)

Figure 10.12 Net flow rates during the 10th cycle and x = 7.1mm (over the outlet). a)effect of actuation frequency f = 1500.0 Hz - 4300.0 Hz. V_{p-p} = 200.0 V and P_b = 0.0 kPa (cases 1, 5-7). b) effect of excitation voltage V_{p-p} = 150.0 V - 200.0 V. f = 3350.0 Hz, and P_b = 0.0 kPa. (cases 6, 8 and 9).

The net flow rate produced by the pump varies with the working fluid. In Figure 10.13 time averaged flow rates through the outlet of the micropump are shown during the 10th cycle for various working fluids considered for pumping (acetone, methanol, ethanol, water, and two hypothetical fluids). Along the x and y axes, kinematic viscosity (in common logarithm scale) and net flow rates are shown respectively in Figure 10.13.

Considered hypothetical fluids have density and speed of sound (in working fluid) similar to ethanol but they have different viscosities. Frequency (f = 2000.0 Hz), back-pressure for the pump (P_b = 0.0 kPa) and excitation voltage (V_{p-p} = 200.0 V) are kept constant in cases 1, 10-14. The present fluid-solid system (the geometry shown in Figures 10.1a-c) shows highest pumping rate with methanol. Acetone, methanol, ethanol and investigated hypothetical fluids have similar densities and speeds of sound in these fluids are similar (Table 10.1). The kinematic viscosities of these fluids mostly cause the differences in net flow rates. Pump net flow increases with kinematic viscosity of the fluid up to a critical value, then decreases with further increase of kinematic viscosity. The pump gives the maximum pump flow with the optimum viscosity fluid (methanol). Net flow generated in water slightly deviates from other flow rate estimates because both density and speed of sound in water are approximately 25.0% greater than other fluids considered.

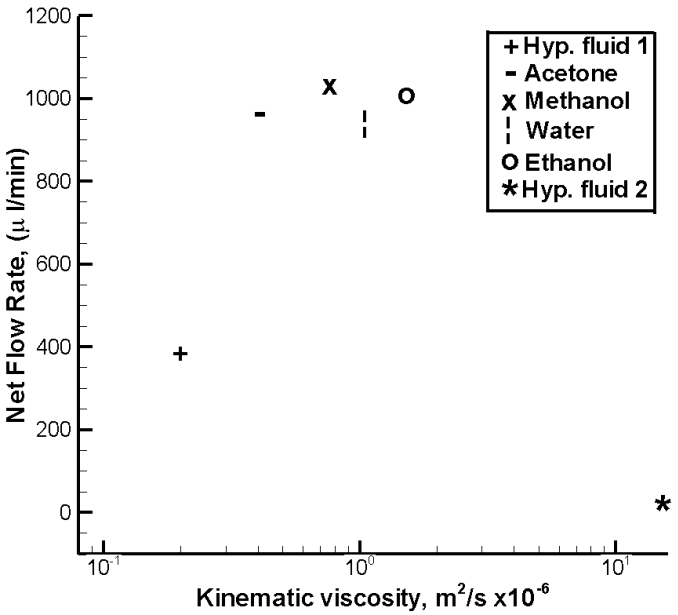

Figure 10.13 Net flow rates for various working fluids during the 10^{th} cycle and x = 7.1mm (over the outlet). f = 2000.0 Hz, V_{p-p} = 200.0 V and P_b = 0.0 kPa (cases 1, 10-14).

10.4.4 Validation of the Model

The valveless piezoelectric micropump problem geometry (Figures 10.1a-c) considered is similar to the one reported in the experimental study [124]. In Figure 10.14 time averaged flow rates through the outlet of the micropump are shown for the present study and [124]. Flow rates of water are reported during the 10^{th} cycle under various back-pressures (Table 10.2: cases 1 thru 4, P_b = 0.0 kPa - 17.8kPa) in Figure 10.14.

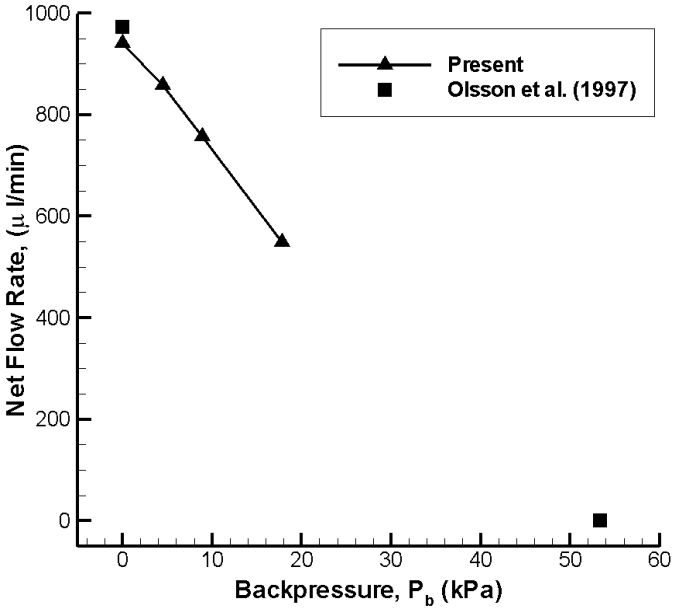

Figure 10.14 Net (time-averaged) flow rates of water during the 10^{th} cycle. f = 2000.0 Hz and V_{p-p} = 200.0 V, x = 7.1mm (over the outlet), cases 1-4.

The excitation voltage and actuation frequency are kept constant as V_{p-p} = 200.0 V and f = 2000.0 Hz. For a single chamber micropump the average flow rate is predicted as 941.0 μl/min (case 1, P_b = 0.0 kPa) according to our three dimensional calculations. Flow rate for piezoelectric double chamber micropump operated in anti-phase mode is

experimentally measured and reported in [124]. Reported [124] flow rate for single chamber micropump is 973.0 µl/min (half of the flow rate for double chamber micropump as suggested in [81]). The coupled multifield model results agree well with the results of [124] where the difference in flow rate prediction is about 3% at P_b = 0.0 kPa. Deflection amplitude of the structural-piezoelectric layers is 0.657 µm in the present work. [124] reports deflection amplitude as 0.64 µm where the difference to present prediction is 2.6%. Increase of back-pressure by 4.45 kPa reduced the flow rate by 8.8% ,flow rate reduced by 19.55% at a back-pressure of P_b = 8.9 kPa and 41.8% at P_b = 17.8 kPa comparing to the net flow at zero back-pressure (941.0 µl/min). Instantaneous velocities are integrated over the outlet area at each time step during one perturbation cycle. Net flow rate is estimated time averaging the instantaneous flow rates over one cycle.

10.5 Summary and Conclusions

The flow fields generated in a piezoelectric micropump by a thin film bulk acoustic resonator are presented considering electrical, mechanical and fluidic fields. The difference in flow resistance due to flow contraction and expansion (through an inlet and an outlet respectively) generates net fluid flow as the bi-layer structural-piezoelectric membrane deflects up and down continuously. The compressibility of the liquid is considered with an isothermal equation of state. The model predictions are compared with results available in the literature [124]. Although, previous investigations [48, 49, 52, 53, 56, 64, 88] considered instantaneous flow rates albeit considering incompressible flow formulation, the net flow generated by the device can be better evaluated by averaging velocity field over sufficient number of perturbation cycles. Instantaneous

velocities are predicted at each time step and the results are time-averaged to get the net flow rates.

The micropumps are made of Pyrex 7740 borosilicate glass structural layer and PZT-5A piezoelectric element. The length and the width of the pump chamber is 6000.0 μm. The length and the width of the piezoelectric element is 3800.0 μm. Total thickness of the square-shaped micropump is 780.0 μm. The present fluid-solid system with the above geometry shows optimum performance (highest pumping rate) at the actuation frequency of 2000.0 Hz (at an excitation voltage V_{p-p} of 200.0 V) due to the combined effect of mechanical and fluidic capacitances, inductances, and damping. At excitation voltage above 200.0 V (for an excitation frequency of 3350.0 Hz) the instantaneous pressure in the pump attained values less than the vapor pressure at the given temperature (leading to cavitation). At frequencies below 2000.0 Hz, the predicted flow rate increases with actuation frequency. Time-averaged flow rate starts to drop with increase of actuation frequency above (2000.0 Hz). Actuation frequency and excitation voltage of the micropump are limited by the presence of the cavitations in the fluid systems and structural integrity of the solid materials used for fabrication (such as fracture and aging). Acetone, methanol, ethanol, water, and two hypothetical fluids are considered as working fluids. For the fluids with lower kinematic viscosity, the oscillatory forces applied on the fluid elements become stronger comparing to viscous forces causing deviation from the typical parabolic velocity profile. The pump gives the maximum flow with the optimum viscosity fluid (methanol).

The coupled model considers the deflection of solid membranes simultaneously with the prediction of fluid flow. A two-way force and displacement coupled fluid-solid interactive model considered here is superior to the past studies [94, 95] which consider a prescribed wall motion. The model predictions of the net flow rate generated by the micropump are compared to experimental results in [124]. Net flow rate results agree well with their results where the difference in flow rate prediction is about 3%. The solid bi-layer deflection results also agree with [124], where difference is 2.6%. The pressure, velocity and flow rate prediction models developed in the present study can be utilized to optimize the design of MEMS based micropumps. This paper quantitatively provides the dependence of net flow rates to the actuation frequency, excitation voltage, back-pressure and working fluid properties.

11. SUMMARY, CONCLUSIONS and FUTURE RESEARCH

Summary and conclusions of the conducted research and recommendations for future work on acoustically and electrokinetically driven transport in microfluidic devices are reported in this chapter. Developed models and completed investigations are summarized first, conclusions from the conducted research are given thereafter. Finally, future research work (related to the present investigations) directions are outlined.

11.1 Summary

Electrokinetic flows, acoustically induced flows, and electrokinetic augmentation in acoustically excited flows in microfluidic devices are addressed. Flexural plate wave devices and thin film resonators provide the acoustic excitations while electrokinetically driven flows are produced by both electroosmosis and electrophoresis. Thin film bulk acoustic resonator structures generate net flow when used with flow rectifiers in piezoelectric valveless micropumps. Electrokinetic flows through straight microchannels are also investigated. For acoustically excited flows, the present research focuses on time averaged flow fields induced by periodic perturbations of piezoelectric elements to pump and mix fluids in microchannels.

Fluid models together with elastic solid deformation models (for the channel walls) have been developed to simulate the transport of fluids in microfluidic devices. The models predict instantaneous velocity, pressure, electrical fields and stress-strain distributions for electrokinetic flows, acoustically excited flows generated by piezoelectric elements and electrokinetic augmentation in acoustically excited flows in

micro-scale systems. The developed models were found to provide accurate characteristics of the generated flows when compared to experimental measurements.

The simulations of transient multidimensional fluid transport through piezoelectric micropumps is complex which involves the interaction among fluidic, mechanical and electrical fields. Fluidic, structural and electrical field quantities are predicted via the developed models. Coupling of mechanical energy to electrical energy is considered. Developed models also involve coupling of normal and shear stresses among fluid and solid layers in dual ways. The simulations provided detailed insight into the acoustically excited flows in flexural plate wave devices and piezoelectric micropumps, electrokinetic flows and electrokinetically augmented flows in flexural plate wave micropumps. Detailed flow and transport characteristics in these high frequency micro-scale systems are difficult to obtain through direct measurements in applications. In a broader aspect the simulations have been used as a tool to understand and analyze the fluid flow and structural deformation characteristics and study the effect of different flow conditions that can lead to the design of novel micropumps and micro total analysis systems.

As the first step towards simulating flows in microchannels driven by and electrokinetics and piezoelectric elements, Poisson-Boltzmann and Nernst-Planck models were used to study fluid dynamics characteristics of electrokinetic flows. The electrokinetic flow models were used to study the effect of intensity of electrokinetic body forces on the generated fluid flow and to study the effect of ionic strength of the electrolyte solution on fluid flow. Electrokinetic flow models were studied to solve mass and momentum conservation equations (with body forces due to electrokinetic effects),

electric double layer streaming potential equation, applied electrostatic field equation and the conservation equations for the distribution of ions, and neutral species (to consider electrophoretic transport of ions). Comparison between the model predictions and experimental measurements were in favorable agreement which validated the developed models. The models were further extended to study electrokinetically augmented flows in flexural plate wave micropumps.

Compressible form of two/three-dimensional fluid mass and momentum equations were considered for simulating propagation of acoustic waves in fluids. Acoustically excited flows in flexural plate wave devices were first investigated by a moving wall model. The effect of the amplitude, frequency and the wave length of the wall motion were studied. The model was validated by comparing the predicted time-averaged velocity profile to micron resolution particle image velocimetry measurements. The model was further extended to study fluid transport in piezoelectric micropumps. The fluid mechanics models were thus coupled to solid deformation models.

Two and three-dimensional coupled fluid/solid deformation models were then developed to study flows generated by piezoelectric elements. Solid deformation models were developed for piezoelectric and non-piezoelectric domains including calculations for mechanical displacement, electric, stress and strain fields. Solid deformation/materials models were modified to include full anisotropy. Normal and shear stresses in fluid and solid fields were coupled to simulate interactions of mechanical, electrical and fluidic fields. Parametric studies were performed to investigate the effects of actuation potential and frequency, working fluid properties and pump back-pressure. The predicted piezoelectric/structural membrane deflections were compared well to the experimental

measurements. The present time-averaged (net) flow rate predictions were also validated with experimental measurements.

Electrokinetic augmentation in acoustically excited flows was also investigated with coupled electrokinetically-acoustically excited flow models. Strength of the electrokinetic body forces and actuation frequency of the acoustic motion were parametrically varied to optimize resulting velocity fields, flow rates and thermodynamic efficiencies of electrokinetically augmented flows in flexural plate wave acoustic micropumps.

11.2 Conclusions

The conclusions resulting from the present research are discussed below. These are organized according to the problems considered.

11.2.1 Electrokinetic Flows Through Microchannels

- Electrokinetic flow velocities were found to increase with the intensity of the electric fields.
- Due to the convective transport of ions, electric double layer streaming potential and pressure field predictions from the Nernst-Planck and Poisson-Boltzmann models are found to be slightly different.
- A dilute electrolyte solution yielded a parabolic velocity whereas a higher concentration electrolyte yielded a plug-like velocity profile.
- The model predictions compared well with the experimental and theoretical results available in the literature for electroosmotic flows.

- A way of determining the static pressures at the inlet and outlet of microchannels was presented.
- The velocity distribution was affected by the generated pressure field and the flow rate was reduced due to the increased dispersion.

11.2.2 Acoustically Generated Flows in Microchannel Flexural Plate Wave Sensors

- Maximum values of the generated time averaged axial velocities were found to quadratically scale ($\bar{u}_f \propto A_{max}^2$) with the acoustic wave amplitudes for a microchannel (H = 50.0 μm).
- The attenuation of the wave away from the actuator surface resulted in a decrease of the magnitude of time averaged velocity for deeper microchannels (H = 25.0 μm - 100.0 μm).
- When channel height was larger than 16.0 μm (the evanescent decay distance, γ), the velocity profiles were found to deviate from the parabolic velocity profile.
- Decrease in actuation frequency by a factor of 3 yielded a drop in time averaged velocity by a factor of 0.29 for a deep microchannel (H = 100.0 μm).
- The flowfields generated in a microchannel due to ultrasonic flexural waves were presented where the compressibility of the liquid is considered.
- The predicted time averaged velocity results in the present study compared more favorably with the measurement data compared to the previous incompressible flow model results.

11.2.3 Electroosmotic Augmentation in Flexural Plate Wave Micropumps

- The non-linear effects in combing the electroosmotic and acoustics were demonstrated. The coupled electroosmotic-FPW micropump induced a much stronger flow field than linear combination of FPW and EOF pumps.
- The time averaged axial velocity showed an attenuating wave pattern away from the actuator surface. A typical electroosmotic flow flat velocity profile was predicted adjacent to the top rigid wall.
- Based on the thermodynamic efficiency, increasing the actuation frequency of the flexural wave was found to be more efficient than increasing the intensity of electric field.
- Simulation results demonstrated that the inclusion of electrokinetic effects is more effective than increasing the intensity of acoustic perturbations whenever high flow rates are required in micromixer applications.
- The predicted velocity field showed the existence of induced vertical velocity component which can enhance mixing process significantly.

11.2.4 Stress, Strain and Displacement Fields Analyses with Solid Deformation Models

- The anisotropy in material elasticity data were clearly shown in the predictions of deformations.

11.2.5 Two Dimensional Multifield Analysis of a Piezoelectric Valveless Micropump

- The fluid-solid system showed a resonance frequency due to the combined effect of mechanical and fluidic capacitances, inductances, and damping. With the

increase of actuation frequency, the velocity profile was found to become relatively flatter.

- The flow rate increased with increasing actuation frequency (200.0 Hz to 5000.0 Hz). Then it dropped significantly with increasing frequency.
- Amplitude of the membrane deflection increased with the increase of the driving electrical potential (80.0 V – 140.0 V) at 400.0 Hz, and the generated flow also increased.
- It was found that time-averaged vectors of velocity patterns do not change significantly with increasing driving voltage.
- The solid bi-layer deflection results agreed well with the results in [88], where difference was below 2%.
- Time-averaged velocity fields were shown for the entire piezoelectric valveless micropump for the first time.

11.2.6 Piezoelectric Valveless Micropump: Development of a Three Dimensional Structural/Fluid Dynamic Model

- The present fluid-solid system can be used to obtain the optimum driving frequency for maximum pumping rate.
- At high excitation voltages the instantaneous pressure in the pump can lead to cavitation.
- Actuation frequency and excitation voltage of the micropump were found to be limited by the presence of the cavitations in the fluid systems and structural integrity of the solid materials used for fabrication (such as fracture and aging).

- Acetone, methanol, ethanol, water, and two hypothetical fluids were considered as working fluids. The pump generated the maximum flow with the optimum viscosity fluid (methanol).

11.3 Recommendations for Future Work

The present research provides insight into the different pumping principles of fluids transport through microchannels. This enabled us to analyze and optimize the flows induced by acoustic interactions, electrokinetic flows and electrokinetic augmentation in acoustically excited flows in microchannels and determine the potential applications. To further advance the knowledge in understanding flows through microfluidic devices and the applications of these devices in micro electromechanical systems the following future research work are recommended.

11.3.1 Experimental Studies on Valveless Piezoelectric Micropumps

An experimental study similar to the flat-walled valveless piezoelectric micropump outlined by Olsson et al. [124] is suggested as future work. The suggested experimental investigations can help further explore the operation of piezoelectric valveless micropumps. The measurements will complement the fluid/solid coupled piezoelectric micropump models developed in the present study. Discussions regarding the fabrication of the suggested device and measurements that can be conducted are given below:

A. Fabrication of the suggested device

A valveless piezoelectric micropump can be constructed as shown in Figure 11.1. In Figure 11.1 only flow channels and the well for the piezoelectric transducer is shown

for simplicity whereas Figure 11.2 shows the entire micropump system to be fabricated. The device is to be composed of a silicone substrate layer, on bottom which is supported with a glass plate (Figure 11.2). The silicone substrate layer consists of a 500 µm thick (100)-type silicon wafer polished on both sides. Piezoelectric layer composed of PZT-5A sits inside the well above the silicon layer (Figure 11.1).

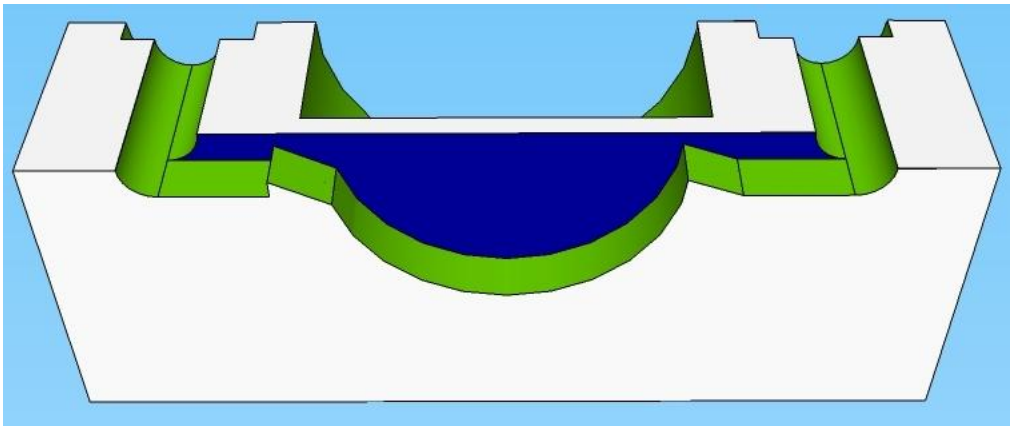

Figure 11.1 Three dimensional view of the flow channels and the silicon substrate.

Two masks are needed to define the complete pump. A thermal silicon dioxide can be grown (about 1.0 µm thick) on silicon substrate by photolithography. The silicon dioxide can then be used in the deep reactive ion etching (DRIE) process to define pump chamber and diffuser elements (to a depth of 80.0 µm approximately). The silicone layer is also to be etched from the top side so that is contains a pyramidal-shaped hole for inlet and outlet ports (Figure 11.2). Below the glass backing-plate (500 µm thick) sits a layer of aluminum plate in order to ensure a stiff silicon pump chamber bottom and facilitate easy handling of the pump.

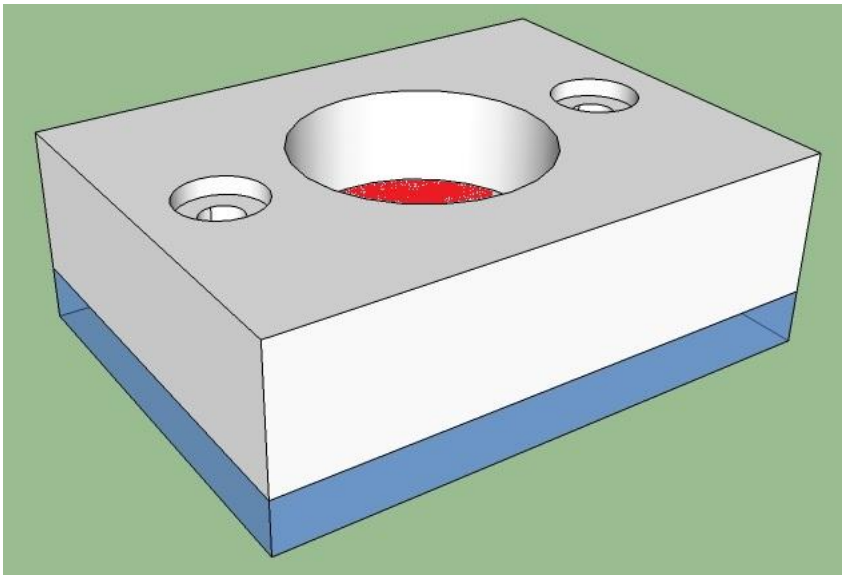

Figure 11.2 Assembled view of the silicon substrate (gray), glass backing-plate(blue) and the piezoelectric transducer (red).

The suggested dimensions of each layer are given below:

- *Silicon substrate:* Dimensions of the substrate is 15 mm by 15 mm and it is 0.5 mm thick and the flow channel is etched into it.
- *Flow channel:* Flow channel is fabricated in the silicon substrate. The depth is 80 µm and nozzle-diffuser elements and pump chamber can be defined with DRIE. The inlet-outlet ports can be etched into the silicone substrate via anisotropic potassium hydroxide and water (KOH) etching after a second oxidation and photolithography on the opposite side for defining. Tube connectors made of aluminum are glued to the inlet and outlet holes.
- *PZT piezoelectric transducer:* Transducer should be 0.15 mm to 0.2 mm thick and it should have a diameter of 3.8 mm to 6.0mm. PZT-5A and PZT-5H piezoelectric transducers could be readily found with patterned electrodes for acoustic wave actuation. Transducers can be cut to the desired diameter via laser

cutting technology and can be glued to the silicon diaphragm of the pump using a conductive epoxy material.

- *Glass backing-plate:* The glass pate should have the dimensions of 15mm by 15 mm and it is 0.5 mm thick. Probably best material to use for the fabrication of the glass backing-plate is Pyrex 7740 borosilicate glass which has a very low thermal expansion coefficient [87]. This grade of glass has good optical (relatively low refractive index of 1.474) and mechanical properties as well as good resistance to chemical and environmental damage. A borosilicate glass cover sufficiently adheres to the silicon substrate using anodic bonding in order to seal the pump cavities and diffusers.
- *Electrodes (Ti/Pt):* Electrodes for piezoelectric actuation should have a circular shape with a diameter slightly smaller than the diameter of the transducer to avoid the edge effects [135]. Typical thicknesses of the electrodes are about 2000.0 angstrom.
- *Aluminum plate:* The complete micropump can be glued on an aluminum plate for the packaging.

B. Suggested measurements

Suggested measurements are discussed below:

- *Flow field visualization/ Instantaneous velocity measurements:* Micro particle imaging velocimetry (μPIV) can be utilized for flow field visualization. This will involve the use of fluorescent polystyrene microspheres that have been seeded into the flow chamber. A flow visualization system includes a fluorescence

microscope to view the luminous microspheres. Diameters of microspheres for flow field visualization should be between 0.7 and 2.2 µm. It is noted that while this measurement is helpful in fully characterizing the flow of the fluid, it may not be an essential if what is desired is simply the bulk/average velocity of the fluid.

- *Average velocity of the fluid:* In order to obtain information about average velocity of the fluid due to the piezoelectric micropump, several measurement methods can be utilized: *a) Liquid micro-flow meter:* This method involves the use of a sensor that is attached to the capillary that carries the pumped fluid away from the micropump. A typical device for this kind of measurement can deliver measurements with a resolution as precise as 100 nL/min providing measurements of flow rate between 30 and 1000 µl/min. *b) Conventional methods involving tracking the meniscus in the outlet capillary:* This technique involves tracking the meniscus in the outlet capillary to obtain information about the volume of fluid that has been pumped at any given time. A temporal derivative can then be taken to obtain volumetric flow rate. Schematic of setup for measurement and visualization of the flow in the channel is shown in Figure 11.3.

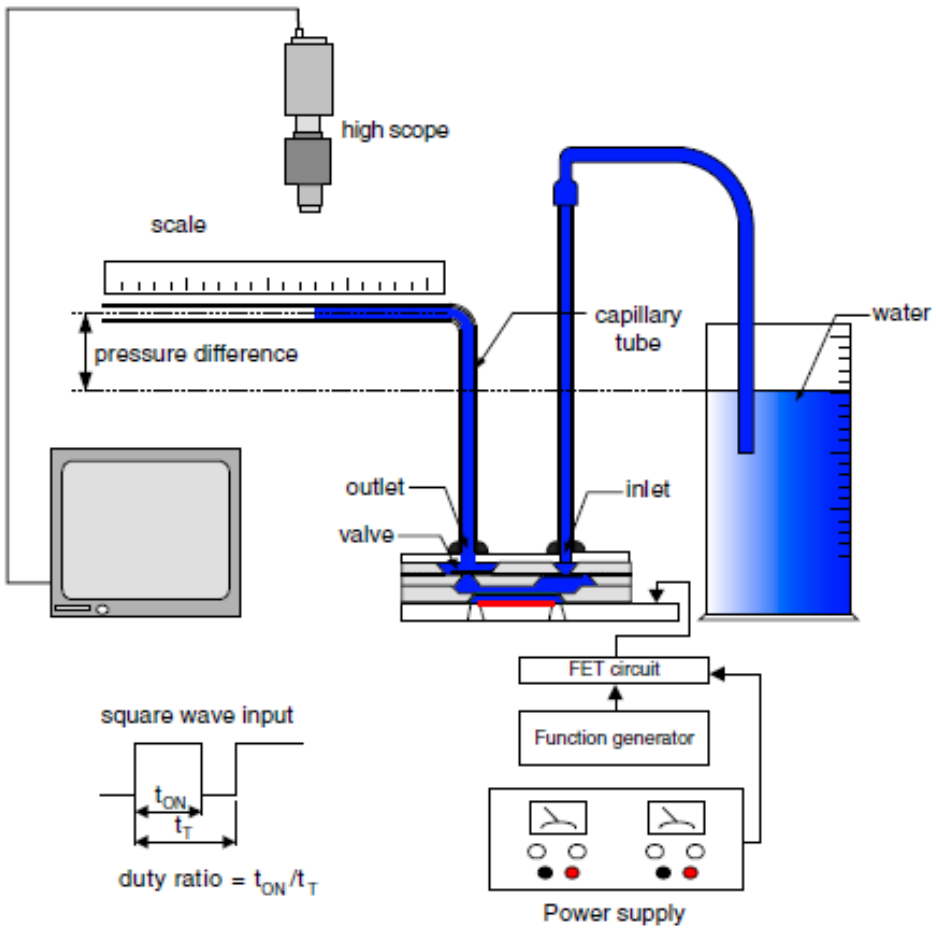

Figure 11.3 Setup to measure volumetric flow rate [136].

- *Deflection of membrane/wave propagation:* A feasible way of collecting data for the wave propagation on the piezoelectric micropump membrane is using a laser-CCD camera system. The laser is used to illuminate the membrane and to create a grid that can be used to track points on the surface. Temporal information about the surface can hence be obtained. Typical devices of this type are: laser confocal displacement meter and laser vibrometer system. It is important to note, these systems may not be cost effective. It may therefore be wise to question the necessity of this particular measurement. With regards to the present piezoelectric

valveless micropump models that has being developed, the value of the particular measurement of the deflection of membrane may not be significant enough to warrant the cost of the set-up required to obtain it.

- *Fluid pressure:* A way of obtaining the measurement of the pressure of the fluid is to use an in-flow measurement device. Such a device does not have a significant effect on the properties of the flow.

11.3.2 Novel Cooling Method for Microelectronic Devices by Piezoelectric Actuators

Piezoelectric oscillating agitator (also known as piezoelectrically actuated fan) is a promising application of acoustic wave devices [26]. A piezoelectrically actuated vibrating cantilever induces fluid flow by converting electrical energy to mechanical vibrations, which in turn agitate the surrounding fluid. Such a vibrating cantilever is referred to as a fan, as it provides localized cooling when the flow generated impinges on a heated surface, such as a heat sink mounted on a microelectronic device or a light-emitting diode (LED) package (see Figure 11.4).

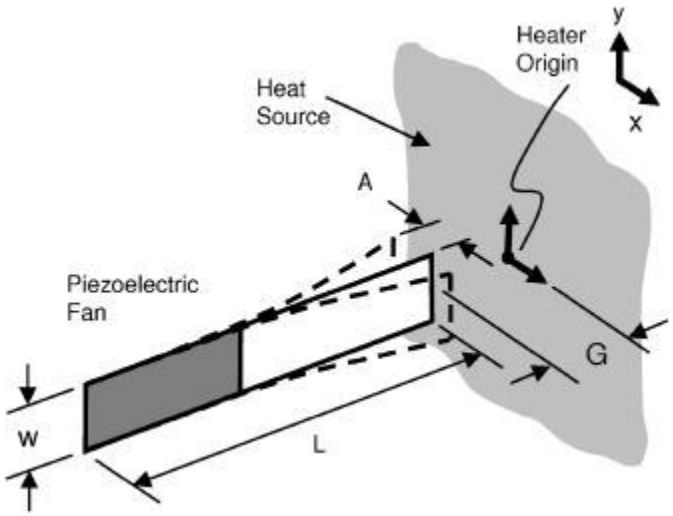

Figure 11.4 Schematic of the piezoelectric oscillating agitator [26].

Our present research effort resulted in the development of piezoelectric transducer generated acoustically excited flow models. The development of a piezoelectrically actuated fan model is still an open field where the only work is a preliminary investigation by Acikalin and Garimella (2009) [25]. The main complication for piezoelectric actuated fan arises due to the deflection of the cantilever beams. The order of the deflections can introduce non-linearity in the solid deformation. For such applications the skewness of computational grid for fluid model might be beyond the acceptable numerical limits. As a result arbitrary Lagrangian- Eulerian methods for the fluid mechanics models is perhaps the only possible choice. As a result non-linearity in solid piezoelectric and structural material deflections have to be considered. Accurate non-linear material elasticity data and a sufficient non-linear solid deformation models are required for that purpose.

11.3.3 Modeling of a Flexural Plate Wave Chemical Sensor

Flexural plate wave (FPW) devices are modeled by wall perturbed acoustic waves in the present work [23] and also investigated in [17, 19, 22, 118] by other researchers. The present developed model can be extended to incorporate the deflection of structural silicon nitride (Si_3N_4 is strongly anisotropic) and piezoelectric thin films (zinc oxide, ZnO) with the solid deformation models. Important applications of the simulation of FPW devices are chemical vapor [33, 115, 137, 138] or liquid sensing [115, 119, 135, 139-143] (see Fig. 11.5). Benzene, toluene, m-xylene, trichloroethylene, perchloroethylene, 2-Butanone, n-Butylacetate, 2-propanol and water vapors in air were measured [138] with the chemical vapor sensor shown in Figure 11.5. Limits of detection as low as 0.3 ppm were achieved from a 34 cm^3 air sample.

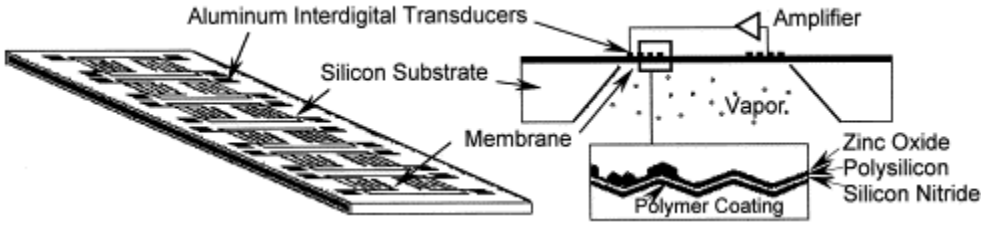

Figure 11.5 Flexural plate wave chemical vapor sensor. Integrated FPW six-sensor array (left) and structure of individual sensor (right) [138].

Silicon nitride is often used as a structural layer of the membrane to support its rigidity and zinc oxide is the most commonly used piezoelectric transducer in FPW devices. The multifield analysis of FPW device including the interaction of the chemical vapor or liquid loading (for viscosity, density and speed of sound in the working fluid measurements) is still an open field. The schematic of liquid sensors for a typical biosensor application are shown in Figure 11.6

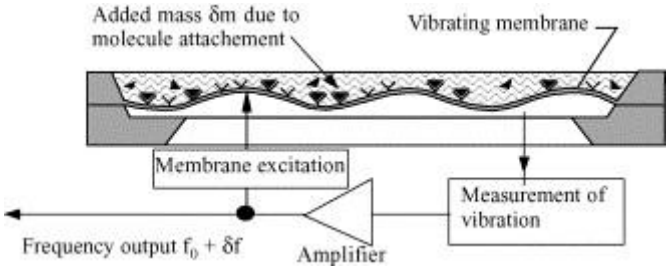

Figure 11.6 The schematic of flexural plate wave liquid sensors [141].

The main complication for FPW sensor model arises due to the extremely thin nature of the structural-piezoelectric membrane (total thickness is about one hundredth of a wave length) and the comparatively very long distance along the acoustic delay path direction (about 20 wave lengths) for guided acoustic wave propagation. A FPW sensor

model requires acoustic energy conserving boundary conditions. The boundary conditions are called 'perfectly matched layer' (PML) type which are currently not implemented to the models of the present work. The numerical models will thus become computationally expensive due to the aspect ratio of about 2000 (in x and y directions) and the required couplings of fluidic, mechanical and electrical fields.

11.3.4 Simulation of Heat Generation and Fluid Flow in a Surface Acoustic Wave Device

Surface acoustic wave devices have been used as sensors in biomedical applications and explosive vapor detectors in military applications [13]. To generate a surface acoustic wave in a single crystal piezoelectric transducer, one needs to have some type of anisotropy. Otherwise, the wave in the solid material dissipates to the bulk of the domain (creating a combination of bulk and surface waves), causing significant loss of the input energy. It also creates electrical noise during operation as a sensor. The coupled fluid-solid model can be used to explore acoustically generated flows in microchannel surface acoustic wave sensors. SAWs generated by ST-quartz (ST is a metallographic orientation) have not been investigated in the literature due to the poor conversion efficiency from electrical to mechanical wave in ST-quartz. The energy loss transforms to heat leading undesirable results in biosensors. However, this device can still be used as a micropump. Heat equation can also be simultaneously solved (possibly with a variable property of water). The periodicity of interdigitated transducer electrode pairs is very small in size and most of the piezoelectric transduction action occurs adjacent to these electrodes. The analysis of fluid flow generated by surface acoustic waves therefore requires very fine computational grid closer to the electrodes and the model is

computationally expensive. Perfectly matched layer boundary conditions can be implemented to overcome the listed limitations.

11.3.5 Development of Smart Structures Using Different Piezoelectric Wave Modes

Each of the devices, shown schematically in Figure 1.4 earlier uses a unique acoustic mode [11] and generates different acoustic wave patterns. The piezoelectric wave modes investigated in the present research are film bulk acoustic resonators and flexural plate wave devices. Both investigations are concentrated on pumping/mixing of fluids in a closed microfluidic conduit. Piezoelectric actuation can also be used in micro particle positioning (concentration, separation or mixing), transporting fluid droplets across a surface, chaotic convection of droplets, surface reactions, sonic cleaning and biological detection. Different piezoelectric wave modes can be investigated for the listed applications and generated acoustic waves can be compared to develop novel microfluidic sensors and actuators. As an example, flow fields generated in a microchannel by $LiNb0_3$ (lithium niobate) and PZT (particulate zirconate titanate) can be compared where $LiNb0_3$ generates surface acoustic waves and PZT generates bulk acoustic waves. Micro-scale smart structures can be fabricated by combining the surface acoustic wave and bulk acoustic wave.

11.3.6 Investigation of Lithium Tantalate for Novel Sensor Applications

The analysis of Piezoelectric SAW chemical sensor is limited to the Hydrogen detection using palladium coated $LiNbO_3$ substrates in the literature [144]. It is found that for liquid sensing applications $LiTa0_3$ is more desirable and it makes the suggested sensor attractive for microfluidics research. To utilize a chemical sensor in liquid environment mass loading and signal change due to a well known surface reaction can be investigated.

Since the effective mass of the membrane will change with time due to the chemical reaction, the electric field generated by the SAW device will change. The developed models should be able to predict the surface acoustic wave actuation and predict the effective mass of the membrane.

11.3.7 Numerical model (code) Improvements

All the simulations conducted were run on a serial machine. The code can be parallelized so that the simulations can be run in cluster machines, which would reduce the computation time significantly. In the present version of the codes, full anisotropy in solid deformation/materials models was implemented with collaboration with ESI CFD. The solid deformation models require the use of direct linear equation solvers since the pre-conditioners for piezoelectric material stress solvers are not readily present. Once the iterative solvers are made possible for solid models, it would reduce the computation time and memory requirement for computations and it would enable the parallelization of the code enabling to run in cluster machines. PISO algorithm is known to handle the simulation of fluid flow in fluid structure interactive problems efficiently, and it can be implemented to the code. The present fluid flow models are purely on Eulerian description of the flows with a transfinite interpolation algorithm to account for remeshing. In the contained flows (closer to the moving boundaries in acoustically excited flows) arbitrary Eulerian-Lagrangian methods are known to be computationally more efficient. Rigid wall boundary conditions for the some walls of piezoelectric actuators were employed; this is an idealized case. The code can be further improved so that it can handle the conservation of acoustic mechanical energy for guided wave applications in flexural plate wave piezoelectric actuators.

LIST OF REFERENCES

[1] Hak, M. G., 2002, The MEMs Handbook, CRC Press, Notre Dame, Indiana.

[2] Ermakov, S. V., Jacobson, S. C., and Ramsey, J. M., 1998, "Computer simulations of electrokinetic transport in microfabricated channel structures " Anal. Chem., 70, p. 4494.

[3] Bercovici, M., Lele, S. K., and Santiago, J. G., 2009, "Open source simulation tool for electrophoretic stacking, focusing, and separation," Journal of Chromatography A, 1216, pp. 1008-1018.

[4] Wong, P. K., Chen, C. Y., Wang, T. H., and Ho, C. M., 2004, "Electrokinetic bioprocessor for concentrating cells and molecules," Anal Chem, 76(23), pp. 6908-6914.

[5] Tsai, C.-H., Yang, R.-J., Tai, C.-H., and Fu, L.-M., 2005, "Numerical simulation of electrokinetic injection techniques in capillary electrophoresis microchips," Electrophoresis, 26(3), pp. 674-686.

[6] Yang, R.-J., Tseng, T.-I., and Chang, C.-C., 2005, "End effects on electro-osmotic flows in micro-channels," J Micromech Microeng, 15(2), pp. 254-262.

[7] Park, H. M., and Choi, Y. J., 2009, "Electroosmotic flow driven by oscillating zeta potentials: Comparison of the Poisson–Boltzmann model, the Debye–Hückel model and the Nernst–Planck model," International Journal of Heat and Mass Transfer, 52(19–20), pp. 4279-4295.

[8] Tang, G. Y., Yan, D. G., Yang, C., Gong, H. Q., Chai, J. C., and Lam, Y. C., 2006, "Assessment of Joule heating and its effects on electroosmotic flow and electrophoretic transport of solutes in microfluidic channels," Electrophoresis, 27(3), pp. 628-639.

[9] Santini, J. T., Richards, A. C., Scheidt, R. A., Cima, M. J., and Langer, R. S., 2000, "Microchip technology in drug delivery," Annals of Medicine, 32(6), pp. 377-379.

[10] Ashraf, M. W., Tayyaba, S., and Afzulpurkar, N., 2011, "Micro electromechanical systems (MEMS) based microfluidic devices for biomedical applications," International Journal of Molecular Sciences, 12(6), pp. 3648-3704.

[11] Ballantine, D. S., and Knovel (Firm), 1997, "Acoustic wave sensors theory, design, and physico-chemical applications," Applications of modern acoustics, Academic Press, San Diego.

[12] Zourob, M., Elwary, S., and Turner, A., 2008, Principles of bacterial detection : biosensors, recognition receptors, and microsystems, Springer, New York.

[13] Durmus, N. G., L.Lin, R., Kozberg, M., Demirci, D., Hosseini, A. K., and Demirci, U., 2008, "Acoustics based biosensors," Encyclopedia of microfluidics and nanofluidics, D. Li, ed., Springer, New York.

[14] Cular, S., Sankaranarayanan, S. K. R. S., and Bhethanabotla, V. R., 2008, "Enhancing effects of microcavities on shear-horizontal surface acoustic wave sensors: A finite element simulation study," Appl Phys Lett, 92(24), p. 244104.

[15] Luginbuhl, P., Collins, S. D., Racine, G. A., Gretillat, M. A., de Rooij, N. F., Brooks, K. G., and Setter, N., 1998, "Ultrasonic flexural Lamb-wave actuators based on PZT thin film," Sensor Actuat a-Phys, 64(1), pp. 41-49.

[16] Luginbuhl, P., Collins, S. D., Racine, G. A., Gretillat, M. A., deRooij, N. F., Brooks, K. G., and Setter, N., 1997, "Microfabricated Lamb wave device based on PZT sol-gel thin film for mechanical transport of solid particles and liquids," J Microelectromech S, 6(4), pp. 337-346.

[17] Moroney, R. M., White, R. M., and Howe, R. T., 1991, "Microtransport induced by ultrasonic Lamb waves," Appl Phys Lett, 59(7), p. 774.

[18] Singh, R., Sankaranarayanan, S. K. R. S., and Bhethanabotla, V. R., 2009, "Enhanced surface acoustic wave biosensor performance via delay path modifications in mutually interacting multidirectional transducer configuration: A computational study," Appl Phys Lett, 95(3), p. 034101.

[19] Weinberg, M. S., Dube, C. E., Petrovich, A., and Zapata, A. M., 2003, "Fluid damping in resonant flexural plate wave device," J. Microelectromech. Syst., 12, pp. 567-576.

[20] Länge, K., Rapp, B. E., and Rapp, M., 2008, "Surface acoustic wave biosensors: a review," Anal Bioanal Chem, 391, pp. 1509–1519.

[21] Loh, B. G., Hyun, S., Ro, P. I., and Kleinstreuer, C., 2002, "Acoustic streaming induced by ultrasonic flexural vibrations and associated enhancement of convective heat transfer," J Acoust Soc Am, 111(2), pp. 875-883.

[22] Nguyen, N. T., and White, R. M., 1999, "Design and optimization of an ultrasonic flexural plate wave micropump using numerical simulation," Sensors and Actuators A Physical, 77(3), pp. 229-236.

[23] Sayar, E., and Farouk, B., 2011, "Acoustically generated flows in microchannel flexural plate wave sensors: Effects of compressibility," Sensors and Actuators A Physical, 171(2), pp. 317-323.

[24] Weinberg, M. S., Cunningham, B. T., and Clapp, C. W., 2000, "Modeling flexural plate wave devices," J. Microelectromech. Syst., 9(3), pp. 370-379.

[25] Acikalin, T., and Garimella, S. V., 2009, "Analysis and prediction of the thermal performance of piezoelectrically actuated fans," Heat Transfer Eng, 30(6), pp. 487-498.

[26] Kimber, M., Garimella, S. V., and Raman, A., 2007, "Local heat transfer coefficients induced by piezoelectrically actuated vibrating cantilevers," Journal of Heat Transfer, 129(9), pp. 1168-1176.

[27] Babchin, A. J., Chow, R. S., and Sawatzky, R. P., 1989, "Electrokinetic measurements by electroacoustical methods," Advances in Colloid and Interface Science, 30(1-2), pp. 111-151.

[28] Tan, M. K. Y., L. Y.; Friend, J. R., 2009, "Rapid fluid flow and mixing induced in microchannels using surface acoustic waves," Europhysics Letters, 87(4), p. 47003.

[29] Barnkob, R., Augustsson, P., Laurell, T., and Bruus, H., "An automated full-chip micro-piv setup for measuring microchannel acoustophoresis: simultaneous determination of forces from acoustic radiation and acoustic streaming," Proc. 14th International Conference on Miniaturized Systems for Chemistry and Life Sciences, Royal society of chemistry, pp. 1247-1249.

[30] Du, X. Y., Swanwick, M. E., Fu, Y. Q., Luo, J. K., Flewitt, A. J., Lee, D. S., Maeng, S., and Milne, W. I., 2009, "Surface acoustic wave induced streaming and pumping in 128° Y-cut LiNbO3 for microfluidic applications," J Micromech Microeng, 19(3), p. 035016.

[31] Guttenberg, Z., Rathgeber, A., Keller, S., Radler, J. O., Wixforth, A., Kostur, M., Schindler, M., and Talkner, P., 2004, "Flow profiling of a surface-acoustic-wave nanopump," Phys Rev E, 70(5), pp. -.

[32] Koster, D., 2007, "Numerical simulation of acoustic streaming on surface acoustic wave-driven biochips," Siam J Sci Comput, 29(6), pp. 2352-2380.

[33] Nguyen, N. T., Meng, A. H., Black, J., and White, R. M., 2000, "Integrated flow sensor for in situ measurement and control of acoustic streaming in flexural plate wave micropumps," Sensor Actuat a-Phys, 79(2), pp. 115-121.

[34] Sankaranarayanan, S. K. R. S., Cular, S., Bhethanabotla, V. R., and Joseph, B., 2008, "Flow induced by acoustic streaming on surface-acoustic-wave devices and its application in biofouling removal: A computational study and comparisons to experiment," Phys Rev E, 77(6), p. 066308.

[35] Sankaranarayanan, S. K. R. S., Singh, R., and Bhethanabotla, V. R., 2010, "Acoustic streaming induced elimination of nonspecifically bound proteins from a surface acoustic wave biosensor: Mechanism prediction using fluid-structure interaction models," J Appl Phys, 108(10), p. 104507.

[36] Sano, A., Rlatsui, Y., and Shiokawa, S., "A new manipulator based on surface acoustic wave streaming," Proc. 1997 IEEE Ultrasonics Symposium, pp. 467 - 470.

[37] Singh, R., Sankaranarayanan, S. K. R. S., and Bhethanabotla, V. R., 2010, "Enhancement of acoustic streaming induced flow on a focused surface acoustic wave device: Implications for biosensing and microfluidics," J Appl Phys, 107(2), p. 024503.

[38] Suh, Y. K., and Kang, S., 2008, "Acoustic streaming," Encyclopedia of microfluidics and nanofluidics, D. Li, ed., Springer, New York.

[39] Uchida, T., Suzuki, T., and Shiokawa, S., "Investigation of acoustic streaming excited by surface acoustic waves," Proc. Ultrasonics Symposium, 1995. Proceedings., 1995 IEEE, pp. 1081-1084 vol.1082.

[40] Gantner, A., Hoppe, R., Köster, D., Siebert, K., and Wixforth, A., 2007, "Numerical simulation of piezoelectrically agitated surface acoustic waves on microfluidic biochips," Computing and Visualization in Science, 10(3), pp. 145-161.

[41] Xu, G. S., and Jiang, Q., 2001, "A finite element analysis of second order effects on the frequency response of a SAW device," J Intel Mat Syst Str, 12(2), pp. 69-77.

[42] Chang, C. C., and Yang, R. J., 2007, "Electrokinetic mixing in microfluidic systems," Microfluid Nanofluid, 3(5), pp. 501-525.

[43] Yasuda, K., 2000, "Non-destructive, non-contact handling method for biomaterials in micro-chamber by ultrasound," Sensors and Actuators B Chemical, 64(1-3), pp. 128-135.

[44] Yang, Z., Matsumoto, S., Goto, H., Matsumoto, M., and Maeda, R., 2001, "Ultrasonic micromixer for microfluidic systems," Sensors and Actuators A Physical, 93(3), pp. 266-272.

[45] Bengtsson, M., and Laurell, T., 2004, "Ultrasonic agitation in microchannels," Analytical and Bioanalytical Chemistry, 378(7), pp. 1716-1721.

[46] Tseng, W.-K., Lin, J.-L., Sung, W.-C., Chen, S.-H., and Lee, G.-B., 2006, "Active micro-mixers using surface acoustic waves on Y-cut 128° LiNbO3," J Micromech Microeng, 16(3), pp. 539-548.

[47] Tsai, M.-C., and Leu, T.-S., 2007, "The study of flexible plate wave device for micro pumping system," IEEE, pp. 452-457.

[48] Ashraf, M. W., Tayyaba, S., Nisar, A., Afzulpurkar, N., Bodhale, D. W., Lomas, T., Poyai, A., and Tuantranont, A., 2010, "Design, fabrication and analysis of silicon hollow microneedles for transdermal drug delivery system for treatment of hemodynamic dysfunctions," Cardiovasc Eng, 10(3), pp. 91-108.

[49] Bodhale, D., Nisar, A., and Afzulpurkar, N., 2010, "Structural and microfluidic analysis of hollow side-open polymeric microneedles for transdermal drug delivery applications," Microfluid Nanofluid, 8(3), pp. 373-392.

[50] Liu, G. J., Shen, C. L., Yang, Z. G., Cai, X. X., and Zhang, H. H., 2010, "A disposable piezoelectric micropump with high performance for closed-loop insulin therapy system," Sensor Actuat a-Phys, 163(1), pp. 291-296.

[51] Ma, B., Liu, S., Gan, Z. Y., Liu, G. J., Cai, X. X., Zhang, H. H., and Yang, Z. G., 2006, "A PZT insulin pump integrated with a silicon microneedle array for transdermal drug delivery," Microfluid Nanofluid, 2(5), pp. 417-423.

[52] Nisar, A., AftuIpurkar, N., Mahaisavariya, B., and Tuantranont, A., 2008, "MEMS-based micropumps in drug delivery and biomedical applications," Sensor Actuat B-Chem, 130(2), pp. 917-942.

[53] Nisar, A., Afzulpurkar, N., Tuantranont, A., and Mahaisavariya, B., 2008, "Three dimensional transient multifield analysis of a piezoelectric micropump for drug delivery system for treatment of hemodynamic dysfunctions," Cardiovasc Eng, 8(4), pp. 203-218.

[54] Laser, D. J., and Santiago, J. G., 2004, "A review of micropumps," J Micromech Microeng, 14(6), pp. R35-R64.

[55] Ahn, C. H., Choi, J.-W., Beaucage, G., Nevin, J. H., Lee, J.-B., Puntambekar, A., and Lee, J. Y., "Disposable smart lab on a chip for point of care clinical diagnostics," Proc. Proceedings of the IEEE, pp. 154-173

[56] Fan, B., Song, G., and Hussain, F., 2005, "Simulation of a piezoelectrically actuated valveless micropump," Smart Mater Struct, 14(2), pp. 400-405.

[57] Kumar, M., Feke, D. L., and Belovich, J. M., 2005, "Fractionation of cell mixtures using acoustic and laminar flow fields," Biotechnol Bioeng, 89(2), pp. 129-137.

[58] Sayar, E., and Farouk, B., 2012, "Multifield analysis of a piezoelectric valveless micropump: effects of actuation frequency and electric potential " Smart Mater Struct, 21(7), p. 075002.

[59] Sayar, E., and Farouk, B., "Modeling of acoustically augmented electroosmotic flows in microchannels," Proc. ASME 2010 International Mechanical Engineering Congress & Exposition, IMECE2010, p. 40395.

[60] Sayar, E., and Farouk, B., "Multifield analysis of a piezoelectric valveless micropump," Proc. ASME 2011 International Mechanical Engineering Congress & Exposition, IMECE2011, p. 65021.

[61] Sayar, E., and Farouk, B., "Three dimensional dynamic analysis of a piezoelectric valveless micropump: Effects of working fluid," Proc. ASME 2012 International Mechanical Engineering Congress & Exposition, IMECE2012, p. 88978.

[62] Nguyen, N. T., Huang, X. Y., and Chuan, T. K., 2002, "MEMS-micropumps: A review," J Fluid Eng-T Asme, 124(2), pp. 384-392.

[63] Olsson, A., Stemme, G., and Stemme, E., 1995, "A valve-less planar fluid pump with two pump chambers," Sensors and Actuators A: Physical, 47(1–3), pp. 549-556.

[64] Cui, Q. F., Liu, C. L., and Zha, X. F., 2007, "Study on a piezoelectric micropump for the controlled drug delivery system," Microfluid Nanofluid, 3(4), pp. 377-390.

[65] Fu, L. M., Lin, J. Y., and Yang, R. J., 2003, "Analysis of electroosmotic flow with step change in zeta potential," Journal of Colloid and Interface Science, 258(2), pp. 266-275.

[66] Bhattacharyya, S., and Nayak, A. K., 2009, "Electroosmotic flow in micro/nanochannels with surface potential heterogeneity: An analysis through the Nernst–Planck model with convection effect," Colloids and Surfaces A: Physicochemical and Engineering Aspects, 339(1–3), pp. 167-177.

[67] Burgreen, D., and Nakache, F. R., 1964, "Electrokinetic flow in ultrafine capillary slits," The Journal of Physical Chemistry, 68(5), pp. 1084-1091.

[68] Wu, C.-H., and Yang, R.-J., 2006, "Improving the mixing performance of side channel type micromixers using an optimal voltage control model," Biomedical Microdevices, 8(2), pp. 119-131.

[69] Lin, C.-H., Fu, L.-M., and Chien, Y.-S., 2004, "Microfluidic t-form mixer utilizing switching electroosmotic flow," Anal Chem, 76(18), pp. 5265-5272.

[70] Fu, L.-M., Leong, J.-C., Lin, C.-F., Tai, C.-H., and Tsai, C.-H., 2007, "High performance microfluidic capillary electrophoresis devices," Biomedical Microdevices, 9(3), pp. 405-412.

[71] Fu, L.-M., and Lin, C.-H., 2003, "Numerical analysis and experimental estimation of a low-leakage injection technique for capillary electrophoresis," Anal Chem, 75(21), pp. 5790-5796.

[72] Mitchell, M. J., Qiao, R., and Aluru, N. R., 2000, "Meshless analysis of steady-state electro-osmotic transport," J Microelectromech S, 9(4), pp. 435-449.

[73] Jin, X., Joseph, S., Gatimu, E. N., Bohn, P. W., and Aluru, N. R., 2007, "Induced electrokinetic transport in micro−nanofluidic interconnect devices," Langmuir, 23(26), pp. 13209-13222.

[74] Zhang, Y., Gu, X.-J., Barber, R. W., and Emerson, D. R., 2004, "An analysis of induced pressure fields in electroosmotic flows through microchannels," Journal of Colloid and Interface Science, 275, pp. 670–678.

[75] Zhang, Y., Barber, R. W., and Emerson, D. R., "Creeping electro-osmotic flow through micro-channels," Proc. 13th Micro-Mechanics Europe Workshop (MME02), pp. 153-156).

[76] Chakraborty, S., and Padhy, S., 2008, "Induced pressure gradients due to entrance and exit effects in electroosmotically driven flows through nanopores within the continuum regime," Journal of Physics D: Applied Physics, 41(6), p. 065502.

[77] Hessel, V., Löwe, H., and Schönfeld, F., 2005, "Micromixers—a review on passive and active mixing principles," Chemical Engineering Science, 60, pp. 2479–2501.

[78] Grate, J. W., Martin, S. J., and White, R. M., 1993, "Acoustic-wave microsensors .1.," Anal Chem, 65(21), pp. A940-A948.

[79] Nabavi, M., 2009, "Steady and unsteady flow analysis in microdiffusers and micropumps: a critical review," Microfluid Nanofluid, 7(5), pp. 599-619.

[80] Ullmann, A., 1998, "The piezoelectric valve-less pump - performance enhancement analysis," Sensor Actuat a-Phys, 69(1), pp. 97-105.

[81] Olsson, A., Stemme, G., and Stemme, E., 1999, "A numerical design study of the valveless diffuser pump using a lumped-mass model," J Micromech Microeng, 9(1), pp. 34-44.

[82] Morris, C. J., and Forster, F. K., 2003, "Low-order modeling of resonance for fixed-valve micropumps based on first principles," J Microelectromech S, 12(3), pp. 325-334.

[83] Gamboa, A. R., Morris, C. J., and Forster, F. K., 2005, "Improvements in fixed-valve micropump performance through shape optimization of valves," J Fluid Eng-T Asme, 127(2), pp. 339-346.

[84] Jang, L. S., Chao, S. H., Holl, M. R., and Meldrum, D. R., 2005, "Microfluidic circulatory flows induced by resonant vibration of diaphragms," Sensor Actuat a-Phys, 122(1), pp. 141-148.

[85] Andersson, H., van der Wijngaart, W., Nilsson, P., Enoksson, P., and Stemme, G., 2001, "A valve-less diffuser micropump for microfluidic analytical systems," Sensor Actuat B-Chem, 72(3), pp. 259-265.

[86] El Gowini, M. M., and Moussa, W. A., 2009, "A reduced three dimensional model for SAW sensors using finite element analysis," Sensors-Basel, 9(12), pp. 9945-9964.

[87] Chen, S. C., Cheng, C. H., and Lin, Y. C., 2007, "Analysis and experiment of a novel actuating design with a shear mode PZT actuator for microfluidic application," Sensor Actuat a-Phys, 135(1), pp. 1-9.

[88] Cui, Q. F., Liu, C. L., and Zha, X. F., 2008, "Simulation and optimization of a piezoelectric micropump for medical applications," Int J Adv Manuf Tech, 36(5-6), pp. 516-524.

[89] Jeong, J., and Kim, C. N., 2007, "A numerical simulation on diffuser-nozzle based piezoelectric micropumps with two different numerical models," Int J Numer Meth Fl, 53(4), pp. 561-571.

[90] Yeo, L. Y., and Friend, J. R., 2009, "Ultrafast microfluidics using surface acoustic waves," Biomicrofluidics, 3, p. 012002.

[91] Cecchini, M., Girardo, S., Pisignano, D., Cingolani, R., and Beltram, F., 2008, "Acoustic-counterflow microfluidics by surface acoustic waves," Appl Phys Lett, 92(10).

[92] Friend, J., and Yeo, L. Y., 2011, "Microscale acoustofluidics: Microfluidics driven via acoustics and ultrasonics," Reviews of Modern Physics, 83(2), pp. 647-704.

[93] Pan, L. S., Ng, T. Y., Liu, G. R., Lam, K. Y., and Jiang, T. Y., 2001, "Analytical solutions for the dynamic analysis of a valveless micropump - a fluid-membrane coupling study," Sensor Actuat a-Phys, 93(2), pp. 173-181.

[94] Nguyen, N.-T., and Huang, X., "Numerical simulation of pulse-width-modulated micropumps with diffuser/nozzle elements," Proc. International Conference on Modeling and Simulation of Microsystems - MSM 2000, M.Laudon, and B. Romanowicz, eds., pp. 636-639.

[95] Tsui, Y. Y., and Lu, S. L., 2008, "Evaluation of the performance of a valveless micropump by CFD and lumped-system analyses," Sensor Actuat a-Phys, 148(1), pp. 138-148.

[96] Bianchi, F., Ferrigno, A., and Girault, H. H., 2000, "Finite element simulation of an electroosmotic-driven flow division at a T-junction of microscale dimensions," Anal Chem, 72, p. 1987.

[97] Yang, R.-J., Fu, L.-M., and Lin, Y.-C., 2001, "Electroosmotic Flow in Microchannels," Journal of Colloid and Interface Science, 239(1), pp. 98–105

[98] Shin, Y. S., Chung, J. W., Kladias, N., Panides, E., Domoto, G. A., and Grigoropoulos, C. P., 2005, "Compressible flow of liquid in a standing wave tube," J Fluid Mech, 536, pp. 321-345.

[99] Van Doormaal, J. P., and Raithby, G. D., 1984, "Enhancements of the SIMPLE method for predicting incompressible fluid flows," Numer. Heat Transfer, 7, pp. 147-163.

[100] ESI-US, R. D., 2010, CFD-ACE+ modules manual V2010, Huntsville, AL.

[101] Tsai, C.-H., Wang, Y.-N., Lin, C.-F., Yang, R.-J., and Fu, L.-M., 2006, "Experimental and numerical investigation into leakage effect in injectors of microfluidic devices," Electrophoresis, 27(24), pp. 4991-4998.

[102] Beyer, R. T., 1997, "Nonlinear acoustics: The parameter B/A," Nonlinear acoustics, M. F. Hamilton, and D. T. Blackstock, eds., Academic Press, San Diego, California, pp. 25-40.

[103] Shutilov, V. A., 1988, Fundamental physics of ultrasound, Gordon and Breach Science Publishers, New York.

[104] Eriksson, L.-E., 1985, "Practical three-dimensional mesh generation using transfinite interpolation," SIAM Journal on Scientific and Statistical Computing, 6(3), p. 712.

[105] Auld, B. A., 1973, Acoustic fields and waves in solids, Wiley, New York,.

[106] Meeker, T. R., 1996, "Publication and proposed revision of ANSI/IEEE standard 176-1987 "ANSI/IEEE standard on piezoelectricity"," Ieee T Ultrason Ferr, 43(5), pp. 717-718.

[107] Fan, Z. H., and Harrison, D. J., 1994, "Micromachining of capillary electrophoresis injectors and separators on glass chips and evaluation of flow at capillary intersections," Anal Chem, 66(1), pp. 177-184.

[108] Alarie, J. P., Jacobson, S. C., Culbertson, C. T., and Ramsey, J. M., 2000, "Effects of the electric field distribution on microchip valving performance, Wiley-VCH Verlag GmbH, 100 pp.," Electrophoresis, 21(1), p. 100.

[109] Oran, E. S., and Boris, J. P., 2001, Numerical simulation of reactive flow, Cambridge University Press, Cambridge, U.K. ; New York.

[110] Chen, C. H., and Santiago, J. G., 2002, "A planar electroosmotic micropump," J Microelectromech S, 11(6), pp. 672-683.

[111] Patankar, N. A., and Hu, H. H., 1998, "Numerical simulation of electroosmotic flow," Anal Chem, 70(9), pp. 1870-1881.

[112] J.Happel, and H.Brenner, 1965, Low Reynolds number hydrodynamics, Prentice-Hall, Englewood Cliffs,NJ.

[113] Schmid, P. J., and Henningson, D. S., 2001, Stability and transition in shear flows, Springer, New York.

[114] Moroney, R. M., 1995, "Ultrasonic microtransport," Ph.D., University of California, Berkeley.

[115] Grate, J. W., Wenzel, S. W., and White, R. M., 1991, "Flexural plate wave devices for chemical-analysis," Anal Chem, 63(15), pp. 1552-1561.

[116] Hu, S. P., Fan, C. M., Chen, C. W., and Young, D. L., 2005, "Method of fundamental solutions for Stokes' first and second problems," J Mech, 21(1), pp. 25-31.

[117] Castellanos, A., Ramos, A., Gonzalez, A., Green, N. G., and Morgan, H., 2003, "Electrohydrodynamics and dielectrophoresis in Microsystems: scaling laws," Journal of Physics D: Applied Physics, 36, pp. 2584-2597

[118] Vellekoop, M. J., 1998, "Acoustic wave sensors and their technology," Ultrasonics, 36, pp. 7-14.

[119] Martin, B. A., Wenzel, S. W., and White, R. M., 1990, "Viscosity and density densing with ultrasonic plate waves," Sensor Actuat a-Phys, 22(1-3), pp. 704-708.

[120] Systèmes, D., 2010, Abaqus Modules Manual 6.8, Villacoublay, France.

[121] Weis, R. S., and Gaylord, T. K., 1985, "Lithium niobate - summary of physical properties and crystal structure," Appl Phys a-Mater, 37(4), pp. 191-203.

[122] Singh, R., Sankaranarayanan, S. K. R. S., and Bhethanabotla, V. R., 2009, "Orthogonal surface acoustic wave device based on langasite for simultaneous biosensing and biofouling removal," Appl Phys Lett, 94(26), p. 263503.

[123] Koike, T., Sakamoto, C., Sakashita, T., Hayashi, K., Kanzaki, S., and Ogawa, K., 2012, "Effects of a perilymphatic fistula on the passive vibration response of the basilar membrane," Hearing Research, 283(1–2), pp. 117-125.

[124] Olsson, A., Enoksson, P., Stemme, G., and Stemme, E., 1997, "Micromachined flat-walled valveless diffuser pumps," J Microelectromech S, 6(2), pp. 161-166.

[125] Stemme, E., and Stemme, G., 1993, "A valveless diffuser/nozzle-based fluid pump," Sensor Actuat a-Phys, 39(2), pp. 159-167.

[126] Olsson, A., Larsson, O., Holm, J., Lundbladh, L., Ohman, O., and Stemme, G., 1998, "Valve-less diffuser micropumps fabricated using thermoplastic replication," Sensor Actuat a-Phys, 64(1), pp. 63-68.

[127] Olsson, A., Enoksson, P., Stemme, G., and Stemme, E., 1996, "A valve-less planar pump isotropically etched in silicon," J Micromech Microeng, 6(1), pp. 87-91.

[128] Olsson, A., Stemme, G., and Stemme, E., 2000, "Numerical and experimental studies of flat-walled diffuser elements for valve-less micropumps," Sensor Actuat a-Phys, 84(1-2), pp. 165-175.

[129] Zhu, M. L., Kirby, P., Wacklerle, M., Herz, M., and Richter, M., 2009, "Optimization design of multi-material micropump using finite element method," Sensor Actuat a-Phys, 149(1), pp. 130-135.

[130] Koch, M., Harris, N., Evans, A. G. R., White, N. M., and Brunnschweiler, A., 1998, "A novel micromachined pump based on thick-film piezoelectric actuation," Sensor Actuat a-Phys, 70(1-2), pp. 98-103.

[131] Schabmueller, C. G. J., Koch, M., Mokhtari, M. E., Evans, A. G. R., Brunnschweiler, A., and Sehr, H., 2002, "Self-aligning gas/liquid micropump," J Micromech Microeng, 12(4), pp. 420-424.

[132] Hsu, Y. C., Lin, S. J., and Hou, C. C., 2008, "Development of peristaltic antithrombogenic micropumps for in vitro and ex vivo blood transportation tests," Microsyst Technol, 14(1), pp. 31-41.

[133] Sollier, E., Murray, C., Maoddi, P., and Di Carlo, D., 2011, "Rapid prototyping polymers for microfluidic devices and high pressure injections," Lab Chip, 11(22), pp. 3752-3765.

[134] CHEMnetBASE., 2009, "Handbook of chemistry and physics online," CRC Press, Boca Raton, Fla.

[135] Wenzel, S. W., and White, R. M., 1990, "Flexural plate-wave gravimetric chemical sensor," Sensor Actuat a-Phys, 22(1-3), pp. 700-703.

[136] Sim, W. Y., Yoon, H. J., Jeong, O. C., and Yang, S. S., 2003, "A phase-change type micropump with aluminum flap valves," J Micromech Microeng, 13(2), pp. 286-294.

[137] Cunningham, B., Weinberg, M., Pepper, J., Clapp, C., Bousquet, R., Hugh, B., Kant, R., Daly, C., and Hauser, E., 2001, "Design, fabrication and vapor characterization of a microfabricated flexural plate resonator sensor and application to integrated sensor arrays," Sensor Actuat B-Chem, 73(2-3), pp. 112-123.

[138] Cai, Q. Y., Park, J., Heldsinger, D., Hsieh, M. D., and Zellers, E. T., 2000, "Vapor recognition with an integrated array of polymer-coated flexural plate wave sensors," Sensor Actuat B-Chem, 62(2), pp. 121-130.

[139] Black, J. P., White, R. M., and Grate, J. W., "Microsphere capture and perfusion in microchannels using flexural plate wave structures," Proc. Ultrasonics Symposium, 2002. Proceedings. 2002 IEEE, pp. 475-479 vol.471.

[140] Laurent, T., Bastien, F. O., Pommier, J.-C., Cachard, A., Remiens, D., and Cattan, E., 2000, "Lamb wave and plate mode in ZnO/silicon and AlN/silicon membrane: Application to sensors able to operate in contact with liquid," Sensors and Actuators A: Physical, 87(1–2), pp. 26-37.

[141] Jia, H., Duhamel, R., Manceau, J. F., de Labachelerie, M., and Bastien, F., 2005, "Improvement of Lamb waves sensors: Temperature sensitivity compensation," Sensors and Actuators A: Physical, 121(2), pp. 321-326.

[142] Li, F., Wu, Y. H., Manceau, J. F., and Bastien, F., 2008, "Temperature compensation of lamb wave sensor by combined antisymmetric mode and symmetric mode," Appl Phys Lett, 92(7).

[143] Zhou, L. Q., Manceau, J. F., and Bastien, F., 2009, "Influence of gases on Lamb waves propagations in resonator," Appl Phys Lett, 95(22).

[144] EL Gowini, M. M., and Moussa, W., 2010, "A finite element model of a MEMS-based surface acoustic wave hydrogen sensor," Sensors-Basel, 10(2), pp. 1232-1250.

LIST OF PUBLICATIONS (from the present research)

Journal Publications

1. E. Sayar and B. Farouk, "Multifield analysis of a piezoelectric valveless micropump: effects of actuation frequency and electric potential, " *Smart Materials and Structures*, vol. 21, p. 075002, 2012.

2. E. Sayar and B. Farouk, "Acoustically generated flows in microchannel flexural plate wave sensors: effects of compressibility," *Sensors and Actuators A-Physical*, vol. 171, pp. 317-323, 2011.

3. E. Sayar and B. Farouk, "Electroosmotic augmentation in flexural plate wave micropumps," *Journal of Microelectromechanical Systems*, submitted July 2012. (under review)

4. E. Sayar and B. Farouk, "Piezoelectric valveless micropump: development of a three dimensional structural/fluid dynamic model," *Microfluidics and Nanofluidics*, submitted June 2012. (under review)

Conference Proceedings

1. E. Sayar and B. Farouk, "Three dimensional dynamic analysis of a piezoelectric valveless micropump: effects of working fluid," *Proc. ASME 2012 International Mechanical Engineering Congress & Exposition*, IMECE2012, Houston, Texas, p. 88978.

2. E. Sayar and B. Farouk, "Multifield analysis of a piezoelectric valveless micropump," *Proc. ASME 2011 International Mechanical Engineering Congress & Exposition*, IMECE2011, Denver, Colorado, 2011, p. 65021.

3. E. Sayar and B. Farouk, "Modeling of acoustically augmented electroosmotic flows in microchannels," *Proc. ASME 2010 International Mechanical Engineering Congress & Exposition, IMECE2010*, Vancouver, Canada, 2010, p. 40395.

VITA

Ersin Sayar was born in Amasya, Turkey in July, 1984. He received his Bachelor's in Mechanical Engineering from Istanbul Technical University (ITU), Turkey in 2006 with concentration on energy. He then joined ITU as a teaching assistant and worked for two years in the Department of Mechanical Engineering. He received his Master's of Science (M.Sc.) in Mechanical Engineering from Istanbul Technical University, where his research work was related to boiling heat transfer from an oscillating liquid column. He received Turkish Government Fellowship for international graduate programs covering his doctoral studies. He was a student of English language program of University of Pennsylvania for six of months. He joined the doctoral program in the department of Mechanical Engineering and Mechanics at Drexel University, Philadelphia, in January 2009. His current research interests include microfluidics and relevant solid deformation / electrokinetics problems. He plans for a teaching and research career when he returns to his homeland.